Pairing and two-fluid physics in low-dimensional quantum systems

Lorenzo Gotta

université
PARIS-SACLAY

Pairing and two-fluid physics in low-dimensional quantum systems

Appariement et modèle à deux fluides dans les systèmes quantiques de basse dimension

Thèse de doctorat de l'université Paris-Saclay

École doctorale n° 564, Physique en Île-de-France (PIF)
Spécialité de doctorat : Physique
Graduate School : Physique, Référent : Faculté des sciences d'Orsay

Thèse préparée dans l'unité de recherche
LPTMS (Université Paris-Saclay, CNRS),
sous la direction de **Guillaume ROUX, Maître de conférences**,
la co-direction de **Pascal SIMON, Professeur des universités**,
le co-encadrement de **Leonardo MAZZA, Maître de conférences**.

Thèse soutenue à Paris-Saclay, le 8 Novembre 2022, par

Lorenzo GOTTA

Composition du jury

Guido PUPILLO Professeur des universités, Université de Strasbourg	Président de jury
Karyn LE HUR Directrice de recherche, Ecole Polytechnique	Rapportrice & Examinatrice
Oded ZILBERBERG Professeur des universités, University of Konstanz	Rapporteur & Examinateur
Jonathan RUHMAN Professeur assistant, Bar-Ilan University	Examinateur

THESE DE DOCTORAT

NNT : 2022UPASP092

université PARIS-SACLAY | ÉCOLE DOCTORALE Physique en Île-de-France (PIF)

Titre : Appariement et modèle à deux fluides dans les systèmes quantiques de basse dimension
Mots clés : appariement, superfluidité, fluides quantiques, simulateurs quantiques

Résumé : Cette thèse traite des propriétés de l'état fondamental de systèmes quantiques à plusieurs corps de fermions sans spin qui présentent une formation d'états liés. Nous commençons par discuter des phénomènes d'appariement induits par les interactions densité-densité, montrant que l'extension de la portée de ces dernières peut conduire à l'observation des phases liquides de Luttinger exotiques avec des agrégats. Nous poursuivons par l'étude de l'appariement dans une chaîne unidimensionnelle des fermions sans spin où le saut d'une seule particule entre en compétition avec une interaction corrélée de sauts de paires. Nous dévoilons une nouvelle transition d'une phase liquide de Luttinger à couplage faible vers une phase liquide de Luttinger de paires. Celle-ci se produit à travers une phase intermédiaire où un liquide de fermions isolés coexiste avec un liquide de paires sans séparation de phase. Nous confirmons la stabilité de cette nouvelle phase de coexistence vis-à-vis d'une faible interaction densité-densité, qui induit plutôt une séparation de phase entre les fermions appariés et non appariés dans le régime de couplage fort. Enfin, nous généralisons le terme de saut de paire à un terme générique de saut de multimère, prouvant ainsi la robustesse de la phase de coexistence en tant que scénario de transition générique entre un liquide de Luttinger avec une granularité à une seule particule et un avec une granularité moléculaire. Nous concluons en montrant que les modèles de fermions sans spin présentant des sauts de paires peuvent héberger des états de type "cicatrices quantiques", ouvrant ainsi de nouvelles voies vers l'étude de la brisure d'ergodicité faible dans des systèmes quantiques isolés à N-corps.

Title : Pairing and two-fluid physics in low-dimensional quantum systems
Keywords : pairing, superfluidity, quantum fluids, quantum simulators

Abstract : The present thesis deals mainly with the ground-state properties of quantum many-body systems of spinless fermions that display bound-state formation. We start by discussing the pairing phenomena induced by density-density interactions, showing that extending the range of the latter can lead to the observation of exotic Luttinger liquid phases with cluster granularity. We continue the study of pairing in a one-dimensional chain of spinless fermions where single-particle hopping competes with a correlated pair-hopping interaction. We unveil a novel transition from a weak-coupling Luttinger liquid phase to a paired Luttinger liquid phase, that occurs through an intervening phase where a liquid of isolated fermions coexists with a liquid of pairs without phase separation. We confirm the stability of this novel coexistence phase against the addition of a weak nearest-neighbor density-density interaction, which is shown to induce instead phase separation between paired and unpaired fermions in the strong-coupling regime. Finally, we generalize the pair-hopping term to a generic multimer-hopping term, thereby proving the robustness of the coexistence phase as the generic transition scenario between a Luttinger liquid with single-particle granularity and one with molecular granularity. We conclude by showing that models of spinless fermions featuring pair-hopping can host quantum many-body scars, thus opening further routes towards the study of weak ergodicity breaking in isolated many-body quantum systems.

Contents

Acknowledgements

I would like to start by thanking my three thesis supervisors Guillaume, Leonardo and Pascal for their daily support and constant availability to discuss problems of any sort. Their careful scientific supervision and competent guidance have been crucial in the development of this manuscript and in conveying me their passion for research in quantum many-body physics. I consider myself very lucky to have been their doctoral student for the past three years.

Similarly, I would like to thank the LPTMS members that I discussed my projects with during these three years, namely L. Zadnik, M. Fagotti, S. Bocini, K. Bidzhiev, A. Biella, D. Petrov, A. Tononi and J. Givois. Our meetings broadened my scientific horizons and allowed me to explore topics and techniques that I would not have encountered by myself. In the same way, I thank A. Kantian, I. Mahyaeh, T. Köhler, H. Katsura, H. Yoshida and O. Zilberberg for expressing interest in our work by reaching out to us and enriching our understanding of perspective research directions connected to our results.

I also want to thank O. Zilberberg, K. Le Hur, G. Pupillo and J. Ruhman for accepting to be part of my PhD jury. In particular, I would like to thank the rapporteurs for accepting the time-consuming task of reviewing the thesis manuscript. I am thankful as well to S. Ouvry and T. Lahaye for monitoring the progress of the PhD work as members of the monitoring committee during our yearly common meetings.

Furthermore, I am extremely grateful to the University of Paris-Saclay, which hosted me at LPTMS during the PhD work, and to DIM Sirteq, whose generous financial support allowed me to carry out our research activities.

I am sincerely happy to have spent these years in the joyful and convivial environment of LPTMS. For this I have to thank all other PhD students and postdocs of the laboratory, who constantly contributed to creating a friendly atmosphere during our uncountably many lunch breaks and kept organizing several initiatives to spend pleasant time together outside of the workplace. Analogously, I have to thank my friends Alessandro, Francesca, Francesco, Giulia, Leonardo and Saverio for the free time that we spent together during these three years and that always managed to release stress and put a smile on my face.

Finally, I am grateful to my family for the unvaluable support and care, both during happy holiday moments and, even more importantly, during some severe difficulties faced during this chapter of my life. Without their unconditional acceptance of my autonomous choices and their daily encouragement, all of this would not have been possible.

Publications related to this thesis

1. L. Gotta, L. Mazza, P. Simon, and G. Roux, *Pairing in spinless fermions and spin chains with next-nearest neighbor interactions*, Phys. Rev. Research **3**, 013114 (2021).
   DOI: https://doi.org/10.1103/PhysRevResearch.3.013114

2. L. Gotta, L. Mazza, P. Simon, and G. Roux, *Two-fluid coexistence in a spinless fermions chain with pair hopping*, Phys. Rev. Lett. **126**, 206805 (2021).
   DOI: https://doi.org/10.1103/PhysRevLett.126.206805

3. L. Gotta, L. Mazza, P. Simon, and G. Roux, *Two-fluid coexistence and phase separation in a one dimensional model with pair hopping and density interactions*, Phys. Rev. B **104**, 094521 (2021).
   DOI: https://doi.org/10.1103/PhysRevB.104.094521

4. L. Gotta, L. Mazza, P. Simon, and G. Roux, *Kinetic formation of trimers and multimers in a spinless fermionic chain*, Phys. Rev. B **105**, 134512 (2022).
   DOI: https://doi.org/10.1103/PhysRevB.105.134512

5. L. Gotta, L. Mazza, P. Simon, and G. Roux, *Condensates of pairs as exact many-body scars in a chain of spinless fermions*, arXiv:2207.07531.
   DOI: https://doi.org/10.48550/arXiv.2207.07531

Introduction: Pairing in condensed-matter physics

The topic of pairing in fermionic systems traverses the history of condensed matter physics since the publication of the seminal work where Bardeen, Cooper and Schrieffer formulated the theory of superconductivity that carries their names [1]. The instability of the Fermi surface to the formation of pairs of electrons with opposite momenta and spin, called Cooper pairs, allows a system to develop nontrivial remarkable properties such as a vanishing electrical resistance and the expulsion of magnetic fields from the bulk. The microscopic mechanism of Cooper pair formation is a phonon-mediated interelectronic attractive interaction; if the latter is sufficiently strong to overcome the screened Coulomb repulsion, then the Fermi liquid description of the electronic system becomes unstable towards the onset of the superconducting state, where the decay of the Cooper pair is inhibited by the presence of a filled Fermi sea of conduction electrons.

Such a discovery paved the way to the understanding of other fascinating phenomena, such as superfluidity in ^3He [2]. The phenomenon challenged the attempts towards its theoretical explanation, as it appeared to be in contradiction with a fundamental quantum property of the system, namely the atomic statistics. Indeed, since the ^4He nucleus consists of an even number of nucleons, its total spin adds up to zero, ensuring that ^4He atoms are bosons. Contrarily, the ^3He atoms are fermions, as they possess an odd number of nucleons and thus a half-integer total spin $\frac{1}{2}$. Before the formulation of the BCS theory, the low-temperature behavior of a Fermi system was believed to be captured without exceptions by the degenerate Fermi gas and was not compatible with the phenomenon of macroscopic quantum coherence occurring in a superfluid system, contrarily to the case of bosons, which are allowed to macroscopically condense into a single quantum state. The discovery of the possibility of Cooper pair formation in fermionic systems was therefore preliminary to the understanding of three distinct ^3He superfluid phases in terms of Cooper pairs with total spin $S = 1$ and nonvanishing relative angular momentum.

The relevance of pairing in superconducting systems acquired more recently a further boost in relation to the search for the exotic Majorana quasiparticle in condensed-matter systems. The Majorana particles were proposed by Ettore Majorana [3] as novel fundamental particles that, unlike electrons and positrons, constitute their own antiparticle. So far, no fundamental particle of the standard model with such properties has been found. Unlike in the context of high-energy physics, Majorana particles can appear in condensed matter physics as exotic emergent quasiparticle excitations, since the fundamental constituents of low-energy many-body systems are ordinary electrons and ions.

Superconductors provide a natural platform for the search of Majorana quasiparticles. As the superconducting phase is a $U(1)$ symmetry-breaking phase, its quasiparticle excitations take the form of Bogoliubov quasiparticles, which consist of a superposition of an electron and a hole. As the form of Bogoliubov quasiparticles suggests, the search for excitations that enjoy the defining properties of Majorana fermions must occur in spinless superconducting systems, namely in paired fermionic systems with a single fermionic species rather than two, as in standard electronic systems. The first major step towards understanding how Majorana quasiparticles appear in condensed-matter systems is the pioneering work of A. Y. Kitaev in Ref. [4], where a paradigmatic lattice model of spinless fermions displaying the representative properties of topologically-protected edge modes is presented. The setup consists of a chain of spinless fermions in proximity to a three-dimensional superconducting reservoir that acts as an effective pairing field acting on the one-dimensional quantum wire.

In its so-called topological phase, the model possesses zero-energy Majorana excitations localized at the boundaries of the system, which realizes a ground-state degeneracy intrinsically protected by the existence of a gap in the excitation spectrum. Remarkably, the existence of boundary zero-energy

Majorana modes reflects itself in the nonzero value of a winding number, defined from the excitation spectrum in periodic boundary conditions, that acts as a topological invariant and allows to discriminate between the topological and the trivial phases of the model. This feature is the simplest manifestation of the so-called bulk-boundary correspondence.

The major motivation towards the experimental realization of platforms supporting such exotic excitations is intimately connected to the goal of achieving quantum computation by taking advantage of topological properties. As briefly mentioned, the zero-energy edge modes of a one-dimensional p-wave superconductor and their two-dimensional analogue, represented by Majorana zero-energy modes bound to superconducting vortices in two-dimensional $p + ip$ spinless superconductors [5], introduce degeneracies in the ground-state subspace separated by a nonvanishing energy gap from the remainder of the spectrum. This general property implies the existence of degenerate ground-state subspaces whose basis states encode quantum information as topologically-protected qubits.

Performing logical operations inside the ground-state degenerate subspace amounts to an adiabatic exchange of Majorana quasiparticles, which results in a unitary non-abelian tranformation of the wavefunction within the ground-state manifold. The resulting rich algebraic braiding properties exhibited by systems where adiabatic exchange processes of Majorana modes can be implemented, such as two-dimensional topological superconductors and networks of one-dimensional topological superconductors [6], represent an ideal implementation of a toplogically-protected quantum information-processing system. We remark that non-abelian anyons, namely quasiparticles hosted by two-dimensional systems exhibiting a statistics that is neither fermionic nor bosonic, emerge in fractional quantum Hall states as well, whose universal properties have been shown to coincide with the ones of two-dimensional topological superconductors in the case of Moore-Read states in the breakthrough work in Ref. [7].

The interest in pairing phenomena is not limited to the study of solid-state devices, but received further inputs and raised several questions within the cold-atom community. The increasingly sophisticated experimental platforms based on cold atoms, thoroughly described by I. Bloch, J. Dalibard and W. Zwerger in Ref. [8], allow to simulate the behavior of complex quantum many-body systems in extreme regimes of parameter and in presence of high-resolution detection schemes to characterize quantitatively the ensuing exotic quantum phenomena. Among the outstanding properties that can be targeted within the framework of cold-atom based quantum simulators, we mention here quantum phase transitions [9, 10], topological phenomena [11, 12, 13] and nonequilibrium dynamics [14, 15].

The flexibility of cold-atom platforms in terms of interaction properties, internal degrees of freedom and dimensionality of the artificial solid realized by means of an optical lattice motivate the investigation of pairing in the one-dimensional setting. The latter is indeed known to exhibit atypical features when compared to its higher-dimensional counterpart, as correlation effects among the microscopic degrees of freedom are enhanced and lead to anomalous properties even in equilibrium at zero temperature, where one is interested in ground-state physics. More precisely, the Fermi liquid picture does not hold anymore and is replaced by the concept of Luttinger liquid, whose low-energy excitations consist of collective acoustic modes rather than individual quasiparticles with long lifetime. Moreover, as the spontaneous breaking of the $U(1)$ symmetry at equilibrium is prohibited in one-dimensional systems with short-range interactions, superconductivity manifests itself by the identification of leading quasi-long-range order in pair correlations, typically accompanied by a gap in suitably defined single-particle correlations.

In view of the aforementioned considerations, the properties of pairing in low-dimensional quantum matter express a remarkably rich landscape of results. The most prominent, paradigmatic case study in the field is that of the Fermi-Hubbard model [16], where an arbitrarily small attractive on-site interaction drives the system to a Luttinger liquid phase with gapped spin excitations, associated to the formation of pairs of fermions with opposite spins in the system. The tunability of the number of internal degrees of freedom of the individual atoms in cold-atom-based quantum simulators stimulated several generalizations of this result to the study of the formation of multiparticle composites in density-imbalanced fermionic mixtures [17, 18, 19] and of the onset of the Fulde-Ferrell-Larkin-Ovchinnikov pairing in spin-imbalanced fermionic mixtures [20, 21, 22]. The latter host an exotic form of superconducting behavior coexisting with magnetism, whose defining microscopic signature is the formation of finite-momentum Cooper pairs.

We conclude by mentioning that the relevance of pairing is not limited to equilibrium properties, since it has recently extended to problems revolving around the question of thermalization of isolated quantum many-body systems thanks to the phenomenon of quantum many-body scars. Their introduction stems

from the observation of long-lived coherent oscillations in the time evolution of local observables in a cold-atom experiment with Rydberg atoms [14]. Many-body scars are exceptional eigenstates in the bulk of the spectrum of a nonintegrable many-body Hamiltonian, as they violate the eigenstate-thermalization hypothesis by exhibiting anomalous entanglement properties and off-diagonal long-range order and by giving rise to infinitely long-lived coherent oscillations in the time evolution of local observables. Among the several systems where they have been discovered, it is worth mentioning a plethora of deformations of the Fermi-Hubbard model [23, 24] that possess η-pairing states, namely condensates of noninteracting on-site singlet pairs of spinful fermions, as exact quantum many-body scars.

This thesis aims at the study of pairing in low-dimensional quantum systems. Signatures supporting the existence of Majorana zero-energy modes have been found in semiconducting nanowires featuring spin-orbit coupling and Zeeman splitting, coupled by proximity to a higher-dimensional superconducting system [25]. Naturally, the high-versatility of cold-atom-based experimental setups makes them ideal candidates for the unambiguous identification of Majorana quasiparticles [11]. However, while a spin-orbit coupling and a Zeeman field can be effectively generated in cold-atom systems, it is significantly more challenging to externally induce pairing correlations than in solid-state devices.

These observations naturally demand to understand whether intrinsic attractive interactions in one-dimensional number-conserving systems can display the topological properties of the Kitaev chain. In order to answer such question, it is crucial to understand preliminarly the features of paired phases and pairing transitions in low-dimensional quantum matter. On a more technical side, the specific instance of pairing in systems of spinless fermions is targeted, as standard approaches to the study of one-dimensional systems fail to describe it and novel *ad hoc* phenomenological approaches are required [26, 27, 28].

Our work puts a particular emphasis on the ground-state properties of models of spinless fermions where bound-state formation is induced via a kinetic term that enhances the delocalization of fermions as tightly-bound pairs or, more generically, multimers. Contrarily to the case of systems where pairing is induced by density-density interactions, we show how the ground-state phase diagram of models featuring the competition between single-particle hopping and correlated multimer-hopping can be naturally interpreted within unconventional effective two-fluid descriptions [27]. By showcasing the simplicity and effectiveness of two-fluid approaches, we hope to pave the way towards further applications of such ideas to the investigation of a wider range of problems in the physics of low-dimensional quantum systems.

Structure of the thesis

The thesis is organized as follows:

1. In chapter 1, we broadly introduce the topic of pairing from a historical perspective. We start from the discussion of superconductivity and of topological phenomena, highlighting the role of pairing as a fundamental ingredient. We conclude with an introduction to the cold-atom platforms and a more focused discussion of the plethora of pairing phases studied in the literature of low-dimensional systems, which are naturally realized in quantum simulators.

2. In chapter 2, we start the discussion of our work, where we investigate in a systematic way the ground-state phase diagram of a chain of spinless fermions with density-density interactions extending up to next-to-nearest-neighbor distance. Coherently with the general spirit of the manuscript, we highlight the observation of exotic Luttinger liquid phases, including a paired phase, among the findings of the study.

3. In chapter 3, we continue the study of pairing in systems of spinless fermions with the analysis of the ground-state properties of a Hamiltonian featuring the competition between single-particle hopping and correlated pair-hopping. The latter induces the kinetic formation of pairs by lowering the energy of states that exhibit pair delocalization. We unveil the existence of a novel pairing transition, that, instead of being direct, occurs through an intervening extended phase where a liquid of pairs coexists with a liquid of unbound fermions without phase-separating from it. We describe such phase with the help of a phenomenological two-fluid model.

4. In chapter 4, we extend the results of chapter 3 by studying the ground-state phase diagram of the aforesaid model in presence of a nearest-neighbor density-density interaction term. We probe

the stability of the coexistence phase at finite values of the additional interaction parameter and describe, in a different parameter regime, a phase separation between pairs and unbound fermions with another phenomenological two-fluid picture.

5. In chapter 5, we generalize the results of chapter 3 to the class of spinless fermion Hamiltonians featuring a competition between single-particle hopping and correlated multimer hopping. We demonstrate once more the usefulness of two-fluid approaches in the description of bound-state formation in systems of spinless fermions and establish the onset of coexistence phases between a liquid of unbound fermions and a liquid of multimers as a generic feature of such a family of Hamiltonians.

6. In chapter 6, we conclude the manuscript with the presentation of our preliminary results on weak ergodicity-breaking in chains of spinless fermions. More precisely, we thoroughly characterize a tower of many-body scar states embedded in the spectrum of a nonintegrable spinless fermion Hamiltonian. We show that the aforesaid many-body scars take the form of a condensate of spinless η-pairs, thus extending known results on spinful η-pairing states as many-body scars to the spinless case.

Introduction en français: Appariement en physique de la matière condensée

Le thème de l'appariement dans les systèmes fermioniques traverse l'histoire de la physique de la matière condensée depuis la publication des travaux fondateurs où Bardeen, Cooper et Schrieffer ont formulé la théorie de la supraconductivité qui porte leurs noms [1]. L'instabilité de la surface de Fermi vis-à-vis de la formation de paires d'électrons d'impulsions et spin opposées, appelées paires de Cooper, permet à un système de développer des propriétés non triviales remarquables telles qu'une résistance électrique qui disparaît et l'expulsion des champs magnétiques du cœur du supraconducteur. Le mécanisme microscopique de formation de paires de Cooper est une interaction interelectronique médiée par les phonons; si cette dernière est suffisamment forte pour surmonter la répulsion de Coulomb, alors la description en liquide de Fermi du système électronique devient instable vis-à-vis de l'état supraconducteur, dans lequel la désintégration de la paire de Cooper est inhibée par la présence d'une mer de Fermi remplie d'électrons de conduction.

Une telle découverte a ouvert la voie à la compréhension d'autres phénomènes fascinants, tels que la superfluidité de ^3He [2]. Le phénomène a posé problème quant à son explication théorique, car il semble être en contradiction avec une propriété quantique fondamentale du système, à savoir les statistiques atomiques. En effet, puisque le noyau ^4He se compose d'un nombre pair de nucléons, son spin total est nul, assurant que les atomes d'^4He sont des bosons. Au contraire, les atomes d'^3He sont des fermions, car ils possèdent un nombre impair de nucléons et donc un spin total $\frac{1}{2}$. Avant la formulation de la théorie BCS, le comportement à basse température d'un système de fermions était considéré comme étant capturé par la théorie du gaz de Fermi dégénéré et n'était pas compatible avec le phénomène de cohérence quantique macroscopique survenant dans un système superfluide, contrairement au cas des bosons, qui sont autorisés à se condenser macroscopiquement dans un état quantique unique. La découverte de la formation de paires de Cooper dans les systèmes fermioniques était donc préliminaire à la compréhension des trois phases distinctes de l'^3He superfluide en termes de paires de Cooper avec spin total $S = 1$ et moment angulaire relatif non nul.

La pertinence de l'appariement dans les systèmes supraconducteurs a acquis plus récemment un nouvel élan dans la recherche des quasiparticules de Majorana dans les systèmes de matière condensée. Les particules de Majorana ont été proposées par Ettore Majorana [3] comme de nouvelles particules fondamentales qui, contrairement aux électrons et aux positrons, constituent leur propre antiparticule. Jusqu'à présent, aucune particule fondamentale du modèle standard avec de telles propriétés n'a été trouvée. Contrairement à la physique des hautes énergies, les particules de Majorana peuvent apparaître dans la physique de la matière condensée comme des excitations émergentes exotiques.

Les supraconducteurs constituent une plateforme naturelle pour la recherche des quasiparticules de Majorana. Comme la phase supraconductrice est une phase qui brise la symétrie $U(1)$, ses excitations prennent la forme de quasiparticules de Bogoliubov, qui consistent en une superposition d'un électron et d'un trou. Comme la forme des quasiparticules le suggère, la recherche d'excitations qui jouissent des propriétés définissant les Majorana fermions doit se produire dans les systèmes supraconducteurs sans spins, à savoir dans les systèmes fermioniques avec une seule espèce fermionique plutôt que deux, comme dans les systèmes électroniques standarts. La première étape majeure pour comprendre comment les quasiparticules de Majorana apparaissent dans les systèmes de matière condensée est le travail pionnier de A. Y. Kitaev dans la référence. [4], où est présenté un modèle paradigmatique de fermions sans spin sur réseau affichant les propriétés typiques des modes de bord protégés topologiquement. La configuration

consiste en une chaîne de fermions sans spins à proximité d'un réservoir supraconducteur tridimensionnel qui agit comme un champ d'appariement sur le fil quantique unidimensionnel.

Dans sa phase dite topologique, le modèle possède des excitations de Majorana à énergie nulle localisées aux extrémités du système, qui réalise une dégénérescence de l'état fondamental intrinsèquement protégée par l'existence d'un gap dans le spectre d'excitation. Remarquablement, l'existence de modes de Majorana d'énergie nulle se reflète dans la valeur non nulle d'un nombre d'entrelacements, défini à partir du spectre d'excitation dans des conditions limites périodiques, qui agit comme invariant topologique et permet de distinguer les phases topologique et triviale du modèle. Cette caractéristique est la manifestation la plus simple de la correspondance bulk-edge.

La principale motivation pour la réalisation expérimentale de plateformes renfermant ces excitations exotiques est intimement liée à l'objectif de réaliser le calcul quantique en tirant parti des propriétés topologiques. Comme on l'a mentionné brièvement, les modes de bord à énergie nulle d'un supraconducteur à ondes P unidimensionnel et leur analogue bidimensionnel, représentés par les modes à énergie nulle de Majorana liés à des vortex supraconducteurs dans des supraconducteurs bidimensionnels $p + ip$ sans spin [5], introduisent des dégénérescences dans le sous-espace de l'état fondamental, séparées par un écart d'énergie constant du reste du spectre. Cette propriété générale implique l'existence de sous-espaces dégénérés à l'état fondamental dont les états de base codent l'information quantique sous forme de qubits protégés topologiquement.

Effectuer des opérations logiques à l'intérieur du sous-espace dégénéré de l'état fondamental équivaut à un échange adiabatique de quasiparticules de Majorana, qui entraîne une transformation unitaire non abélienne de la fonction d'onde dans le sous-espace fondamental. Les riches propriétés de tressage algébriques résultantes des processus d'échange adiabatique des modes de Majorana peuvent être mis en œuvre, tels que des supraconducteurs topologiques bidimensionnels et des réseaux de supraconducteurs topologiques unidimensionnels [6]. Nous remarquons que les anyons non-abéliens, à savoir les quasiparticules hébergées par des systèmes bidimensionnels présentant une statistique qui n'est ni fermionique ni bosonique, émergent également dans les états quantiques fractionnaires de Hall, dont les propriétés universelles coïncident avec celles des supraconducteurs topologiques bidimensionnels dans le cas des états de Moore-Read [7].

L'intérêt pour l'appariement des phénomènes ne se limite pas à l'étude des dispositifs à semiconducteurs, mais a soulevé plusieurs questions au sein de la communauté des atomes froids. Les plateformes expérimentales de plus en plus sophistiquées basées sur des atomes froids, décrites en détail par I. Bloch, J. Dalibard et W. Zwerger dans Ref. [8], permettent de simuler le comportement de systèmes quantiques complexes à plusieurs corps dans des régimes extrêmes de paramètres et en présence de détection à haute résolution pour caractériser quantitativement les phénomènes quantiques exotiques qui en découlent. Parmi les propriétés exceptionnelles qui peuvent être ciblées dans le cadre des simulateurs quantiques basés sur les atomes froids, nous mentionnons ici les transitions de phase quantiques [9, 10], les phénomènes topologiques [11, 12, 13] et la dynamique hors d'équilibre [14, 15].

La flexibilité des plateformes à atomes froids en termes d'interaction, de degrés de liberté et de dimensionnalité du solide artificiel réalisé au moyen d'un réseau optique motivent l'étude de l'appariement dans le cadre unidimensionnel. Ce dernier est en effet connu pour présenter des caractéristiques atypiques par rapport à sa contrepartie de dimension supérieure, car les effets de corrélation entre les degrés de liberté sont amplifiés et conduisent à des propriétés anormales même en équilibre à température nulle, où l'on s'intéresse à la physique du fondamental. Plus précisément, l'image du liquide de Fermi ne tient plus et est remplacée par le concept de liquide de Luttinger, dont les excitations à basse énergie consistent en des modes acoustiques collectifs plutôt que des quasiparticules individuelles à longue durée de vie. De plus, comme la brisure spontanée de la symétrie $U(1)$ à l'équilibre est interdite dans les systèmes unidimensionnels avec des interactions à courte portée, la supraconductivité se manifeste des corrélations de paires à quasi-longue portée, et s'accompagne généralement de corrélations à une seule particule à courte portée.

Compte tenu des considérations susmentionnées, les propriétés de l'appariement dans la matière quantique de faible dimension présentent un paysage de résultats remarquablement riche. L'étude de cas la plus importante et paradigmatique dans ce domaine est celle du modèle de Fermi-Hubbard [16], où une petite interaction attractive conduit le système à une phase liquide de Luttinger avec des excitations gappées en spin, associée à la formation de paires de fermions avec des spins opposés. La possibilité de régler le nombre de degrés de liberté internes des atomes individuels dans les simulateurs quantiques

à base d'atomes froids a stimulé plusieurs généralisations de ce résultat à l'étude de la formation de multimères dans les mélanges fermioniques à densité inégales [17, 18, 19] et du début de l'appariement Fulde-Ferrell-Larkin-Ovchinnikov dans des mélanges fermioniques à spin déséquilibré [20, 21, 22]. Ce dernier héberge une forme exotique de comportement supraconducteur coexistant avec le magnétisme, dont la signature microscopique déterminante est la formation de paires de Cooper à impulsion finie.

Nous concluons en mentionnant que la pertinence de l'appariement ne se limite pas aux propriétés d'équilibre, puisqu'elle s'est récemment étendue à des problèmes tournant autour de la question de la thermalisation des systèmes quantiques isolés grâce au phénomène des cicatrices quantiques à N-corps. Leur introduction découle de l'observation d'oscillations cohérentes à longue durée de vie dans l'évolution temporelle des observables locales dans une expérience d'atomes froids avec des atomes de Rydberg [14]. Les états cicatrices sont des états propres rares du spectre d'un hamiltonien non intégrable, car ils violent l'hypothèse de thermalisation en présentant des propriétés d'intrication anormales et un ordre diagonal à longue portée et en donnant lieu à des oscillations cohérentes d'une durée infiniment longue dans l'évolution temporelle. Parmi les nombreux systèmes où ils ont été découverts, il convient de mentionner une pléthore de déformations du modèle de Fermi-Hubbard [23, 24] qui possèdent des états d'appariement η, à savoir des condensats de paires de fermions sans spin, comme états cicatrices quantiques.

Cette thèse vise l'étude de l'appariement dans les systèmes quantiques de faible dimension. Des signatures soutenant l'existence des modes d'énergie nulle de Majorana ont été trouvées dans des nanofils semi-conducteurs comportant un couplage spin-orbite et une levée de dégénérescence Zeeman, couplés par la proximité d'un système supraconducteur de plus grande dimension [25]. Naturellement, la grande polyvalence des installations expérimentales à base d'atomes froids en fait des candidats idéaux pour l'identification sans ambiguïté de quasiparticules de Majorana [11]. Cependant, alors qu'un couplage spin-orbite et un champ Zeeman peuvent être générés efficacement dans les systèmes à atomes froids, il est beaucoup plus difficile d'induire des corrélations d'appariement externes que dans les dispositifs à semi-conducteurs.

Ces observations exigent naturellement de comprendre si les interactions attractives dans les systèmes unidimensionnels qui conservent le nombre de particules peuvent afficher les propriétés topologiques de la chaîne de Kitaev. Afin de répondre à cette question, il est crucial de comprendre de façon préliminaire les caractéristiques des phases appariées et des transitions d'appariement dans la matière quantique de faible dimension. D'un côté plus technique, l'appariement dans les systèmes de fermions sans spin est abordé, comme les approches standard à l'étude des systèmes unidimensionnels ne parviennent pas à le décrire et *ad hoc* approches phénoménologiques sont nécessaires [26, 27, 28].

Notre travail met un accent particulier sur les propriétés d'état fondamental des modèles de fermions sans spin où la formation de l'état lié est induite par un terme cinétique qui améliore la délocalisation des fermions en tant que paires étroitement liées ou, plus généralement, en tant que multimères. Contrairement aux systèmes où l'appariement est induit par des interactions densité-densité, nous montrons comment le diagramme de phase des modèles présentant une concurrence entre le saut d'une particule unique et le saut corrélé de multimères peut être interprété naturellement dans des descriptions type modèles à deux fluides [27]. En montrant la simplicité et l'efficacité du modèle à deux fluides, nous espérons ouvrir la voie à d'autres applications comme l'étude d'un plus large éventail de problèmes dans la physique des systèmes quantiques de faible dimension.

Structure de la thèse

La thèse est organisée comme suit :

1. Au chapitre 1, nous présentons de façon générale le sujet de l'appariement dans une perspective historique. Nous partons de la discussion de la supraconductivité et des phénomènes topologiques, en soulignant le rôle de l'appariement comme ingrédient fondamental. Nous concluons par une introduction aux plates-formes à atomes froids et une discussion plus ciblée de la pléthore de phases d'appariement étudiées dans la littérature des systèmes à faible dimension, qui sont naturellement réalisées dans les simulateurs quantiques.

2. Dans le chapitre 2, nous commençons la discussion de notre travail, où nous étudions de manière systématique le diagramme de phase d'une chaîne de fermions sans spin avec des interactions

densité-densité s'étendant jusqu'à la distance plus proche voisin. En cohérence avec l'esprit général du manuscrit, nous soulignons l'observation des phases liquides exotiques de Luttinger, y compris une phase appariée, parmi les résultats de l'étude.

3. Dans le chapitre 3, nous poursuivons l'étude de l'appariement dans les systèmes de fermions sans spin avec l'analyse des propriétés de l'état fondamental d'un Hamiltonien mettant en exergue la concurrence entre le saut d'une seule particule et le saut de paire corrélé. Ce dernier induit la formation de paires en abaissant l'énergie des états qui présentent une délocalisation de paire. Nous dévoilons l'existence d'une nouvelle transition d'appariement, qui, au lieu d'être directe, se produit à travers une phase intermédiaire où un liquide de paires coexiste avec un liquide de fermions non liées sans séparation de phase. Nous décrivons cette phase à l'aide d'un modèle phénoménologique à deux fluides.

4. Dans le chapitre 4, nous étendons les résultats du chapitre 3 en étudiant le diagramme de phase du modèle susmentionné en présence d'un terme d'interaction densité-densité plus proche voisin. Nous étudions la stabilité de la phase de coexistence aux valeurs finies du paramètre d'interaction et décrivons, dans un régime de paramètre différent, une séparation de phase entre les fermions et les paires avec une autre image phénoménologique à deux fluides.

5. Dans le chapitre 5, nous généralisons les résultats du chapitre 3 à la classe des Hamiltoniens de fermion sans spin qui présente une compétition entre le saut à particule unique et le saut multimère corrélé. Nous démontrons une fois de plus l'utilité des approches à deux fluides afin d'établir la phase de coexistence entre un liquide de fermions non liés et un liquide de multimères comme une caractéristique générique d'une telle famille de Hamiltoniens.

6. Dans le chapitre 6, nous concluons le manuscrit avec la présentation de nos résultats préliminaires sur la brisure de l'ergodicité faible dans les chaînes de fermions sans spin. Plus précisément, nous caractériserons une tour d'états cicatrices enchâssés dans le spectre d'un Hamiltonien de fermions sans spin non intégrable. Nous montrons que les états cicatrices sus-mentionnés prennent la forme d'un condensat de η-paires sans spin, étendant ainsi les résultats connus sur les états de paires avec spin au cas d'états cicatrices de fermions sans spin.

Chapter 1

Pairing in low-dimensional quantum systems

In the present chapter we introduce the cornerstone of the thesis work, namely the problem of bound-state formation in many-body quantum systems. The first section reviews the theoretical analysis of bound-state formation in the many-body problem from a historical perspective, highlighting the role of paramount phenomena such as superconductivity and topological edge modes in attracting interest for the problem. More specialized material on the topic of pairing phenomena in low-energy physics of one-dimensional quantum many-body systems is presented in the second section.

1.1 Pairing phenomena in condensed matter and cold atoms

In the present section, we review the most important scientific breakthroughs in quantum many-body physics related to pairing phenomena. We start with superconductivity, present its features, mention its use in technological applications and conclude by touvhing upon the unsolved mechanism responsible for high-temperature superconductivity. We proceed by discussing the onset of topological superconductivity in the paradigmatic Kitaev chain, its implications for quantum computation and the proposals for its experimental realization.

1.1.1 Superconductivity

The phenomenon of pairing in condensed matter systems has been a main focus of the scientific community since the formulation of the Bardeen-Cooper-Schrieffer (BCS) theory [1]. The latter interprets the phenomenon of superconductivity in terms of an instability of the Fermi surface of a conventional metal to the formation of pairs of electrons with opposite momenta and spin, named Cooper pairs. The root of the instability is a phonon-mediated attractive electron-electron interaction, which induces a counterintuitive bound-state formation in the electronic system despite the presence of the bare repulsive Coulomb interaction among electrons.

The discovery of the phenomenon of BCS superconductivity has sparked a significant amount of interest both from a fundamental and from an application-oriented point of view. On the theoretical side, it represents a paradigmatic example of symmetry-breaking phase transition in quantum condensed matter systems. The system, when entering the superconducting phase, spontaneously breaks the global $U(1)$ symmetry associated to particle number conservation and develops a nonvanishing value of the superconducting order parameter associated to the opening of a superconducting gap [29]. The microscopic mechanisms at play can be understood within the universal, phenomenological approach of Ginzburg-Landau (GL) theory to symmetry-breaking phase transitions and have been linked directly to the phenomenological GL formulation [30], introduced before the microscopic treatment.

From a technological point of view, the most notorious experimental signatures of superconductivity, namely the lack of resistance and the expulsion of magnetic fields from the bulk of the material (Meissner effect), have found high-level applications in technical settings. Indeed, as superconductors can curry large currents without dissipation effects, they can serve as high-magnetic-field generators, with applications ranging from experimental physics to medical diagnostics. Similarly, the Meissner effect allows for the ideation of magnetic shields and levitation trains based on superconducting materials.

In view of all the opportunities offered by superconductors, the low value of the critical temperature T_c from the superconducting to the normal phase of the first examples of superconducting materials represented a barrier to the practical exploitation of the aforesaid properties. The discovery of high-T_c superconductors in 1986 in cuprates [31] was therefore accompanied with enthusiasm by the scientific community and motivated many efforts towards the theoretical understanding of the phenomenon. The complete understanding of the high-T_c superconducting mechanism remains a subject of ongoing research in theoretical condensed matter physics [32, 33]. Yet, the main novel ingredient in the emergence of superconducting pairing is the presence of strong correlations among the electrons, which fully invalidate the adoption of Fermi liquid theory as a starting point for the investigation of the instability towards superconducting order.

1.1.2 One-dimensional topological superconductivity and its realizations in condensed matter setups

The interest in pairing phenomena received an additional boost from the prediction of topological superconductivity and its relation with topological quantum computation, exemplified in the paradigmatic Kitaev model [4]. The model Hamiltonian describes a system of spinless fermions and reads:

$$\hat{H} = -t \sum_j \left(\hat{c}_j^\dagger \hat{c}_{j+1} + H.c. \right) - \mu \sum_j \hat{n}_j - \Delta \sum_j \left(\hat{c}_j \hat{c}_{j+1} + H.c. \right), \tag{1.1}$$

where t is the hopping parameter, μ is the chemical potential and Δ is an external pairing field imposed by proximity effect between the one-dimensional (1D) wire and a three-dimensional (3D) BCS superconductor. The operators $\hat{c}_j$, $\hat{c}_j^\dagger$ satisfy the canonical anticommutation relations $\{\hat{c}_j, \hat{c}_l\} = \{\hat{c}_j^\dagger, \hat{c}_l^\dagger\} = 0$, $\{\hat{c}_j, \hat{c}_l^\dagger\} = \delta_{l,j}$.

The model described by Hamiltonian (1.1) features, for every $\Delta \neq 0$, a topological phase transition from a trivial phase ($|\mu| > 2t$) to a topologically nontrivial phase ($|\mu| < 2t$). In the latter, when open boundary conditions (OBC) are used, the system admits a zero-energy excitation associated to a nonlocal fermionic mode defined by Majorana modes localized at the boundaries of the system. The striking feature that this observation entails is the topological protection of the ground-state degeneracy: the spatial separation between the boundary Majorana modes prevents any local operator from distinguishing between the two degenerate ground states and/or couple them; as a result the quantum state encoded in the occupation of the nonlocal zero-energy fermionic mode is protected from local perturbations.

The latter observation lies at the heart of the field of topological quantum computation [34]. In conventional platforms designed for quantum computation purposes, the information stored in individual qubits is affected by decoherence processes due to the presence of an environment. In the case of systems with topologically-protected ground state degeneracy, however, one aims at encoding quantum information into the nonlocal qubits forming a basis of the degenerate ground state subspace, as the latter are intrinsically protected from decoherence as a result of the exotic properties of the many-body system itself.

The interest around the experimental observation of Majorana zero-energy modes resulted in several theoretical proposals of condensed matter setups that would allow for their observation [35]. A first proposal [36] involves the exotic properties of two-dimensional (2D) topological band insulators [37, 38], namely insulating materials in the bulk that possess counterpropagating spin-polarized chiral modes at their boundaries. When proximitized to an s-wave superconductor, as in Fig. 1.1, the Hamiltonian of the system takes the form:

$$\hat{H} = \int dx \hat{\psi}^\dagger(x) \left[-iv\hat{\sigma}_z \partial_x - \mu \right] \hat{\psi}(x) + \Delta \int dx \left[\hat{\psi}_\uparrow \hat{\psi}_\downarrow + H.c. \right], \tag{1.2}$$

where μ is the chemical potential, v is the edge-state velocity and $\hat{\psi} = (\hat{\psi}_\uparrow, \hat{\psi}_\downarrow)^T$ is a two-component spinor containing the field operators $\hat{\psi}_\sigma(x)$ that annihilate an electron with spin σ at position x along the edge of the 2D topological insulator. The pairing field Δ inherited from the s-wave superconductor generates an effective intraband topological superconductive coupling between the quasimomentum modes belonging to the upper and lower band of the edge mode spectrum, which has acquired a gap due to the nonvanishing superconductive coupling Δ. Such an interaction term mimicks the second term in Hamiltonian (1.1), thus allowing to recover the Kitaev chain properties in a realistic condensed matter setup.

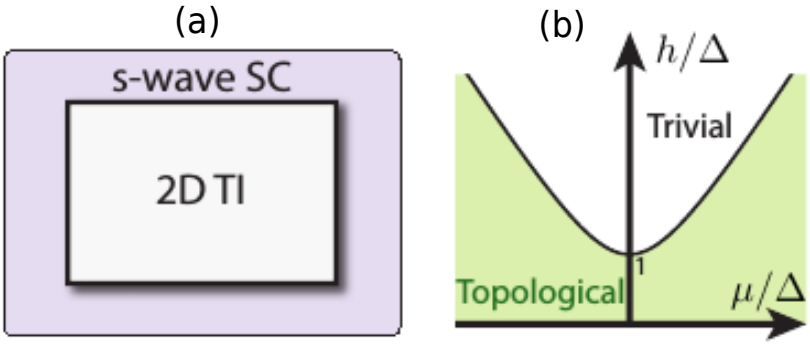

Figure 1.1: After Ref. [35]. (a) Schematic setup describing a 2D topological insulator in proximity to an s-wave superconductor. (b) Phase diagram of the edge of the system in Fig. (a) in the presence of an additional Zeeman field h.

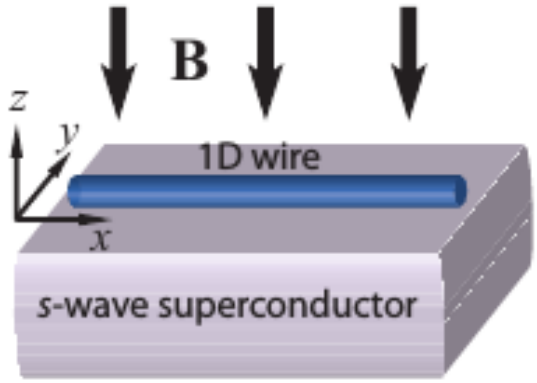

Figure 1.2: After Ref. [35]. Schematic representation of the setup required to stabilize a topological superconducting state in a Rashba nanowire.

A more careful analysis shows that, in the sole presence of a proximity-induced superconducting coupling in the edge-mode Hamiltonian, the effective Kitaev chain Hamiltonian resulting from it resides exclusively in the topological phase of model (1.1). Since interfaces between the topological and the trivial phase are needed in order to localize zero-energy Majorana modes in the system, it has been shown that the addition of a transverse magnetic field $\hat{H}_{TMF} = -h \int dx \hat{\psi}^\dagger \hat{\sigma}^x \hat{\psi}$ is necessary to induce a transition between the aforesaid phases of the effective Kitaev chain Hamiltonian and thus attain the goal of successfully observing boundary Majorana modes. In practice, the transverse magnetic field is created along the edge of the 2D topological insulator via proximity to a ferromagnetic insulator, application of supercurrents near the edge of the sample or a uniform magnetic field combined with electrostatic gating. By modulating its strength, the aforementioned interfaces between the topological and trivial phase of the effective Kitaev chain Hamiltonian for the edge modes are predicted to be realized.

A further proposal to realize the topological phase of the Kitaev chain involves a setup consisting of a 1D wire with spin-orbit coupling, named Rashba nanowire, in proximity to a 3D BCS superconductor and subject to a transverse magnetic field [39, 40], as sketched in Fig. 1.2. The Hamiltonian of the model takes the form:

$$\hat{H} = \int dx \hat{\psi}^\dagger \left(-\frac{\hbar^2}{2m}\partial_x^2 - \mu - i\alpha\hat{\sigma}^y\partial_x + h\hat{\sigma}^z \right) \hat{\psi} + \Delta \int dx \left[\hat{\psi}_\uparrow \hat{\psi}_\downarrow + H.c. \right], \tag{1.3}$$

where μ is the chemical potential, α is the strength of the spin-orbit coupling, $\hat{\psi} = (\hat{\psi}_\uparrow, \hat{\psi}_\downarrow)^T$, h is the strength of the applied transverse magnetic field and Δ is the superconducting pairing field. Similarly to the previously discussed proposal, the superconducting pairing field induces an effective intraband coupling between fermionic modes residing on either the upper or lower band of the spectrum. The strength of the transverse magnetic field determines whether the effective Kitaev chain Hamiltonian resides in the topological or in the trivial phase and, by choosing values corresponding to the former, a

1D wire with open boundaries is expected to display boundary Majorana modes at the edges.

We mention finally that topological superconductivity and the related quest for Majorana modes in condensed matter systems is not limited to 1D systems and has been discussed in 2D systems as well. The most prominent theoretical model hosting a topological phase transition from a trivial to a topological phase and the emergence of boundary Majorana modes at the interface between the two is a two-dimensional spinless electron system subject to a p-wave superconducting pairing [7]. The Hamiltonian takes the form:

$$\hat{H} = \int \frac{d^2x}{(2\pi)^2} \left\{ \hat{\psi}^\dagger(\vec{x}) \left(-\frac{\hbar^2}{2m}\partial_x^2 - \mu \right) \hat{\psi}(\vec{x}) + \frac{\Delta}{2} e^{i\phi} \hat{\psi}(\vec{x}) \left(\partial_x + i\partial_y\right) \hat{\psi}(\vec{x}) \right\}, \tag{1.4}$$

where μ is the chemical potential, m is the effective mass of the spinless fermions, Δ is the superconducting pairing field amplitude and ϕ is its phase. The system undergoes a topological phase transition when the energy gap closes, i.e., for $\mu = 0$. As a result, boundary Majorana modes appear at the interface between regions where the chemical potential is positive and regions where it is negative, such as the inner and outer circumferences of an annular region hosting a topological superconducting phase.

The concrete proposals to observe Majorana zero-modes in such a 2D setup aim at realizing 2D topological p-wave superconductivity. The main routes to achieve this goal rely either on the search for systems which intrinsically display the desired superconducting properties as a result of interactions or on engineered heterostructures that induce it in an effective way. In the first case, a prominent example is given by quantum Hall systems [41], consisting of 2D electron gases under a strong perpendicular magnetic field, which have been shown to provide a deep connection with the physics of 2D p-wave superconductivity. In particular, the Moore-Read state is adiabatically connected to the ground state of the topological phase of Hamiltonian (1.4) and shows the same topological properties, such as chiral Majorana edge modes and Majorana zero-modes bound to vortices. Therefore, a significant effort to unveil quantum Hall states described by the Moore-Read ansatz is crucial to experimentally observe nontrivial topological properties.

In the second case, the general ingredients employed in the stabilization of Majorana zero-modes resemble those employed in the 1D case, namely proximity-induced superconductive pairing, spin-orbit coupling and external magnetic field. Some of the most influential proposals have relied on the surface states of a 3D topological insulator proximitized to an s-wave superconductor [42] or on 2D electronic systems with Rashba spin-orbit coupling coupled to an s-wave superconductor and a ferromagnetic insulator in suited heterostructure arrangements [43].

1.1.3 Cold-atom-based proposals for topological superconductivity

The intense development of cold-atom experimental platforms has been a driving force towards the goal of realizing an analog quantum simulator, i.e., a quantum system that is modeled by the same Hamiltonian as the one of a physical system of interest while allowing for a high degree of tunability of its interaction parameters[8, 44]. The efforts devoted to ultracold atoms carry the hope of a better understanding of a variety of complex quantum phenomena that evade standard theoretical paradigms and challenge simulations on classical computers. This comprises phase transitions in strongly-correlated systems, quantum magnetism, topological phases of matter and out-of-equilibrium dynamics [9, 10].

One of the most prominent class of Hamiltonians targeted by cold-atom-based quantum simulation is represented by lattice systems. The basic principle behind their implementation is the generation of an optical lattice mimicking the crystal lattice of a field by means of interfering several laser beams. Atoms can be loaded in such light field configurations, which in turn offer considerable flexibility in terms of geometry, dimensionality, disorder and interatomic interaction control. The development of single-site-resolution imaging techniques allows to monitor many-body correlation properties that are hardly accessible in solid-state setups [45, 46].

In view of the aforementioned properties, the detection and manipulation of Majorana zero-modes has been discussed in the context of cold-atom systems. As an example, a notable proposal in this direction relies on reproducing the properties of Hamiltonian (1.3) in a cold-atom experiment [11]. More precisely, fermionic atoms trapped in an optical lattice are subject to two laser beams that, via optical Raman transitions, induce an effective spin-orbit interaction and a transverse magnetic field. The pairing field is inherited by the system through the coupling of the atomic system to a Bose-Einstein condensate (BEC) of Feshbach molecules by means of a radiofrequency field. The setup is presented in Fig. 1.3.

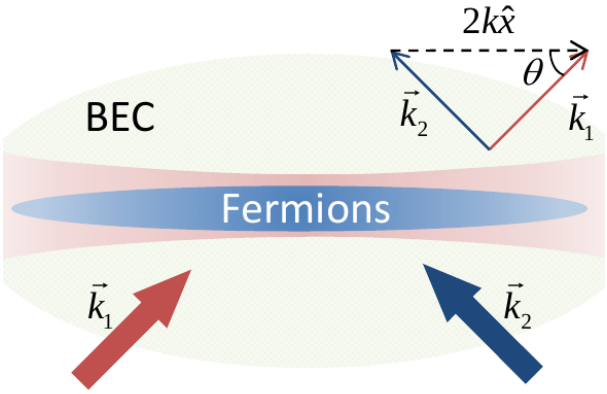

Figure 1.3: After Ref. [11]. 1D wire of optically trapped cold atoms in a 3D molecular BEC and subject to two Raman beams propagating with wave vectors $\vec{k_1}$ and $\vec{k_2}$, coupling the states $(p-k,\downarrow)$ and $(p+k,\uparrow)$, where the first component refers to the momentum and the second one to the z-axis spin orientation.

In view of the versatility of experimental platforms based on ultracold atoms with regard to the high degree of control of a periodic driving, the routes towards the observation and manipulation of Majorana zero-modes have been further enriched by the notion of Floquet Majorana modes. This expression refers to the possibility of dynamically inducing topological properties via a periodic driving of the physical system, even though the latter lies in a topologically trivial phase at equilibrium. In particular, a periodic modulation of Hamiltonian parameters such as the effective chemical potential or the effective transverse magnetic field has been predicted to stabilize Majorana modes potentially suitable to braiding operations [11, 47, 48].

1.2 Low-energy properties of one-dimensional systems with bound-state formation

In the present section we examine more closely some key results concerning the ground-state and low-energy properties of 1D quantum many-body systems displaying bound-state formation. We start by discussing spinful models, where, generically, properly chosen interactions among particles with different internal flavor induce the formation of multiparticle aggregates. Subsequently, we perform a survey of the latest works carried out on spinless fermionic systems, thereby underlining the inadequacy of standard investigation tools to unveil the observed ground-state properties.

1.2.1 Pairing in spinful models

The most studied model for strongly-correlated fermions on a one-dimensional lattice is the 1D Fermi-Hubbard model. Hence, we start our analysis of pairing phenomena in the ground state of low-dimensional many-body quantum systems from its properties, that will in turn elucidate the basic principle behind the subsequently presented studies. The Hamiltonian of the model reads:

$$\hat{H} = -t\sum_{j,\sigma}\left[\hat{c}^{\dagger}_{j,\sigma}\hat{c}_{j+1,\sigma} + H.c.\right] + U\sum_{j}\hat{n}_{j\uparrow}\hat{n}_{j\downarrow}, \tag{1.5}$$

where the operators $\hat{c}_{j,\sigma}$ and $\hat{c}^{\dagger}_{j,\sigma}$ are creation and annihilation operators for fermions with z-spin projection $\sigma = \pm 1$ at site j, satisfying the canonical anticommutation relations $\{\hat{c}_{j,\sigma}, \hat{c}^{\dagger}_{j',\sigma'}\} = \delta_{j,j'}\delta_{\sigma,\sigma'}$, and $\hat{n}_{j,\sigma} = \hat{c}^{\dagger}_{j,\sigma}\hat{c}_{j,\sigma}$.

When $U < 0$, we expect on physical grounds that the system will favor energetically the formation of on-site spin-singlets as a result of the attractive on-site interaction. In order to show it more formally, we employ the bosonization representation of fermionic operators $\hat{c}_{j,\sigma} \approx \sqrt{a}\left(\hat{\psi}_{R,\sigma}(ja)e^{ik_F ja} + \hat{\psi}_{L,\sigma}(ja)e^{-ik_F ja}\right)$, where:

$$\hat{\psi}_{r,\sigma}(x) = \frac{1}{\sqrt{2\pi\alpha}}\hat{U}_{r,\sigma}e^{-\frac{i}{\sqrt{2}}[sgn(r)\hat{\phi}_{\rho}(x)-\hat{\theta}_{\rho}(x)+\sigma(sgn(r)\hat{\phi}_{\sigma}(x)-\hat{\theta}_{\sigma}(x))]}, \tag{1.6}$$

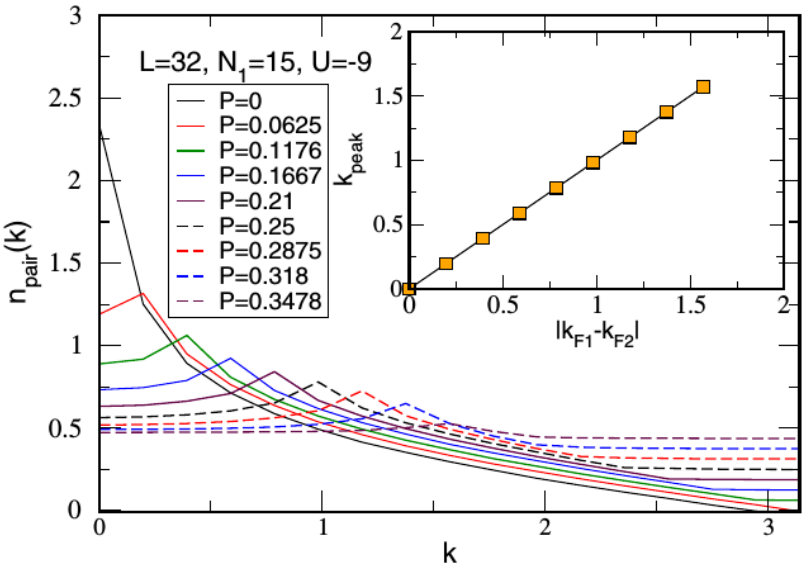

Figure 1.4: After Ref. [21]. Fourier transform n_k^{pair} of the pair-pair correlation function for several values of the polarization $P = \frac{|n_\uparrow - n_\downarrow|}{n_\uparrow + n_\downarrow}$. Inset: location of the peak in n_k^{pair} as a function of the Fermi momentum difference between the two species $|k_{F,\uparrow} - k_{F,\downarrow}|$.

with $sgn(R) = +1$ and $sgn(L) = -1$ and where the canonically conjugate pairs of bosonic fields $(\hat{\phi}_\rho, \frac{1}{\pi}\partial_x\hat{\theta}_\rho)$ and $(\hat{\phi}_\sigma, \frac{1}{\pi}\partial_x\hat{\theta}_\sigma)$ describe charge and spin fluctuations, respectively. The ensuing bosonization representation of the Hamiltonian away from half-filling takes the form:

$$\hat{H} = \frac{1}{2\pi}\int dx \left[u_\rho K_\rho (\partial_x\hat{\theta}_\rho)^2 + \frac{u_\rho}{K_\rho}(\partial_x\hat{\phi}_\rho)^2\right] + \tag{1.7}$$

$$+ \frac{1}{2\pi}\int dx \left[u_\sigma K_\sigma (\partial_x\hat{\theta}_\sigma)^2 + \frac{u_\sigma}{K_\sigma}(\partial_x\hat{\phi}_\sigma)^2\right] + \frac{2U}{(2\pi\alpha)^2}\int dx \cos\left(\sqrt{8}\hat{\phi}_\sigma\right). \tag{1.8}$$

where u_ρ, u_σ and K_ρ, K_σ denote the velocities and Luttinger parameters of the charge and spin channel, respectively.

Remarkably, the low-energy effective Hamiltonian of the system decouples into an excitation channel associated to charge degrees of freedom and one associated to spin degrees of freedom, thus realizing an instance of the phenomenon of spin-charge separation. From a renormalization group analysis [16], it can be shown that the cosine term in Eq. (1.7) is responsible for the opening of a gap in the spin excitation spectrum for any value $U < 0$ of the on-site density-density interaction. The latter is the manifestation of the formation of singlet pairs in the system, whose charge fluctuations remain gapless. Thus, the Fermi-Hubbard model stabilizes a gapless phase described by a single-mode Luttinger liquid, whose characteristic feature is the novel granularity that it displays, given by a nontrivial bound state of fermions rather than single fermions in terms of which the model is defined.

The studies of pairing in 1D two-component Fermi gases have been further enriched by the prediction of the Fulde-Ferrell-Larkin-Ovchinnikov (FFLO) state in spin-imbalanced mixtures. The latter state results from an unconventional pairing mechanism occurring in presence of two fermionic species with different Fermi surface, where Cooper pairing consequently occurs between electrons with different momenta. The associated real-space superconducting order parameter becomes spatially modulated with the characteristic wavevector $Q = |k_{F,\uparrow} - k_{F,\downarrow}|$ as a result, where Q is given by the absolute value of the difference between the Fermi momenta $k_{F,\uparrow\downarrow}$ of the two species $\uparrow, \downarrow$. Several studies of such an exotic superconducting state model the system through a 1D Fermi-Hubbard model in its attractive regime in a nonvanishing total z-magnetization sector, i.e., for $S_z = \frac{1}{2}\sum_j (n_{j\uparrow} - n_{j\downarrow}) \neq 0$ [22, 20, 21].

The choice of 1D systems allows for the use of powerful numerical techniques such as density-matrix-renormalization-group (DMRG) simulations, on top of its fundamental interest and experimental feasability. Armed with such a tool, the computation of the Fourier transform of the pair momentum distribution

Figure 1.5: After Ref. [19]. Schematic illustration of the role of the commensurability condition $pn_\uparrow - qn_\downarrow = 0$ in the case $p = 1$, $q = 2$, enforced on the densities of the two fermionic species in the bosonization construction presented in Ref. [17].

function:

$$n_k^{pair} = \frac{1}{L}\sum_{l,m} e^{ik(l-m)}\rho_{lm}, \tag{1.9}$$

where $\rho_{lm} = \langle c_{l\uparrow}^\dagger \hat{c}_{l\downarrow}^\dagger \hat{c}_{m\downarrow}\hat{c}_{m\uparrow}\rangle$, reveals the characteristic feature associated to the onset of the FFLO state in the context of 1D systems. Indeed, for any value $U < 0$, when $S_z = 0$ one observes a sharp peak at $k = 0$ in the profile of the pair momentum distribution function signaling the quasi-condensation of on-site spin-singlet pairs around zero momentum; contrarily, as shown in Fig. 1.4, when $S_z \neq 0$, n_k^{pair} develops a maximum at a finite value of $k = \frac{2\pi}{L}S_z$, consistently with the onset of Cooper pairing of fermions with opposite spins residing on different Fermi surfaces.

Theoretical predictions support the evidence that the polarized superconductivity of the FFLO state is indeed more easily stabilized in 1D systems rather than 3D ones. This observation has stimulated experimental work directed towards the observation of the FFLO state in 1D setups. More precisely, measurements of density profiles in spin-imbalanced two-component fermionic mixtures of ^6Li atoms [49] revealed the existence of a partially polarized core, presumably to be identified with FFLO superconductivity, that is spatially segregated from wings of an either fully-paired or fully-polarized Fermi gas, depending on the chosen polarization of the system.

Ideas revolving around bound-state formation in low-dimensional systems have been further generalized to the study of pairing of a generic number of particles. In particular, a general mechanism for the formation of multiparticle composites in two-component fermionic mixtures has been argued from bosonization arguments [17]. The low-energy theory of the mixture reads generically:

$$\hat{H}_0 = \sum_{\sigma=\pm}\frac{1}{2\pi}\int dx\left[u_\sigma K_\sigma(\partial_x\hat{\theta}_\sigma)^2 + \frac{u_\sigma}{K_\sigma}(\partial_x\hat{\phi}_\sigma)^2\right], \tag{1.10}$$

where $\sigma = \uparrow, \downarrow$ labels the two fermionic species and the u_σ, K_σ denote the velocity and Luttinger parameter of species σ, respectively. In presence of generic density-density interactions, the Hamiltonian is enriched of the following terms:

$$\hat{H}_{int} = g\int dx(\partial_x\phi_\uparrow)(\partial_x\phi_\downarrow) + \sum_{s,s'>0} G_{ss'}\int dx\cos\left[2(sk_{F,\uparrow} - s'k_{F,\downarrow})x - 2(s\hat{\phi}_\uparrow - s'\hat{\phi}_\downarrow)\right] + \tag{1.11}$$

$$+ \sum_{s,s'>0}\tilde{G}_{ss'}\int dx\cos\left[2(sk_{F,\uparrow} + s'k_{F,\downarrow})x - 2(s\hat{\phi}_\uparrow + s'\hat{\phi}_\downarrow)\right], \tag{1.12}$$

where $k_{F,\uparrow\downarrow}$ are the Fermi momenta of the two species and $g, G_{ss'}, \tilde{G}_{ss'}$ are nonuniversal amplitudes. The only terms contributing to the above sum are those that do not oscillate on the length scale k_F^{-1}, thus suggesting that a mode-locking may occur provided that a commensurability condition on the species densities $n_{\uparrow,\downarrow}$ of the form $pn_\uparrow - qn_\downarrow = 0$, with p, q relatively prime integers (see Fig. 1.5 for a physical intuition of the condition).

Assuming the commensurability condition to be satisfied and after a proper redefinition of the bosonic fields, the low-energy theory takes the generic form of a gapless Luttinger liquid mode and a sine-Gordon theory:

$$\hat{H} = \sum_{\sigma=a,b}\frac{1}{2\pi}\int dx\left[u_\sigma K_\sigma(\partial_x\hat{\theta}_\sigma)^2 + \frac{u_\sigma}{K_\sigma}(\partial_x\hat{\phi}_\sigma)^2\right] + G\int dx\cos\left(2\sqrt{2}\hat{\phi}_a\right), \tag{1.13}$$

where G is once again a nonuniversal amplitude. When the cosine operator is irrelevant, the resulting theory is that of two gapless modes; consequently, all correlators decay algebraically in space and,

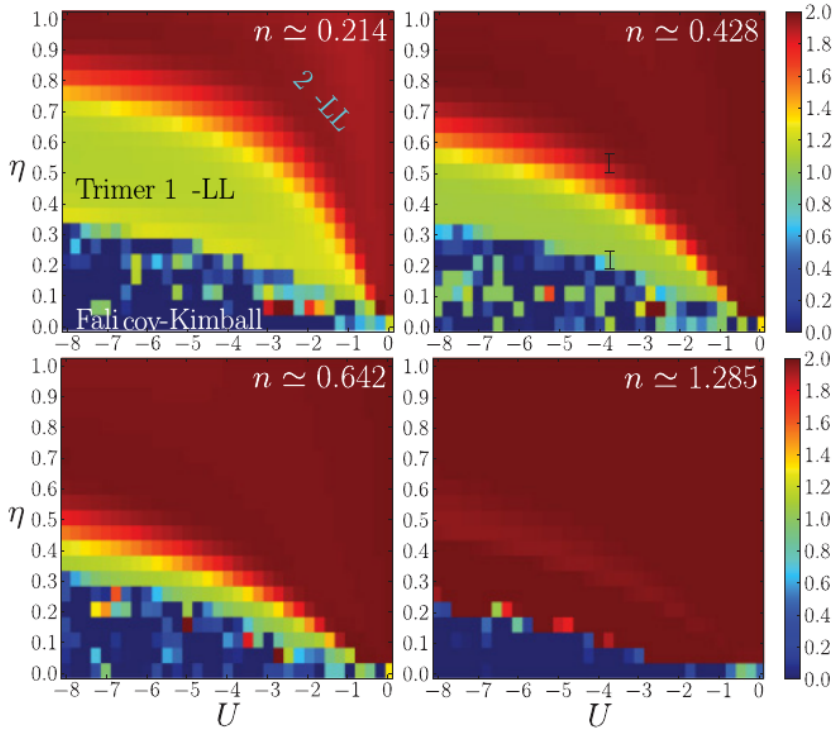

Figure 1.6: After Ref. [19]. Map of the central charge of the low-energy theory of a system described by Eq. (1.14) as a function of $\eta = \frac{t_\downarrow}{t_\uparrow}$ and U for various densities $n = n_\uparrow + n_\downarrow$.

provided that the superconducting quasi-long-range order is the leading one, the pair correlations display a real-space modulation with momentum $Q = |k_{F,\uparrow} - k_{F,\downarrow}|$, thus realizing the 1D FFLO state as the ground state of the system.

On the other hand, when the cosine operator is relevant, it opens a gap in the spectrum associated to the mode a, and the low-energy theory comprises a gapped and a gapless mode. Such a phase corresponds to quasi-long-range-order of peculiar bound states whose constituent elements are determined by the density ratio $\frac{n_\uparrow}{n_\downarrow} = \frac{p}{q}$, namely multiparticle composites made of p fermions belonging to the species $\uparrow$ and q fermions belonging to the species $\downarrow$.

Microscopic realizations of two-component mixtures with a commensurate density imbalance that display the predicted phenomenology have been showcased in the literature. Key ingredients in favouring the instability towards a Luttinger liquid of multimers are identified from the field-theoretical construction to be attractive interspecies density-density interactions and mass asymmetry between the two species. Hence, extensive DMRG simulations have been carried out on the ground-state phase diagram of the asymmetric attractive Fermi-Hubbard model [18, 19]:

$$\hat{H} = -\sum_{j,\sigma=\uparrow,\downarrow} [t_\sigma \hat{c}^\dagger_{j+1,\sigma} \hat{c}_{j,\sigma} + H.c.] + U \sum_j \hat{n}_{j,\uparrow} \hat{n}_{j,\downarrow}, \tag{1.14}$$

where t_σ is the species-dependent hopping parameter and U is the on-site interaction.

To be specific, targeting the formation of trimers via the commensurate density choice $n_\downarrow = 2n_\uparrow$, the phase diagram of the model has been studied for different choices of total density as a function of the asymmetry $\eta = \frac{t_\downarrow}{t_\uparrow}$ and interaction U. The result is best exemplified through a map of the central charge in parameter space, as it represents a direct way to probe the number of gapless modes in the low-energy theory of the system and identify phases exhibiting mode-locking. As presented in Fig. 1.6, the realization of a trimer phase relies on both strong enough attractive interactions and large enough mass imbalance, while being favoured by a small enough density.

We move on to consider multimer formation in mixtures with more than two species, which has emerged as the main alternative platform for the stabilization of molecular Luttinger liquid phases in

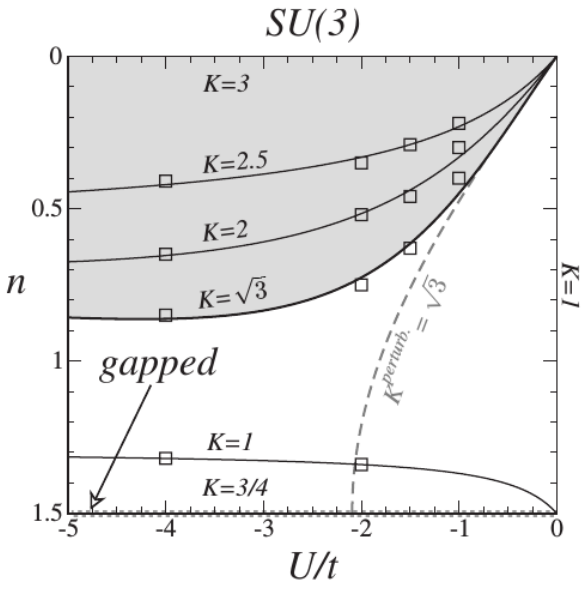

Figure 1.7: After Ref. [50]. Phase diagram of a system described by Hamiltonian (1.15) in the case of $N = 3$ fermionic species as a function of the density n and the interaction strength U. The gray area denotes the trimer superfluid phase, identified through the calculation of the Luttinger parameter K as a route towards the identification of the dominant algebraic order.

1D systems [50, 51, 52]. The representative example of this class of physical systems can be taken to be the $SU(N)$ Hubbard model:

$$\hat{H} = -t \sum_j \sum_{\alpha=1}^{N} [\hat{c}^\dagger_{j+1,\alpha} \hat{c}_{j,\alpha} + H.c.] + \frac{U}{2} \sum_j \hat{n}_j^2, \tag{1.15}$$

where N is the number of components of the fermionic mixture, U is the interspecies density-density interaction and $\hat{n}_j = \sum_{\alpha=1}^{N} \hat{c}^\dagger_{j,\alpha} \hat{c}_{j,\alpha}$.

A combination of bosonization arguments and numerical DMRG simulations leads to the conclusion that, in presence of an attractive interaction U and for small enough density, the system enters a molecular superfluid phase. In the latter, the dominant algebraic order is given by the power law decay of the molecular correlation function $M(x) = \langle \hat{M}_j \hat{M}^\dagger_{j+x} \rangle$, with $\hat{M}_j = \prod_{\alpha=1}^{N} \hat{c}_{j,\alpha}$, while for higher densities the dominant correlations are given by the density-density correlations $N(x) = \langle \hat{n}_j \hat{n}_{j+x} \rangle$, linked to charge-density-wave (CDW) quasi-long-range-order. The single-particle and on-site pair correlation functions $G(x) = \langle \hat{c}^\dagger_{j,\alpha} \hat{c}_{j+x,\alpha} \rangle$ and $P(x) = \langle \hat{c}^\dagger_{j,\alpha} \hat{c}^\dagger_{j,\beta} \hat{c}_{j+x,\beta} \hat{c}_{j+x,\alpha} \rangle$, respectively, become instead exponentially decaying functions of spatial separation x, certifying that pair superfluidity is not the correct scenario in such systems.

Extensions of this work aim at probing the stability of the molecular superfluid phase to the addition of $SU(N)$-symmetry-breaking terms. An example of such term whose effects have been analyzed is an on-site singlet pairing term of the form $\hat{H}_{singlet} = V \sum_j \hat{P}^\dagger_j \hat{P}_j$, with $\hat{P}^\dagger_j = \hat{c}^\dagger_{\frac{3}{2},j} \hat{c}^\dagger_{-\frac{3}{2},j} - \hat{c}^\dagger_{\frac{1}{2},j} \hat{c}^\dagger_{-\frac{1}{2},j}$ for $N = 4$ [53]. At a generic low filling, the phase diagram is separated into two regions: a first region, featuring the competition between molecular correlations $M(x)$ and the $2k_F$ component of density-density correlations $N(x)$, displays indeed a subregion where $M(x)$ is the leading algebraic order, thus demonstrating that multiparticle-composite formation is not an artifact of the $SU(N)$ symmetry of the model; a second region naturally appears, which is similarly partitioned into a subregion with dominant superconducting correlations $P(x)$ and one with dominant $4k_F$ component of the density-density correlations $N(x)$.

1.2.2 Pairing in spinless fermions

As pairing in chains of spinless fermions lies at the heart of remarkable phenomena such as 1D topological superconductivity, it is natural to investigate the onset and properties of pairing phases in strictly 1D number-conserving spinless fermion systems. The characteristic signature of pairing in such systems

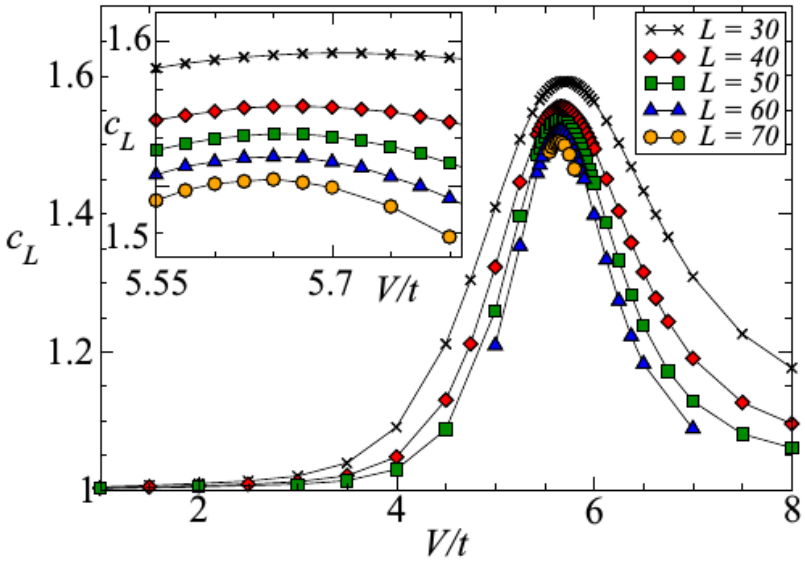

Figure 1.8: After Ref. [54]. Plot of the finite-size estimate of the central charge c, strongly suggesting the presence of a critical point with central charge $c = 1 + \frac{1}{2}$ separating the weak-coupling Luttinger liquid phase from the CLL phase.

is the emergence of a new fundamental granularity given by the bound state of two fermions, whose collective density excitations are described by a Luttinger liquid field theory. The opening of a gap in the single-particle excitation spectrum, linked to the energy cost associated to breaking a pair, manifests itself in the exponential decay of the fermionic single-particle correlator $G(r) = \langle \hat{c}_j^\dagger \hat{c}_{j+r} \rangle$.

The characterization of the low-energy physics in systems of spinless fermions with pairing interactions is intrinsically more challenging. The technique of bosonization does not account for the prediction of a Luttinger liquid phase with pair granularity, as the latter does not simply emerge via a mode-locking mechanism on a weak-coupling single-mode Luttinger liquid theory for a generic weakly-interacting system of spinless fermions. Thus, the analysis of such 1D setups relies either on extensive numerical simulations or on *ad hoc* field theory descriptions.

A first class of model Hamiltonians studied in the context of spinless fermions exploits naturally density-density interactions to induce pairing. The fundamental idea underlying these studies arises from considering the Hamiltonian:

$$\hat{H} = -t \sum_j \left[\hat{c}_j^\dagger \hat{c}_{j+1} + H.c. \right] + U_1 \sum_j \hat{n}_j \hat{n}_{j+1} + U_2 \sum_j \hat{n}_j \hat{n}_{j+2}. \tag{1.16}$$

Heuristically, pairing is naturally favoured in the regime of attractive nearest-neighbor interactions ($U_1 < 0$) and stabilized against an instability towards phase separation when a sufficiently strong repulsive next-to-nearest-neighbor interaction is present ($U_2 > 0$). Specific instances of this model and closely-related ones have been studied in the to uncover exotic Luttinger liquid phases in 1D systems.

A remarkable example in this direction is represented by the work carried out on the model (1.16) in [55, 54], where it has been analyzed in the fully repulsive regime $U_1, U_2 > 0$. The Hamiltonian under investigation takes the form:

$$\hat{H} = -t \sum_j \left(\hat{b}_j^\dagger \hat{b}_{j+1} + H.c. \right) + V \sum_j \sum_{l=1}^{r_c} \hat{n}_j \hat{n}_{j+l}, \tag{1.17}$$

where $\hat{b}_j, \hat{b}_j^\dagger$ are fermionic or hard-core-bosonic creation and annihilation operators. When the average interparticle spacing $r^* = \frac{1}{n} - 1$, n being the density, is smaller than the interaction range r_c, as in the considered instance $n = \frac{2}{5}$, $r_c = 2$, the classical limit $t = 0$ supports an exponentially degenerate ground-state subspace with peculiar frustration-induced cluster properties: the configurations are given by all possible permutations of blocks of type A, given by $\bullet\bullet\circ\circ$, and blocks of type B, given by $\bullet\circ\circ$,

where filled dots denote occupied sites and empty dots denote empty sites. The relative number of blocks depends on the total filling n.

Once quantum fluctuations are reintroduced via $t \neq 0$, the strong-coupling phase of the lattice Hamiltonian (1.17) is given by an exotic quantum liquid where the underlying cluster features highlighted by the classical limit manifest themselves in the spatial modulation of the correlation functions. In particular, we mention as an example that the lowest momentum peak of the structure factor:

$$S(q) = \frac{1}{L} \sum_{l,j} e^{i(l-j)q} \left[\langle \hat{n}_l \hat{n}_j \rangle - n^2 \right] \tag{1.18}$$

appears at $k_c = 2\pi \frac{1-n}{r_c}$. Since $\frac{1-n}{r_c} = \frac{N_A+N_B}{L}$, where N_A (N_B) is equal to the number blocks of type A (B), the peak k_c is related to the density of single-particle (B) and two-particle (B) clusters rather than to the bare filling n, as in a conventional Luttinger liquid phase.

Moreover, as the single-particle gap is nonzero in the cluster Luttinger liquid (CLL) phase, such a phase must be separated by a phase transition from the weak-coupling phase adiabatically connected to the noninteracting point. The critical point is obtained by computing the central charge as a function of the interaction strength V. The latter is extracted from a fit of the entanglement entropy profile to the formula (valid in PBC) [56]:

$$S_L(l) = \frac{c}{3} \log \left[\frac{L}{\pi} \sin \left(\frac{\pi l}{L} \right) \right] + C + O(1/l^\alpha), \tag{1.19}$$

where L is the system size, l is the block length, c is the central charge, C is a nonuniversal constant and the last term represents subleading finite-size corrections. The result indicates that the critical point separating the two phases features an enhanced central charge $c = 1 + \frac{1}{2}$, consistently with the presence of an emergent Ising field at criticality, on top of a gapless bosonic mode appearing on either side of the transition.

A study on model (1.16) at half-filling ($n = \frac{1}{2}$) in the fully-repulsive regime has been presented in [57]. For such choice of filling, the ground state phase diagram highlights instabilities of the weak-coupling Luttinger liquid to different gapped phases due to commensurability effects rather than targeting liquid phases with bound-state formation. In particular, it features two CDW insulating phases, whose unit cells are $\bullet\circ$ (CDW-I) and $\bullet\bullet\circ\circ$ (CDW-II), respectively, as well as a regular Luttinger liquid phase and a bond-order (BO) phase. While the Luttinger liquid phase is gapless, the remaining phases are gapped. The CDW-I phase is induced at strong coupling when the effect of the interaction term proportional to U_1 is dominant, while the CDW-II phase is similarly due to the effect of the next-to-nearest-neighbor repulsion proportional to U_2. Finally, the BO phase appears as an intermediate phase between the Luttinger liquid phase and the CDW-II phase and is identified by a nonvanishing value of the order parameter:

$$O_{BO} = \frac{1}{L} \sum_j (-1)^j \langle \hat{c}_j^\dagger \hat{c}_{j+1} + H.c. \rangle \tag{1.20}$$

in the thermodynamic limit.

A work that targets more directly bound-state formation in 1D systems of spinless fermions in presence of extended density-density interactions is presented instead in [28], where the model Hamiltonian takes the form:

$$\hat{H} = -t \sum_j \left[-\frac{1}{2} \left(\hat{c}_j^\dagger \hat{c}_{j+1} + H.c. \right) + \sum_{m=1}^{3} V_m \hat{n}_j \hat{n}_{j+m} \right], \tag{1.21}$$

and is studied at the generic low-filling regime $n = \frac{1}{5}$. The choice of parameters is defined by $V_1 = V_2 < 0$, $V_3 > 0$, so as to promote the formation of pairs and trimers while preventing a straightforward instability towards phase separation. As presented in Fig. 1.9, the significant result of the analysis can be read off from the behavior of the central charge as a function of the interaction parameters: systems of spinless fermions with pairing interactions display a nontrivial reshaping of the nature of the low-energy excitations, as both the regular Luttinger liquid as well as the multi-fermion bound state liquids are arguably descendants of a phase with 2 gapless modes (2M phase) via mode-locking mechanisms. Noticeably, the transition from a regular Luttinger liquid to a Luttinger liquid of pairs is identified via a central charge $c = 1 + \frac{1}{2}$, as for the transition to the CLL phase discussed in [54].

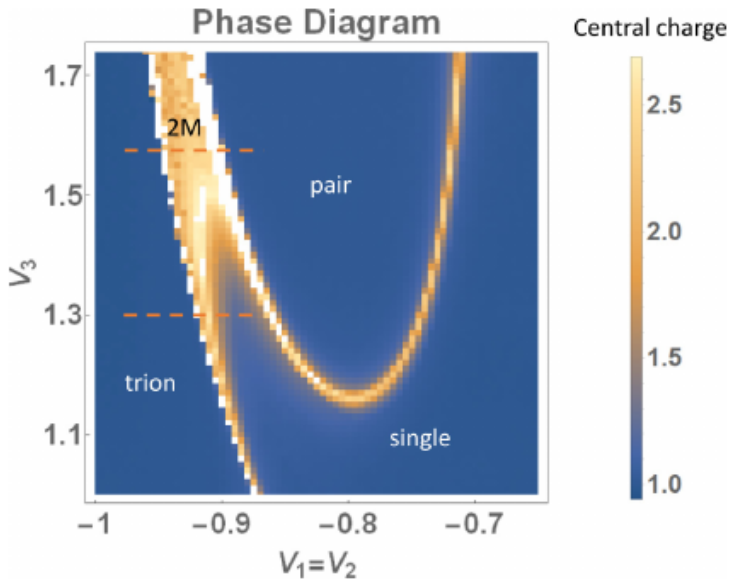

Figure 1.9: After Ref. [28]. Map of the central charge as a function of the interaction parameters $U_1 = U_2$ and U_3 at filling $n = \frac{1}{5}$ for the model Hamiltonian (1.21).

This observation motivates the introduction of unconventional phenomenological models to capture the observed ground-state properties. A remarkable step in this direction had been accomplished in [27], where the the pairing transition in a model of the form (1.16) with $U_1 < 0$ and $U_2 > 0$ was phenomenologically explained via a two-fluid (2F) field-theoretical model. The latter consists of a fluid of charge e fermions of average density $\hat{\rho}_f$ coupled to a fluid of charge $2e$ bosons of average density $\bar{\rho}_b$ via a term that breaks a pair into two fermions and viceversa:

$$\hat{H} = \frac{v}{2\pi}\left[K(\partial_x\hat{\varphi})^2 + \frac{1}{K}(\partial_x\hat{\theta})^2\right] - 2\mu\left(\frac{\partial_x\hat{\theta}}{2\pi} + \bar{\rho}_b\right) + \\ + \hat{\psi}^\dagger\left(\epsilon_0 - \frac{\partial_x^2}{2m} - \mu\right)\hat{\psi} + u\left(\hat{\psi}\partial_x\hat{\psi}e^{i2\hat{\varphi}} + H.c.\right), \tag{1.22}$$

where v and K are the velocity and Luttinger parameter of the bosonic mode, μ is the chemical potential, the field $\hat{\psi}(x)$ is fermionic and the bosonic fields satisfy $[\hat{\varphi}(x), \hat{\theta}(x')] = i\pi\Theta(x - x')$. A similar effective Hamiltonian was introduced in Ref. [58] to study the quantum phase transition occurring in a quantum wire with two subbands of spin-polarized electrons when the second subband starts to get filled as a fuction of the gate voltage.

After preforming the unitary transformation $\hat{H} \to \hat{U}\hat{H}\hat{U}^\dagger$, with $\hat{U} = e^{i\int dx(\hat{\psi}^\dagger\hat{\psi} - \bar{\rho}_f)\hat{\varphi}(x)}$, and identifying new fermionic and bosonic fields $\hat{\psi}_\sigma, \hat{\varphi}_\rho, \hat{\theta}_\rho$, the Hamiltonian can be rewritten as $\hat{H} = \hat{H}_\rho + \hat{H}_\sigma + \hat{H}_{int}$, with:

$$\hat{H}_\rho = \frac{v}{2\pi}\left[K_\rho(\partial_x\hat{\varphi}_\rho)^2 + \frac{1}{K_\rho}(\partial_x\theta_\rho)^2\right] - \mu\left(\frac{\partial_x\hat{\theta}_\rho}{\pi} + \bar{\rho}_e\right), \tag{1.23}$$

$$\hat{H}_\sigma = \hat{\psi}_\sigma^\dagger\left(\epsilon_0 - \frac{\partial_x^2}{2m}\right)\hat{\psi}_\sigma + iu(\hat{\psi}_\sigma\partial_x\hat{\psi}_\sigma + \hat{\psi}_\sigma^\dagger\partial_x\hat{\psi}_\sigma^\dagger), \tag{1.24}$$

$$\hat{H}_{int} = \frac{\partial_x\hat{\varphi}_\rho^2}{2m}\hat{\psi}_\sigma^\dagger\hat{\psi}_\sigma - \frac{i\partial_x\hat{\varphi}_\rho}{m}\hat{\psi}_\sigma^\dagger\partial_x\hat{\psi}_\sigma - \frac{v}{K_\rho}\partial_x\theta_\rho(\hat{\psi}_\sigma^\dagger\hat{\psi}_\sigma - \bar{\rho}_f), \tag{1.25}$$

where $K_\rho = K$ and $\bar{\rho}_e = \bar{\rho}_f + 2\bar{\rho}_b$. The term $\hat{H}_\rho$ represents a background bosonic mode for the total charge fluctuations, whereas the term $\hat{H}_\sigma$ represents the continuum limit of the 1D transverse-field Ising model:

$$\hat{H}_I = \sum_j \left(h\hat{\sigma}_j^z - J\hat{\sigma}_j^x\hat{\sigma}_{j+1}^x\right), \tag{1.26}$$

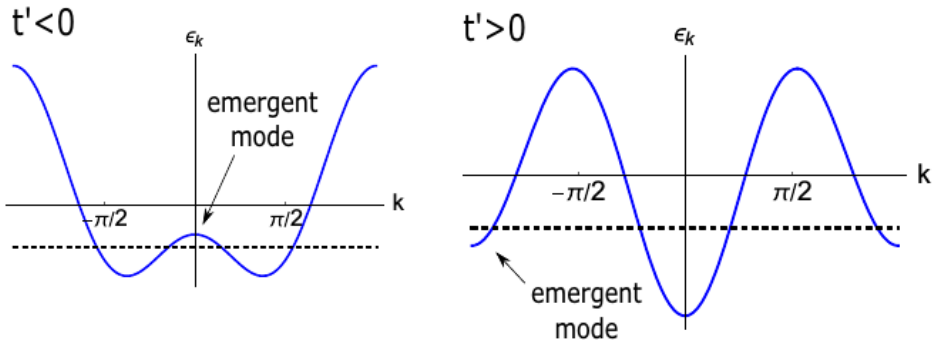

Figure 1.10: After Ref. [26]. Plot of the mean-field dispersion relation $\epsilon(k) = -2t\cos k - 2nt'\cos(2k)$ for large $|t'/t|$. The dashed line indicates the Fermi surface and is included to illustrate the microscopic origin of the emergent mode in the low-energy theory of the system.

with $\epsilon_0 = 2(h - J)$. A careful analysis shows that the weak coupling Luttinger liquid phase corresponds to the ordered phase of model (1.26), while the Luttinger liquid of pairs with a gap to single-particle excitations corresponds to its disordered phase. The two phases are separated by a critical point where the Ising mode becomes gapless, contributing to the central charge with an additional $c = \frac{1}{2}$ contribution. This result is also in agreement with the weak-coupling RG analysis performed in Ref. [58].

The unveiled criticality characterizing the pairing transition in 1D systems of spinless fermions, already recovered in [28], has been discovered in a different class of model Hamiltonians expected to display a pairing transition in their phase diagram [26]. The model of interest induces pairing of fermions via a correlated pair-hopping interaction that gains energy from pair delocalization:

$$\hat{H} = -t\sum_j \left(\hat{c}_j^\dagger \hat{c}_{j+1} + H.c.\right) - t'\sum_j \left(\hat{c}_j^\dagger \hat{n}_{j+1}\hat{c}_{j+2} + H.c.\right), \tag{1.27}$$

where t' is the pair-hopping parameter. The analysis carried out on model (1.27) allows for a more microscopically transparent derivation of the emergent mode that controls the opening of a gap in the single-particle excitation spectrum across the transition from a weak-coupling Luttinger liquid to a Luttinger liquid of pairs.

The construction proceeds by first performing a mean-field approximation on Hamiltonian (1.27) via the substitutions $\hat{n}_j = n + \delta\hat{n}_j$, $\hat{c}_{j+1}^\dagger \hat{c}_{j-1}^\dagger = \chi + \delta\hat{\chi}_j$, where n is the average density and $\chi = \langle \hat{c}_{j+1}^\dagger \hat{c}_{j-1}^\dagger \rangle$, the resulting mean-field Hamiltonian takes the form:

$$\hat{H} = -t\sum_j \left(\hat{c}_j^\dagger \hat{c}_{j+1} + H.c.\right) - nt'\sum_j \left(\hat{c}_j^\dagger \hat{c}_{j+2} + H.c.\right), \tag{1.28}$$

which results in the mean-field dispersion relation $\epsilon(k) = -2t\cos k - 2nt'\cos(2k)$ displayed in Fig. 1.10. The effective next-to-nearest-neighbor hopping term generated at the mean-field level from the pair-hopping interaction term has the effect of introducing an emergent mode in the topology of the low-energy spectrum of the system. The fluctuations neglected at the mean-field level can then be reintroduced through a modified bosonization approach that assumes the presence of two low-energy modes at the Fermi surface of the system.

More specifically, the treatment proceeds by expanding the fermionic creation operator $\hat{\psi}(x) = \frac{\hat{c}_j}{\sqrt{a}}$, a being the lattice constant, as:

$$\hat{\psi}(x) \approx e^{ik_F x}\hat{R}_0(x) + e^{-ik_F x}\hat{L}_0(x) + e^{ik_1 x}\hat{R}_1(x) + e^{-ik_1 x}\hat{L}_1(x), \tag{1.29}$$

where k_F represents the mode existing at weak coupling, whereas k_1 denotes the emergent mode. Similarly, the subscripts $\nu = 0, 1$ label the left- and right-moving fields of the two low-energy modes, whose expressions read $\hat{R}_\nu \sim \frac{1}{\sqrt{2\pi a}} e^{i(\hat{\theta}_\nu - \hat{\phi}_\nu)}$, $\hat{L}_\nu \sim \frac{1}{\sqrt{2\pi a}} e^{i(\hat{\theta}_\nu + \hat{\phi}_\nu)}$. After including, on top of the quadratic contribution given by the approximate linear dispersion and by the forward scattering terms in the interaction, a backscattering term generated by the quartic contribution to the lattice Hamiltonian

and a phenomenological term giving a mass to the emergent mode, the bosonized Hamiltonian reads $\hat{H} = \hat{H}_+ + \hat{H}_-$, where:

$$\hat{H}_+ = \frac{u_+}{2\pi} \int dx \left[K_+ (\partial_x \hat{\theta}_+)^2 + \frac{1}{K_+} (\partial_x \hat{\phi}_+)^2 \right], \tag{1.30}$$

$$\hat{H}_- = \frac{u_-}{2\pi} \int dx \left[K_- (\partial_x \hat{\theta}_-)^2 + \frac{1}{K_-} (\partial_x \hat{\phi}_-)^2 \right] - \int dx \left[g_1 \cos\left(2\hat{\phi}_-\right) + g_i \cos\left(2\hat{\theta}_-\right) \right], \tag{1.31}$$

given that the following canonical transformation has been performed:

$$\hat{\phi}_+ = \hat{\phi}_0 + \hat{\phi}_1, \quad \hat{\phi}_- = \hat{\phi}_1, \tag{1.32}$$

$$\hat{\theta}_+ = \hat{\theta}_0, \quad \hat{\theta}_- = \hat{\theta}_1 - \hat{\theta}_0. \tag{1.33}$$

The phase predicted by the low-energy theory $\hat{H}_+ + \hat{H}_-$ depends on the ratio of the couplings $\frac{g_1}{g_i}$. When the coupling g_1 is dominant, the field $\hat{\phi}_-$ gets pinned to one of the minima of the corresponding cosine term: this phase is the one displayed by the system when the emergent mode is still gapped and is thus the regular weak-coupling Luttinger liquid phase for a system of spinless fermions, featuring an algebraic decay of the single-particle correlator $\langle \hat{c}_j^\dagger \hat{c}_{j+r} \rangle$. On the other hand, when the coupling g_i dominates, the realized phase is a liquid of pairs, as demonstrated by the nonvanishing single-particle gap inferred from the exponentially decaying single-particle correlator $\langle \hat{c}_j^\dagger \hat{c}_{j+r} \rangle$. The criticality by the effective field theory $\hat{H}_-$ belongs to the 2D Ising universality class [59], thus implying once more an enhanced central charge $c = 1 + \frac{1}{2}$ at the transition that results from the gapless charge mode $\hat{H}_+$ and the emergent gapless Ising mode realized by H_-.

1.3 Conclusions

As we have discussed above, the phenomenon of pairing has a long-standing tradition in condensed-matter physics as a result of the discovery of superconductivity and the more recent introduction of topologically-protected edge modes. The research lines opened by these phenomena are still active and bear the promise of paving the way towards major technological advances, such as the achievement of high-temparature superconductivity and topologically-protected quantum computation.

Most of the existing literature on ground state physics in 1D many-body quantum systems has directed its attention to spinful systems, where the combination of DMRG simulations and bosonization has led to the prediction of Luttinger liquid phases with molecular granularity and of 1D magnetic superconductivity, realized in the FFLO phase.

We focus instead the remaining part of the manuscript on the low-energy properties of 1D systems of spinless fermions featuring bound-state formation, where fewer results are available [26, 27, 28, 55, 54] and standard analytical techniques largely employed in the study of 1D systems fail to predict the correct critical behavior. We apply systematically a two-fluid description (inspired by Ref. [27]) of a class of lattice systems with kinetically-induced pairing and thereby show its usefulness and simplicity in describing bound-state formation in 1D chains of spinless fermions. We hope that our work will serve as a starting point for further applications of unconventional techniques inspired by the two-fluid models to be described in the following.

Chapter 2

Pairing in spinless fermions and spin chains with next-to-nearest-neighbor interactions

In the present chapter we discuss the results obtained in Ref. [60], namely L. Gotta, L. Mazza, P. Simon, and G. Roux, *Pairing in spinless fermions and spin chains with next-nearest neighbor interactions*, Phys. Rev. Research **3**, 013114, Feb. 2021, where an extensive study of the phase diagram of a lattice model of spinless fermions with single-particle hopping and nearest-neighbor and next-to-nearest-neighbor interactions at several densities is presented. In the following, we first provide a general introduction to the scientific background that led to the aforesaid study. Then, we proceed by presenting the model definition, the detailed goals of the work and the structure of its presentation. We conclude with the structured discussion of the results.

2.1 Introduction to the problem

As anticipated in the previous chapter, the physics of pairing has been the focus of intensive research due to its relation to the prediction of boundary Majorana zero-energy modes in topological superconductors. Given the versatility of cold-atom platforms in the realization of number-conserving 1D models, it has become important to determine whether it is possible to stabilize topologically nontrivial phases without resorting to proximity coupling to a pair reservoir.

Given the low dimensionality of the system, mean-field approaches reducing the problem to the Kitaev chain Hamiltonian cannot be applied and more refined approaches were devised. A first group of studies has focused on quasi-1D systems, where the combination of exactly solvable regimes and numerical simulations showed that ladder systems interacting through leg-subparity-conserving terms can display topologically nontrivial phases with localized boundary Majorana modes in OBC. [61, 62, 63, 64, 65, 66]

Another set of works has been devoted to the prediction of the existence of Majorana zero modes localized at the interfaces between weak-pairing and strong-pairing phases in purely 1D inhomogeneous setups, both with spinful [67] and spinless fermions [26, 27]. Thus, it is a relevant question to identify pairing phases in 1D number-conserving systems as a potential guide to the search of Majorana boundary modes in cold-atom systems.

A paradigmatic model for investigating pairing physics is a 1D lattice model of fermions with density-density interactions which extend up to next-to-nearest neighbors (NNN), which has been the focus of a series of works that target its ground-state phase diagram properties and bear no relation to the physics of Majorana zero modes [68, 69, 70, 71, 72, 73, 74, 75, 76, 77]. Some parts of its phase diagrams have already been studied and identified as paired phases, which appear both for repulsive [55, 54] and attractive [27, 28] interactions. A systematic analysis has been only presented at half filling, but limited to the fully-repulsive case [57]. Extensions to longer-range interactions have been the focus of Ref. [78]. In general, the employed techniques are various, and the study of one-dimensional setups naturally benefits from the possibility of using ad-hoc field-theory methods such as bosonization [79, 80, 16], or numerical tensor-network approaches based on matrix-product states [81, 82].

Before discussing the results of the work, it is worth remarking that the scope of the article goes beyond the search for Majorana fermions in electronic systems. Thanks to the Jordan-Wigner mapping, our results can be easily recast in spin language and provide insights into the physics of arrays of Rydberg atoms. Recent experiments have shown that it is now possible to organize individual atoms according to periodic arrays of microscopic dipole traps separated by few micrometers [83, 84, 85, 86, 87, 88, 89, 90, 91]. The excitation of such trapped atoms to a Rydberg state [92, 93] characterized by a strong electronic dipole ensures that atoms interact notwithstanding their distances, and this has produced a setup which is an almost paradigmatic realization of a quantum simulator for quantum spin models [94, 95, 96, 97]. In some special regimes, the realized model is an instance of our Hamiltonian.

In the following, we present a comprehensive study of the general structure of the phase diagram of the aforementioned model using both approximate analytical treatments and extensive numerical simulations. Our study reproduces the mentioned known results, and extends the analysis to a larger parameter space focusing on four representative densities, namely $n = \frac{1}{5}, \frac{1}{3}, \frac{2}{5}, \frac{1}{2}$. Naturally, we put a particular emphasis on pairing phenomena, since, by completely mapping out the phase diagram, we expect to significantly ease the future search for Majorana fermions in number-conserving systems. We start each discussion with the presentation of analytical results in the weak-coupling, strong-coupling and classical limit and complement them with numerical results in the intermediate regime, where no perturbative analysis is possible. We progressively highlight mainly the new features as the discussion progresses.

2.2 Model, methods and observables

2.2.1 Hamiltonian

The Hamiltonian that we are going to characterize is defined on a lattice of L sites and admits two equivalent formulations in terms of fermionic or spin degrees of freedom. The fermionic model reads:

$$\hat{H} = \sum_{j=1}^{L} \left[-t(\hat{c}_j^\dagger \hat{c}_{j+1} + h.c.) + U_1 \hat{n}_j \hat{n}_{j+1} + U_2 \hat{n}_j \hat{n}_{j+2} \right], \tag{2.1}$$

where $\hat{c}_j, \hat{c}_j^\dagger$ are fermionic creation and annihilation operators satisfying the canonical anticommutation relations $\{\hat{c}_j, \hat{c}_j\} = 0$ and $\{\hat{c}_j, \hat{c}_j^\dagger\} = \delta_{i,j}$, $\hat{n}_j = \hat{c}_j^\dagger \hat{c}_j$ is the number operator at site j, t denotes the hopping amplitude (we set $t = 1$ in the rest of the paper) and U_1, U_2 represent, respectively, the strength of the nearest neighbour (NN) and NNN density-density interactions. In the fermionic formulation (2.1), which we are going to refer to in the rest of the work, the model Hamiltonian that we consider describes fermions on a $1D$ lattice interacting via a soft-shoulder potential with interaction range $r_c = 2$. In what follows, we study the zero-temperature properties of (2.1) for real U_1 and positive $U_2 \geq 0$ at a given density $n = \frac{1}{L}\sum_j \langle \hat{n}_j \rangle = N/L$ with N the fixed total number of particles.

In order to switch from the fermionic to the spin Hamiltonian, we use the Jordan-Wigner transformation

$$\begin{cases} \hat{c}_j = \prod_{l=1}^{j-1} e^{-i\pi\left(\hat{S}_l^z + \frac{1}{2}\right)} \hat{S}_j^-, \\ \hat{c}_j^\dagger \hat{c}_j = \hat{S}_j^z + \frac{1}{2}, \end{cases} \tag{2.2}$$

where $\hat{S}_j^k$ with $k \in \{x, y, z\}$ are spin 1/2 operators, leading to the following spin Hamiltonian:

$$H = \sum_j \left[-2t \left(\hat{S}_j^+ \hat{S}_{j+1}^- + h.c. \right) + U_1 \hat{S}_j^z \hat{S}_{j+1}^z + U_2 \hat{S}_j^z \hat{S}_{j+2}^z \right], \tag{2.3}$$

where we have dropped constant terms and terms proportional to the full magnetization, which commutes with the Hamiltonian. It thus corresponds to the well-known XXZ spin chain model with an extra antiferromagnetic NNN Ising term.

We mention that, by performing a particle-hole transformation $\hat{c}_j \to \hat{c}_j^\dagger$, the Hamiltonian transforms according to:

$$\hat{H}(t, U_1, U_2) \to \hat{H}(-t, U_1, U_2) + (U_1 + U_2)(L - 2N). \tag{2.4}$$

Following it up with the unitary transformation $\hat{c}_j \to (-1)^j \hat{c}_j$, we infer that the behavior of holes for densities $n > \frac{1}{2}$ coincides with that of particles at density $n' = 1 - n$ with the same interaction parameters, thus allowing to restrict the analysis to the density range $0 \leq n \leq \frac{1}{2}$.

2.2.2 Methods and observables

On the analytical side, we employ bosonization, perturbation theory calculations and classical limit pictures to elucidate the nature of the ground state in either weak- or strong-coupling regimes. On the numerical side, we carry out extensive DMRG simulations using both a traditional implementation and a matrix-product-state (MPS) implementation based on the ITensor library [98]. We perform simulations both in systems with PBC and OBC, limiting ourselves to the fermionic formulation (2.1) of the model Hamiltonian.

In order to discriminate between different phases and establish phase boundaries, we compute the p-particle gap $\Delta_p(L)$ via the relation:

$$\Delta_p(L) = E_0(N+p, L) + E_0(N-p, L) - 2E_0(N, L), \tag{2.5}$$

for $p = 1, 2$, where $E_0(N, L)$ denotes the ground state energy of a system of size L with N particles. Secondly, we evaluate the second derivative of the ground state energy density $\epsilon_{GS} = \frac{E_0(N,L)}{L}$ along a curve $\gamma : \mathbb{R} \to \mathbb{R}^2$, $\gamma(s) = (U_1(s), U_2(s))$ in the $U_1 - U_2$ parameter space:

$$\partial_s^2 \epsilon_{GS} = \frac{d^2}{ds^2} \epsilon_{GS}\left(\gamma(s)\right), \tag{2.6}$$

as its non-analyticities should signal zero-temperature quantum phase transitions. Finally, we consider the von Neumann entanglement entropy:

$$S_A = -Tr[\hat{\rho}_A \log \hat{\rho}_A], \tag{2.7}$$

where $\hat{\rho}_A$ is the reduced density matrix of subsystem A with respect to the full system. The latter quantity allows to extract a finite-size estimate of the central charge in a critical phase via the Cardy-Calabrese formula [56, 99]:

$$S_L(l) = \frac{c}{\alpha} \log\left[\frac{\beta L}{\pi} \sin\left(\pi \frac{l}{L}\right)\right] + C, \tag{2.8}$$

where l is the size of the left block A length, C represents a nonuniversal constant, and we have $\alpha = 3, \beta = 1$ for PBC. Additional oscillations in $S_L(l)$ are taken into account from the local kinetic energy profile [100, 101, 53, 102] by adding to Eq. (2.8) a term of the form $B\langle c_l^\dagger c_{l+1} + h.c.\rangle$, where B is to be treated as a fitting parameter.

Finally, we evaluate several observables to characterize the encountered phases. We compute the Fourier transform of the density fluctuations $\langle \delta\hat{n}_j \rangle = \langle \hat{n}_j \rangle - n$ and of the density-density correlation function, namely, the structure factor $S(k)$:

$$\delta n(k) = \sum_{j=1}^{L} \langle \delta\hat{n}_j \rangle e^{-i\frac{(j-1)k}{L}}; \tag{2.9}$$

$$S(k) = \sum_{j=1}^{L} \left[\langle \hat{n}_1 \hat{n}_j \rangle - \langle \hat{n}_1 \rangle \langle \hat{n}_j \rangle\right] e^{-i\frac{(j-1)k}{L}}. \tag{2.10}$$

Additionally, we compute the decay of the single-particle correlation function and of the pair correlation functions:

$$G(r) = \langle \hat{c}_j^\dagger \hat{c}_{j+r} \rangle, \qquad P(r) = \langle \hat{c}_j^\dagger \hat{c}_{j+1}^\dagger \hat{c}_{j+r} \hat{c}_{j+r+1} \rangle, \tag{2.11}$$

and the so called average pair kinetic energy:

$$K_P = \frac{1}{L} \sum_j \langle \hat{c}_j^\dagger \hat{c}_{j+1}^\dagger \hat{c}_{j+2} \hat{c}_{j+3} + h.c.\rangle, \tag{2.12}$$

quantifying the magnitude of local pairing fluctuations. Finally, we identify the BO phase via the BO parameter:

$$O^{\mathrm{BO}} = \frac{1}{L} \sum_{j=1}^{L} (-1)^j \langle c_j^\dagger \hat{c}_{j+1} + h.c.\rangle, \tag{2.13}$$

and the U_2-induced CDW order via the following CDW order parameter:

$$O_j^{\mathrm{CDW}} = \langle \hat{n}_{j+2} \rangle - \langle \hat{n}_j \rangle, \tag{2.14}$$

computed in the bulk of the system, so that the unavoidable boundary effects are minimized.

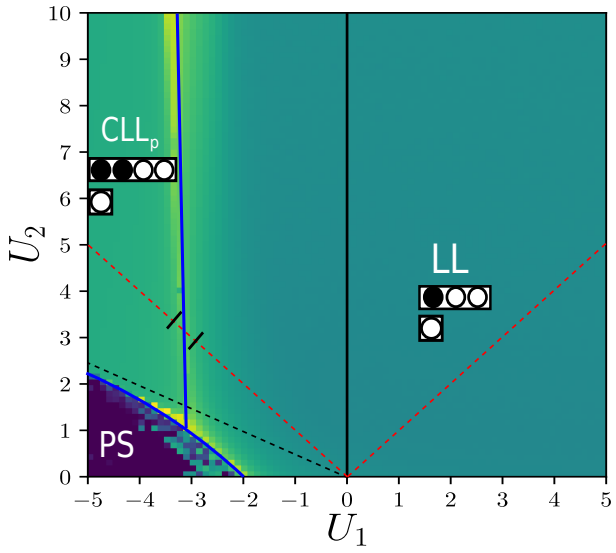

Figure 2.1: Phase diagram for $n = \frac{1}{5}$. The color map for the background displays the half-chain entanglement entropy on $L = 70$ chain with PBC. Black lines are classical transition lines obtained neglecting quantum fluctuation. Additional numerical simulations are presented for the points lying on the red lines. Blue lines are a guide to the eye for the main phase boundaries.

2.3 Phase diagram for $n = \frac{1}{5}$

We discuss in this section the phase diagram for $n = \frac{1}{5}$. The nontrivial feature of the latter is the appearance of an exotic pair CLL whose fundamental low-energy degrees of freedom are given by pair bound states. Despite its observation not being totally surprising in presence of an attractive NN interaction, its correlation properties and the quantum phase transition separating it from the standard LL phase require a precise characterization. The phase diagram is shown in Fig. 2.1.

2.3.1 Classical limit and perturbative quantum fluctuations: the attractive regime

We start to develop an understanding of the phase diagram depicted in Fig. 2.1 by considering the case $t = 0$, where quantum fluctuations are neglected, for both $U_1 < 0$ and $U_1 > 0$. When $U_1 < 0$, we compare the energy of two candidate classes of product-state configurations: (i) the classical configurations where the particles form a macroscopic cluster of N sites and leave the remainder of the system empty, corresponding to phase separation (PS), and (ii) the exponentially degenerate set of states made of all possible permutations of blocks of type A ($\bullet\bullet\circ\circ$) and B ($\circ$), coinciding with the collection of states where fermions form pairs that are seperated from each other by at least 2 sites; the latter condition ensures the absence of energetic contribution from the repulsive U_2.

The energy density of the phase-separated configurations is given by $(U_1 + U_2)n$, whereas the one of the degenerate paired configurations is $\frac{U_1}{2}n$. The comparison between the two leads to the result that, in the classical limit, phase separation is the optimal configuration when $U_2 < -\frac{U_1}{2}$, consistently with its prediction for $U_2 = 0, U_1 < -2$, where model (2.1) reduces to the fermionic formulation of the XXZ Hamiltonian. On the other hand, the optimal set of states when $U_2 > -\frac{U_1}{2}$ is the exponentially large set of fully-paired configurations described above, whose degeneracy is expected to be lifted once quantum fluctuations are reintroduced by allowing $t \neq 0$, thus giving rise to a pair CLL.

To better illustrate this point, we study the effect of the presence of perturbative quantum fluctuations $t \neq 0$ by assuming that, in the limit of small t, the ground state belongs to the subspace described in terms of blocks A and B; by mapping such configurations onto an equivalent spin chain of magnetization $M = N_A - N_B$ via the identification of a block A (respectively, B) with a spin-up (respectively, spin-down) state according to the rules:

$$|\bullet\bullet\circ\circ\rangle \to |\uparrow\rangle\,, \quad |\circ\rangle \to |\downarrow\rangle\,, \tag{2.15}$$

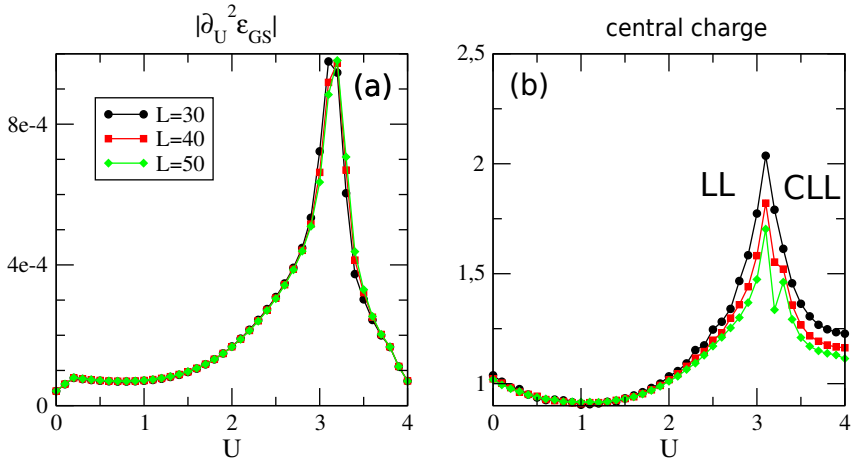

Figure 2.2: DMRG results for $n = \frac{1}{5}$ along the $U = U_2 = -U_1$ line. **(a)** ground state energy density curvature (2.6) for various sizes. The apparent non-analytic behavior suggests a critical point located in the range $3.1 \leq U \leq 3.2$. **(b)** Extrapolated central charge from Eq. (2.8). The numerics are compatible with a critical point with $c = 3/2$ surrounded by the two $c = 1$ LL and CLL phases.

and applying standard degenerate perturbation theory[55, 54, 103], one obtains the effective Hamiltonian:

$$\hat{H} = -\frac{J}{2}\sum_j \left[\hat{\mathcal{S}}_j^+ \hat{\mathcal{S}}_{j+1}^- + h.c.\right] + J\Delta \sum_j \hat{\mathcal{S}}_j^z \hat{\mathcal{S}}_{j+1}^z, \tag{2.16}$$

in which the $\mathcal{S}^\alpha$ are effective spin operators for the blocks and we drop the constant terms. This XXZ model has effective couplings:

$$J = \frac{2t^2}{U_2 + |U_1|}, \tag{2.17}$$

$$\Delta = \frac{U_2}{2U_2 + |U_1|}, \tag{2.18}$$

with an anisotropy parameter $\Delta \in (0, 1)$. In such regime, the effective XXZ chain is in the gapless LL regime, described by a $c = 1$ conformal field theory. Consequently, the qualitative picture for the strong-coupling regime of the CLL phase is a Luttinger liquid of pairs that map to hard-core bosons living on bonds.

2.3.2 Classical limit and perturbative quantum fluctuations: the repulsive regime

Turning our attention to the purely repulsive interaction regime ($U_1 > 0, U_2 > 0$), the degenerate ground-state subspace in the classical limit is the subspace generated by the basis states described as a sequence of blocks C ($\bullet \circ \circ$) and blocks B, since such states have zero energy density, which is the minimum energy value that can be achieved in the classical limit of the purely repulsive interaction regime. The line $U_1 = 0$ thus constitutes another classical phase-transition line, and it is plotted in black in Fig. 2.1.

We study the effect of additional perturbative quantum fluctuations by performing a mapping to an effective spin model. We proceed along the same lines that led to Eq. (2.16) and obtain the effective Hamiltonian:

$$H \simeq -t\sum_j \left[\hat{\mathcal{S}}_j^\dagger \hat{\mathcal{S}}_{j+1}^- + h.c.\right]. \tag{2.19}$$

Again, this XX model is described at low energies by a $c = 1$ conformal field theory. As the fundamental granularity of the classical configurations comprises single particles, the strong-coupling limit is expected to be effectively adiabatically connected to the weak-coupling LL regime. At low densities, such short range interactions, will never be able to drive the system to an instability towards nontrivial phases induced by frustration or commensurability effects. This claim that the LL phases extends over the whole repulsive region is supported by numerical calculations.

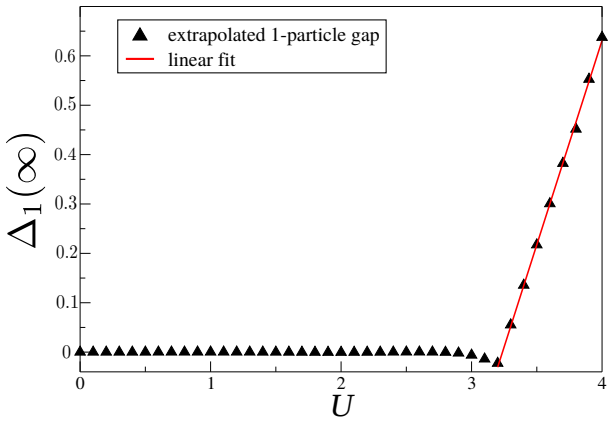

Figure 2.3: Single-particle gap $\Delta_1(\infty)$ obtained by extrapolating finite size gaps (2.5) with $L = 20, 40, 60, 80$ on the same line as in Fig. 2.2.

2.3.3 Luttinger liquid approach

Last, we recall the usual LL treatment of the weak-coupling regime stemming from the non-interacting point $U_1 = U_2 = 0$. Bosonization maps the lattice operators to long-wavelength field operators $\psi_R(x), \psi_L(x)$ through $c_j \sim \sqrt{a}\left[\psi_R(ja)e^{ik_F ja} + \psi_L(ja)e^{-ik_F ja}\right]$ (a being the lattice spacing and $k_F = \frac{\pi n}{a}$ being the Fermi wave-vector) and then re-expresses the latter as a function of two canonically conjugate bosonic fields $\phi(x), \partial_x\theta(x)$ satisfying $[\phi(x), \partial_{x'}\theta(x')] = i\delta(x - x')$. The resulting effective Hamiltonian capturing the low-energy properties of the system is the celebrated LL Hamiltonian [16]:

$$H = \frac{v}{2\pi}\int dx \left[\frac{1}{K}(\partial_x\phi)^2 + K(\pi\partial_x\theta)^2\right], \tag{2.20}$$

where K denotes the Luttinger parameter and v is the sound velocity of the gapless, linearly dispersing, collective density excitation modes. Such theory develops algebraic correlations parameterized by the K parameter that, from pertubative calculations, reads:

$$K(U_1, U_2; n) = \frac{1}{\sqrt{1 + \frac{U_1[1-\cos(2\pi n)] + U_2[1-4\cos(4\pi n))]}{\pi \sin(\pi n)}}}. \tag{2.21}$$

2.3.4 Numerical results in the attractive regime

We characterize the transition from the regular LL phase to the pair CLL phase by performing numerical simulations on the line $U_2 = -U_1$. We start by showing in Fig. 2.2(a) the second derivative of the ground-state energy density, which manifests a nonanalytic behavior pointing towards the presence of a quantum critical point, even though the finite-size numerical data do not suffice to discriminate between a cusp and a genuine divergence.

We corroborate this result by monitoring in Fig. 2.2(b) the central charge along the very same line, thereby observing a peak compatible with a critical point with central charge $c = \frac{3}{2}$ separating two $c = 1$ phases. This feature is consistent with a criticality belonging to the 2D Ising universality class, which contributes an additional $c = \frac{1}{2}$ on top of the background central charge $c = 1$ carried by the conformal field theory of a compactified boson. We underline that this result is consistent with previous numerical findings on transitions to exotic CLL phases [54, 104, 26] and with the field-theoretical two-fluid description of this transition presented in [27].

In order to probe signatures of pairing, we compute the 1-particle and 2-particle gap across the critical point. We observe in Fig. 2.3 the opening of a finite single-particle gap, whereas the pairing gap has been checked to vanish, which in turn confirms the gapless nature of the $c = 1$ CLL phase beyond the critical point. Notice that the opening of the single-particle gap agrees well with a linear behavior expected for the Ising universality class.

To fully characterize such a novel state of matter, we investigate the behaviour of the Fourier transform of the density profile $\delta n(k)$ and of the density structure factor $S(k)$. The reason for such a choice lies in

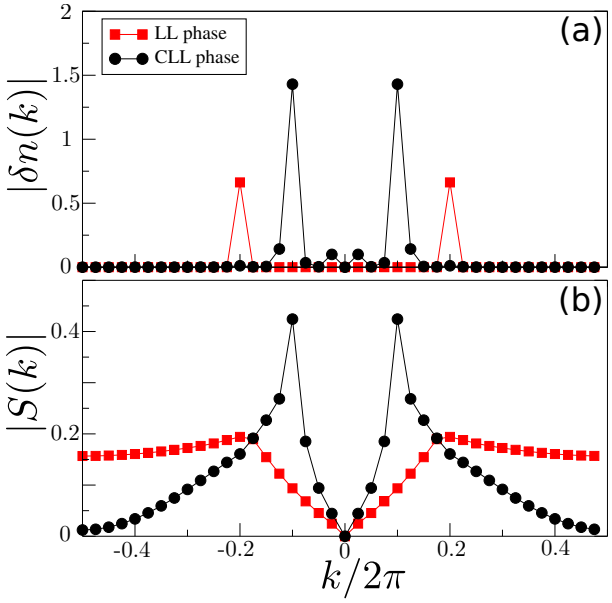

Figure 2.4: **(a)** Density fluctuations Fourier transform (2.9) and density structure factor (2.10) **(b)** on the same line as in Fig. 2.2 for $L = 40$. $U = 1$ for the LL phase and $U = 5$ for the CLL phase.

the bosonization prediction that the expectation value of the aforementioned observables is given by an expansion whose lowest order harmonics oscillate with wavevector $k = 2\pi\rho$, ρ being the mean density of the microscopic granularity of the Luttinger liquid phase. More explicitly, the lowest order contributions to the density-density correlations read [16]:

$$\langle \rho(x)\rho(0)\rangle = \frac{A}{x^2} + B\frac{\cos(2\pi\rho x)}{x^{2K}}, \tag{2.22}$$

where A and B are non-universal amplitudes. For the LL phase, we have $\rho = n$ while for the CLL phase, we expect $\rho = n/2$. The two phases are thus signaled by their corresponding peaks in both $\delta n(k)$ and $S(k)$ at wave-vectors $k = 2\pi\rho$. As shown in Fig. 2.4(a-b), we do observe a shift in the momentum peak from $k = 2\pi \cdot \frac{1}{5}$ to $k = 2\pi \cdot \frac{1}{10}$, indicating the emergence of pairs as the elementary constituent of the CLL phase.

2.3.5 Repulsive regime

We mention briefly that the ground-state phase diagram in the repulsive regime is compatible with the considerations presented in the treatment of its classical limit. Since the average interparticle spacing $\frac{1}{n}$ satisfies $\frac{1}{n} > 1 + r_c$, r_c being the interaction range, the interactions are too short-ranged to induce any instabilities due to commensurability or frustration effects. Thus, the entire repulsive regime is occupied by a Luttinger liquid phase with a standard single-particle granularity.

2.4 Phase diagram for $n = \frac{1}{3}$

We present in this section the phase diagram at filling $n = \frac{1}{3}$, shown in Fig. 2.5. Its main differences with respect to the one shown in Fig. 2.1 consist in the appearance of (i) a highly entropic region for moderate values of $|U_1|$ and large values of U_2, and (ii) a gapped insulating phase characterized by charge-density-wave (CDW) order. We characterize here the latter, denoted as CDW_3 phase due to its classical limit unit cell being given by one particle for each three sites ($\bullet\circ\circ$), while the discussion of the former is postponed to the subsequent section, where a proper analytical interpretation will be presented.

2.4.1 Classical limit

The classical limit of the model for the filling choice $n = \frac{1}{3}$ remains unaltered for $U_1 < 0$, whereas it gets modified when one considers the $U_1 > 0$ regime. In the repulsive regime $U_1 > 0, U_2 > 0$, the only

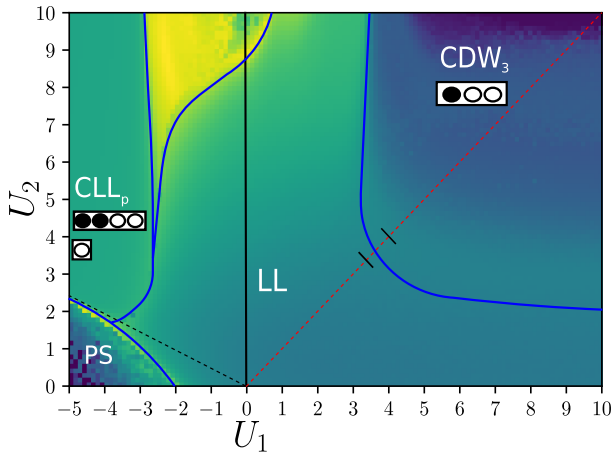

Figure 2.5: Phase diagram for n = $\frac{1}{3}$. The color map for the background displays the half-chain entanglement entropy on a L = 42 chain with PBC. Black lines are classical transition lines obtained neglecting quantum fluctuations. Additional numerical simulations are presented for the points lying on the red lines. Blue lines are a guide to the eye for the main phase boundaries.

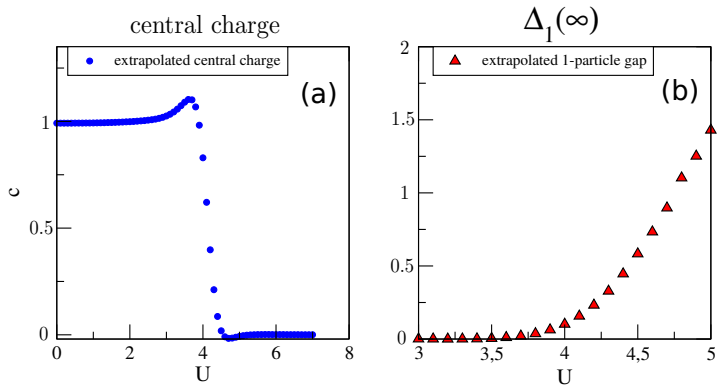

Figure 2.6: DMRG results for $n = \frac{1}{3}$ along the $U = U_2 = U_1$ line. (a) Extrapolated central charge from $L = 61, 82, 100, 121, 142$. (b) Extrapolated single-particle gap from sizes $L = 73, 97, 121$ showing its opening around the critical point.

classical configuration reaching the minimal value of energy density $\epsilon_{GS} = 0$ that is attainable is the one obtained by the periodic repetition of block C ($\bullet\circ\circ$). Such a periodic arrangement is expected to give rise at strong coupling to the gapped CDW_3 phase, which must be separated by a quantum phase transition from the LL phase at weak coupling. The existence of such a phase results naturally from the observation that the average interparticle spacing $\frac{1}{n} = 3$ exceeds the interaction range by one lattice site, thus making configurations where particles are effectively locked at distance $1 + r_c = 3$ energetically favorable.

2.4.2 The CDW_3 insulator

We now present numerical results aimed at characterizing the transition to the CDW_3 phase and its properties along the line $U_2 = U_1$. We start by providing in Fig. 2.6(a-b) the behavior of the central charge and of the 1-particle gap. The former shows a clear jump from the value $c = 1$ of the LL phase to a vanishing value, as expected from a gapped phase obeying an entanglement area law. Similarly, the 1-particle gap opens in a qualitatively slow fashion. The expected universality class for the transition to a gapped CDW phase in 1D systems is that of Berezinsky-Kosterlitz-Thouless (BKT) type [16], with an expected critical Luttinger exponent of $K_c = 2/9$ at the transition line. Interestingly, we notice that our model, or deformations of it, may be suitable for stabilizing an incommensurate floating phase [105] in the vicinity of the CDW_3 phase, where the LL phase shows density-density correlations decaying so slowly that the structure factor diverges at some incommensurate wave-vectors. Recent intensive numerical works on qualitatively related models have shown the possible realization of such unusual

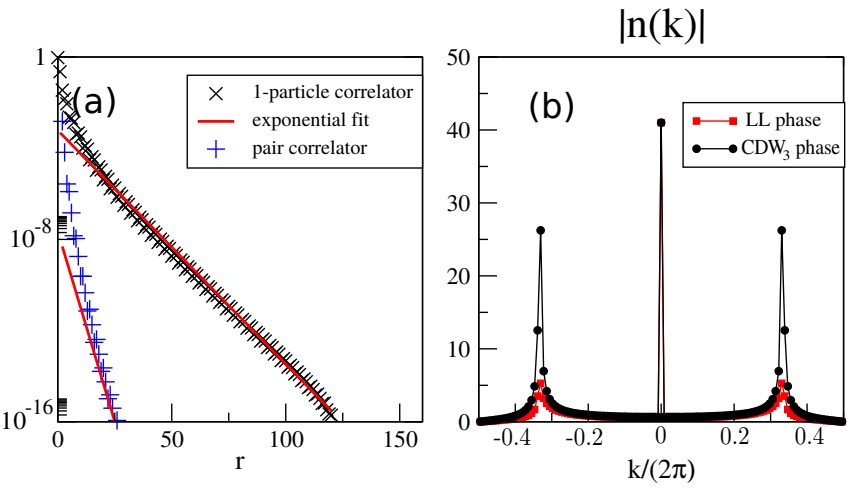

Figure 2.7: DMRG results for $n = \frac{1}{3}$ along the $U = U_2 = U_1$ line. (a) Decay of the single-particle and pair correlators $G(r)$ and $P(r)$ as a function of separation for $L = 121$ and $U = 5$, deep in the CDW phase. (b) Density profile Fourier spectrum $n(k) = \delta n(k) + n\delta_{k,0}$ for $U = 3$ (LL phase) and $U = 5$ (CDW$_3$ phase).

behavior [106, 107].

Finally, we monitor correlation properties in the CDW$_3$ phase by showing in Fig. 2.7(a-b) the sigle-particle correlator $G(r)$, the pair correlator $P(r)$ and the Fourier transform of the density profile. Consistently with the gapped nature of the phase, both $G(r)$ and $P(r)$ show exponentially-decaying correlations rather than algebraic order. The Fourier transform of the density profile corroborates the classical limit picture on the spatial structure of the CDW order by presenting distinct peaks at quasi-momentum $k = 2\pi\frac{1}{3}$ of the same order as the zero mode, thus signaling the onset of long-range crystalline order.

2.5 Phase diagram for $n = \frac{2}{5}$

In the present section we devote our attention to the study of the phase diagram for $n = \frac{2}{5}$, chosen as a representative of the density interval $\frac{1}{3} < n < \frac{1}{2}$. While the attractive part of the phase diagram is once more qualitatively unaltered, we highlight the observation of a novel, frustration-induced, exotic CLL phase in the repulsive regime to be contrasted with the pair CLL found for $U_1 < 0$ and interpret the high entropy region observed for high values of U_2 and moderate values of $|U_1|$. The general structure of the phase diagram is presented in Fig. 2.8.

2.5.1 Classical limit

While the classical limit predictions for $U_1 < 0$ remain unmodified, the classical limit ground state when $U_1 > 0$ changes radically and turns out to depend on the ratio $\frac{U_2}{U_1}$. When $\frac{U_2}{U_1} < \frac{1}{2}$, the degenerate ground-state configurations are generated by all possible permutations of blocks of type C and D ($\bullet\circ$). Since the elementary granularity in the classical limit ground-state eigenspace is given by single fermions and the effective Hamiltonian describing the effect of small quantum fluctuations within this subspace is given by Eq. (2.19), it is natural to expect that the standard LL around the noninteracting point will survive at arbitrarily strong coupling in a region compatible with the classical limit transition line $U_2 = \frac{U_1}{2}$.

Contrarily, when $\frac{U_2}{U_1} > \frac{1}{2}$, the ground-state eigenspace with $t = 0$ is obtained by considering all possible permutations of blocks C and blocks A. The strong-coupling effective description for perturbative values of t takes once more the form of a XX-Hamiltonian, described at low energy by a $c = 1$ Luttinger liquid theory. Nonetheless, since the elementary blocks carry in this case both single particles and frustration-induced pairs, we anticipate the observation of anomalous cluster features in the associated quantum liquid, as first discussed in Refs. [55, 54].

Finally, a special treatment is reserved to the line $U_1 = 0$. In such a case, the classical ground-state configurations have a richer structure, as they can be obtained by blocks of type A ($\bullet\bullet\circ\circ$), B ($\circ$) and C

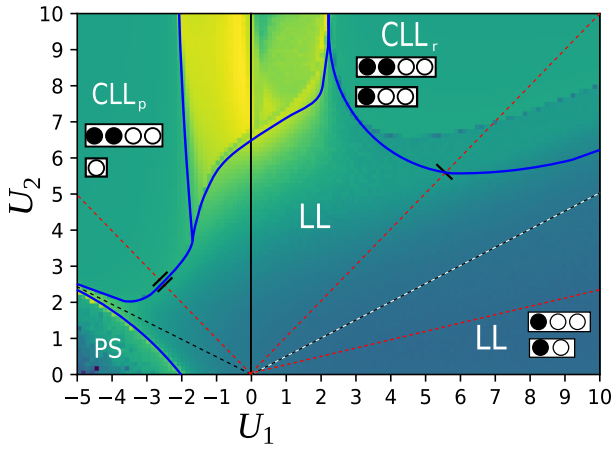

Figure 2.8: Phase diagram for $n = \frac{2}{5}$. The color map for the background displays the half-chain entanglement entropy on a system with $L = 30$ and PBC. Black lines are classical transition lines obtained neglecting quantum fluctuation. Additional numerical simulations are presented for the points lying on the red lines. Blue lines are a guide to the eye for the main phase boundaries.

$(\bullet\circ\circ)$. Denoting the number of blocks A in a ground-state configuration as N_A and similarly for blocks B and C, the following constraints must hold:

$$\begin{cases} 2N_A + N_C = N, \\ 4N_A + 3N_C + N_B = L, \end{cases} \tag{2.23}$$

which, for $n = \frac{2}{5}$, gives $N_A = \frac{L}{10} + \frac{N_B}{2}, N_C = \frac{L}{5} - N_B$, whereas N_B acts as a free parameter interpolating between the neighboring attractive regime ground-state eigenspace ($N_B = \frac{L}{5}$) and the neighboring repulsive regime one ($N_B = 0$).

To get insights on the expected quantum phase to appear when adding quantum fluctuations, we compute the effective strong-coupling Hamiltonian within the subspace spanned by the degenerate classical configurations to first order, which takes the form:

$$\hat{H} \approx -t \sum_j \left(\hat{M}_j^\dagger \hat{M}_{j+1} + H.c. \right), \tag{2.24}$$

where $\hat{M}_j = |B\rangle_j \langle C|_j$. Thus, within a first-order description, the blocks B and C obey a spin-$\frac{1}{2}$ XX dynamics, while blocks A are completely immobile. Heuristically, such a Hamiltonian favors states displaying kinetic-induced hybridization between the blocks B and C and therefore with minimal number of blocks A.

Depending on the density, two scenarios are possible: (i) when $n < \frac{1}{3}$, then one can set $N_A = 0$ in Eqs. (2.23), leading to $N_B = L - 3N_C$ and $N_C = N$ and a regular LL phase as observed in Fig. 2.1; (ii) when $\frac{1}{3} \leq n < \frac{1}{2}$, one must have $N_A \neq 0$. Since, however, the ground state of the spin-$\frac{1}{2}$ XX Hamiltonian for blocks B and C lies in the zero magnetization sector, we assume that the optimal condition is $N_B = N_C$. Specializing to the case $n = \frac{2}{5}$, we get $N_B = N_C = \frac{L}{10}$ and $N_A = \frac{3}{20}L$. As a consequence, we conjecture that the system enters a new regime of phase separation, where the CDW_2 phase coexists with a LL region at effective density $\frac{N_C}{3N_C+N_B} = \frac{1}{4}$. The latter is expected to account for the observed nontrivial behavior in the limit $\frac{U_2}{|U_1|} \gg 1$ in Fig.2.5 and 2.8.

2.5.2 Numerics: attractive regime

The phase diagram in the attractive regime is qualitatively identical to the one presented for lower values of the density. Thus, we simply mention that a CLL of pairs is still separated from the weak-coupling LL by an Ising transition, leading to a central charge $c = \frac{3}{2}$ at the critical point. In view of a comparison with the findings in the repulsive regime, we present in Fig. 2.9(a-b) the Fourier transform of the density profile and the structure factor both in the LL and in the pair CLL phases along the line $U_2 = -U_1$. The former manifestly displays a shift of the peak location from the value $k = 2\pi\frac{2}{5}$ at weak-coupling,

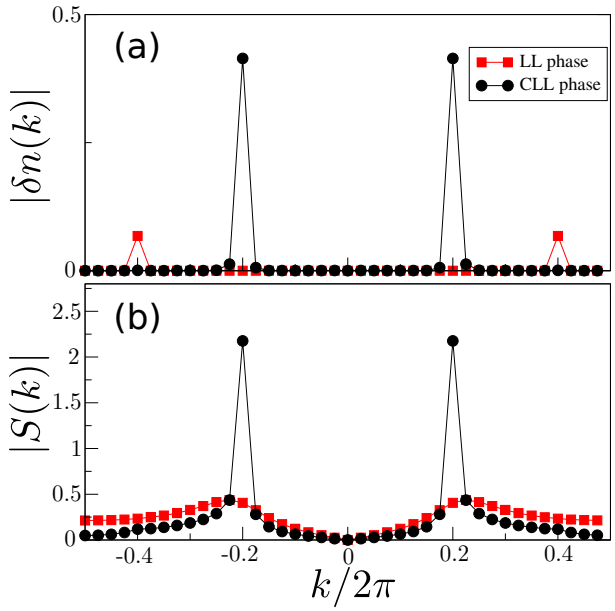

Figure 2.9: DMRG results for $n = \frac{2}{5}$ along the $U = U_2 = -U_1$ line for $L = 40$ and PBC. (a) Density fluctuations Fourier spectrum Eq. (2.9) and (b) density structure factor Eq. (2.10) both in the LL ($U = 1.5$) and CLL phase ($U = 3.5$). The momentum peak shift at value $k = 2\pi\frac{1}{5}$ is incompatible with a standard LL theory and supports that the physics of the CLL phase in the attractive regime is ruled by pair degrees of freedom.

compatible with a regular LL at density $n = \frac{2}{5}$, to the value $k = 2\pi\frac{1}{5}$ at strong coupling. Analogously, a visible peak at $k = 2\pi\frac{1}{5}$ appears in the density structure factor. The effective halving of the effective liquid density is indicative of the fact that tightly bound pairs are the low-energy degrees of freedom in the pair CLL phase.

2.5.3 Numerics: repulsive regime

At density $n = \frac{2}{5}$, the nontrivial structure of the classical limit in the repulsive region for $U_2 > \frac{U_1}{2}$ hints at the opportunity of observing an exotic liquid phase. Indeed, the main result of Refs. [55, 54] has revealed that the fitted central charge along the line $U_1 = U_2$ is compatible with a $c = \frac{3}{2}$ critical point, similarly to what observed in the attractive region. Furthermore, the behavior of the single-particle and pair gaps has been shown in Refs. [55, 54] to coincide with the ones shown in the case of the negative U_1 CLL phase, suggesting that the phase under investigation is of the same nature of the one discussed above.

Nevertheless, the classical limit cluster structure of the exotic CLL phase discovered along the line $U_2 = U_1$ differs from its $U_1 < 0$ counterpart, as the latter exhibits only tightly bound pairs of fermions, whose density is naturally $\frac{n}{2}$. On the other hand, the classical limit cluster structure in the repulsive regime for $U_2 > \frac{U_1}{2}$ comprises both blocks containing isolated fermions and blocks containing pairs. As the density of the elementary degrees of freedom in the latter case is $\frac{1-n}{2} = \frac{3}{10}$, we expect density correlation properties to allow to discriminate the repulsive regime CLL phase from the attractive regime one. Indeed, as shown in Fig. 2.10(a-b), we recover the theoretical prediction of a peak in the profile of the Fourier tranform of the density fluctuations and in the one of the structure factor at the theoretically predicted quasi-momentum $k = 2\pi\frac{3}{10}$, thus confirming the unique microscopic granularity of the $U_1 > 0$ CLL phase.

We conclude by mentioning that, in the parameter region identified by the condition $U_2 < \frac{U_1}{2}$, namely where the classical limit analysis suggests the survival of a regular LL phase at arbitrary coupling strength, we have verified it to be the case. An extrapolation of the 1-particle gap and of the central charge along the line $U_2 = \frac{U_1}{4}$ shows indeed that the former scales to zero and the latter deviates from the value $c = 1$ by at most 1% up to large values of the interaction strength and without any signature of an intervening phase transition.

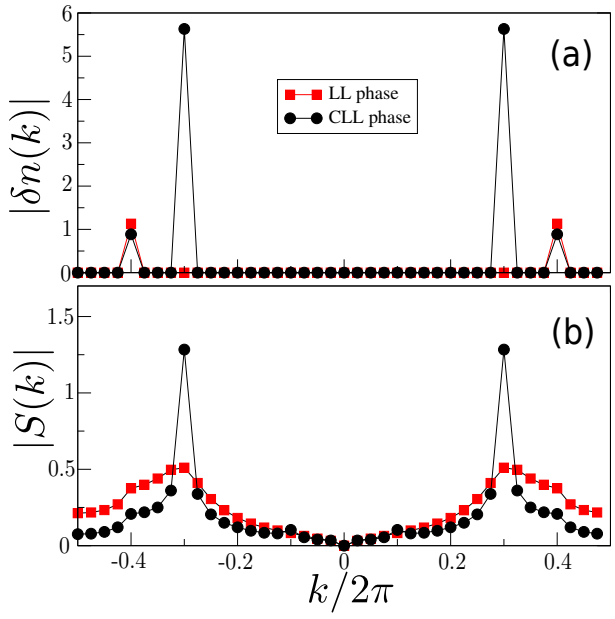

Figure 2.10: DMRG results for $n = \frac{2}{5}$ along the $U = U_2 = U_1$ line for $L = 40$ and PBC. (a) Density fluctuations Fourier spectrum Eq. (2.9) and (b) density structure factor Eq. (2.10) both in the LL ($U = 1$) and the CLL ($U = 7$) phases. The momentum peak shift to the value $k = 2\pi\frac{3}{10}$ is incompatible with a standard LL and supports that the physics of the CLL phase in the repulsive regime is ruled by the composite cluster degrees of freedom stemming from the classical limit analysis.

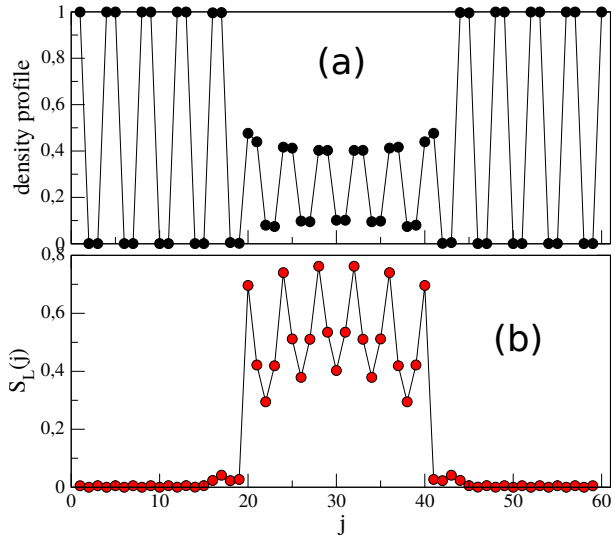

Figure 2.11: DMRG results for $n = \frac{2}{5}$ along the $U_1 = 0$ line for $U_2 = 20$, $L = 60$ and PBC. (a) Density profile. (b) Entanglement entropy profile $S_L(j)$.

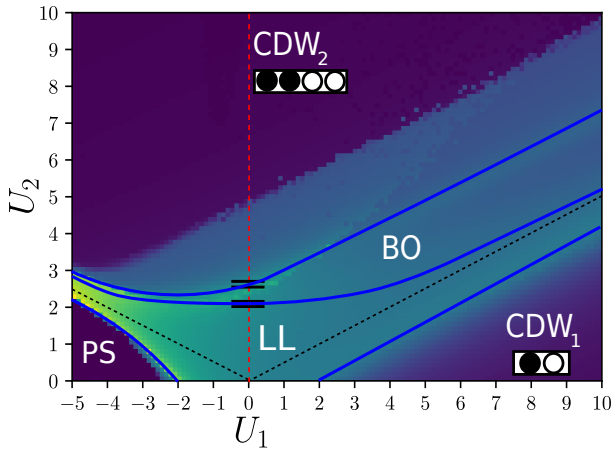

Figure 2.12: Phase diagram for $n = \frac{1}{2}$. The color map for the background displays the half-chain entanglement entropy on a $L = 28$ chain with PBC. Black lines are classical transition lines obtained neglecting quantum fluctuation. Additional numerical simulations are presented for the points lying on the red lines. Blue lines are a guide to the eye for the main phase boundaries.

2.5.4 Phase separation along the $U_1 = 0$ axis

We provide numerical evidence for the phase separation predicted for large values of $\frac{U_2}{|U_1|}$ by computing the density and the entanglement entropy profile in the aforesaid limit, as shown in Fig. 2.11(a-b). Firstly, the density pattern shows manifestly hosts the expected phase separation between a region occupied by a CDW pattern with unit cell $(\bullet\bullet\circ\circ)$, which we name CDW_2, and a region showing liquid behavior, despite the strong oscillations occurring due to a large NNN repulsion. Extracting the average effective density in the region hosting LL behavior as $n_{eff} = \frac{1}{2}\left(\langle \hat{n}_{\frac{L}{2}-1}\rangle + \langle \hat{n}_{\frac{L}{2}}\rangle\right)$, one obtains the result $n_{eff} \approx 0.25$, which coincides with its analytical estimate apart from corrections of order 10^{-3}. Secondly, the entanglement entropy vanishes in the region occupied by the CDW_2 pattern, whereas it is enhanced in the central liquid region, as expected in presence of LL behavior.

2.6 Phase diagram for $n = \frac{1}{2}$

In this section, we characterize the phase diagram for $n = \frac{1}{2}$ displayed in Fig. 2.12. For such a choice, commensurability effects give rise to two distinct gapped CDW phases at strong coupling, while a peculiar BO phase appears at intermediate coupling. We conclude by showing signatures of the transition to the PS phase. For a detailed account of the phase diagram of model (2.1) in the repulsive region $U_1 > 0$ and $U_2 > 0$, we refer to Ref. [57].

2.6.1 Classical limit

When the density takes the value $n = \frac{1}{2}$, the classical limit predictions get largely modified. While for $U_2 < -\frac{U_1}{2}$, the phase-separated classical configuration remains the optimal one, the ground-state configuration for $t = 0$ in between the lines $U_2 = -\frac{U_1}{2}$ and $U_2 = \frac{U_1}{2}$ is obtained by the periodic repetition of the U_2-induced unit cell $(\bullet\,\bullet\,\circ\circ)$, which is naturally expected to turn into a gapped CDW phase in the strong-coupling limit. Similarly, when $U_2 < \frac{U_1}{2}$, the U_1 repulsion is dominant and the classical limit ground state is given by the periodic repetition of the unit cell $(\bullet\circ)$, which we name CDW_1 order and supports the stability of the gapped CDW phase, known to occur for $U_2 = 0$ (corresponding to the fermionic formulation of the XXZ model), to the addition of a small enough value of U_2 at strong coupling.

2.6.2 Bosonization treatment

We start to elucidate the features of the phase diagram by means of a weak-coupling bosonization treatment of Hamiltonian (2.1). At density $n = \frac{1}{2}$, an additional Umklapp term contributes to the

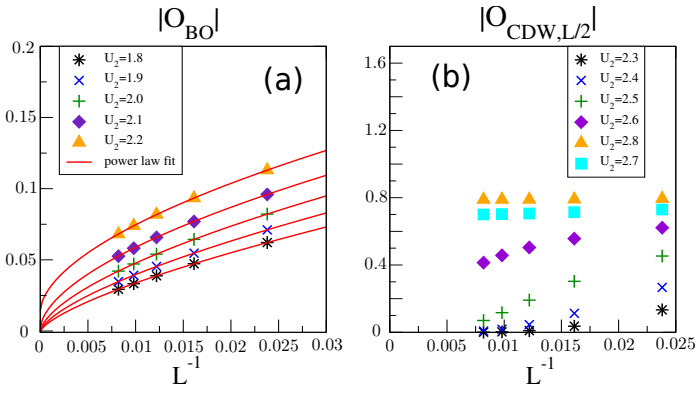

Figure 2.13: DMRG results for $n = \frac{1}{2}$ along the $U_1 = 0$ line. (a) Finite-size scaling of the BO parameter (2.13). A power law fit of the form $a_0 + a_1 L^{-a_2}$ is used. The results show the onset of the BO regime, given that for $U_2 = 2.2$ the BO parameter extrapolates to a finite nonzero value of an order of magnitude larger than the extrapolated values for smaller U_2 . (b) Finite-size scaling of the CDW order parameter (2.14). The result demonstrates that the CDW order parameter scales to zero for $U_2 < 2.6$ but acquires a finite value for $U_2 > 2.6$. Thus, there exists an intervening BO phase.

low-energy theory (2.20) with a term of the form $\hat{H}_g = g \int dx \cos\left[4\hat{\phi}(x)\right]$, leading to a Sine-Gordon field theory. The first-order renormalization group (RG) equation for the coupling $g \propto U_2 - U_1$ reads [16]:

$$\frac{dg}{dl} = (2 - 4K)g, \tag{2.25}$$

therefore implying that, when $K < \frac{1}{2}$, the system develops a finite gap in the low-energy excitation spectrum.

In order to understand the nature of the resulting phase, we consider the behavior of the local density fluctuations:

$$\delta n_j = \langle \hat{n}_j - \frac{1}{2} \rangle \sim \langle \frac{1}{\pi} \partial_x \hat{\phi} + \frac{(-1)^{\frac{x}{a}}}{\pi a} \cos\left[2\hat{\phi}(x)\right] \rangle \,, \tag{2.26}$$

and of the local BO parameter:

$$B_j = (-1)^j \langle \hat{c}_j^\dagger \hat{c}_{j+1} + h.c. \rangle \sim \langle \cos\left[2\hat{\phi}(x) - \frac{\pi}{2}\right] \rangle \,, \tag{2.27}$$

when the term $\hat{H}_g$ is relevant and the limit $|g| \to +\infty$ is considered, so that the field $\hat{\phi}(x)$ is strongly pinned around the constant value that minimizes the cosine term in $\hat{H}_g$. When $U_1 > U_2$, then $g < 0$ and $\hat{\phi}(x) \approx \phi_n = \frac{\pi}{2} n$ for some integer n. This implies $B_j \approx 0$ and $\delta n_j \approx (-1)^j$, which is compatible with a CDW_1 phase, which has unit cell $(\bullet\circ)$. Contrarily, when $U_2 > U_1$, then $g > 0$ and the field $\hat{\phi}(x)$ satisfies $\hat{\phi}(x) \approx \phi_n = \frac{\pi}{4} + \frac{\pi}{2} n$. As a result, $B_j \neq 0$ and $\delta n_j \approx 0$, which is consistent with a gapped BO phase, whose characteristic signature is indeed the emergence of a staggered bond kinetic fluctuation profile.

2.6.3 Numerics: BO and CDW_2 phases

We probe the results obtained from the bosonization analysis by computing the BO parameter (2.13) and the CDW_2 order parameter(2.14) along the line $U_1 = 0$, where we expect a first transition to a BO phase, followed by a further transition to the CDW_2 phase, which is expected to occur for a sufficiently large value of U_2 from the results of the classical limit analysis. As shown in Fig. 2.13(a-b), the BO parameter scales to a nonzero value above a critical value of U_2. Since, simultaneously, the CDW_2 order parameter vanishes in the thermodynamic limit up to a larger threshold value U_2, we conclude that there exists a stripe-shaped region occupied by a BO phase that separates the regular LL phase from the CDW_2 phase and we argue that it exists along all directions where the classical limit is given by the CDW_2 order, namely between the lines $U_2 = -\frac{U_1}{2}$ and $U_2 = \frac{U_1}{2}$.

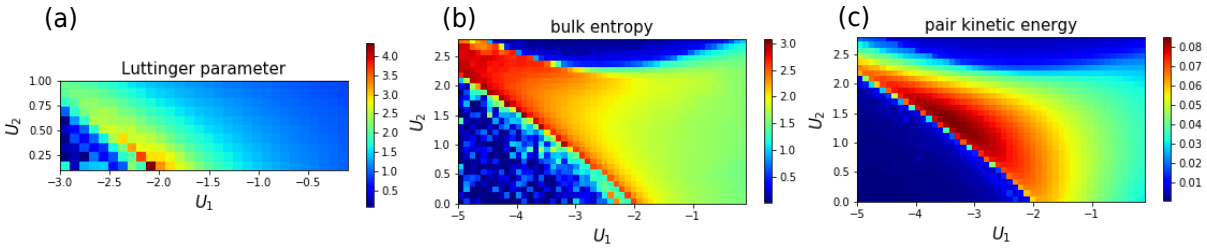

Figure 2.14: DMRG results for $n = \frac{1}{2}$ for attractive U_1. (a) Luttinger parameter K obtained from fitting the pair correlation functions to a power law. It displays large values close to the PS phase, as it is known on the XXZ line showing that pair correlations are favored. [values inside the phase-separated region are meaningless and shown to visually identify the transition line]. (b) Entanglement entropy (2.7) of half the system displaying the emergence of a characteristic peak separating the LL phase from phase separation and the appearance of the classical line $U_2 = -\frac{U_1}{2}$ as the threshold above which phase separation turns into the ($\bullet\bullet\circ\circ$) CDW_2 configuration in the infinite coupling limit. (c) Pair kinetic energy providing evidence for the enhancement of pairing fluctuations close to the transition line between the LL phase and phase separation, as expected from the divergent behavior of the Luttinger parameter in the corresponding phase diagram region.

2.6.4 Numerics: PS phase

We conclude by mentioning some characteristic signatures of the onset of phase separation in the attractive NN interaction regime, which exists for all values of n. It is indeed known from the phase diagram of the XXZ model that phase separation must occur for all values of the density on the $U_2 = 0$ line when $U_1 < -2$. Heuristically, the phase boundary is expected to shift towards more negative values of U_1 when U_2 is increased, as the NNN repulsion adds a positive contribution to the energy of the phase-separated configurations.

We confirm these expectations by plotting in Fig. 2.14(a-b-c) the map of the luttinger parameter K, the half-chain entanglement entropy and the pair kinetic energy (2.12). A large value of the Luttinger parameter is naturally linked to the dramatic increase in attractive correlations in the LL phase close to the transition to the PS phase. More explicitly, along the $U_2 = 0$ line, the expression of the Luttinger parameter is known explicitly by the formula [108]:

$$K = \frac{\pi}{2(\pi - \arccos \Delta)}, \tag{2.28}$$

where Δ is the anisotropy parameter of the XXZ chain. The expression (2.28) gives thus direct account for the occurring divergence of K at the critical point $\Delta = -1$. Naturally, the high value of K gives rise to enhanced pairing correlations, as the enhancement of the pair kinetic energy demonstrates. Finally, monitoring the bulk entropy magnitude nicely shows the boundaries separating the LL regime from the low-entropy gapped CDW_2 phase and the phase-separated phase. The bump in the bulk entropy value close to the PS phase is consistent with the behavior of the entanglement entropy in Heisenberg-like models predicted in Ref. [109], which are expected to describe the low-energy universality class of the system at the boundary between LL phase and PS phase.

2.7 Conclusions

In this chapter we have presented a systematic study of the general structure of the phase diagram of a 1D lattice model of spinless fermions interacting through NN and NNN density-density interactions for several distinct fillings. The presented work concludes a series of studies, reported in Refs. [70, 71, 73, 57, 76, 55, 54, 77], where only very specific parts of the phase diagram had been investigated. The addressed model Hamiltonian (2.1), chosen as a paradigmatic model for the characterization of pairing in spinless fermions, has been shown to display a wide variety of phases. Beyond the most conventional ones in 1D quantum many-body systems, such as CDW orders and phase-separated regimes (including a novel U_2-induced phase separation between a Luttinger liquid pahse and a CDW_2 phase), the departure from the paradigm of NN interactions via the introduction of a NNN repulsion generates unconventional liquid phases whose low-energy description is given by a Luttinger liquid field theory,

while their microscopic effective low-energy degrees of freedom have a nontrivial cluster structure. We characterized such exotic Luttinger liquid phases both in the $U_1 > 0$ regime, where their properties were first discussed in Refs. [55, 54], and in the $U_1 < 0$ regime, where a novel paired liquid phase is introduced. The analytical and numerical characterization of these phases and of the phase transitions separating them from the weak-coupling LL phase are to be regarded as particularly insightful in view of further investigations.

As previously mentioned, the obtained results aim at paving the way towards the experimental realization of pairing phases in experimentally available cold-atom platforms. Since pairing is a key ingredient in models featuring Majorana zero modes, the discovery of such pairing phases may represent a significant step in the direction of their observation in cold-atom quantum simulators. Moreover, our results may serve the more general purpose to guide the understanding of the ground-state properties of arrays of Rydberg atoms, which may realize an experimental instance of Hamiltonian (2.1) for specific choices of the setup's parameters.

Chapter 3

Two-fluid coexistence in a chain of spinless fermions with pair-hopping

The present chapter is devoted to the study of the transition from a regular Luttinger liquid phase to a Luttinger liquid of pairs in a model of spinless fermions with correlated pair-hopping. The main result of the analysis, presented in Refs. [110, 111], is the discovery of a novel intermendiate phase where a liquid of pairs coexists with a liquid with single-particle granularity without phase separation. The discussion of the results proceeds from a description of the phase diagram of the model that identifies the location of the unexpected coexistence phase. A phenomenological model and several numerical probes in its support are presented to characterize the properties of the novel phase.

3.1 Introduction

The search for zero-energy Majorana modes, which naturally appear in topological superconducting models [4], has raised a remarkable interest in the problem of pairing in number-conserving models [112, 113, 114, 115, 116, 117, 118, 119, 120, 121, 122, 123, 124, 125, 126]. A paired phase is a phase where two (or more) fermions bind together and behave as a singular molecular object. In one dimension (1D), the characteristic signature of pairing is the absence of any fermionic order, whereas pairs display quasi-long-range order. For spin-1/2 fermions, the attractive Hubbard model naturally favors onsite singlet pairing [127, 128]. Increasing the number of internal degrees of freedom allows a pairing mode to coexist with a remaining decoupled fermionic mode [129]. For spinless fermions, pairing requires finite-range interaction but no coexistence with unpaired fermions is observed [55, 54, 28, 60]. Importantly, spatial interfaces between paired and unpaired phases should host Majorana zero modes, which could then be realised without resorting on superconducting proximity effects [67, 26].

The difficulty in studying the pairing transition in systems of fermions with no internal degrees of freedom is that it implies a reshaping of the low-energy sector of the model, with the appearance (or disappearance) of Fermi points, to be taken into account by unconventional bosonisation treatments [67, 26]. A particularly visual model based on two fluids, a bosonic one describing the pairs, and a fermionic one describing the unpaired fermions, has been presented recently [27]. These studies agree on the fact that paired and unpaired phases are separated by a continuous phase transition with central charge $c = 3/2$ [67, 27] originating from a standard gapless mode and an additional Ising/Majorana degree of freedom. This prediction has been verified by several numerical analyses [55, 54, 28, 60].

In this chapter, we show that the phenomenology of the pairing transition is richer. We revisit a 1D spinless-fermion model introduced in Ref. [26] in which pair hopping competes with single fermion hopping. Related electronic models with correlated hopping, such as the Penson-Kolb-Hubbard model [130, 131, 132, 133, 134, 135], have been proposed in the context of high-T_c superconductors [136] and lead to rich and complex phase diagrams [137]; our model also bears some relations with the folded spin-1/2 model [138, 139] and the Bariev model, which are exactly-solvable with Bethe ansatz [140], and with models for ultra-cold gases with synthetic dimension [141, 142].

We start by a thorough characterization of the paired Luttinger liquid phases emerging in the strong-coupling regime of the model via exact analytical results and numerical simulations. Afterwards, we proceed to demonstrate the emergence of a coexistence phase comprising neighbouring paired fermions

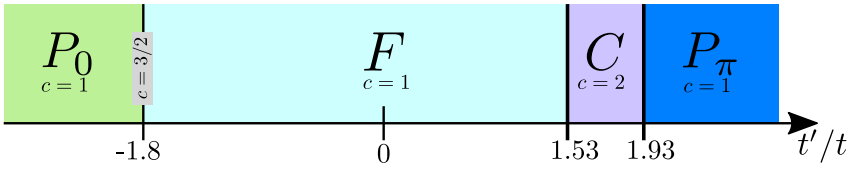

Figure 3.1: Sketch of the phase diagram of model (3.1) for density $n = 0.25$. Four phases appear: a regular Luttinger liquid fermionic phase F, paired Luttinger liquid phases P_0 and P_π and a coexistence phase C with central charge $c = 2$, where fermions and P_π pairs are mixed.

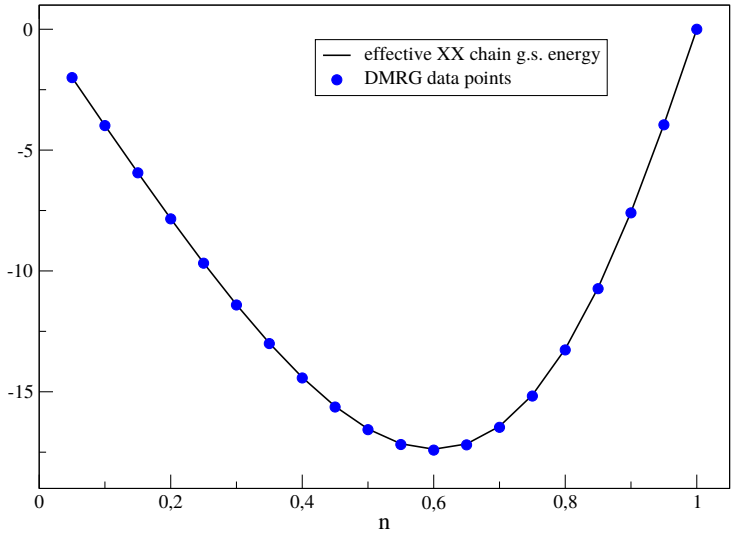

Figure 3.2: Ground state energy of a system described by Hamiltonian (3.1) with PBC on a lattice of size $L = 40$ as a function of the filling $n \in (0, 1]$.

in a sea of unpaired fermions that is stable towards phase separation. Since pairs are composed of two fermions, it is not obvious that they could coexist with gapless fermionic excitations. Indeed, semiclassical intuition and the standard Luttinger liquid (LL) approach lead to the conclusion that all fermions are either paired or unpaired. Yet, taking superfluids as a paradigmatic example, phases with two coexisting fluids are not novel to condensed-matter physics [143]. We start the discussion of the coexistence phase by introducing a phenomenological two-fluid ($2F$) model inspired by Ref. [27] and get predictions on the expected behavior of energetic observables and on the critical behavior resulting from their nonanalyticities. Our analytical findings are then supported and largely complemented by numerical simulations, which are fully interpreted with a phenomenological $2F$ picture. We conclude by pinpointing under which conditions the two kinds of scenarios, extended coexistence phase or a $c = \frac{3}{2}$ transition point, take place (see also Ref. [58]).

3.2 Model Hamiltonian and phase diagram

The model Hamiltonian whose ground-state phase diagram is the focus of the work reads:

$$\hat{H} = -t \sum_j \left[\hat{c}_j^\dagger \hat{c}_{j+1} + H.c. \right] - t' \sum_j \left[\hat{c}_{j+1}^\dagger \hat{n}_j \hat{c}_{j-1} + H.c. \right], \tag{3.1}$$

where $\hat{c}_j^{(\dagger)}$ are annihilation (creation) operators for spinless fermions, t is the single-particle hopping amplitude and t' is the pair-hopping amplitude. We work in a generic low-density regime by fixing the filling to the value $n = \frac{N}{L} = 0.25$ (N being the total number of fermions and L being the number of lattice sites), with the goal of characterizing the competition between single-particle and pair kinetic fluctuations. The numerical DMRG simulations are carried out with two implementations of the DMRG algorithm [144, 145, 81, 82], one of which being based on the ITensor library [98].

The phase diagram as a function of $\tau = \frac{t'}{t}$ is sketched in Fig. 3.1. While a regular Luttinger liquid phase, which we call F phase, surrounds the $t' = 0$ point, at large values of $|\tau|$ two paired Luttinger

liquid phases with gapped 1-particle excitations and gapless pair excitations are observed. They are denoted as P_0 and P_π phases, depending on whether the pairs quasicondense around quasimomentum $k = 0$ or $k = \pi$. The transition from the F to the P_0 phase is direct, in agreement with Ref. [26], whereas the transition from the F to the P_π phase is mediated by an intervening coexistence phase C between a liquid of single fermions and a liquid of pairs.

3.3 The paired phases

We start the description of the phase diagram in Fig. 3.1 by describing the properties of the paired phases P_0 and P_π. When $t = 0$, since the interaction term favours energetically configurations where fermions delocalize as tightly-bound pairs, we argue [142, 138] that the ground state lies in the subspace $\mathcal{H}_P$ where the $2N_b$ fermions in the system are arranged into N_b nearest-neighbor pairs. Each configuration in the subspace $\mathcal{H}_P$ can be mapped onto a configuration on a spin-$\frac{1}{2}$ chain of length $L_b = L - N_b$ via the rules $|\bullet\bullet\rangle \to |\uparrow\rangle$, $|\circ\rangle \to |\downarrow\rangle$.

Then, the action of the fermionic Hamiltonian on a configuration of $\mathcal{H}_P$ is equivalent to that of an effective XX Hamiltonian:

$$\hat{H}_{eff} = t' \sum_{j=1}^{L_b} \left[\hat{\sigma}_j^+ \hat{\sigma}_{j+1}^- + H.c.\right] \tag{3.2}$$

on the corresponding configuration in the equivalent spin chain. To be precise, the equivalence is rigorously correct only in OBC, but, as detailed below, the quality of the approximation when considering PBC foth for Hamiltonian (3.1) and (3.2) is excellent, as the corrections are expected to be given by boundary terms that do not affect the thermodynamic limit.

Hamiltonian (3.2) can be brought to the diagonal form $\hat{H}_{eff} = \sum_k \epsilon_p(k)\hat{n}_k$, where the pair dispersion relation reads $\epsilon_p(k) = 2t' \cos k$, and the ground-state energy density $e_{eff} = \frac{\langle \hat{H}_{eff} \rangle}{L}$ can be evaluated as:

$$e_{eff} = \frac{1}{L} \sum_{|k|<\pi\frac{N_b}{L_b}} \epsilon_p(k) = -\frac{2|t'|}{\pi}\left(1 - \frac{n}{2}\right) \sin\left(\frac{\pi n}{2-n}\right). \tag{3.3}$$

The result (3.3) agrees with the DMRG data on Hamiltonian (3.1) for $t = 0$, as shown in Fig. 3.2, thus confirming the correctness of the initial assumption.

The reciprocal space picture obtained in the limiting case $t = 0$ predicting quasicondensation of pairs around $k = 0$ when $t' < 0$ and around $k = \pi$ when $t' > 0$ is robust to the addition of a sufficiently small value of $t \neq 0$, thus demonstrating the stability of the paired P_0 and P_π phases in the strong-coupling limit $|\tau| \ll 1$. We probe this statement by computing the pair occupation number:

$$P(k) = \frac{1}{L} \sum_{j,j'} e^{ik(j-j')} \langle \hat{c}_j^\dagger \hat{c}_{j+1}^\dagger \hat{c}_{j'} \hat{c}_{j'+1} \rangle, \tag{3.4}$$

namely, the Fourier transform of the pair correlation function. As shown in Fig. 3.3, the momentum distribution function is qualitatively captured by the pair dispersion relation $\epsilon_p(k)$ at small but nonzero t.

Moreover, the two curves are essentially related by a shift of π along the momentum axis. The latter feature can be explained naturally when $t = 0$, as the unitary transformation $\hat{c}_j \to e^{i\frac{\pi}{2}j}\hat{c}_j$ implements the transformation $\hat{H}(t = 0, t') \to \hat{H}(t = 0, -t')$ on Hamiltonian (3.1). This implies that $P(k) \to P(k - \pi)$ when $t = 0$. Even though the aforesaid transformation rule does not relate the ground-state properties for $t' > 0$ to the ones for $t' < 0$ when $t \neq 0$, the dominant weights of fully-paired configurations in the ground state at strong coupling makes it effectively still applicable.

3.4 The coexistence phase

In the present section, we discuss the properties of the C phase and the phase transitions separating it from the weak- and strong-coupling phases. We start by introducing a phenomenological model aimed at describing the intermediate-coupling regime where the C phase is expected to occur and derive several

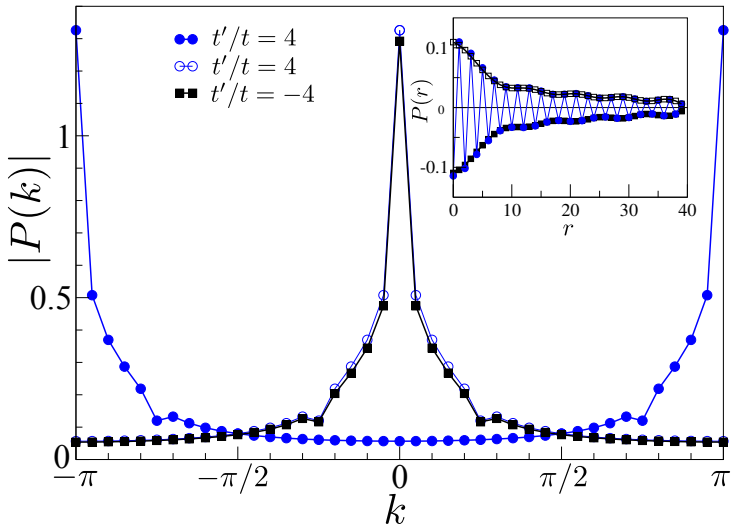

Figure 3.3: bsolute value of the Fourier transform of pair correlations for an open chain with $L = 80$ and $\frac{t'}{t} = \pm 4$. Open symbols are the $\frac{t'}{t} = 4$ data shifted by π. Inset: Pair correlations.

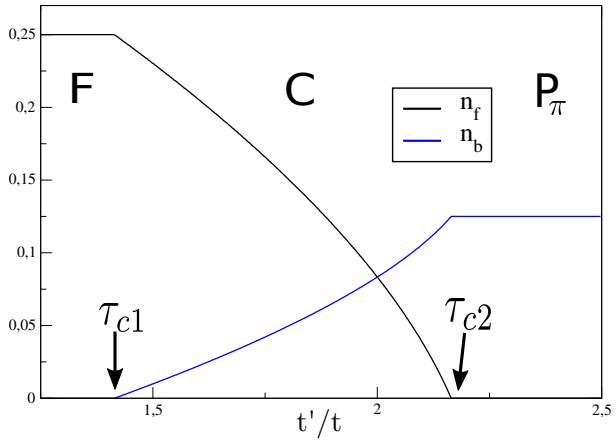

Figure 3.4: Optimal fermionic and bosonic densities obtained by minimizing $\frac{e_{2F}}{t}$ for a total density $n = 0.25$. Two critical points, τ_{c1} and τ_{c2}, divide the phase diagram into three distinct phases: (i) the fermionic F phase, where the system is populated by fermions only, (ii) the C phase, characterized by the coexistence of fermions and hard-core bosons, and (iii) the P_π phase, where the system is populated by hard-core bosonic particles only.

predictions with regard to the critical behavior. We follow it up with a detailed overview of the numerical evidences for the existence of such a phase, comparing the results to the corresponding analytical predictions, when possible. We conclude with a heuristic discussion of the mechanism underlying the onset of the C phase via simple considerations.

3.4.1 The two-fluid model

Since the ground state of model (3.1) is given by a noninteracting Fermi sea when $t' = 0$ and by a liquid of pairs that map to noninteracting hard-core bosons when $t = 0$, we now aim at describing the intermediate-coupling behavior by means of a phenomenological model that interpolates between the two extreme cases. More precisely, we consider a system comprising two species of particles, namely fermionic particles (modelling unpaired fermions) and hard-core bosonic ones (modelling pairs), described respectively by a free fermion Hamiltonian $\hat{H}_f$ and a XX-chain Hamiltonian $\hat{H}_b$:

$$\hat{H}_f = -t \sum_j \hat{d}_j^\dagger \hat{d}_{j+1} + H.c., \tag{3.5}$$

$$\hat{H}_b = t' \sum_j \hat{\sigma}_j^+ \hat{\sigma}_{j+1}^- + H.c., \tag{3.6}$$

where the fermionic operators $\hat{d}_j, \hat{d}_j^\dagger$ and the hard-core bosonic operators $\hat{\sigma}_j^-, \hat{\sigma}_j^+$ do not bear any exact relation with the original lattice fermionic operator $\hat{c}_j, \hat{c}_j^\dagger$. The two species interact solely through the total density constraint $n = n_f + 2n_b$, where n_f is the fermionic density and n_b is the hard-core bosonic one. Then, the total energy density of the Hamiltonian $\hat{H}_{2F} = \hat{H}_f + \hat{H}_b$ reads:

$$e_{2F} = -\frac{2t}{\pi}\left[\sin(\pi n_f) + \tau \sin\left(\pi \frac{n - n_f}{2}\right)\right]. \tag{3.7}$$

By minimizing e_{2F} with respect to n_f for different values of τ, we are able to predict the structure of the phase diagram of model 3.1 and the nature of the quantum phase transitions that it displays in the parameter regime $t' > 0$.

Density in the 2F model

The behaviour of the optimal fermionic density, and therefore of the optimal value of the populations n_f and n_b, can be captured by estimating numerically the value of n_f that minimizes the rescaled ground state energy density $\frac{e_{2F}}{t}$, e_{2F} being given in Eq. (3.7), as a function of $\tau = t'/t$. The result is presented in Fig. 3.4. We naturally identify three distinct phases: (i) a fully fermionic region, for $0 < \tau < \tau_{c1}$ with $\tau_{c1} = 2\cos(\pi n) \approx 1.41$, in which $n_f = n$ and $n_b = 0$, that we interpret as the F phase; (ii) an intermediate region, for $\tau_{c1} < \tau < \tau_{c2}$ with $\tau_{c2} = \frac{2}{\cos\left(\frac{\pi n}{2}\right)} \approx 2.16$, in which both n_f and n_b are nonzero, that we interpret as the C phase; and (iii) a fully bosonic region, for $\tau > \tau_{c2}$, in which $n_f = 0$ while $n_b = \frac{n}{2}$, corresponding to the P_π phase.

In order to obtain the behaviour of the optimal fermionic density as approaching the phase boundaries of the coexistence phase, as well as the position of the phase boundaries, we consider the stationarity condition $\dfrac{\partial e_{2F}}{\partial n_f} = 0$, which reads:

$$\cos(\pi n_f) = \frac{\tau}{2} \cos\left(\pi \frac{n - n_f}{2}\right) \tag{3.8}$$

Assuming self-consistently that $n_f \approx n$, which amounts to enforce the system to approach the fully fermionic region from the coexistence phase, the r.h.s. of Eq. (3.8) takes the form $\frac{\tau}{2}[1 + O\left((n - n_f)^2\right)]$, whereas the l.h.s. reads:

$$\cos(\pi n_f) = \cos(\pi n)\left[1 + O\left((n - n_f)^2\right)\right] - \sin(\pi n)\left[\pi(n_f - n) + O\left((n - n_f)^2\right)\right]. \tag{3.9}$$

Neglecting the terms proportional to $(n_f - n)^m$ for $m > 1$ and solving for the fermionic density n_f, one obtains:

$$n_f(\tau) \approx n - \frac{\frac{\tau}{2} - \cos(\pi n)}{\pi \sin(\pi n)}, \tag{3.10}$$

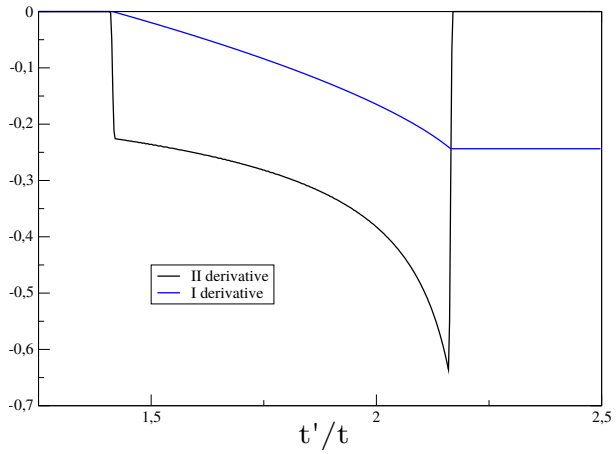

Figure 3.5: First and second derivative of $\epsilon_{GS}\left(\tau, n_f(\tau)\right)$ as a function of τ for a total density $n = 0.25$.

which allows to identify the location of the critical point separating the fermionic phase and the mixed phase with:

$$\tau_{c1} = 2\cos(\pi n) \simeq 1.41 \tag{3.11}$$

and justifies neglecting higher order contributions in $n_f - n$ as they would scale as increasing powers in the deviation from the critical point $\tau - \tau_{c1}$.

Similarly, assuming $n_f \approx 0$, we can explore the asymptotic behaviour of n_f as the system approaches the transition to the fully bosonic phase. In this case, the l.h.s. of Eq. (3.8) reads $1 + O\left((n_f)^2\right)$, while the r.h.s. takes the form:

$$\frac{\tau}{2}\cos\left[\pi\frac{n-n_f}{2}\right] = \frac{\tau}{2}\left\{\cos\left(\frac{\pi n}{2}\right)\left[1+O(n_f^2)\right] + \sin\left(\frac{\pi n}{2}\right)\left[\frac{\pi n_f}{2} + O(n_f^2)\right]\right\}. \tag{3.12}$$

Neglecting terms of order higher than one in the density, we derive the asymptotic behaviour:

$$n_f(\tau) \approx \frac{1-\cos\left(\frac{\pi n}{2}\right)\frac{\tau}{2}}{\frac{\pi}{2}\sin\left(\frac{\pi n}{2}\right)\frac{\tau}{2}}, \tag{3.13}$$

from which we extract the value of the critical point:

$$\tau_{c2} = \frac{2}{\cos\left(\frac{\pi n}{2}\right)} \simeq 2.16 \tag{3.14}$$

separating the mixed phase from the bosonic phase and we justify a posteriori the truncation of the Taylor expansion in powers of the density.

Energy in the 2F model

Let us consider the rescaled energy density in the 2F model $\hat{H}_{2F}$:

$$\epsilon_{GS}\left(\tau, n_f(\tau)\right) = \frac{e_{2F}}{t} = -\frac{2}{\pi}\left[\sin(\pi n_f(\tau)) + \tau\sin\left(\pi\frac{n-n_f(\tau)}{2}\right)\right], \tag{3.15}$$

where $n_f(\tau)$ is the optimal fermionic density as a function of τ. Its first derivative with respect to τ can be written as:

$$\begin{aligned}\frac{\mathrm{d}\epsilon_{GS}\left(\tau, n_f(\tau)\right)}{\mathrm{d}\tau} &= \frac{\partial\epsilon_{GS}\left(\tau, n_f(\tau)\right)}{\partial\tau} + \left.\frac{\partial\epsilon_{GS}\left(\tau, n_f\right)}{\partial n_f}\right|_{n_f=n_f(\tau)}\frac{\mathrm{d}n_f(\tau)}{\mathrm{d}\tau} = \frac{\partial\epsilon_{GS}\left(\tau, n_f(\tau)\right)}{\partial\tau} = \\ &= -\frac{2}{\pi}\sin\left(\pi\frac{n-n_f(\tau)}{2}\right),\end{aligned} \tag{3.16}$$

where the stationarity condition $\left.\frac{\partial\epsilon_{GS}\left(\tau, n_f\right)}{\partial n_f}\right|_{n_f=n_f(\tau)} = 0$ satisfied by the optimal fermionic density has been used to get rid of the second contribution.

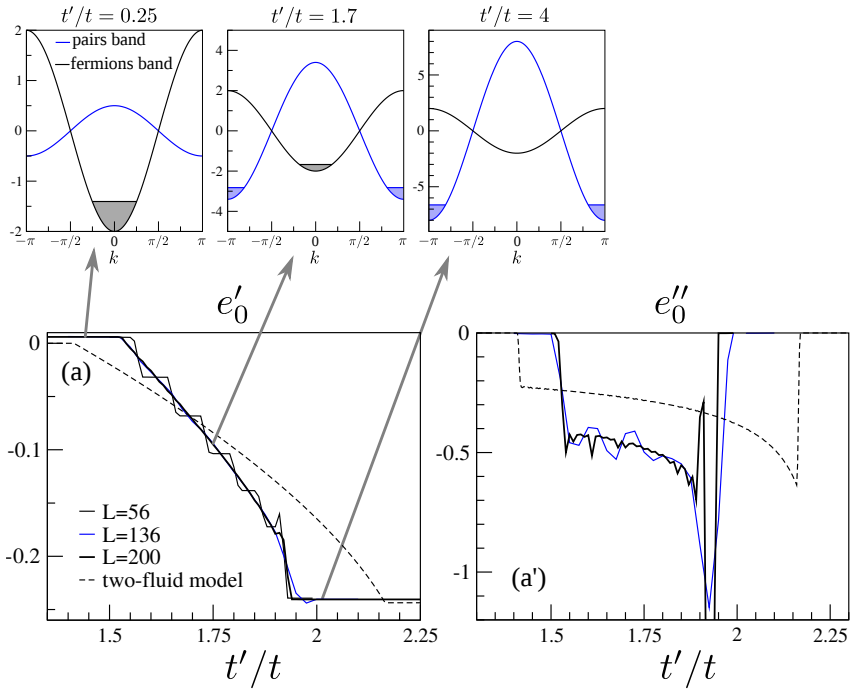

Figure 3.6: (a) First and (a') second derivatives of the energy density e_0 as a function of $\frac{t'}{t}$ for three system sizes: $L = 56, 136, 200$. Dotted lines are predictions of the 2F model. Arrows point toward typical band structures of the $2F$ model for $\frac{t'}{t} = 0.25$, $\frac{t'}{t} = 1.7$, and $\frac{t'}{t} = 4$.

Consequently, given that $n_f = n$ in the fermionic phase, $n_f = 0$ in the bosonic phase and the asymptotic behaviour of n_f while approaching the critical point from the coexistence phase is given in Eqs. (3.10) and (3.13), it is straightforward to obtain that:

$$\frac{\mathrm{d}\epsilon_{GS}\left(\tau, n_f(\tau)\right)}{\mathrm{d}\tau} = \begin{cases} 0 & 0 \leq \tau \leq 2\cos(\pi n) \\ -\frac{1}{2\pi\sin(\pi n)}\left(\tau - 2\cos(\pi n)\right) & \tau \to \left(2\cos(\pi n)\right)^+ \\ -\frac{2}{\pi}\left[\sin\left(\frac{\pi n}{2}\right) + \frac{\cos^3\left(\frac{\pi n}{2}\right)}{2\sin\left(\frac{\pi n}{2}\right)}\left(\tau - \frac{2}{\cos\left(\frac{\pi n}{2}\right)}\right)\right] & \tau \to \left(\frac{2}{\cos\left(\frac{\pi n}{2}\right)}\right)^- \\ -\frac{2}{\pi}\sin\left(\frac{\pi n}{2}\right) & \tau > \frac{2}{\cos\left(\frac{\pi n}{2}\right)}. \end{cases} \tag{3.17}$$

From the above formula, the singular behavior of the second derivative of the rescaled ground state energy density can be characterized as follows:

$$\frac{\mathrm{d}^2\epsilon_{GS}\left(\tau, n_f(\tau)\right)}{\mathrm{d}\tau^2} = \begin{cases} 0 & 0 \leq \tau \leq 2\cos(\pi n) \\ -\frac{1}{2\pi\sin(\pi n)} & \tau \to \left(2\cos(\pi n)\right)^+ \\ -\frac{\cos^3\left(\frac{\pi n}{2}\right)}{\pi\sin\left(\frac{\pi n}{2}\right)} & \tau \to \left(\frac{2}{\cos\left(\frac{\pi n}{2}\right)}\right)^- \\ 0 & \tau > \frac{2}{\cos\left(\frac{\pi n}{2}\right)}, \end{cases} \tag{3.18}$$

thus proving that the two transitions are of second order type, as the first derivative is continuous and the second derivative exhibits a finite jump discontinuity at the critical points. The results are summarized in Fig. 3.5, where the first and second derivative of the ground state energy density are shown as a function of τ.

3.4.2 Numerical signatures of the C phase

We notice that the jumps in the second derivative of the energy are directly related to jumps in the first derivative of the order parameter n_f, as one can show that:

$$\frac{\mathrm{d}^2\epsilon_{GS}\left(\tau, n_f(\tau)\right)}{\mathrm{d}\tau^2} = \cos\left(\frac{\pi}{2}(n - n_f(\tau))\right)\frac{\mathrm{d}n_f}{\mathrm{d}\tau}\,. \tag{3.19}$$

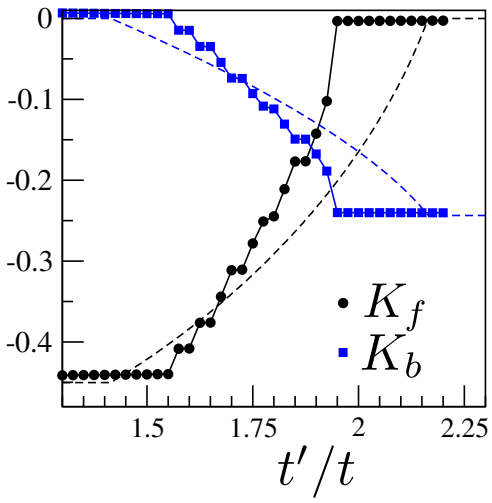

Figure 3.7: Total single-particle kinetic energy density K_f and pair kinetic energy density K_b, probing almost directly n_f and n_b. The black dotted line corresponds the $2F$ model prediction for K_f, while the blue dotted line is the one for K_b. The sequence of small plateaus in K_f and K_b corresponds to the progressive formation of tightly-bound pairs when increasing the value of $\frac{t'}{t}$.

Therefore, the nature of the phase transitions can be inferred from a reciprocal space picture. Indeed, as the critical points τ_{c1} and τ_{c2} correspond to points in parameter space where either the band populated by fermions or the one populated by hard-core bosons start to get filled or are fully depleted, then the quantum phase transitions are linked to the appearance/disappearance of a pair of gapless points in the low-energy spectrum, namely an abrupt change in the structure of the Fermi surface. Such transitions are named Lifschitz phase transitions and encompass the ones predicted by the effective $2F$ model.

We now proceed to probe the existence and properties of the C phase by performing numerical DMRG simulations of the model Hamiltonian (3.1). We start the discussion by monitoring energetic observables, which allow for a direct comparison with the $2F$ model prediction. We proceed by discussing entanglement properties, which give direct evidence for a nontrivial reshaping of the low-energy sector of the model. We conclude with the discussion of correlation properties in the C phase, that are further interpreted in light of the picture of a coexistence between a regular Luttinger liquid and a Luttinger liquid of pairs.

Energetic observables

The first quantities that we monitor are the first and second derivative of the ground-state energy density of model (3.1). We provide their behavior in Fig. 3.6 and compare it with the $2F$ model prediction. Strikingly, the $2F$ model reproduces the qualitative features of the behavior of the ground-state energy density first and second derivative. The numerical data for the latter show decisively the robustness of two distinct critical points against the increase in the considered system's size, thus demonstrating the stability of the C phase on a finite intermediate range of interaction parameters in between the weak-coupling and the strong-coupling phase.

We complement this analysis by providing in Fig. 3.7 the behavior of the total single-particle kinetic energy density:

$$K_f = -\frac{1}{L}\sum_j \left[\hat{c}_j^\dagger \hat{c}_{j+1} + H.c.\right], \tag{3.20}$$

and the total pair kinetic energy density:

$$K_b = -\frac{1}{L}\sum_j \left[\hat{c}_{j+1}^\dagger \hat{c}_j^\dagger \hat{c}_j \hat{c}_{j-1} + H.c.\right], \tag{3.21}$$

which correspond to the two contributions to the total energy density of model (3.1). As the main contribution to K_f is expected to come from single fermions and the main contribution to K_b from

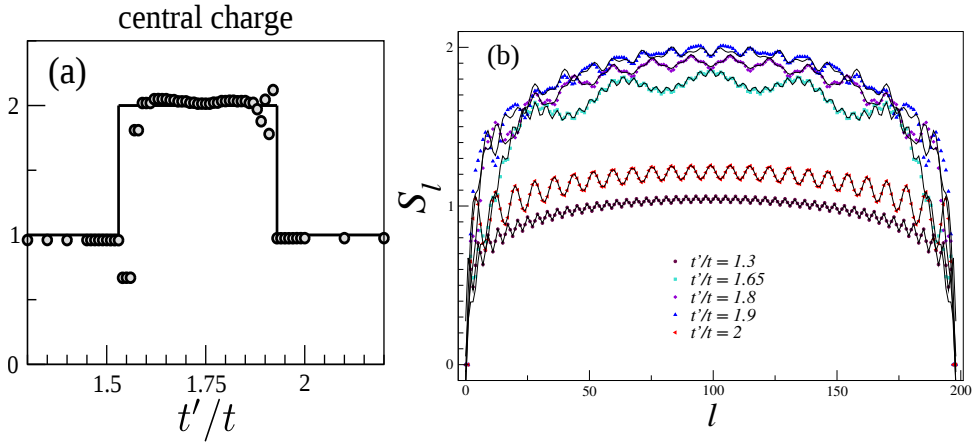

Figure 3.8: (a) Fitted central charge as a function of $\frac{t'}{t}$. (b) Fits of the entropy on an open chain with $L = 200$: symbols are DMRG data, black lines are fits with Eq. (3.22).

paired fermions, we compare K_f and K_b as a function of τ to the energy density contribution stemming from the fermionic channel and from the hard-core bosonic one, respectively, in the $2F$ model. These correspond simply to the first and second term of e_{2F}, namely $-\frac{2}{\pi}\sin(\pi n_f)$ and $-\frac{2}{\pi}\sin\left(\pi\frac{n-n_f}{2}\right)$.

The result shows once again consistency with the predictions of the $2F$ model. Consistently with the observation that K_f and K_b capture the behavior of the populations n_f and n_b as a function of τ up to a sine function in the $2F$ model framework, the numerical data show indeed saturation of these two quantities to constant values in the single-species F and P_π phases, whereas they interpolate from zero to their maximal value inside the C phase. We conclude therefore that the kinetic observables K_f and K_b represent a direct probe of the order parameter n_f that allows to discriminate between the F, C and P_π phases.

Entanglement properties

We proceed our numerical overview of the phase diagram for $\tau > 0$ by considering entanglement properties of the encountered phases. We show in Fig. 3.8(a) the behavior of the central charge c as a function of τ. The obtained result shows explicitly the presence of two phases with $c = 1$ at small and large values of τ, that are identified with the weak-coupling Luttinger liquid and the Luttinger liquid of pairs, respectively. These are separated by an intervening phase with $c = 2$, namely a phase with two gapless Luttinger liquid modes, that is naturally identified with the C phase, where the two sound modes are the phononic excitations resulting from single-particle and pair density-wave excitations, respectively.

We complement our analysis of the entanglement properties by providing in Fig. 3.8(b) some examples of the entanglement entropy profiles, whose fit to the formula:

$$S_L(l) = \frac{c}{6}\log\left[\frac{2L}{\pi}\sin\left(\frac{\pi l}{L}\right)\right] + A + C_f\left\langle c^\dagger_{\ell+1}c_l + \text{H.c.}\right\rangle + C_b\left\langle c^\dagger_{l+2}c^\dagger_{l+1}c_l c_{l-1} + \text{H.c.}\right\rangle, \tag{3.22}$$

allows to obtain an estimate of the central charge c. In Eq. (3.22), c is the central charge, L is the system size and A and $C_{f,b}$ are constants to be treated as fit parameters, together with c. Firstly, the jump of the bulk entanglement entropy for values lying inside the C phase is qualitatively associated to the doubling of the central charge in the latter. Secondly, the finite-size oscillations in the entanglement entropy profile account for a real space picture of the three phases: in the F and P_π phases the oscillations occur at a period $\frac{1}{n}$ and $\frac{2}{n}$, respectively, which coincide with the average interparticle and interpair spacing in a liquid of either single-particle or pair microscopic granularity; in the C phase, instead, one observes a long-wavelength modulation related to the presence of pairs and a short-wavelength one linked to the simultaneous presence of isolated fermions.

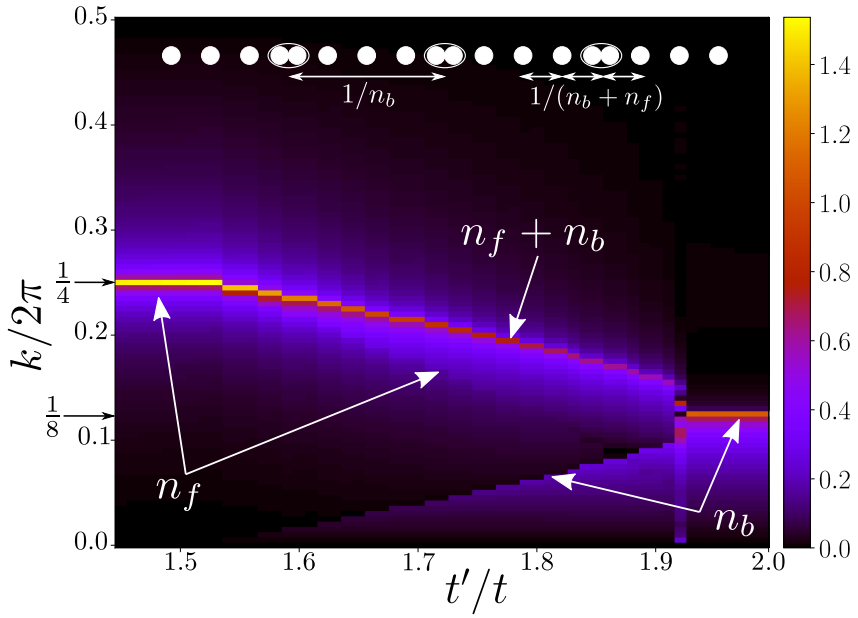

Figure 3.9: Map of the absolute value of the Fourier transform of local density fluctuations $\langle \hat{n}_j - n$ as a function of $\frac{t'}{t}$ for an open chain with $L = 200$.

Density fluctuations and single-particle and pair correlators

We clarify the latter point by monitoring in Fig. 3.9 the Fourier transform of the density fluctuations:

$$\delta n(k) = \sum_{j=0}^{L-1} e^{-ikj} \langle \hat{n}_j - n \rangle. \tag{3.23}$$

Luttinger liquid theory predicts the leading modulation in the density fluctuations on top of its average value to occur at $k = 2\pi n_{micro}$, where n_{micro} is the density of the fundamental constituents of the liquid. In the F phase, we recover a distinct peak at $k = 2\pi n$, as expected for a regular Luttinger liquid phase. Similarly, in the P_π phase one obtains a dominant peak at $k = 2\pi\frac{n}{2}$, where the halving of the density of the microscopic low-energy degrees of freedom is readily explained by the formation of $\frac{N}{2}$ pairs from the starting N bare fermions. Finally, the structure is richer in the C phase. Since in this case both unpaired fermions and pairs populate the system, we recover a leading peak in the Fourier transform of the density fluctuations at $k = 2\pi(n_f + n_b)$, n_f and n_b being the density of unpaired and paired fermions, respectively, which in turn corresponds to a spatial modulation whose wavelength corresponds to the average interparticle spacing between the fundamental units of a liquid with $N_f + N_b$ effective particles. Simultaneously, a second main peak interpolating from a zero value to the full pair density $\frac{n}{2}$ is observed and is identified with a spatial modulation with period given by the average interpair distance $\frac{1}{n_b}$, whereas a strongly subleading peak interpolating from the full fermionic filling n to zero is naturally linked to a modulation with period given by $\frac{1}{n_f}$. We underline that the result displayed in Fig. 3.9 cannot be extracted from the noninteracting 2F model $\hat{H}_f + \hat{H}_b$, as the latter does not take into account that the two species coexist over the same lattice and thus undergo nontrivial excluded-volume constraints that determine the properties of the density fluctuation profile.

The decay of the single-particle correlator $G(r) = \langle \hat{c}_j^\dagger \hat{c}_{j+r} \rangle$ and of the pair correlator $P(r) = \langle \hat{c}_j^\dagger \hat{c}_{j+1}^\dagger \hat{c}_{j+r} \hat{c}_{j+r+1} \rangle$ further supports the physical picture of the three phases identified for $\frac{t'}{t} > 0$. As displayed in Fig. 3.10, $P(r)$ is manifestly subleading with respect to $G(r)$ in the F phase, whereas, as the system enters the C phase, the decay of the pair correlator gets enhanced by several orders of magnitude and appears to be much slower in the C and P_π phases than in the sampled point in the F phase. The latter has been chosen to be very close to the critical point separating the F phase from the C phase in order to highlight the dramatic change in the correlation properties as the system enters the C phase. Since $G(r)$ decays exponentially in the P_π phase and is comparable with $P(r)$ in the C phase, we conclude that the P_π phase features genuine pairing phenomena, while the C phase displays pair correlations that are not compatible with a simple fermionic Luttinger liquid, like in the F phase.

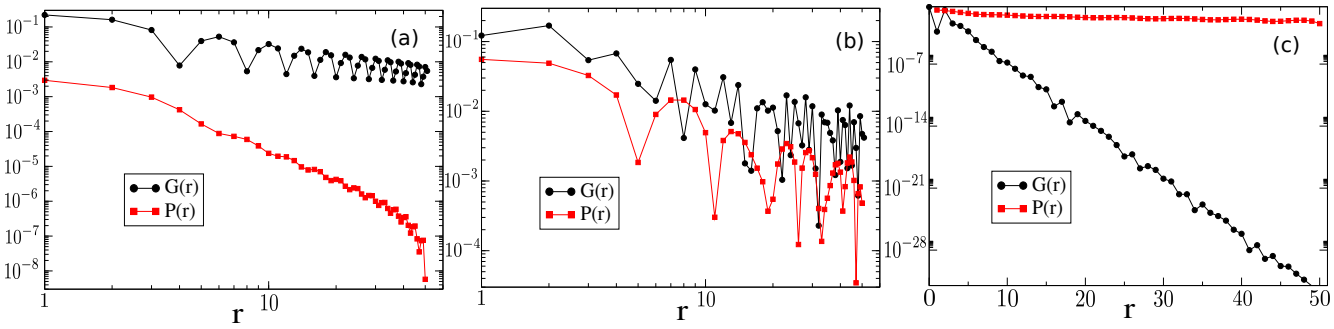

Figure 3.10: Decay of the (absolute value of the) single-particle correlator $G(r)$ and of the pair correlator $P(r)$ (a) in the F phase ($\frac{t'}{t} = 1.4$), (b) in the C phase ($\frac{t'}{t} = 1.8$) and (c) in the P_π phase ($\frac{t'}{t} = 2.0$) for a system of size $L = 104$ in OBC and at filling $n = 0.25$.

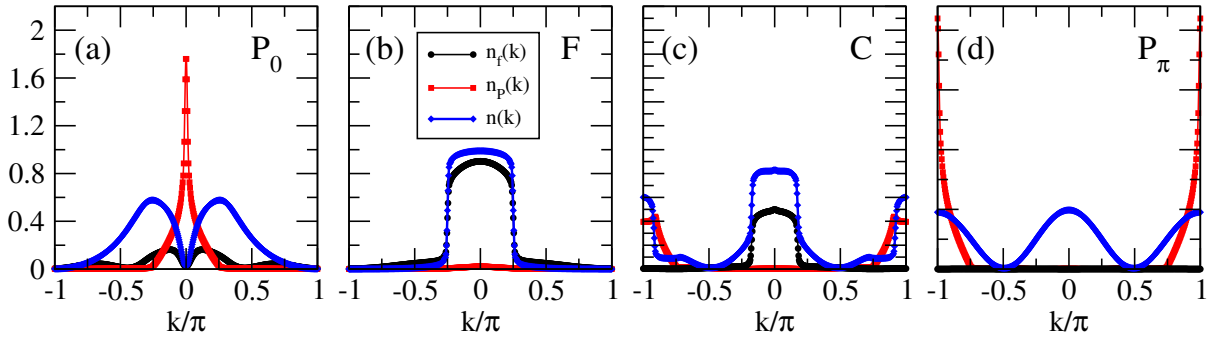

Figure 3.11: Effective occupation factors for unpaired fermions $n_f(k)$ and for pairs $n_P(k)$, see definitions in Eqs. (3.27). The numerical parameters are $L = 104, N = 26$. Different panels refer to different points of the phase diagram: (a) $\frac{t'}{t} = -2.2$ in the P_0 phase; (b)$\frac{t'}{t} = 1.2$ in the F phase; (c) $\frac{t'}{t} = 1.85$ in the C phase; (d) $\frac{t'}{t} = 2.2$ in the P_π phase. Simulations are performed with OBC.

Momentum occupation function of unpaired fermions and pairs

The study of correlation properties allows for a further direct probe of the band picture put forward by the analytical $2F$ model. The key ingredients in this effort are the following operators:

$$\hat{f}_j^\dagger = (1 - \hat{n}_{j-1})\hat{c}_j^\dagger(1 - \hat{n}_{j+1}), \tag{3.24}$$

$$\hat{P}_j^\dagger = (1 - \hat{n}_{j-1})\hat{c}_j^\dagger\hat{c}_{j+1}^\dagger(1 - \hat{n}_{j+2}), \tag{3.25}$$

which are heuristically aimed at capturing separately the behavior of isolated fermions and paired fermions, decoupling their contributions to the standard momentum occupation function:

$$n(k) = \frac{1}{L}\sum_{j,j'} e^{ik(j-j')}\langle\hat{c}_j^\dagger\hat{c}_{j'}\rangle \tag{3.26}$$

from each other. More precisely, we monitor the isolated fermion occupation function $n_f(k)$ and the isolated pair occupation function $n_P(k)$, defined respectively as:

$$n_f(k) = \frac{1}{L}\sum_{j,j'} e^{ik(j-j')}\langle\hat{f}_j^\dagger\hat{f}_{j'}\rangle \tag{3.27}$$

$$n_P(k) = \frac{1}{L}\sum_{j,j'} e^{ik(j-j')}\langle\hat{P}_j^\dagger\hat{P}_{j'}\rangle. \tag{3.28}$$

The result is provided in Fig. 3.11 for all phases displayed in Fig. 3.1. While in the F phase $n_f(k)$ resembles the standard Fermi sea given by $n(k)$, the P_0 and P_π phases show quasicondensation of pairs around $k = 0$ and $k = \pi$, respectively, as signaled by the distinct peak reported in $n_P(k)$ in the aforesaid

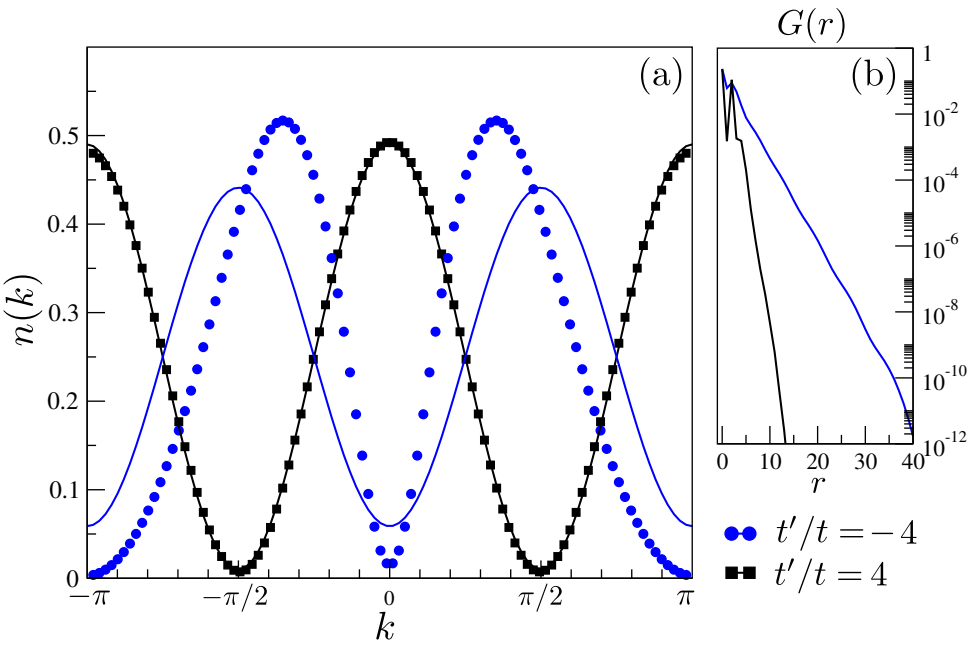

Figure 3.12: (a) Absolute value of the fermionic occupation factor (blue dots for $\tau = -4$ and black squares for $\tau = 4$) compared to its analytical estimate (continuous lines).The numerical parameters are $L = 80$, $n = \frac{1}{4}$ with OBC. (b) decay of the absolute value of the single-particle correlator $G(r)$ for the same parameters values (blue line for $\tau = -4$ and black line for $\tau = 4$).

phases. The C phase shows instead the simultaneous presence of quasicondensate of isolated fermions around $k = 0$ and a quasicondensate of pairs around $k = \pi$, as demonstrated by the behavior of $n_f(k)$ and $n_P(k)$.

Further insights are obtained from the behavior of the bare momentum occupation function $n(k)$. Firstly, one may notice that the latter is ineffective in discriminating the momentum weight carried by unpaired fermions from that of paired fermions, even though it captures both contributions. Secondly, interesting insights can be obtained by computing $n(k)$ analytically when $t = 0$ and comparing it to the numerical results in the P_0 and P_π phases. Indeed, when $t = 0$, only fully paired configurations contribute to the ground state, meaning that one can rewrite single-particle correlations as follows:

$$\langle \hat{c}_j^\dagger \hat{c}_{j'} \rangle = \delta_{j,j'} \langle \hat{n}_j \rangle + \delta_{j',j+2} \langle \hat{c}_j^\dagger \hat{c}_{j+2} \rangle + \delta_{j',j-2} \langle \hat{c}_j^\dagger \hat{c}_{j-2} \rangle. \tag{3.29}$$

Plugging Eq. (3.29) into the definition of $n(k)$ in Eq. (3.26), one obtains:

$$n(k) = n + \frac{1}{L} \sum_j \left(e^{-i2k} \langle \hat{c}_j^\dagger \hat{c}_{j+2} \rangle + e^{i2k} \langle \hat{c}_j^\dagger \hat{c}_{j+2} \rangle^* \right). \tag{3.30}$$

Since $\langle \hat{c}_j^\dagger \hat{c}_{j+2} \rangle$ is nonvanishing when evaluated on the fully-paired ground state only if the site $j+1$ is occupied, then $\sum_j \langle \hat{c}_j^\dagger \hat{c}_{j+2} \rangle = \sum_j \langle \hat{c}_j^\dagger \hat{n}_{j+1} \hat{c}_{j+2} \rangle$ when the expectation value is taken over the ground state of Hamiltonian (3.1) with $t = 0$. Following the discussion in Section 3.3, $\sum_j \langle \hat{c}_j^\dagger \hat{n}_{j+1} \hat{c}_{j+2} \rangle$ equals $-\sum_j \langle \hat{\sigma}_j^+ \hat{\sigma}_{j+1}^- \rangle$, where the expectation value is taken over the ground state of the effective XX chain. The latter can be easily computed and gives the result:

$$n(k) = n \pm \frac{2}{\pi} \sin\left(\frac{\pi n}{2 - n} \right) \cos(2k), \tag{3.31}$$

where the $+$ sign refers to the $t' > 0$ case and the $-$ sign to the $t' < 0$ case. We thus recover a cosine oscillation, whose miscoscopic origin relies on the assumption (3.29), which expresses formally the assumption that only states where the fermions are arranged into pairs contribute to the ground state.

As one can notice in Fig. 3.11(a) and (d), the cosine behavior of $n(k)$ predicted at $t = 0$ in Eq. (3.31) is robust to the addition of a perturbative value of the single-particle hopping t when $t' > 0$, while it

is largely modified when $t' < 0$. Similarly, $n_f(k)$ is vanishing in the P_π phase, whereas it takes nonzero values in the P_0 phase. As explicitly shown in Fig. 3.12(b), such features are compatible with a stronger robustness of the pairs in P_π phase rather than in the P_0 phase, as the single-particle correlator $G(r)$, which roughly measures the spatial extent of pairs in a pairing phase, displays a significantly slower decay in the P_0 phase, despite being exponentially suppressed in both cases. This observation can be strengthened quantitatively by comparing the numerical data for $n(k)$ with its estimate (3.30), where the numerical value of the correlators at the corresponding value of τ has been substituted in the aforesaid expression. Since the comparison is excellent for $t' > 0$ and unsatisfactory for $t' < 0$, and given that Eq. (3.30) relies on the assumption of tightly bound pairs, we conclude that pairs are indeed more spatially extended in the P_0 phase than in the P_π phase. We propose qualitative arguments for such a discrepancy in the following subsection.

3.4.3 Asymmetry between the P_0 and the P_π phases

The observed asymmetry in the rigidity of the paired phases against the addition of single-particle hopping t for different signs of t' is further reflected in the different critical behavior that separates the P_0 and P_π phases from the F phase at intermediate coupling. Heuristically, since the paired and unpaired fermions coexist on the same 1D setup, they interact between each other; in view of this, the success of the $2F$ model (3.5), which neglects these effects completely, looks rather surprising.

We need therefore to evaluate the effects of a generic interspecies interaction term to probe how it is expected to impact the ground-state properties of the system. At a first level of approximation, the single-particle hopping is responsible for creating a pair by putting two isolated fermions on neighboring sites (and viceversa), thus leading to the addition of a term of the form $\hat{H}_{int} = -t \sum_j \left(\hat{\sigma}_j^+ \hat{d}_j \hat{d}_{j+1} + H.c. \right)$ to the $2F$ model Hamiltonian.

The momentum space picture of the processes induced by $\hat{H}_{int}$ can be described as the annihilation of two fermions with momenta k_1 and k_2 and the creation of a pair with momentum $k_1 + k_2 + 2\pi m$, $m \in \mathbb{Z}$. Since, however, for $t' > 0$ the unpaired fermions have $k_1, k_2 \sim 0$ and the pairs have momentum $k \sim \pi$, no momentum-conserving process induced by the interspecies interaction H_{int} is allowed to take place in presence of momentum mismatch between the bands occupied by the two species and interactions are thus effectively suppressed. On the other hand, when $t' < 0$ both the pairs and the unpaired fermions quasicondense around $k = 0$, allowing for the interspecies interactions to hybridize fermionic and hard-core bosonic degrees of freedom. These lead to the effects displayed at strong coupling in Fig. 3.11 and 3.12 and result in a nontrivial Ising critical point with central charge $c = \frac{3}{2}$ separating the P_0 phase from the F phase.

A more refined treatment of the quantum fluctuations leading to the distinct critical behaviors observed above relies on a field theory formulation of the $2F$ model, which follows closely the treatments of Refs. [58, 27]. We describe the low-energy physics of Hamiltonian (3.1) via an effective Hamiltonian $\hat{H} = \hat{H}_f + \hat{H}_b + \hat{H}_I$. The Hamiltonian $\hat{H}_b$ is a Luttinger liquid Hamiltonian with sound velocity v and Luttinger parameter K describing a partially filled band of pairs, whereas $\hat{H}_f$ models a quadratic fermionic band of unpaired fermions:

$$\hat{H}_b = \frac{v}{2\pi} \int dx \left[K(\partial_x \hat{\phi})^2 + \frac{1}{K} (\partial_x \hat{\theta})^2 - 2\mu \left(\frac{\partial_x \hat{\theta}}{2\pi} + \rho_b \right) \right], \tag{3.32}$$

$$\hat{H}_f = \int dx\, \hat{\psi} \left(\epsilon_0 - \frac{\partial_x^2}{2m} - \mu \right) \hat{\psi}, \tag{3.33}$$

where the chemical potential μ couples to the total density in the system, ρ_b is the average pair density and $[\hat{\phi}(x), \hat{\theta}(x')] = i\pi\Theta(x - x')$. The Hamiltonian $\hat{H}_I$ describes instead the interaction between unpaired fermions and pairs as a process that transforms two unpaired fermions into a pair (and viceversa):

$$\hat{H}_I = \int dx\, u(x) \left(e^{i2\hat{\phi}} \hat{\psi} \partial_x \hat{\psi} + H.c. \right). \tag{3.34}$$

The key quantity in the ensuing analysis is the behavior of the coupling $u(x)$. Indeed, when $t' < 0$, the coupling is non-oscillating, namely $u(x) = u$, because both the paired and the unpaired fermions occupy momenta $k \sim 0$, thus allowing for momentum-conserving exchange processes to take place. In this case,

the model has been studied in Ref. [27], where it is shown that a bosonic phase with a gap to single particle excitations and a fermionic phase coinciding with a standard Luttinger liquid are separated by a critical point with central charge $c = \frac{3}{2}$. On the other hand, when $t' > 0$, the pair band is centered around $k = \pi$, thus implying that each tranfer process is accompanied by a net momentum tranfer $\delta k \sim \pi$. The function $u(x)$ inherits this spatial modulation, namely $u(x) \sim e^{i\pi\frac{x}{a}}$, and is then averaged out by the integral. This process is thus is strongly suppressed, while the next leading contribution involves the conversion of four fermions into two pairs and can be neglected. The resulting phenomenology has been studied in Ref. [146] and is known to give rise to a Lifschitz transition to a phase with a pair of gapless modes, consistently with the behaviour found in such a parameter regime for Hamiltonian (3.1).

3.5 Conclusions

In the present chapter we have discussed the unexpected properties of the pairing transition in the realm of dilute 1D systems of spinless fermions through a simple paradigmatic model featuring the interplay between single-particle hopping processes and correlated pair-hopping processes. Firstly, the analysis revealed a novel pairing transition, that, instead of being direct, occurs through an intervening phase where a regular Luttinger liquid coexists with a Luttinger liquid of pairs. The onset of such a phase has been linked to a nontrivial reshaping of the structure of the low-energy excitation spectrum, that occurs through the appearance/disappearance of a gapless mode at the phase boundaries of the coexistence phase.

This feature is directly connected to the $2F$ model employed to discuss the phase diagram of model (3.1). Indeed, this work represents the first one giving microscopic foundations to the two-fluid field-theoretical approach to the study of pairing transitions in low-dimensional systems, first discussed in Ref. [27] on a purely phenomenological basis. As comprehensively shown above, two-fluid approaches are very fruitful in the study of bound-state formation in systems of spinless fermions, as they give account for the nontrivial reshaping of the low-energy sector of such systems through the appearance of an emergent mode, consistently with the numerical and analytical treatments developed in Refs. [26, 27, 28].

Chapter 4

Phase separation in a one-dimensional model with pair hopping and density-density interactions

The present chapter investigates the effects of a nearest-neighbor density-density interaction on the lattice model of spinless fermions with correlated pair-hopping studied in Refs. [26, 110] by illustrating the results presented in Ref. [111]. We provide a general overview of the phase diagram by describing the main properties of the observed phases and, in particular, we underline the stability of the coexistence phase introduced in Ref. [110] to the presence of nonperturbative values of the density-density term, therefore showing that it is not a unphysical artifact of a fine-tuned model. Subsequently, we focus our discussion on the parameter regime where a liquid of isolated fermions becomes immiscible with a liquid of pairs due to the addition of nearest-neighbor repulsion, thus determining the onset of a peculiar form of phase separation. We successfully apply phenomenological models based on a two-fluid picture [58, 27] to describe this regime as well, showing once more the usefulness of unconventional two-fluid descriptions in the study of pairing in low-dimensional systems of spinless fermions.

4.1 Introduction

We expand the discussion of the model studied in Refs. [26, 110] by characterizing the phase diagram of the model in presence of an additional nearest-neighbor density-density interaction. The aim of the following analysis is twofold. On one hand, we probe the stability of the coexistence phase unveiled in Ref. [110] to the addition of a simple nearest-neighbor interaction. More specifically, we provide unambiguous signatures of the survival of a two-fluid coexistence for finite and non-perturbative values of the interaction, both in the attractive and in the repulsive case. Therefore, our study demonstrates the thermodynamic stability of the coexistence phase and proves that it is not a unphysical artifact of a fine-tuned model.

Moreover, we show the onset of phase separation for even larger interaction strengths, with different features depending on the sign of the interaction. When the interaction is attractive, fermions cluster together in a small region of the lattice. When the interaction is repulsive, the paired and fermionic phases become immiscible and are spatially separated, contrarily to what observed in the case of the coexistence phase.

The results obtained in the regime where phase separation occurs have an interest that goes beyond the study of the phase diagram of the model Hamiltonian under investigation. Indeed, as they have been obtained in the limiting case where the single-particle hopping amplitude is negligible with respect to the leading energy scale, set by the interaction terms, our results shed light on the properties of flat-band models. These systems represent a paradigmatic platform for the study of the effect of strong correlations, as they feature suppression of single-particle hopping and can display competition between density-assisted hopping and density-density interactions [147, 148, 149].

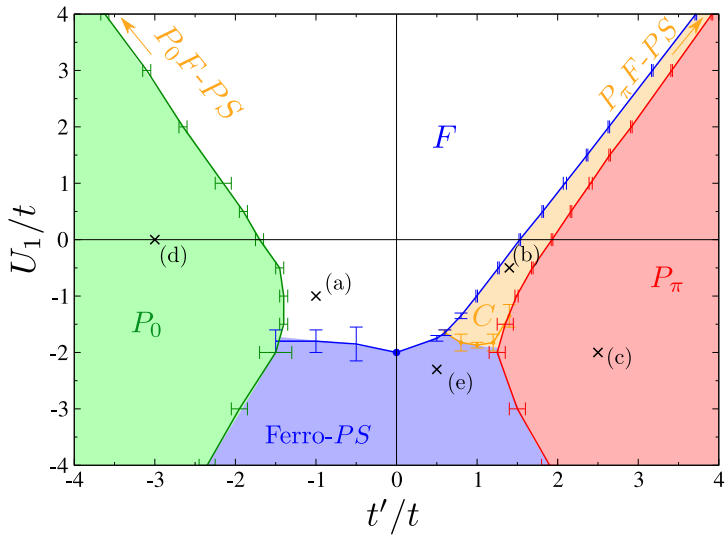

Figure 4.1: Phase diagram of Hamiltonian (4.1) for fermionic density $n = \frac{1}{4}$, obtained with DMRG simulations. F is a Fermi Luttinger liquid phase, $P_{0,\pi}$ are paired phases, C is the coexistence phase and PS stands for phase separation, which can be of different kinds (see text). The crosses and labels (a-e) refer to representative points for which data are presented in the remainder of the section.

The relevance of flat-band systems to the understanding of strong correlations in quantum many-body systems is paramount. Among the several exotic properties of strongly-correlated systems studied in models exhibiting flat bands, we mention pair quasi-condensation [147], strongly-correlated topological insulators [149], interaction-driven Bose condensation [150] and superconductivity. Moreover, flat-bands occur in twisted-bilayer graphene [151], where the leading interaction effects induce correlated insulator states [152] and superconducting behavior [153, 154, 155, 156].

4.2 Model, methods and phase diagram

We consider a 1D chain of length L hosting N spinless fermions, so that $n = \frac{N}{L} = 0.25$. The model Hamiltonian that we investigate takes the form:

$$\hat{H} = -t \sum_j \left(\hat{c}_j^\dagger \hat{c}_{j+1} + H.c. \right) - t' \sum_j \left(\hat{c}_{j+1}^\dagger \hat{n}_j \hat{c}_{j-1} + H.c. \right) + U_1 \sum_j \hat{n}_j \hat{n}_{j+1}, \tag{4.1}$$

where t is the single-particle hopping parameter, t' is the pair-hopping parameter, U_1 is the strength of the nearest-neighbor density-density interaction and $\hat{c}_j, \hat{c}_j^\dagger$ are the fermionic annihilation and creation operators, with $\hat{n}_j = \hat{c}_j^\dagger \hat{c}_j$. The addition of a simple form of fermion-fermion interaction is designed in first instance to characterize the stability of the properties of the phase diagram discussed in Ref. [110] to a generic perturbation.

We target the properties of the zero-temperature phase diagram of model (4.1) by means of extensive numerical simulations based on the DMRG algorithm [144, 145, 81, 82]. We have performed numerical simulations with both open boundary conditions (OBC) and periodic boundary conditions (PBC) for a wide range of parameters, keeping up to $m = 2600$ states and reaching sizes up to $L = 200$ and $L = 56$, respectively. Moreover, we complement the numerical observations with several effective analytical descriptions that account for observed phenomenology and that are either based on perturbative treatments or on phenomenological two-fluid models [27, 58].

The nature of the phases and the transition lines among them are estimated by monitoring local observables, correlation properties and entanglement entropy profiles. More precisely, we exploit the local density $n_j = \langle \hat{n}_j \rangle$, the local kinetic energy of unpaired and paired fermions, defined respectively as:

$$k_j^{(1)} = -\langle \hat{c}_j^\dagger \hat{c}_{j+1} + H.c. \rangle, \tag{4.2}$$

$$k_j^{(2)} = -\langle \hat{c}_j^\dagger \hat{n}_{j+1} \hat{c}_{j+2} + H.c. \rangle, \tag{4.3}$$

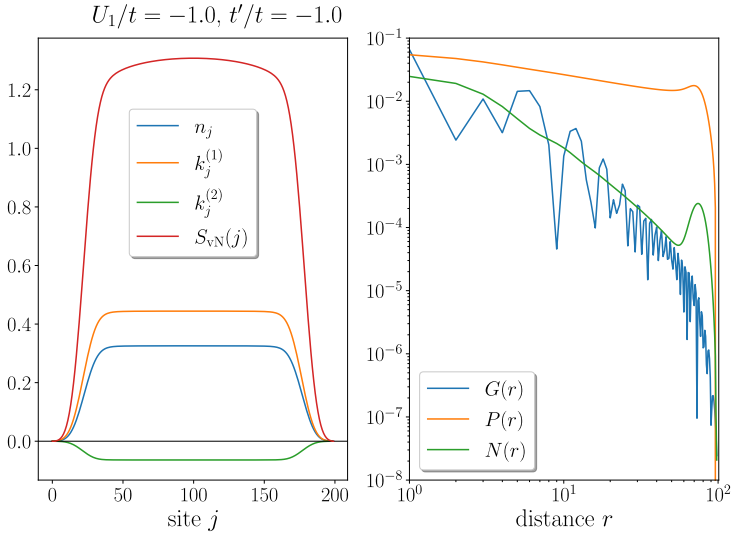

Figure 4.2: Local observables n_j, $k_j^{(1)}$, $k_j^{(2)}$ and $S_{vN}(j)$, together with absolute values of correlators $G(r)$, $P(r)$ and $N(r)$ in the F phase at the cross (a) in Fig. 4.1.

and the von Neumann entanglement entropy profile $S_{vN}(j)$ obtained as a function of the cut $(j, j+1)$ across which it is computed. From the latter, the central charge c of a critical phase can be obtained via a fit [99]. Furthermore, we compute the single-particle correlation function $G(r) = \langle \hat{c}_j^\dagger \hat{c}_{j+r} \rangle$, the pair correlation function $P(r) = \langle \hat{c}_j^\dagger \hat{c}_{j+1}^\dagger \hat{c}_{j+r} \hat{c}_{j+r+1} \rangle$ and the density-density correlation function $N(r) = \langle \hat{n}_j \hat{n}_{j+r} \rangle - \langle \hat{n}_j \rangle \langle \hat{n}_{j+r} \rangle$, where j is chosen to be in the bulk of the system when considering OBC.

The phase diagram of model (4.1) is presented in Fig. 4.1. We start its description from the F phase, which coincides with a regular Luttinger liquid phase. Such a phase is gapless with vanishing single-particle gap and is described at low energies by a quadratic bosonic mode with central charge $c = 1$, that describes the collective density excitations in the system. The F phase is characterized by quasi-long-range-ordered correlation functions, where the nonuniversal decay exponents depend on the Luttinger parameter K of the low-energy field theory. As the latter is a function of the microscopic interactions, the leading correlations vary across the phase diagram and, more specifically, the scenario where $P(r)$ is the leading correlation function is indeed observed in presence of a negative U_1, as presented in Fig. 4.2, despite the phase is not a paired phase due to the vanishing single-particle gap.

As one can notice, the observables shown in Fig. 4.2 vanish at the edges of the system in OBC. This signature can be interpreted as a precursor to the onset of phase separation. The latter behavior is indeed to be expected when the dominant energy scale in the problem is set by a large and negative U_1. Specifically, for $t' = 0$, Hamiltonian (4.1) maps via a Jordan-Wigner transformation onto the XXZ-chain Hamiltonian, which is known to have a transition to a ferromagnetic phase when $U_1 = -2t$. In fermionic language, this behavior corresponds to the formation of macroscopic clusters of fermions in the ground state and is therefore referred to as Ferro-PS. The DMRG simulations in such a phase output typical configurations such as the one displayed in Fig. 4.3, where the particles are arranged in several unequal domains. It is however challenging to determine the transition line with high precision due to the fact that the DMRG algorithm, being a variational approach, does not allow to discriminate the optimal energy state among the many low-lying states featuring one or more particle domains.

We proceed the overview of the phase diagram by observing that, when the t' term is dominating, a Luttinger liquid phase with pair granularity is reported [26, 110]. Such a phase features a finite nonvanishing single-particle gap related to the energetic cost associated to breaking a pair. The latter manifests itself in the lack of single-particle coherence, namely the exponential decay of the single-particle correlator $G(r)$, whereas the leading algebraic order is given by the slowly decaying pair correlator $P(r)$, as displayed in Fig. 4.4. Similarly, local observables betray pair formation, as the single-particle kinetic energy $k_j^{(1)}$ is largely suppressed compared to the pair kinetic energy $k_j^{(2)}$ and, similarly, the number of peaks in the local density profile matches the total number of pairs that the system can form ($\frac{N}{2} = 25$ for $L = 200$), as predicted for a density that is modulated with a spatial period given by the average interpair spacing in a liquid of pairs, namely $\frac{2}{n}$.

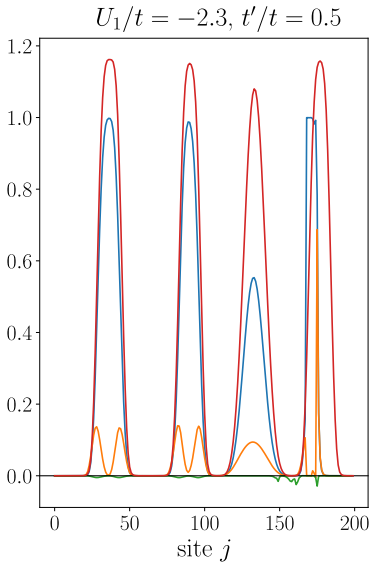

Figure 4.3: Local observables n_j, $k_j^{(1)}$, $k_j^{(2)}$ and $S_{vN}(j)$ in the Ferro-PS phase at the cross (e) in Fig. 4.1. The color legend is the same as the one introduced in Fig. 4.2.

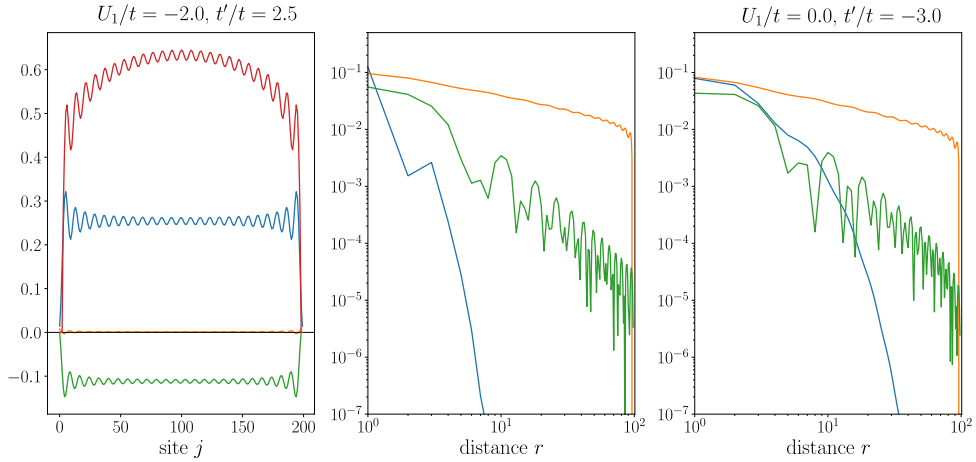

Figure 4.4: Left: local observables n_j, $k_j^{(1)}$, $k_j^{(2)}$ and $S_{vN}(j)$, together with absolute values of correlators $G(r)$, $P(r)$ and $N(r)$ in the P_π phase at the cross (c) in Fig. 4.1. Right: absolute values of correlators $G(r)$, $P(r)$ and $N(r)$ in the P_0 phase at the cross (d) in Fig. 4.1.

Depending on the sign of t', the pairs quasicondense either around quasimomentum $k = 0$ ($t' < 0$) or around quasimomentum $k = \pi$ ($t' > 0$) [110]. As already known, the phase transition separating the F phase from the P_0 phase is predicted to be a second-order transition with central charge $c = \frac{3}{2}$ [26], whose low-energy theory is given by a gapless bosonic mode contributing with a central charge $c = 1$, accompanied by an emergent Ising mode with central charge $c = \frac{1}{2}$. The latter has been related to the possibility of observing boundary Majorana zero-energy modes at the interfaces of weak- and strong-pairing phases in 1D number-conserving systems. For simplicity, we compute the transition line by monitoring the position of the maximum of the fitted central charge for several constant U_1 horizontal cuts on a system with size $L = 200$, without systematically checking its consistency with the $c = \frac{3}{2}$ value, but the findings are compatible with the results shown in Ref. [26].

On the other hand, the transition from the F phase to the P_π phase is not direct, but mediated by an intervening coexistence phase C [110], characterized by two miscible Luttinger liquids with single-particle and pair granularity, appearing at weak and strong coupling in the F and P_π phase, respectively. The C phase is thus a $c = 2$ phase, due to the simultaneous presence of two phononic modes describing collective density fluctuations of the two unveiled fluids. An intuitive real-space picture of the C phase can be inferred from the local observables shown in Fig. 4.5, where, e.g., the density pattern n_j exhibits

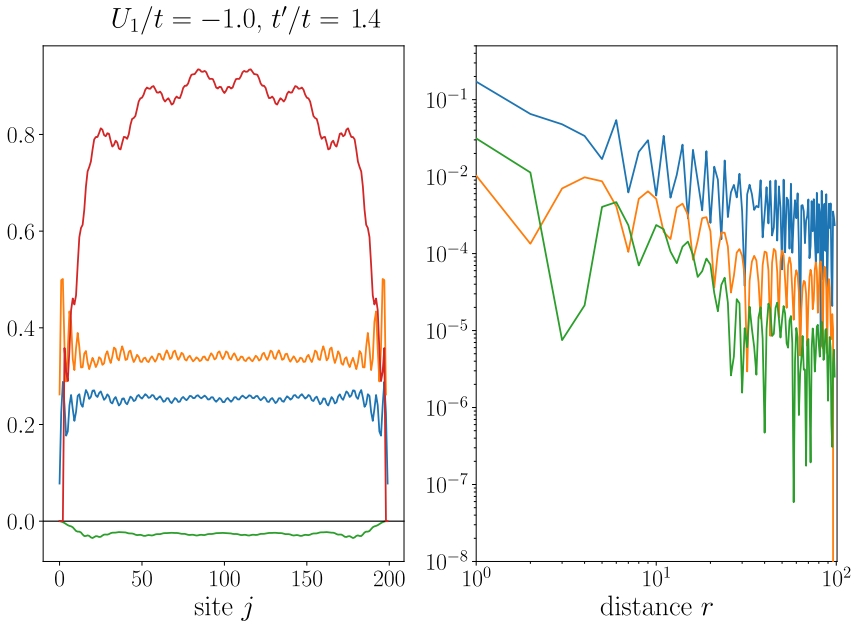

Figure 4.5: Local observables n_j, $k_j^{(1)}$, $k_j^{(2)}$ and $S_{vN}(j)$, together with absolute values of correlators $G(r)$, $P(r)$ and $N(r)$ in the C phase at the cross (b) in Fig. 4.1.

a long-wavelength modulation related to the presence of pairs of neighboring fermions together with a short-wavelength modulation that can be interpreted as the signature of single-particle degrees of freedom coexisting with the aforementioned pairs. Similarly, the correlation properties provided in Fig. 4.5 are qualitatively different from the one found in the neighboring F phase, as the decay of $G(r)$ and $P(r)$ is qualitatively similar, whereas it has been shown to display a clear hierarchy in the magnitude of the decay exponents in the F phase.

In order to manifestly exhibit the stability of the C phase to the addition of the nearest-neighbor interaction U_1, we provide in Fig. 4.6(a) for a nonperturbative value of U_1 the total kinetic energy density of single-particles and pairs, defined respectively as:

$$K_1 = \frac{1}{L}\sum_j |k_j^{(1)}|, \quad K_2 = \frac{1}{L}\sum_j |k_j^{(2)}|, \tag{4.4}$$

which are known to faithfully track the effective density of unbound fermions n_f, the order parameter that distinguishes between the F, C and P_π phases. [110]. The result allows to identify the C phase in the interval $2.11 < \frac{t'}{t} < 2.43$ for $\frac{U_1}{t} = 1$, surrounded by the F and P_π phases, where K_1 and K_2 take constant values, as the order parameter n_f does not vary as a function of $\frac{t'}{t}$ in the aforesaid single-species phases. Simultaneously, the spatial profile of the local single-particle and pair kinetic fluctuations, quantified in Fig. 4.6(b) through $k_j^{(1)}$ and $k_j^{(2)}$, demonstrates that the two species of pairs and unbound fermions are indeed intertwined and do not show any form of spatial segregation, as in a phase-separated regime.

We conclude the overview of the phase diagram by describing the $P_\pi F$-PS and the $P_0 F$-PS phases, occurring at values of the radius:

$$r = \sqrt{\left(\frac{t'}{t}\right)^2 + \left(\frac{U_1}{t}\right)^2} \tag{4.5}$$

that are too large to be represented in Fig. 4.1. Such phases realize a novel form of phase separation, where unbound fermions and pairs become immiscible and display spatial segregation, contrarily to what observed in the C phase. Characteristic signatures of the $P_\pi F$-PS phase are investigated by choosing a large value of r and varying the ratio $\frac{U_1}{t'}$. We start by showing in Fig. 4.7 the behavior of the total single-particle and pair kinetic energy densities K_1 and K_2, which point towards the existence an intervening phase between the F and the P_π phases, characterized by the simultaneous presence of unpaired and paired fermions in the system. In order to discriminate the $P_\pi F$-PS phase from the C phase, we thus resort to local observables, such as $k_j^{(1)}$ and $k_j^{(2)}$, that instead clearly display the presence

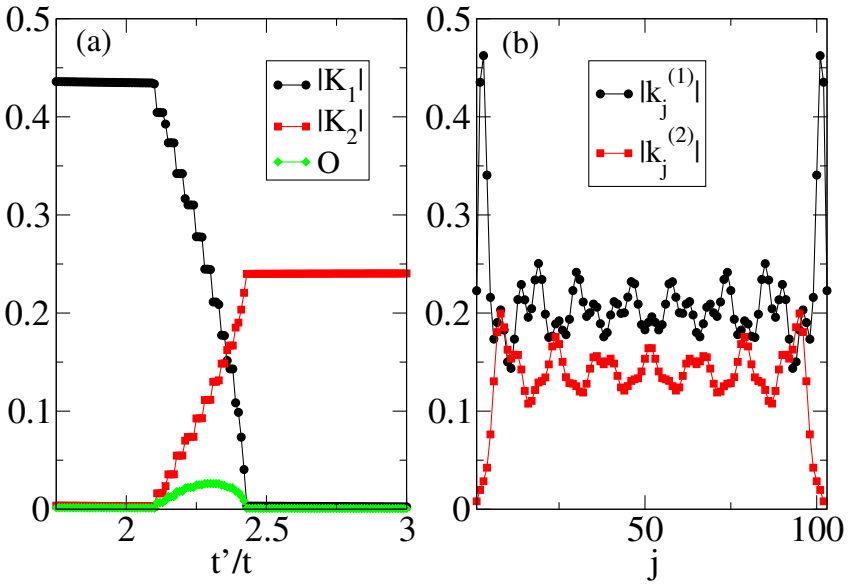

Figure 4.6: Cut along the $\frac{U_1}{t} = 1$ line showing the C phase with $L = 104$ and OBC. (a) Total kinetic energies K_1, K_2 and overlap O as a function of $\frac{t'}{t}$, see definitions in Eqs. (4.4) and (4.6). (b) Local single-particle and pair kinetic energy profiles $k_j^{(1)}$ and $k_j^{(2)}$ for $\frac{t'}{t} = 2.31$.

of an interface between a region dominated by local pairing fluctuations and one where the latter are suppressed. Moreover, the region occupied by unpaired fermions shows two different regimes, depending on the value of $\frac{U_1}{t'}$: for smaller values of this ratio, the profile of $k_j^{(1)}$ is vanishing, whereas for larger values it shows nonnegligible fluctuations. We will interpret this phenomenology by showing that the optimal configuration in the subsystem occupied by unbound fermions can be either a CDW pattern with unit cell $(\bullet\circ)$ or a liquid of strongly repulsive isolated fermions, depending on the ratio $\frac{U_1}{t'}$ and on the radius r.

Additionally, since K_1 and K_2 are not spatially resolved, we introduce an energetic observable aimed at distinguishing the $P_\pi F$-PS phase from the C phase, namely the overlap O, defined as:

$$O = \frac{1}{L}\sum_j |k_j^{(1)}| \times |k_j^{(2)}|, \tag{4.6}$$

which measures whether single-particle and pair kinetic energies are nonzero in the same region of space or not, vanishing in the latter case. The results displayed in Figs. 4.6(a) and 4.7(a) are perfectly consistent with the physical interpretation of O and confirm our expectations on the two aforesaid phases. Last, we mention that for negative t', positive U_1 and large radius r, DMRG calculations also demonstrate the existence of a $P_0 F$-PS intervening phase, which shares the same phenomenology as the $P_\pi F$-PS phase, but with P_0 pairs instead.

4.3 Characterization of the phase diagram for large values of r

In this section, we characterize in detail the phase diagram of the model Hamiltonian (4.1) for large values of r as a function of $\frac{U_1}{t'}$ by means of a combination of numerical results and effective analytical descriptions. We start by treating the small and the large and negative $\frac{U_1}{t'}$ limits, where the phases dominated by attractive correlations, namely the P_π and the Ferro-PS phases, are to be found. We then proceed to discuss the large and positive $\frac{U_1}{t'}$ limit, where we encounter the F phase, whose properties in this limit are instead determined by strongly repulsive interactions. Finally, we capture the observed properties of the $P_\pi F$-PS phase and formulate conjectures on its crossover to the C phase.

4.3.1 Overview of the phase diagram

The phase diagram under investigation is shown in Fig. 4.8 and captures the ground-state properties of the system in the limit of large r, which corresponds to declaring the single-particle hopping t to

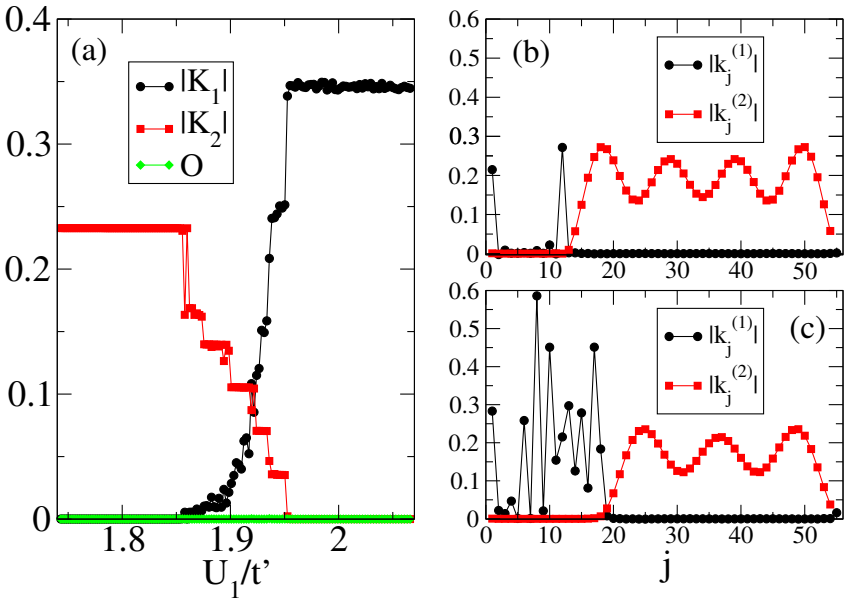

Figure 4.7: Cut showing the $P_\pi F$-PS phase for a chain with $L = 56$ and PBC. In this small t limit, we fix $\frac{t}{t'} = \frac{1}{2000}\sqrt{1+\left(\frac{U_1}{t'}\right)^2}$. (a) Kinetic energies K_1, K_2 and overlap O as a function of $\frac{U_1}{t'}$. (b) Local kinetic energy profiles $k_j^{(1)}$ and $k_j^{(2)}$ for $\frac{U_1}{t'} = 1.891646$, indirectly showing a CDW fermionic domain. (c) Same for $\frac{U_1}{t'} = 1.912426$, without CDW domain.

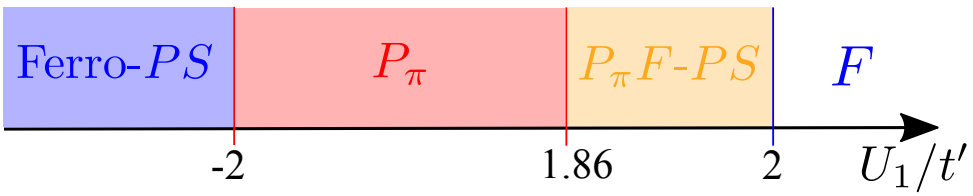

Figure 4.8: Phases of the system for large values of r as a function of $\frac{U_1}{t'}$.

be much smaller than at least one of the other energy scales U_1 and t'. The ratio $\frac{U_1}{t'}$ determines the angle along which one takes the limit $t \to 0^+$ and varying it with positive t', one encounters four different phases, as summarized in Fig. 4.8. For weak interactions, $-2 < \frac{U_1}{t'} \lesssim 1.86$, the system is in the P_π phase. For strong attractive interactions, $\frac{U_1}{t'} < -2$, the system enters the Ferro-PS phase. For strong repulsive interactions, $1.86 \lesssim \frac{U_1}{t'} < 2$, the system first enters the $P_\pi F$-PS phase. For even more repulsive interactions, $\frac{U_1}{t'} > 2$, all pairs are broken and the system enters the F phase, that is adiabatically connected to the non-interacting limit.

4.3.2 The paired phase and the ferromagnetic phase separation

Reminder on the $U_1 = 0$ case

We present here an argument in support of the onset of a pairing phase for moderate values of $\frac{U_1}{t'}$ by quickly reviewing the treatment of the point $U_1 = t = 0$ [157, 158, 110]. In such a case, it is possible to restrict the search for the ground state in the subspace $\mathcal{H}_P$ where fermions form even-sized nearest-neighbor particle clusters, i.e., they are arranged into $N_b = \frac{N}{2}$ pairs. Each configuration in such a subspace is bijectively mapped onto a configuration of a spin chain with $L_b = L - N_b$ sites via the rule $|\bullet\bullet\rangle \to |\uparrow\rangle$, $|\circ\rangle \to |\downarrow\rangle$.

Then, the action of the original fermionic Hamiltonian in Eq. 4.1 with $t = U_1 = 0$ on the subspace $\mathcal{H}_P$ is equivalent to the action of an effective spin-$\frac{1}{2}$ XX-chain Hamiltonian $\hat{H}_{eff} = t' \sum_{j=1}^{L_b} \left(\hat{\sigma}_j^+ \hat{\sigma}_{j+1}^- + H.c.\right)$. The latter is readily diagonalized after a Jordan-Wigner transformation and switching to a Fourier representation, where it takes the form $\hat{H}_{eff} = \sum_k \epsilon_p(k) \hat{n}_k$, with the pair dispersion relation $\epsilon_p(k) = 2t' \cos k$. The ground state energy density reads:

$$e_{eff} = -\frac{2|t'|}{\pi} \left(1 - \frac{n}{2}\right) \sin\left(\frac{\pi n}{2-n}\right), \tag{4.7}$$

where the latter does not depend on the sign of t' as a result of the unitary equivalence $\hat{U}\hat{H}(t = 0, t', U_1)\hat{U}^\dagger = \hat{H}(t = 0, -t', U_1)$ implemented by the unitary operator $\hat{U} = e^{i\frac{\pi}{2}\sum_j j\hat{n}_j}$.

Pairing and ferromagnetic phase separation for $U_1 \neq 0$

As soon as $U_1 \neq 0$, while keeping $t = 0$, the model is not amenable to an exact diagonalization anymore. Firstly, let us assume that the ground state lies in the subspace $\mathcal{H}_P$. In such a case, the effective Hamiltonian in spin language becomes that of a XXZ spin chain and takes the form:

$$\hat{H}_{eff} = t' \sum_{j=1}^{L_b} \left(\hat{\sigma}_j^+ \hat{\sigma}_{j+1}^- + H.c.\right) + \frac{U_1}{4} \sum_{j=1}^{L_b} \left(1 + \hat{\sigma}_j^z\right)\left(1 + \hat{\sigma}_{j+1}^z\right) + U_1 \frac{N}{2}. \tag{4.8}$$

Since an attractive nearest-neighbor interaction ($U_1 < 0$) further enhances pairing, the assumption that the ground state lies in $\mathcal{H}_P$ is expected to be valid in the attractive nearest-neighbor regime and therefore the Hamiltonian (4.8) is to be considered effective in describing the ground-state phase diagram in Fig. 4.8 when $U_1 < 0$. As the XXZ Hamiltonian features a transition to phase separation for $\frac{U_1}{t'} = -2$ and in view of the mapping $|\bullet\bullet\rangle \to |\uparrow\rangle$, $|\circ\rangle \to |\downarrow\rangle$ employed to map the original fermionic particles to spin degrees of freedom, we predict a phase transition from the P_π phase to the Ferro-PS phase at $\frac{U_1}{t'} = -2$. This transition extends up to lower values of $\frac{t'}{t}$, $\frac{U_1}{t}$ as the transition line separating the P_π phase from the Ferro-PS phase in Fig. 4.1.

Let us now turn our attention to the more challenging case of repulsive density-density interactions ($U_1 > 0$). In this case, we expect configurations with unbound fermions to contribute to the ground state, thus challenging the applicability of the assumption to restrict the action of Hamiltonian (4.1) to the subspace $\mathcal{H}_P$ of fully-paired fermionic configurations. By simple energetic arguments, we can however estimate the values of $\frac{U_1}{t'}$ at which a transition to a different phase of matter is expected. Indeed, the correlated pair-hopping term favors the formation of a Fermi sea of pairs with energies ranging from the bottom of the band $-2t'$ to the Fermi energy $-2\cos\left(\frac{\pi n}{2-n}\right)t'$, which for density $n = 0.25$ takes the value $\sim -1.8t'$. Noticing that unbound fermions do not incur in energy penalties resulting from the repulsive u_1 term, we conclude that the F phase should appear for $\frac{U_1}{t'} > 2$ and that the P_π phase should not be destroyed for $\frac{U_1}{t'} \lesssim 1.8$. We test the above considerations by performing numerical simulations

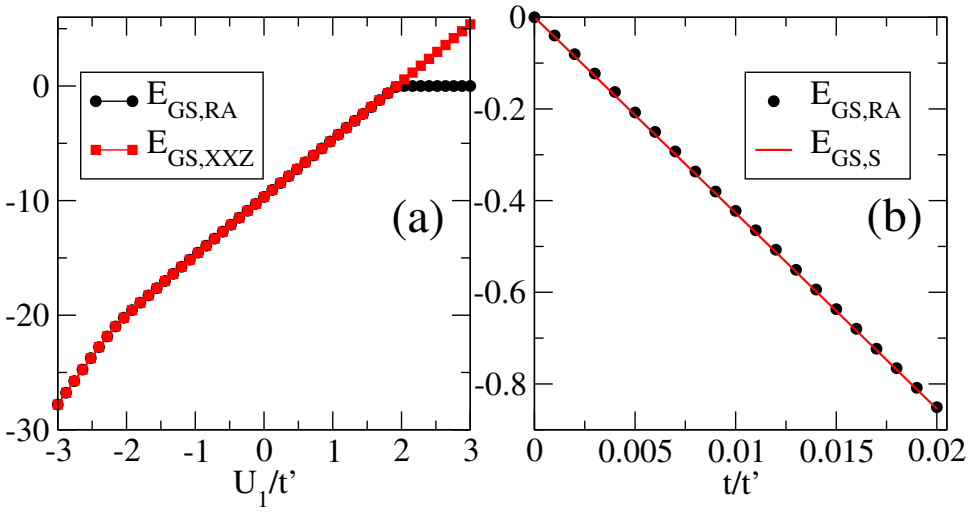

Figure 4.9: Comparison of the ground-state energy $E_{GS,RA}$ of Hamiltonian (4.1) with that of the effective models. (a) for $t = 0$, with $L = 40$, $N = 10$ and PBC for Hamiltonian (4.1), with $L = 35$, $N = 5$ and PBC for Hamiltonian (4.8). (b) for small $\frac{t}{t'}$ with $L = 104$, $N = 26$, $\frac{U_1}{t'} = 4$ and OBC for Hamiltonian (4.1). The line $E_{GS,S}$ is the ground state energy of Hamiltonian (4.10) with the same parameters.

on model (4.1) with $t = 0$ and comparing the obtained energy with the same quantity computed for the corresponding effective model (4.8), as shown in Fig. 4.9(a). We conclude that the two results are consistent with each other up to the value $\frac{U_1}{t'} \sim 2$, where a zero-energy ground state in the fermionic model (4.1) appears. While we will devote the remainder of the chapter to elucidate the phenomenology in such a regime, we conclude by remarking that the stability of the P_π phase for a wide range of values of $U_1 \neq 0$ is confirmed, as well as the transition to the Ferro-PS, as signaled by the change in the slope of the finite-size energy as a function of $\frac{U_1}{t'}$ (characteristic of a first-order phase transition) for a value compatible with the analytical prediction $\frac{U_1}{t'} = -2$.

4.3.3 The fermionic phase

A quick inspection of the density profiles obtained for $\frac{U_1}{t} > 2$ shows that they point towards the presence of immobile unpaired fermions distributed over the lattice. As the fermions never occupy neighboring sites, such configurations are zero-energy eigenstates of Hamiltonian (4.1) with $t = 0$ and span a highly degenerate subspace, that we denote as $\mathcal{H}_S$. The aforementioned Fock states that span $\mathcal{H}_S$ are efficiently described by considering all permutations of two fundamental blocks, namely $|\bullet\circ\rangle$ and $|\circ\rangle$, where the black dot denotes an occupied site and the white dot refers to an empty site.

We now proceed to show that the addition of a perturbative value of single-particle hopping t lifts the degeneracy found for $t = 0$ in this strongly repulsive regime and predicts the onset of a Luttinger liquid phase with single-particle granularity, that is expected to be adiabatically connected to the F phase. In order to prove this claim, we employ a standard perturbative approach. We consider the Hamiltonian (4.1) with $t = 0$ as the unperturbed one and the single-particle hopping term proportional to t as the perturbative term. By denoting the projector onto the subspace $\mathcal{H}_S$ as $\hat{P}_S$, the effective Hamiltonian for the system in such a low-energy subspace reads:

$$\hat{H}_S = \hat{P}_S\big(-t\sum_j \hat{c}_j^\dagger \hat{c}_{j+1} + H.c.\big)\hat{P}_S, \tag{4.9}$$

which coincides with a single-particle hopping Hamiltonian with the additional hard-core constraint of avoided nearest-neighbor occupancy.

More explicitly, we compute the resulting ground-state energy by mapping each basis state in the reduced subspace $\mathcal{H}_S$ to an equivalent state defined on a spin chain of length $L - N$ via the rules $|\bullet\circ\rangle \to |\uparrow\rangle$, $|\circ\rangle \to |\downarrow\rangle$. The action of Hamiltonian $\hat{H}_S$ in the subspace $\mathcal{H}_S$ is equivalent in the spin-chain

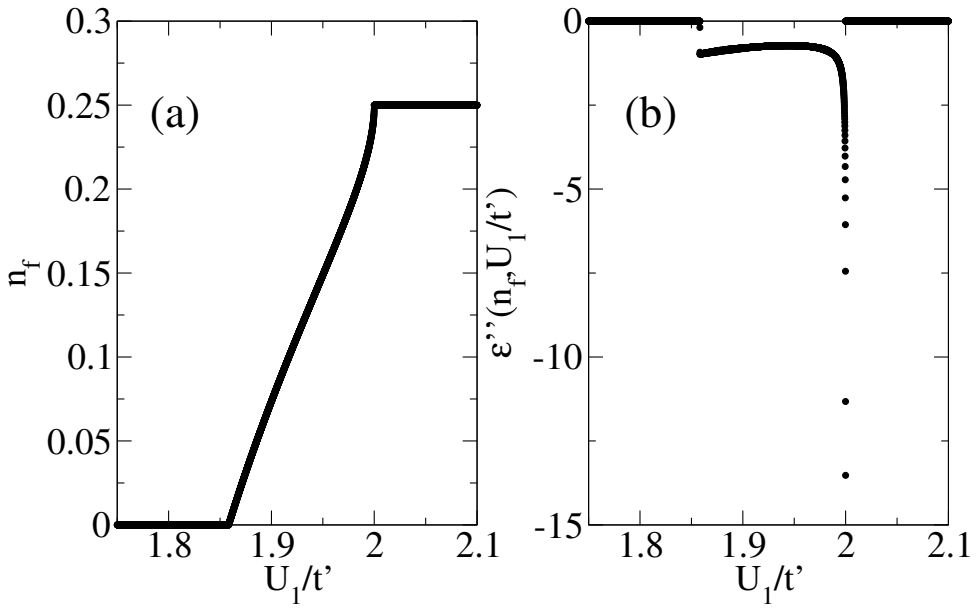

Figure 4.10: (a) Optimal fermionic density $n_f(\theta)$ as a function of $\tan\theta = \frac{U_1}{t'}$ according to the effective phase separation model (4.12). (b) Second derivative of the energy density $\mathcal{E}(n_f(\theta),\theta)$ in Eq. (4.12) as a function of $\tan\theta = \frac{U_1}{t'}$.

representation to that of the following XX-chain Hamiltonian:

$$\hat{H}_S = -t \sum_{j=1}^{L-N} \left(\hat{\Sigma}_j^+ \Sigma_{j+1}^- + H.c. \right), \tag{4.10}$$

where the operators $\hat{\Sigma}_j^\alpha$, $\alpha = x, y, z$, are the Pauli operators and $\hat{\Sigma}_j^\pm$ are the spin-$\frac{1}{2}$ raising and lowering operators. The ground-state energy density is then evaluated by performing a Jordan-Wigner transformation to diagonalize $\hat{H}_S$, leading to the thermodynamic limit result:

$$\epsilon_{GS,S} = -\frac{2t(1-n)}{\pi} \sin\left(\frac{\pi n}{1-n}\right). \tag{4.11}$$

A comparison between a finite size and OBC version of formula (4.11) and the corresponding exact DMRG simulation for $\frac{t}{t'} < 0.02$ and $\frac{U_1}{t'} = 4$ is presented in Fig. 4.9(b). The result displays a remarkable agreement.

4.3.4 Pair-fermion phase separation

We are now in the position to tackle the study of the properties of the intervening phase separation denoted as $P_\pi F$-PS phase, that separates the F phase from P_π phase and whose onset has been demonstrated for $r = 2000$ by the data presented in Fig. 4.7. In order to study the phase diagram in the parameter region where the $P_\pi F$-PS phase is undoubtedly expected to occur, we use polar coordinates to parametrize the phase diagram of the model, namely r and $\theta = \arctan\left(\frac{U_1}{t'}\right)$.

Moreover, in the following we perform numerical simulations always with $t \neq 0$, as the DMRG variational optimization for $t = 0$ is hindered by the existence of additional conserved quantities, given by the total number of particles on even sites $\hat{N}_e = \sum_j \hat{n}_{2j}$ and the one on odd sites $\hat{N}_o = \sum_j \hat{n}_{2j+1}$. As a result, if the initial state does not lie in the same symmetry sector as the ground state, the DMRG algorithm will fail to converge and faithfully reproduce the ground-state properties. The results obtained for nonvanishing values of t are then continuously connected to the $t = 0$ case with the support of its analytical interpretation.

An effective model for $t = 0$

In order to understand the onset of the intermediate $P_\pi F$-PS phase, we develop a phenomenological model for $t = 0$. As it will become more transparent later, such a choice considerably simplifies the

analytical treatment, while mantaining many of the qualitative and quantitative features of the $P_\pi F$-PS phase. The model is based on an ansatz for the energy of generic phase-separated configurations of N_f unpaired fermions and $\frac{N-N_f}{2}$ pairs. We characterize a generic variational configuration with N_f unpaired fermions as follows. On one side, unpaired fermions are immobile, since $t = 0$, and form a zero energy CDW domain of length $2N_f$ (with unit cell $|\bullet\circ\rangle$). On the other side, pairs delocalize on the rest of the lattice, a domain of length $L - 2N_f$. Their kinetic contribution to the energy density of the configuration is derived in analogy to Eq. (4.7), provided that N_b equals the number of pairs in the given configuration, namely $\frac{N-N_f}{2}$, and L_b takes the form $L - 2N_f - \frac{N-N_f}{2}$, as it equals the size of the lattice region available to pairs, $L - 2N_f$, minus the number of pairs, $\frac{N-N_f}{2}$. Finally, the U_1 interaction energy density contribution is taken into account in the low density limit by only considering the potential energy density cost $U_1 \frac{N-N_f}{2L}$ associated to the formation of $\frac{N-N_f}{2}$ pairs. After introducing the unpaired fermionic density $n_f = N_f/L$, the ansatz for the ground-state energy density in units of t' as a function of n_f reads

$$\mathcal{E}(n_f,\theta) = -\frac{2}{\pi}\left(1 - 2n_f - \frac{n-n_f}{2}\right)\sin\left[\pi\frac{n-n_f}{2\left(1-2n_f-\frac{n-n_f}{2}\right)}\right] + \frac{n-n_f}{2}\tan\theta, \tag{4.12}$$

where the relation $U_1/t' = \tan\theta$ has been used.

For each value of θ, we compute the optimal value of the density of isolated fermions n_f that minimizes the variational energy function (4.12) and thus obtain a prediction for the ground-state properties of the system. The behavior of the optimal density in depicted in Fig. 4.10(a). When $\frac{U_1}{t'} \lesssim 1.86$, one obtains $n_f = 0$, which implies that the system is fully paired. We identify this phase with the P_π phase. On the other hand, when $\frac{U_1}{t'} > 2$, one has $n_f = n$, meaning that the strong interparticle repulsion rules out the formation of pairs, so that the optimal configuration is given by any of the degenerate zero-energy basis states of the subspace $\mathcal{H}_S$, where immobile isolated fermions are distributed over the lattice. Finally, one obtains an intermediate range of values $\frac{U_1}{t'}$ where the optimal density n_f satisfies $0 < n < n_f$, therefore signaling that the system is partitioned into a region populated by immobile fermions in a CDW profile with unit cell $|\bullet\circ\rangle$ and a region occupied by a liquid of pairs. We identify the latter phase with the $P_\pi F$-PS phase.

The simple structure of model (4.12) allows to determine analytically (i) the location of the boundaries of the $P_\pi F$-PS phase and (ii) the critical behavior of the ground-state energy density at the critical points. More specifically, the transition from the P_π phase to the $P_\pi F$-PS phase occurs at the critical point:

$$\left(\frac{U_1}{t'}\right)_{c1} = \frac{6}{\pi}\sin\left(\frac{\pi n}{2-n}\right) - \frac{4(2n-1)}{2-n}\cos\left(\frac{\pi n}{2-n}\right). \tag{4.13}$$

For $n = 0.25$, this formula gives $\left(\frac{U_1}{t'}\right)_{c1} \approx 1.858$. Similarly, the critical point separating $P_\pi F$-PS phase from the F phase is located at $\left(\frac{U_1}{t'}\right)_{c2} = 2$. Both values match very well with those obtained numerically in Fig. 4.7(a) for a nonvanishing value of t. We are also able to derive analytically the critical behavior predicted by the phenomenological model (4.12) at the two aforesaid critical points: the result for the second derivative of the optimal energy density, plotted in Fig. 4.10(b), consists in a finite jump discontinuity at the critical point $\left(\frac{U_1}{t'}\right)_{c1}$ and in a square root singularity at $\left(\frac{U_1}{t'}\right)_{c2}$.

An effective model for $t \neq 0$

We probe the stability of the predicted $P_\pi F$-PS phase by allowing $t \neq 0$ and correspondingly modifying the phenomenological variational energy density that captures the behavior of the ground state, as fermions can lower the total energy by delocalizing through the single-particle hopping term. As we do not know a priori the size of the domain occupied by unpaired fermions in this case, we introduce it as an additional parameter that we need to optimize over, namely the effective fermionic length $l_f = \frac{L_f}{L}$, where L_f is the size of the aforementioned domain.

The variational ground-state energy density in units of rt now reads:

$$\mathcal{E}_2(n_f,l_f,r,\theta) = \begin{cases} -\frac{\cos\theta}{\pi}(2-n)\sin\left(\frac{\pi n}{2-n}\right) + \sin\theta\frac{n}{2}, & \text{if } (n_f,l_f) = (0,0) \\ -\frac{2}{\pi r}(1-n)\sin\left(\frac{\pi n}{1-n}\right), & \text{if } (n_f,l_f) = (n,1) \\ -\frac{2}{\pi r}(l_f-n_f)\sin\left(\frac{\pi n_f}{l_f-n_f}\right) - \frac{\cos\theta}{\pi}\left[2(1-l_f)-n+n_f\right]\sin\left[\frac{\pi(n-n_f)}{2(1-l_f)-n+n_f}\right] + \sin\theta\frac{n-n_f}{2}, & \text{otherwise.} \end{cases} \tag{4.14}$$

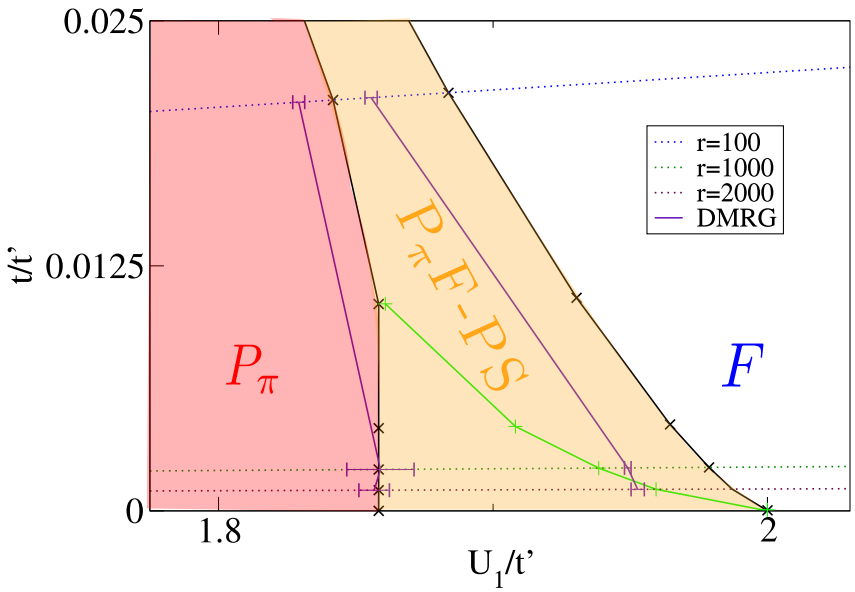

Figure 4.11: Phase diagram in the $\frac{t}{t'} \to 0$ limit. Black lines are the boundaries of the $P_\pi F$-PS phase obtained from model (4.14) for several values of the radius r. Violet lines are DMRG estimates of the phase boundaries for $r = 100, 1000, 2000$. The green line sketches the boundary between the phase separation regime with a fermionic CDW domain (below the line) and the one with a fermionic liquid domain (above the line).

The expression corresponding to the fully paired configuration with $n_f = l_f = 0$ is nothing but Eq. (4.7) enriched with the U_1 interaction energy density contribution arising from the formation of tight pairs only. Similarly, the energy density expression corresponding to the fully unpaired configuration with $n_f = 1, l_f = 0$ coincides with Eq. (4.11): indeed, since the model aims at describing the onset of the P$_\pi$F-PS phase for large values of r, the kinetic energy contribution of unpaired fermions is estimated by restricting the ground state energy search in the subspace $\mathcal{H}_S$ of forbidden nearest-neighbor occupancy, where the interaction energy term proportional to U_1 evaluates to zero. Finally, the formula given for a properly phase-separated configuration is given by the sum of the two preceding expressions, after they have been straightforwardly generalized to the case where the unpaired fermions occupy an arbitrary fraction l_f of the lattice. Note that the parameters n_f and l_f are constrained by $n_f \in [0, n]$ and $l_f \in [2n_f, n_f + 1 - n]$. The latter range is an excluded-volume effect: $l_f \geq 2n_f$ because of forbidden nearest-neighbor occupancy on unpaired fermions; $n - n_f \leq 1 - l_f$ because k pairs occupy a region with at least $2k$ lattice sites.

The minimization of $\mathcal{E}_2(n_f, l_f, r, \theta)$ for several choices of r as a function of θ is presented in Fig. 4.11, where the phase boundaries of the $P_\pi F$-PS phase obtained via model (4.14) (black lines) are compared to the numerical DMRG results for $r = 100, 1000, 2000$ (violet lines). It is therefore possible to conclude that the analytical model (4.14) correctly predicts the robustness to a perturbative single-particle hopping amplitude t, as expected from the data shown in Fig. 4.7. Analogous results can be obtained for the $P_0 F$-PS phase, despite not shown here.

Two different kinds of $P_\pi F$-PS phase separations

As anticipated in Fig. 4.7, two different regimes are observed numerically for large values of r. When $t = 0$, the unpaired fermion domain is arranged in a CDW pattern with unit cell $|\bullet\circ\rangle$, which corresponds to the highest density achievable in presence of forbidden nearest-neighbor occupancy. On the other hand, when $t \neq 0$, two distinct forms of phase separation are predicted by model (4.14), depending on the behavior of the unpaired fermions: the latter either arrange in the aforesaid CDW configuration or they form a Luttinger liquid of strongly repulsive particles that delocalize over the subregion that they occupy. Thus, the phase separation occurs as a spontaneous segregation of a gapped CDW phase and a gapless liquid phase with pair granularity or as the demixing of two gapless liquid phases. The separatrix between the two behaviors is obtained by computing the value of the parameters inside the $P_\pi F$-PS phase where the value of the effective density in the fermionic subregion $\frac{n_f}{l_f}$ deviates from the CDW

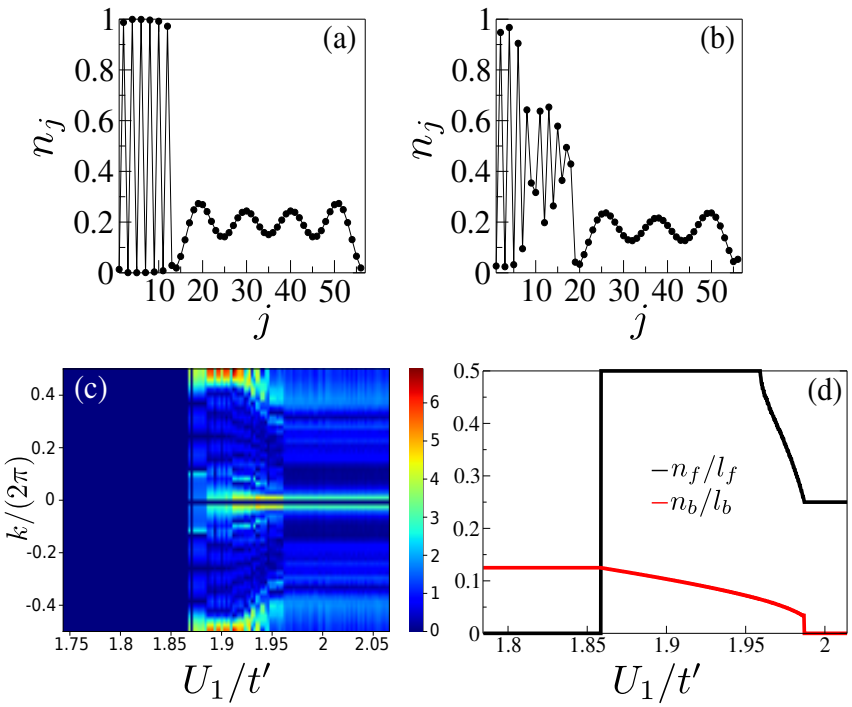

Figure 4.12: Density profiles for the same parameters as in Fig. 4.7 ($r = 2000$) (a) for a $P_\pi F$-PS phase with a CDW domain, (b) for a $P_\pi F$-PS phase with a liquid fermionic domain. (c) Absolute value of $\delta n(k)$ as a function of $\frac{U_1}{t'}$. (d) Predictions from the minimization of Eq. (4.14) for the fermionic density $\frac{n_f}{l_f}$ and the pair density $\frac{n_b}{l_b}$ as a function of $\frac{U_1}{t'}$.

value $\frac{1}{2}$ and is shown in Fig. 4.11 (green line).

We recover these qualitative features in DMRG simulations with $r = 2000$. We provide in Fig. 4.12(a-b) the local density profiles for two different parameter choices: while the profile in Fig. 4.12(a) is fully compatible with the presence of a CDW domain with unit cell $|\bullet\circ\rangle$, the one presented in Fig. 4.12(b) shows fluctuations that are consistent with a liquid phase. Moreover, in order to discriminate between a CDW and a fluid domain, we compute the Fourier transform of the deviation of the density profile from the filling n:

$$\delta n(k) = \sum_j e^{-ikj} \left(\langle \hat{n}_j \rangle - n \right), \tag{4.15}$$

which allows to capture the leading modulations of the density fluctuations.

Indeed, Fig. 4.12(c) allows to follow the transition from the P_π to the $P_\pi F$-PS phase and from the $P_\pi F$-PS to the F phase. More interestingly, inside the intermediate $P_\pi F$-PS phase, a sharp peak at $k = 2\pi\frac{1}{2}$ (corresponding to the formation of a CDW domain) that decreases to lower values (as it is the case in presence of a liquid domain) before the transition to the F phase is clearly visible, whereas a low-k peak associated to the low-density pair subregion is captured as well. Remarkably, these properties are reproduced by the phenomenological model (4.14) with very high quantitative accuracy and support its effectiveness in describing this portion of the phase diagram, as demonstrated by Fig, 4.12(d), where the expected peaks in $\delta n(k)$ predicted from the effective unbound fermion density $\frac{n_f}{l_f}$ and pair density $\frac{n_b}{l_b}$, with $n_b = \frac{n-n_f}{2}$ and $l_b = 1 - l_f$, are shown. Noticeably, despite the use of PBC in the numerical simulations, $\delta n(k)$ does not vanish identically in the F phase, as a flat density profile can hardly be achieved with such a small ratio $\frac{U_1}{t}$. Nevertheless, the pattern remains substantially unchanged, thus signaling the stability of the F phase while increasing the value of $\frac{U_1}{t'}$.

4.3.5 Phase separation vs. coexistence phase

We have shown in the previous subsections that, for large values of r, the intervening phase between the F phase and the P_π phase is a phase-separated one. On the other hand, the phase diagram in Fig. 4.1

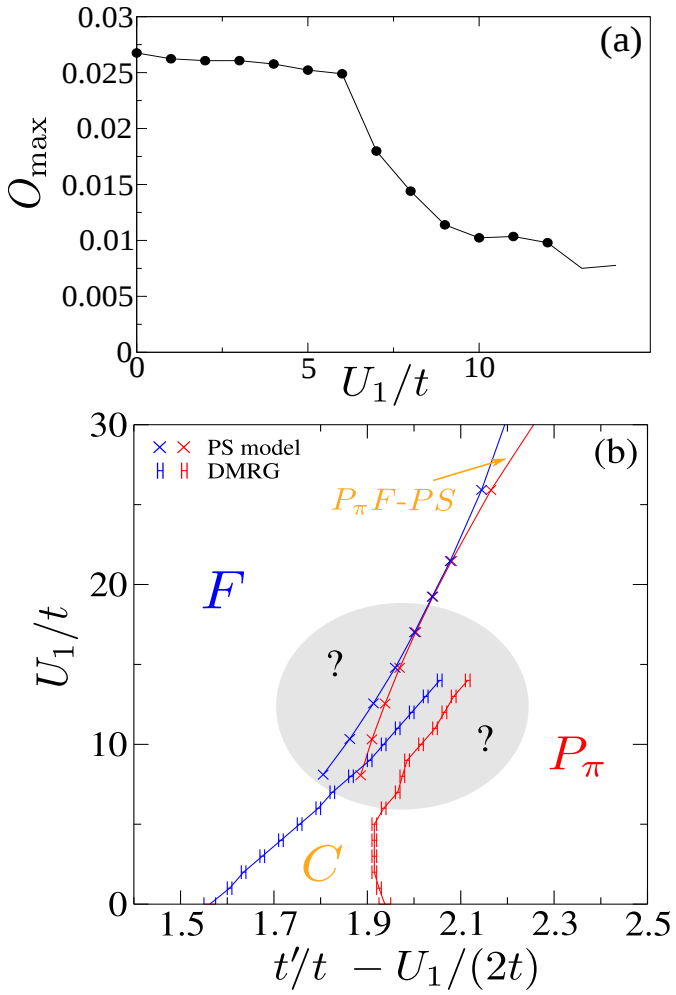

Figure 4.13: Maximum value O_{max} along a cut at constant $\frac{U_1}{t}$ as a function of $\frac{U_1}{t}$. (b) Lines connecting crosses indicate the boundaries of the $P_\pi F$-PS phase as predicted by model (4.14). Lines connecting bars are DMRG estimates for the boundaries of the intermediate phase between the F and P_π phases.

indicates the C phase as the intermediate phase for small values of r. It is thus natural to investigate how the C phase and the $P_\pi F$-PS phase are connected in parameter space.

We start the analysis by monitoring systematically the overlap O defined in Eq. (4.6), which measures the spatial overlap between single-particle and pair hopping and is thus suited to investigate the onset of phase separation. To this end, we plot in Fig. 4.13(a) the maximum value of the overlap:

$$O_{max}\left(\frac{U_1}{t}\right) = max_{\frac{t'}{t}}\, O\left(\frac{t'}{t}, \frac{U_1}{t}\right) \tag{4.16}$$

along a cut at constant $\frac{U_1}{t}$ as a function of $\frac{t'}{t}$, ranging from the F to the P_π phase. Noticeably, the maximum is always reached inside the intermediate phase, so that the observable defined in Eq. (4.16) probes the properties of the latter. The finite-size numerical data indicate that the value of O_{max} remains stable with respect to its $U_1 = 0$ value up to $\frac{U_1}{t} = 6$, thus further demonstrating the stability of the C phase to nonperturbative values of U_1. Contrarily, its value starts to drop when $\frac{U_1}{t} > 6$, thus providing evidence for the progressive onset of phase separation as the radius r increases.

When $U_1/t \gtrsim 14$, the region separating the F and P_π phases is shrinking so much that it makes the DMRG simulations particularly demanding. This shrinking is illustrated on the phase diagram of Fig. 4.13(b), in which the abscissa has been rescaled to follow the main diagonal line of Fig. 4.1 along which this phase develops. The DMRG red lines are compared to the results of the effective large-r model (4.14) pushed towards smaller values of r. We observe that the latter model also predicts a shrinking of the P_πF-PS phase, until the two phase boundaries touch at $\frac{U_1}{t} \sim 20$. A possible scenario is that of a critical point occurring when the two boundaries meet and separating the $P_\pi F$-PS phase from the C phase. Alternatively, the two phases might smoothly evolve one into the other, through a continuous crossover. We leave as an open question the study of the onset of phase separation from the C phase and the determination of whether it occurs through a direct transition or a smooth crossover. Our results already provide essential guidelines for investigating this phase diagram.

4.4 Conclusions

In the present chapter, we have thoroughly investigated the effects of a nearest-neighbor interaction on the properties of the model studied in Ref. [26, 110]. Firstly, we have provided evidence of the stability of the C phase to the addition of a nonperturbative value of the strength U_1 of a simple form of nearest-neighbor density-density interaction. More generally, the phase diagram found for $U_1 = 0$ preserves its qualitative features up to comparatively large values of the additional interaction, both in the attractive and in the repulsive regime.

Moreover, we have further explored a different limiting regime of model (4.1), which can be denoted as flat band limit, where the single-particle hopping amplitude t is always much smaller than the leading energy scale of the system. Such a limit is the large r limit discussed in the main text and displays notably, on top of a regular and of a pair Luttinger liquid phase, two different kinds of phase separation: (i) the Ferro-PS phase, which coincides with the phase separation driven by attractive nearest-neighbor density-density interactions and features the formation of macroscopic fermionic domains, and (ii) the $P_{0,\pi}F$-PS phase, occurring instead in presence of repulsive nearest-neighbor density-density interactions and displaying the spatial segregation of unpaired fermions and pairs. The latter is properly discriminated from the C phase found at smaller values of interaction strength, where the unpaired fermions and the pairs coexist as fully miscible liquids.

Chapter 5

Kinetic formation of trimers and multimers in a spinless fermionic chain

In the present chapter, following Ref. [159], namely L. Gotta, L. Mazza, P. Simon, and G. Roux, *Kinetic formation of trimers and multimers in a spinless fermionic chain*, Phys. Rev. B **105**, 134512, Apr. 2022, we generalize the results obtained for a Hamiltonian with a correlated pair-hopping interaction by replacing the latter with a more general multimer-hopping term, that lowers the energy of configurations where the fermions delocalize as a nearest-neighbor l-particle cluster, with $l \geq 2$. In the interpretation of the numerical data, we rely once more on two-fluid-based phenomenological approaches. We provide evidence that, for arbitrary molecular size, a coexistence phase between unbound fermions and molecules exists as an intermediate phase separating a regular Luttinger liquid from a Luttinger liquid with leading molecular algebraic order. We complement the investigation by studying the effects of fermion-molecule hybridization in a different parameter regime and speculating on its relevance in reshaping the critical properties of the system.

5.1 Introduction

Pairing of more than two particles to form multimers, is a transverse topic in physics, from nuclear and particle physics to condensed matter and cold-atom gases [160, 161, 162, 163]. The first kind of multimers beyond pairs are naturally trimers, three-body bound states. Beyond neutrons and protons made of three bound quarks, trimers have been widely discussed in the context of Efimov states [164, 165, 166, 167, 168] and in Helium physics [169, 170]. With the versatility of cold-atom platforms in terms of internal degrees of freedom and interactions, many proposals for trimers formation arose in the quantum matter literature, using spin balanced [171, 50, 52, 172, 129, 173, 174, 175, 176] or spin-imbalanced fermionic mixtures [177, 178, 179], or fermions with different masses [17, 18, 19]. Signatures of bosonic trimers have also been discussed both in one [180, 181, 182, 183], two [184, 185, 186] and three dimensions [187].

Forming trimers composed of a unique fermionic species – spin-polarized fermions – is particularly challenging despite seminal results in the context of the quantum Hall effect [188]. The pairing of spinless fermions already shows a rich phenomenology [41, 7, 4, 55, 54, 26, 27, 28, 60, 110, 111], and it is a crucial mechanism for some topological phases of matter, motivating further investigations in this direction. An intuitive route is to use attractive density interactions [28] on a chain and stabilize trimers using a third neighbor repulsion to prevent phase separation. In order to develop a low-energy description, as a trimer phase cannot be interpreted as an instability of the Luttinger liquid theory, the authors of Ref. [28] propose an emergent-mode description, which is then treated with bosonisation tools. Unfortunately, such approach is not conclusive on the nature of the transition from the Luttinger liquid to the trimer phase.

In the following, we start by generalizing the two-fluid (2F) model used to capture the properties of the coexistence phase with paired and unbound fermions [110, 111] and discussed in chapter 3 to the case of multimers, showing how a coexistence phase is predicted to exist for every molecule size.

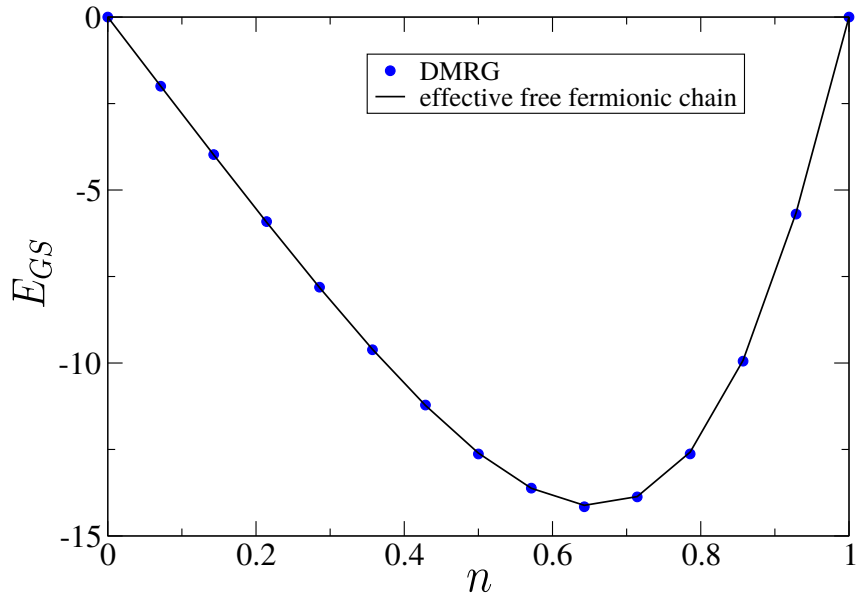

Figure 5.1: DMRG ground state energy $E_G S = N\epsilon_G S$ for $M = 3$ and $L = 42$ sites with PBC with $t' = 1$ and $t = 10^{-4}$ as a function of the filling n and compared with the analytical expression provided in Eq. (5.3).

We proceed to probe the phase diagram of the Hamiltonian with competing single-particle and trimer hopping, thereby providing evidence for a coexistence phase of trimers and unbound fermions. In a different parameter regime of the model, however, interspecies interaction effects are present and lead us to introduce a variational approach based on a two-fluid picture which qualitatively captures the effects of a nonnegligible interaction among the effective low-energy degrees of freedom. We conclude by formulating heuristing arguments and presenting numerical data on the phase diagram of models consisting of single-particle and correlated n-particle hopping, with $n > 3$. We argue the irrelevance of interspecies interactions as the molecular size increases and a non-interacting two-fluid coexistence as the generic intervening scenario between the weak- and the strong-coupling phases of the model.

5.2 Hamiltonian and two-fluid phenomenology

We consider a chain of length L hosting N spinless fermions, so that the filling $n = \frac{N}{L}$ satisfies $n = 0.25$. We generalize the correlated pair-hopping term of the Hamiltonian introduced in Ref. [26] by replacing it with a more general multimer-hopping term that competes with the single-particle hopping one:

$$\hat{H} = -t \sum_j \left(\hat{c}_j^\dagger \hat{c}_{j+1} + H.c. \right) - t' \sum_j \hat{c}_j^\dagger \left(\prod_{m=1}^{M-1} \hat{n}_{j+m} \right) \hat{c}_{j+M} + H.c., \tag{5.1}$$

where $t > 0$ is the single-particle hopping amplitude, t' is the multimer-hopping amplitude and $M \geq 2$ is the multimer spatial extension. In order to elucidate the physical meaning of Hamiltonian (5.1), we reexpress it in the form:

$$\hat{H} = -t \sum_j \left(\hat{c}_j^\dagger \hat{c}_{j+1} + H.c. \right) - (-1)^{M-1} t' \sum_j \left(\hat{M}_j^\dagger \hat{M}_{j+1} + H.c. \right), \tag{5.2}$$

where $\hat{M}_j = \hat{c}_j \hat{c}_{j+1} \dots \hat{c}_{j+M-1}$ is the multimer annihilation operator. Depending on the value of M, the operators $\hat{M}_j$ either commute or anticommute for spatial separations larger than or equal to M and possess the hard-core property $\hat{M}_j^2 = 0$, thus behaving effectively as fermions or hard-core bosons. No exact mapping to fermionic or hard-core bosonic operators exists nevertheless due to the spatial extent of the mulltimers. Generalized Kitaev chains possessing $\hat{M}_j$ as an interaction term have been discussed in Ref. [189], where they lead to the prediction of nontopological parafermions. The numerical data presented in the following are obtained with the DMRG algorithm [144, 145, 81, 82] in the implementation available from the ITensor library [98].

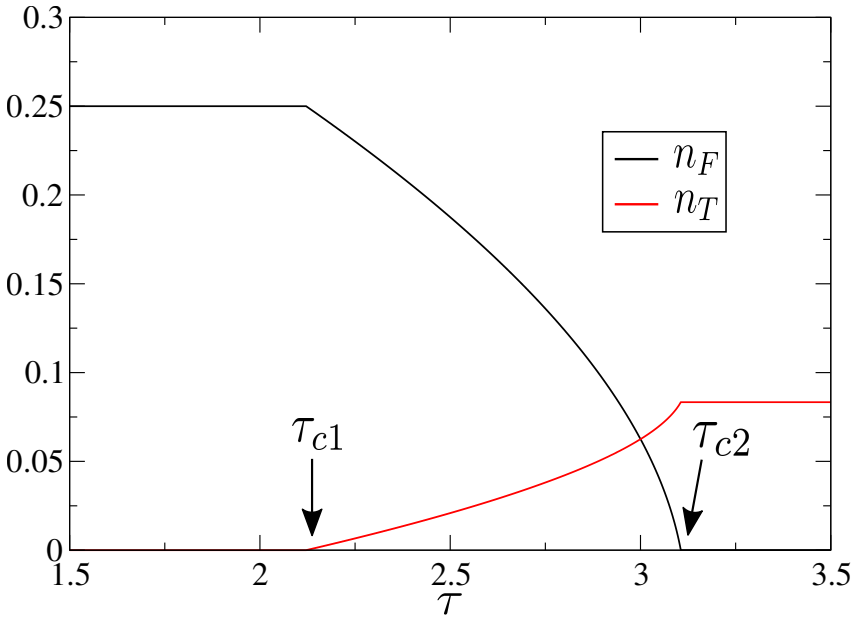

Figure 5.2: Optimal fermionic density n_F and trimer density n_T as a function of $\tau = \left|\frac{t'}{t}\right|$ obtained by minimizing the total energy $\langle \hat{H}^{(3)}_{2F} \rangle$ for a density $n = 0.25$. We observe (i) the F phase ($n_F = n$) for $\tau < \tau_{c1} \simeq 2.12$, (ii) the T phase ($n_F = 0$) for $\tau > \tau_{c2} \simeq 3.11$ and (iii) the TF-C phase ($0 < n_F < n$) for $\tau_{c1} < \tau < \tau_{c2}$.

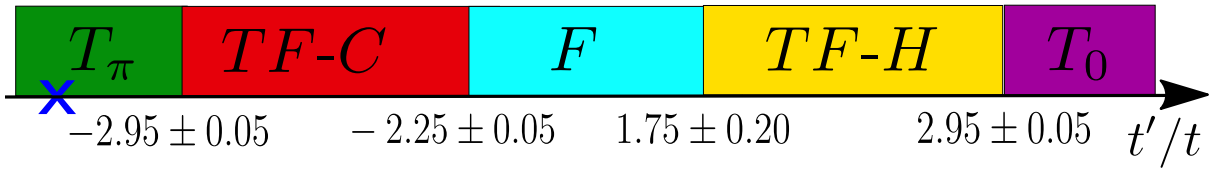

Figure 5.3: Phase diagram of the model in Eq. (5.1) in the case $M = 3$ (not in scale).

5.2.1 $t' = 0$ and multimer formation

We extend to the general M case the considerations that lead to the characterization of the ground state when $t = 0$. As for the aforesaid choice of parameters the Hamiltonian consists only of the correlated multimer-hopping term, we suppose that the ground state lies in the subspace $\mathcal{H}_M$ where the fermions are arranged into nearest-neighbor clusters of size M. Each such configuration can be mapped onto an equivalent configuration of a spin-$\frac{1}{2}$ chain of length $L_M = L - (M-1)N_M$, $N_M = \frac{N}{M}$ being the number of multimers in the system, by replacing a multimer of size M with $|\uparrow\rangle$ and $|\downarrow\rangle$.

The action of Hamiltonian (5.1) on the states belonging to $\mathcal{H}_M$ is then equivalent to the action of an effective spin-$\frac{1}{2}$ XX-chain Hamiltonian on the equivalent spin configuration. The latter can be easily diagonalized, giving $\epsilon_M(k) = (-1)^M 2t' \cos k$ as the effective dispersion relation of multimers. The minimum occurs either at $k_0 = 0$ or at $k_0 = \pi$, depending on the value of M and on the sign of t', while the Fermi points are located at $k_0 \pm \pi \frac{N_M}{L_M}$. The ground-state energy density $\epsilon_{GS} = \frac{\epsilon_{GS}}{L}$ reads:

$$\epsilon_{GS} = -\frac{2|t'|}{\pi}\left(1 - \frac{(M-1)n}{M}\right)\sin\left(\frac{\pi n}{M-(M-1)n}\right). \tag{5.3}$$

The prediction given by Eq. (5.3) as a function of the filling n is compared for the case $M = 3$ with DMRG numerical data in Fig. 5.1, and the agreement is excellent.

5.2.2 The two-fluid picture

In order to capture the behavior of the system in the intermediate-coupling regime, as a first guess we generalize the 2F model applied successfully in the case $M = 2$ with $\frac{t'}{t} > 0$ [110, 111]. Namely, we

assume phenomenologically that the system is populated by two non-interacting species, modelling the unbound fermions and the multimers, whose respective densities are adjusted in such a way that the total energy of the system is minimized. The 2F model Hamiltonian reads:

$$\hat{H}_{2F}^{(M)} = \sum_k \epsilon_F(k)\hat{a}_k^\dagger \hat{a}_k + \sum_k \epsilon_M(k)\hat{d}_k^\dagger \hat{d}_k, \tag{5.4}$$

where the $\hat{a}_k$ operators are fermionic operators associated to unbound fermions, $\epsilon_F(k) = -2t\cos k$ is their dispersion relation, and the $\hat{d}_k$ operators are fermionic or fermionized hard-core bosonic operators describing the multimers, with dispersion relation $\epsilon_M(k) = (-1)^M 2t'\cos k$.

After subjecting the density of unbound fermions n_F and the multimer density n_M to the constraint $n_F + Mn_M = n$, the minimization of the energy obtained from Hamiltonian (5.4) allows to recover the behavior of the density of each species as a function of $\tau = \left|\frac{t'}{t}\right|$. The general structure of the obtained phase diagram is as follows: (i) at small values of τ, one obtains a purely fermionic phase (F phase), with $n_F = n$ and $n_M = 0$; (ii) at large values of τ, one recovers instead a multimer phase (M phase), where $n_F = 0$ and $n_M = \frac{n}{M}$; (iii) for an intermediate range of values of τ, a coexistence phase of unbound fermions and multimers (MF-C phase) is predicted, where $0 < n_F < n$ and $0 < n_M < \frac{n}{M}$. An example of such a phase diagram is displayed in Fig. 5.2 in the case $M = 3$.

We determine the phase boundaries of the MF-C phase by considering the stationarity condition on the variational energy that determines the optimal fermionic density n_F:

$$\cos(\pi n_F) = \frac{\tau}{M}\cos\left(\pi\frac{n - n_F}{M}\right). \tag{5.5}$$

The critical point $\tau_{c1}^{(M)}$ separating the F phase from the MF-C phase can be determined self-consistently by taking the limit $n_F \to n^-$ in Eq. (5.5), obtaining that saturation of the fermionic density n_f to its maximal value n occurs at $\tau_{c1}^{(M)} = M\cos(\pi n)$. Similarly, the critical point $\tau_{c2}^{(M)}$ separating the MF-C phase from the M can be computed by taking the limit $n_F \to 0^+$ in Eq. (5.5), obtaining as a result $\tau_{c2}^{(M)} = \frac{M}{\cos\left(\frac{\pi n}{M}\right)}$.

Finally, we remark that the predictions obtained from the minimization of the energy of Hamiltonian (5.4) are identical irrespectively of the sign of t'. However, it is known that in the case $M = 2$ they do not account correctly for the phase diagram properties when $t' < 0$ [26, 110, 111], where interspecies interactions are relevant and modify the critical properties. Hence, in the following, when specializing to the cases $M = 3$ and $M = 4$, we will highlight the regime of applicability of the noninteracting 2F model (5.4).

5.3 Trimer formation and trimer-fermion mixtures

In the present section, we specialize to the case of trimers ($M = 3$) and describe thoroughly the associated phase diagram of model (5.1) in this specific instance. We complement the extensive numerical simulations with the predictions obtained from the 2F model (5.4) and with an *ad hoc* variational ansatz aimed at capturing the effect of correlations between unbound fermions and trimers. When referring to the unveiled phases, we replace the label M with the label T to make explicit reference to trimers.

5.3.1 Phase diagram

The phase diagram of the model is summarized in Fig. 5.3. We perform its systematic analysis by computing local observables and the decay properties of the single-particle, pair and trimer two-point correlation functions, which read:

$$G(r) = \langle \hat{c}_j^\dagger \hat{c}_{j+r}\rangle,\ \ P(r) = \langle \hat{c}_j^\dagger \hat{c}_{j+1}^\dagger \hat{c}_{j+r}\hat{c}_{j+r+1}\rangle,\ \ T(r) = \langle \hat{T}_j^\dagger \hat{T}_{j+r}\rangle, \tag{5.6}$$

respectively, where $\hat{T}_j = \hat{c}_j\hat{c}_{j+1}\hat{c}_{j+2}$. We start our discussion by providing in Fig. 5.4(a-b) the correlators defined in Eq. (5.6) for $\frac{t'}{t} = -3.5$. While $G(r)$ and $P(r)$ decay exponentially with equal correlation length, $T(r)$ shows a leading modulated algebraic decay. Such signatures are compatible with the existence of a Luttinger liquid phase with trimer granulatìrity, where both single-particle and pair excitations are

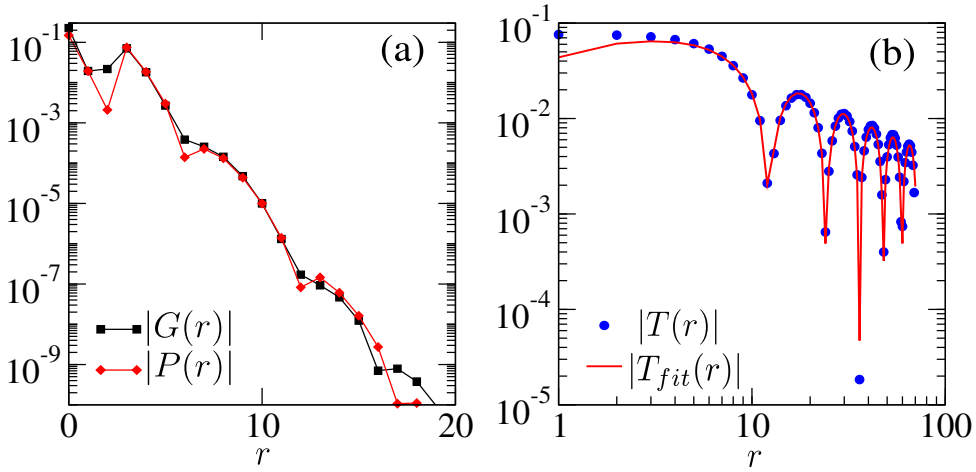

Figure 5.4: (a,b) Correlators for $\frac{t'}{t} = -3.5$ (blue cross in Fig. 5.3): $G(r)$ for single-particle, $P(r)$ for pairs (both exponential), $T(r)$ for trimers (algebraic) and $T_{fit}(r)$ for the fitting function of trimer two-point correlators.

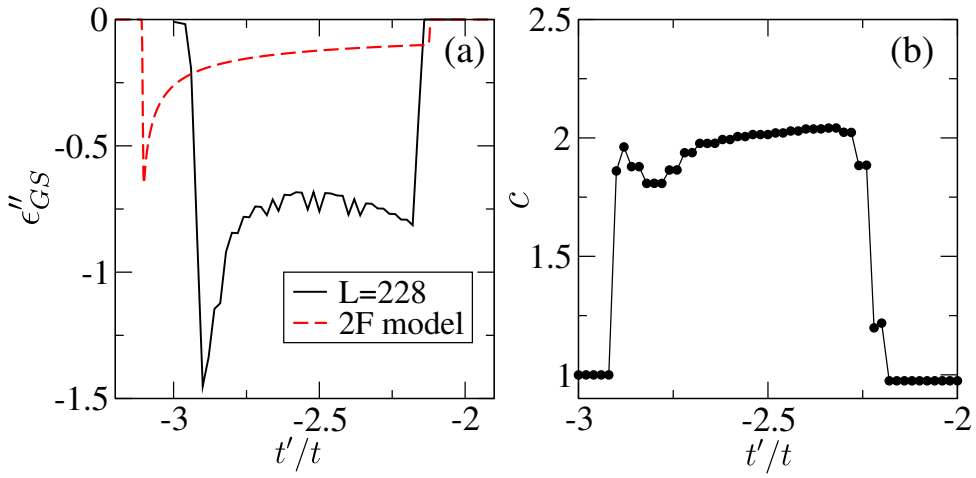

Figure 5.5: (a) Second derivative of the ground-state energy density ϵ''_{GS} with respect to $\frac{t'}{t}$ for the Hamiltonian in Eq. (5.1) (continuous line) and for the model $\hat{H}_{2F}$ (dashed line). (b) Central charge c as a function of $\frac{t'}{t}$.

gapped, while three-particle excitations are gapless. We name these strong-coupling phases T_0 and T_π phases, depending on whether the trimers quasicondense around quasimomentum $k = 0$ or $k = \pi$, as further investigated in later subsections. The fit of $T(r)$ to the curve $T_{fit}(r) = A\frac{\cos(kr+\varphi)}{r^\alpha}$ (A, k, φ and α being fitting parameters) shows that the effective Luttinger liquid description of the trimer fluid corresponds to that of almost free fermions, as $\alpha \simeq 1$, while the modulation occurs at wavevector $k = k_T = \pi n_T$, commensurately with the underlying trimer density.

On the other hand, a regular Luttinger liquid phase, denoted as F phase, extends around the non-interacting point $t' = 0$ and features quasi-long-range order in all correlation functions. By monitoring the energy density and its derivatives, it is finally possible to estimate the phase boundaries of the two intervening phases separating the weak-coupling phase from the strong-coupling phases, as presented in Fig. (5.3). These phases are coexistence phases between unbound fermions and trimers, but, while the TF-C phase occurring for $\frac{t'}{t} < 0$ is well captured by the noninteracting 2F model (5.4), the TF-H phase properties are affected by hybridization effects among the two species. Therefore, we focus here on the former and postpone the treatment of the latter to a later subsection.

In particular, we present in Fig. 5.5(a) the second derivative of the ground-state energy density obtained from DMRG simulations and compare it with the same quantity computed from the energy profile as a function of τ derived from the 2F model (5.4): the agreement between the two results is not

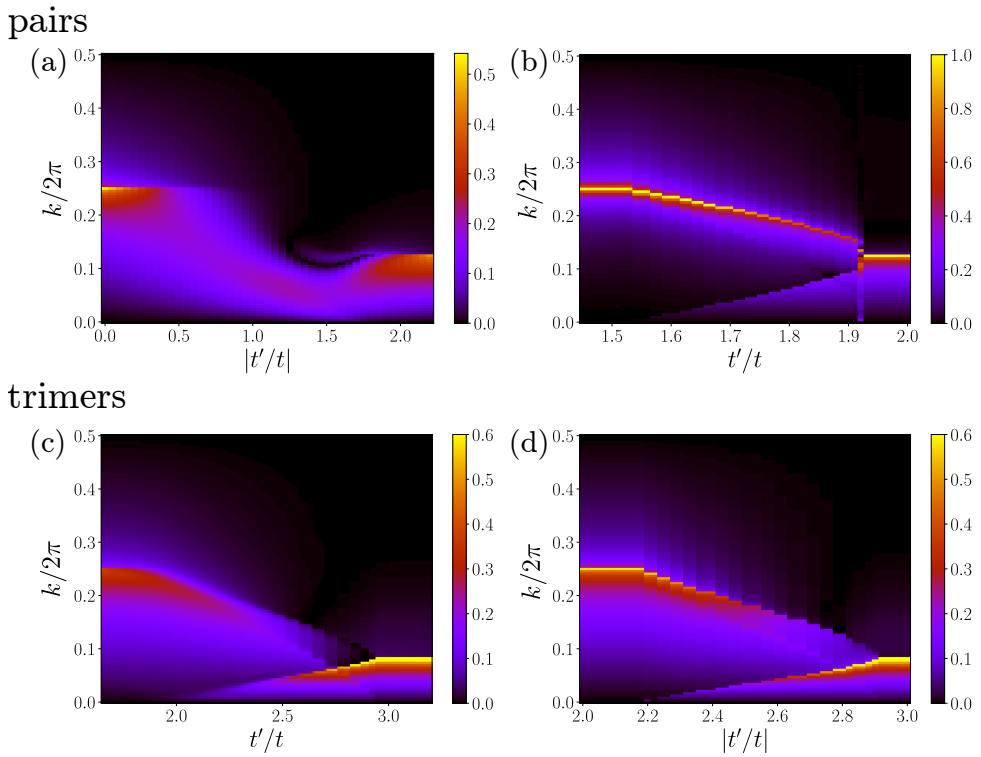

Figure 5.6: (a-b) Fourier transform of the density profile in the ground state of the model with correlated pair hopping studied in Ref. [110] for $\frac{t'}{t} < 0$ (a) and $\frac{t'}{t} > 0$ (b). (c-d) Fourier transform of the density profile in the ground state of the model defined in Eq. (5.1) of the main text for $\frac{t'}{t} > 0$ (c) and $\frac{t'}{t} < 0$ (d).

only qualitative with regards to the nature of the criticality, predicted to be of second order due to the jump discontinuity in the second derivative, but also almost quantitative in the position of the critical points. Moreover, we provide in Fig. 5.5(b) the fitted central charge as a function of $\frac{t'}{t}$, obtaining a value $c = 1$ for the F and the T_π phases and a value $c = 2$ for the intermediate TF-C phase. Such a result supports the interpretation of the intervening TF-C phase as the coexistence phase proposed in the framework of the 2F model (5.4) and the critical points as the parameter values at which two Lifschitz transitions characterized by a nontrivial reshaping of the low-energy excitation spectrum occur.

As in the case of pairs, such a remarkable agreement is explained by the fact that the Fermi sea filled by unbound fermions and the one filled by trimers are significantly displaced from each other in reciprocal space, as the minimum of the trimer band lies at $k = \pi$ in the 2F model interpretation for $M = 3$ and $t' < 0$. Hence, momentum-conserving scattering processes among the two species are effectively suppressed and do not alter the critical behavior at intermediate coupling strength, whereas residual density-density interactions and exxcluded-volume effects contribute solely to the shift of the position of the phase boundaries.

5.3.2 Fourier transform of the density profile

We proceed with the study of the Fourier transform of the local density profile fluctuations $n_j = \langle \hat{n}_j - n \rangle$. We present in Fig. 5.6(c-d) its behavior in the regime of parameters where the transition from the trimer phases $T_{0,\pi}$ to the F phase takes place. We observe in the F phase a distinct peak at $k = 2\pi n$, as expected for the density modulation in a weak-coupling Luttinger liquid with single-particle granularity. Meanwhile, in the $T_{0,\pi}$ phases we recover a peak at $k = 2\pi n_T$, consistently with the density $n_T = \frac{n}{3}$ of the microscopic degrees of freedom exhibiting liquid behavior in these parameter regimes, namely the trimers.

A richer structure occurs in the intermediate phases. In the TF-C and in the TF-H phases, we observe a leading peak interpolating between the one observed in the F phase and the one occurring in

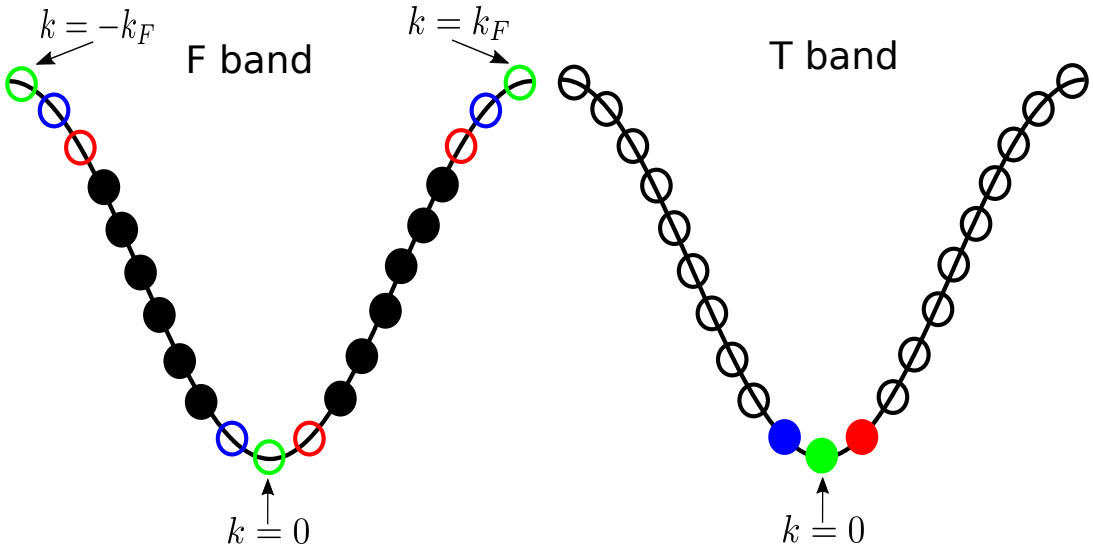

Figure 5.7: Schematic representation of the gradual filling of the trimer band (T band) and depletion of the fermionic band (F band) built into the structure of the 3BCS ansatz. The color of the boundary of the empty dots on the fermionic band denotes the fermionic states that have been annihilated to create the trimer state depicted as a filled dot of the same color on the trimer band.

the $T_{0,\pi}$ phases. We interpret its location as the wavevector $k = 2\pi(n_F + n_T)$ determining the leading modulation in the density of a liquid displaying coexistence between unbound fermions at density n_F and trimers at density n_T. Moreover, we observe a sharp peak increasing from a zero value at the boundary with the F phase to the value $k = 2\pi\frac{n}{3}$ in the $T_{0,\pi}$ phases, which can be interpreted as a signal at $k = 2\pi n_T$ linked to the trimer density, and a further subleading peak interpolating between $k = 2\pi n$ in the F phase to a zero value in the $T_{0,\pi}$ phases, associated to the density of unbound fermions via $k = 2\pi n_F$.

We can formulate further considerations by comparing the results obtained in the trimer case with the ones observed in the pair case ($M = 2$) [110, 111]. On one hand, when the 2F picture predicts the effective fermionic and molecular bands to be mismatched in reciprocal space, namely for $\frac{t'}{t} > 0$ in the case of pairs and for $\frac{t'}{t} < 0$ in the case of trimers, the aforementioned phenomenology compatible with a coexistence phase is present. On the other hand, in the opposite sign cases, one can make the following two observations: (i) in the pair case, a nontrivial direct Ising transition from the F phase to the P_π phase is known to occur and, in proximity to the critical point, the relevant hybridization effects do not allow to observe any sharply-defined peaks associated to effective gapless modes of two mutually noninteracting species; (ii) in the trimer case, signatures of a coexistence phase in the TF-H phase are still present, but the sharp peaks associated to the two species become less well defined close to the boundary with the F phase as a biproduct of interspecies interactions. We devote the next subsection to the investigation of this parameter regime.

5.3.3 A BCS-like approach for the transition from the T_0 to the F phase

When $\frac{t'}{t} > 0$, the noninteracting 2F picture predicts both the fermionic and the trimer band to have their minima at $k = 0$. Thus, it is natural to expect momentum-conserving interspecies interaction processes to affect the ground-state properties of the system in this parameter regime. In order to take it into account, we enrich the noninteracting 2F model (5.4) with an interspecies interaction term as follows:

$$\hat{H}_{2F} = \hat{H}^{(3)}_{2F} + g\sum_j \left(\hat{d}^\dagger_j \hat{a}_{j-1}\hat{a}_j\hat{a}_{j+1} + H.c.\right), \tag{5.7}$$

where we refer to the notation used in Eq. (5.4) and define the operators $\hat{a}_j$ and $\hat{d}_j$ as the inverse Fourier transform of $\hat{a}_k$ and $\hat{d}_k$. The interaction strength g is introduced on a purely phenomenological basis and is taken to be $O(1)$, i.e., it does not scale extensively with system size. The model can be rewritten

in the reciprocal space basis as:

$$\hat{H}_{2F} = \sum_k (\epsilon_{k,F} - \mu)\hat{a}_k^\dagger \hat{a}_k + \sum_k (\epsilon_{k,T} - 3\mu)\hat{d}_k^\dagger \hat{d}_k + \frac{ig}{3L} \sum_{k_1,k_2,k_3} f(k_1,k_2,k_3)\hat{d}_{k_1+k_2+k_3}^\dagger \hat{a}_{k_1}\hat{a}_{k_2}\hat{a}_{k_3} + \text{H.c.}, \tag{5.8}$$

where $f(k_1,k_2,k_3) = \sin(k_3-k_1) + \sin(k_2-k_3) + \sin(k_1-k_2)$ and we assume in the following $\epsilon_{k,F} = -2t\cos k$, $\epsilon_{k,T} = -2t'\cos k$.

In order to write a variational ansatz for model (5.7), we need to identify the most relevant interspecies correlations induced by the interaction term and include them in the former. To this goal, we consider the problem of identifying the optimal way of creating a trimer with momentum $k = 0$, i.e., at the bottom of the trimer band, via annihilation of 3 fermions from a filled Fermi sea of unpaired fermions with Fermi momentum $k_F = \pi n$. Formally, we need to determine a triplet of momenta $k_1, k_2, k_3 \in [-\pi n, \pi n]$ satisfying $\sum_{i=1}^3 k_i = 0$ such that the total energy loss $-2t\cos k_1 - 2t\cos k_2 - 2t\cos k_3$ due to the annihilation of fermions at momenta k_1, k_2, k_3 is maximal. By symmetry, we can always assume that $k_1 \leq 0$ and $k_2, k_3 \geq 0$. This simple observation allows the following manipulation:

$$\begin{aligned} &\max_{\substack{(k_1,k_2,k_3)\in[-\pi n,\pi n]^3 \\ \sum_{i=1}^3 k_i = 0}} \big\{ -2t\cos k_1 - 2t\cos k_2 - 2t\cos k_3 \big\} = \\ &= \max_{-\pi n \leq k_1 \leq 0} \big\{ -2t\cos k_1 + \max_{0\leq k_2 \leq -k_1} \{-2t\cos k_2 - 2t\cos(k_1+k_2)\} \big\}. \end{aligned} \tag{5.9}$$

Since $\max_{0\leq k_2\leq -k_1}\{-2t\cos k_2 - 2t\cos(k_1+k_2)\}$ is achieved by choosing $k_2 = 0$ (or equivalently $k_2 = -k_1$), we are left with the problem of finding:

$$\max_{-\pi n \leq k_1 \leq 0} \{-4t\cos k_1\} - 2t, \tag{5.10}$$

which manifestly leads to the optimal value $k_1 = -\pi n$. The third momentum value is obtained from the constraint $k_3 = -k_1 - k_2 = \pi n$ (or equivalently $k_3 = 0$ after the alternative choice $k_2 = -k_1$). The optimal choice is therefore given by the annihilation of unpaired fermions with $k = 0, \pm k_F$, i.e., at the bottom and at the Fermi edges of the band.

We incorporate this observation into a many-body BCS-like variational ansatz for the ground state of Hamiltonian (5.7), denoted as 3BCS ansatz, by considering a trial state of the form:

$$|\Psi_3\rangle = \prod_{-\frac{k_F}{3}<k<\frac{k_F}{3}} \left(\alpha_k + \beta_k \hat{d}_k^\dagger \hat{a}_{-k_F+\delta_k}\hat{a}_k\hat{a}_{k_F-\delta_k}\right)|n_F\rangle \otimes |v_T\rangle\,, \tag{5.11}$$

where we denoted the Fermi sea of unpaired fermions filled up to Fermi momentum $k_F = \pi n$ as $|n_F\rangle$, the trimer vacuum as $|v_T\rangle$, whereas $\delta_k = 2k$ for $k \geq 0$ and $\delta_k = -2k - \frac{2\pi}{L}$ for $k < 0$. The variational parameters are given by the set of coefficients α_k and β_k, that the energy computed on the state $|\Psi_3\rangle$ needs to be optimized over. We notice that the ansatz (5.11) interpolates between the filled Fermi sea of unpaired fermions, obtained when $\beta_k = 0\ \forall k$, and the filled trimer band with Fermi momentum $k_T = \pi\frac{n}{3}$, recovered when $\alpha_k = 0\ \forall k$, via quantum correlations between unpaired fermions with momenta k and $\sim \pm(k_F - 2|k|)$ (see Fig. 5.7 for a schematic illustration). The latter are qualitatively reminiscent of the optimal process derived above and that they reduce to when $k = 0$, while simultaneously allowing to perform analytical calculations due to the fact that the variational ansatz $|\Psi_3\rangle$ is entirely composed of mutually commuting operator terms.

We proceed our analysis by evaluating the ground-state energy density. By virtue of the normalization condition $|\alpha_k|^2 + |\beta_k|^2 = 1$, we parametrize the variational coefficients as $\alpha_k = \cos\theta_k$, $\beta_k = e^{i\varphi_k}\sin\theta_k$, with $\theta_k \in [0, 2\pi)$, $\varphi_k \in [0, 2\pi)$. By denoting the energy of the noninteracting Fermi sea of unpaired fermions filled up to momentum k_F as E_{FS}, the variational ground-state energy density is defined as:

$$\epsilon_{GS} = \frac{\langle\Psi_3|\,\hat{H}_{2F}\,|\Psi_3\rangle - E_{FS}}{Lt} \tag{5.12}$$

and, when expressed as a function of the variational parameters, it reads:

$$\epsilon_{GS} = 2\int_0^{\frac{k_F}{3}} \frac{\mathrm{d}k}{2\pi}\,\left[A_k \sin^2\theta_k - B_k \sin 2\theta_k \sin\varphi_k\right], \tag{5.13}$$

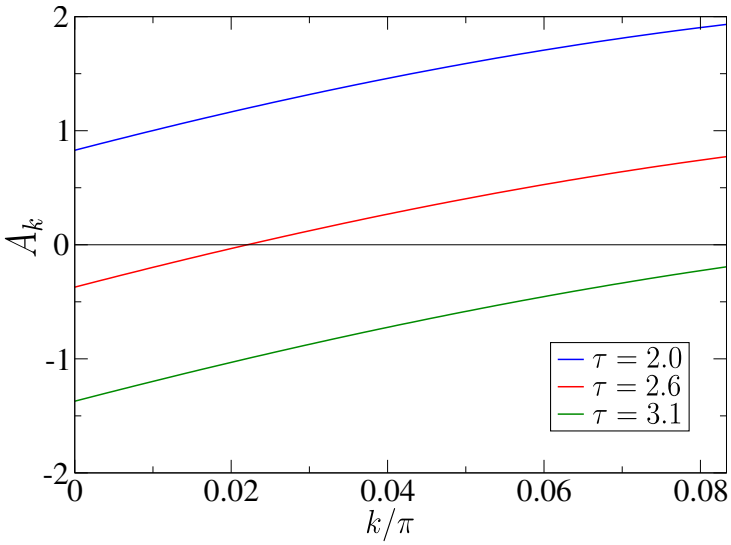

Figure 5.8: A_k as a function of k for $\tau < \tau_1$ (blue curve), $\tau_1 < \tau < \tau_2$ (red line) and $\tau > \tau_2$ (green line).

where $L \gg 1$ has been assumed and:

$$A_k = 2(1 - t'/t)\cos k + 4\cos(k_F - 2k), \tag{5.14a}$$

$$B_k = \frac{2g}{Lt}\left[\sin(k_F - k) + \sin(4k - 2k_F) + \sin(k_F - 3k)\right]. \tag{5.14b}$$

Minimizing the functional (5.13) yields the solutions

$$\theta_k = \frac{1}{2}\arctan\left(\frac{2B_k}{A_k}\right) + \frac{\pi}{2}\Theta\left(-A_k\right), \quad \varphi_k = \frac{\pi}{2}, \tag{5.15}$$

where $\Theta(x)$ is the Heaviside step function.

As one can infer from Eq. (5.15), the value of the optimal variational parameters depends on the sign of the function A_k on the interval $\left[0, \frac{k_F}{3}\right]$. Hence, we plot in Fig 5.8 its behavior in the three parameter regimes yielding qualitatively different results. For small values of $\tau = \frac{t'}{t}$, where the F phase is to be expected, the function A_k satisfies $A_k > 0\ \forall k \in \left[0, \frac{k_F}{3}\right]$. For large values of τ, where one anticipates the onset of the T_0 phase, one has $A_k < 0\ \forall k \in \left[0, \frac{k_F}{3}\right]$. Finally, in an intermediate range of values, A_k changes sign at a point in the interior of the interval $\left[0, \frac{k_F}{3}\right]$; we expect this parameter regime to be host the TF-H phase. The values τ_1 and τ_2 that enclose such an intermediate parameter range and that will be identified as the variational prediction of the phase boundaries of the TF-H phase are obtained from the conditions $A_{k=0} = 0$ and $A_{k=\frac{k_F}{3}} = 0$, respectively, resulting in the formulas:

$$\tau_1 = 1 + 2\cos(\pi n), \qquad \tau_2 = 3. \tag{5.16}$$

We confirm the aforementioned interpretation of τ_1 and τ_2 by computing an order parameter that allows to discriminate the F, TF-H and T_0 phases from each other, namely the trimer density. The expression of this observable is easily written as:

$$n_T = \frac{1}{L}\sum_k \langle \hat{d}_k^\dagger \hat{d}_k \rangle = \frac{1}{\pi}\int_0^{\frac{k_F}{3}} dk \sin^2\theta_k. \tag{5.17}$$

Since in the thermodynamic limit $\theta_k = \frac{\pi}{2}\Theta(-A(k))$ because $B_k \propto L^{-1}$, the evaluation of n_T becomes trivial. In particular, when $\tau < \tau_1$ one has a strictly positive $A(k)$ profile, which implies $\theta_k = 0$ and thus $n_T = 0$. Thus, we identify this regime with the F phase. In a similar manner, since $A(k)$ is strictly negative when $\tau > \tau_2$, we get $\theta_k = \frac{\pi}{2}$, which results in $n_T = n/3$. We link this result with the T_0 phase. Finally, when $\tau_1 < \tau < \tau_2$, one has $A(k) < 0$ for $0 < k < K(\tau)$ and $A(k) > 0$ for $K(\tau) < k < k_F/3$,

where $K(\tau)$ denotes the intermediate zero of $A(k)$ as a function of τ. In this case, the trimer density takes the form:

$$n_T = \frac{1}{\pi}\left(\int_0^{K(\tau)} dk \sin^2\theta_k + \int_{K(\tau)}^{\frac{k_F}{3}} dk \sin^2\theta_k\right) = \frac{1}{\pi}\int_0^{K(\tau)} dk = \frac{K(\tau)}{\pi}. \tag{5.18}$$

Hence, the trimer density takes an intermediate value $0 < n_T < n/3$, which implies that the fermionic density $n_F = n - 3n_T$ is nonvanishing as well and the two species coexist, as expected for a TF-H phase. Eq. (5.18) forces the interpretation of the zero of $A(k)$ as the Fermi momentum of the trimer Fermi sea as a function of τ.

Lastly, we evaluate the variational energy density ϵ_{GS} to fully establish the onset of critical behavior at $\tau = \tau_1$ and $\tau = \tau_2$ in the thermodynamic limit. In the F phase, $A_k > 0 \ \forall k \in [0, \pi n/3]$, implying that $\theta_k = \frac{1}{2}\arctan\left(\frac{2B_k}{A_k}\right)$ and therefore resulting in the optimal energy:

$$\frac{\langle \hat{H}_{2F}\rangle_{\Psi_3} - E_{FS}}{Lt} = 2\int_0^{\frac{k_F}{3}} \frac{dk}{2\pi}\left\{A_k \sin^2\left[\frac{1}{2}\arctan\left(\frac{2B_k}{A_k}\right)\right] - B_k \sin\left[\arctan\left(\frac{2B_k}{A_k}\right)\right]\right\}. \tag{5.19}$$

As $L \to +\infty$, $B_k \propto L^{-1}$ vanishes and therefore:

$$\lim_{L\to+\infty} \frac{\langle \hat{H}_{2F}\rangle_{\Psi_3} - E_{FS}}{Lt} = 0, \tag{5.20}$$

indicating that the energy of the system equals the energy of the fermionic Fermi sea.

In the T_0 phase, instead, one has $A_k < 0 \ \forall k \in [0, \pi n/3]$, which implies that $\theta_k = \frac{1}{2}\arctan\left(\frac{2B_k}{A_k}\right) + \frac{\pi}{2}$ and gives as a result the optimal energy:

$$\frac{\langle \hat{H}_{2F}\rangle_{\Psi_3} - E_{FS}}{Lt} = 2\int_0^{\frac{k_F}{3}} \frac{dk}{2\pi}\left\{A_k \sin^2\left[\frac{\pi}{2} + \frac{1}{2}\arctan\left(\frac{2B_k}{A_k}\right)\right] - B_k \sin\left[\pi + \arctan\left(\frac{2B_k}{A_k}\right)\right]\right\}. \tag{5.21}$$

As $L \to +\infty$, the second term clearly vanishes, as it is bounded from above by an expression proportional to L^{-1}, while the first term converges to A_k and gives:

$$\lim_{L\to+\infty} \frac{\langle \hat{H}_{2F}\rangle_{\Psi_3} - E_{FS}}{Lt} = \frac{1}{\pi}\int_0^{\frac{k_F}{3}} A_k = -\frac{2}{\pi}\left(\tau - \frac{\sin(\pi n)}{\sin\left(\frac{\pi n}{3}\right)}\right)\sin\left(\frac{\pi n}{3}\right) \tag{5.22}$$

In the intermediate regime $\tau_1 < \tau < \tau_2$, one has that $A_k < 0 \ \forall k \in [0, K(\tau))$ and $A_k > 0 \ \forall k \in (K(\tau), \pi n/3]$; therefore, the optimal energy takes the form:

$$\begin{aligned}\frac{\langle \hat{H}_{2F}\rangle_{\Psi_3} - E_{FS}}{Lt} = \ & 2\int_0^{K(\tau)} \frac{dk}{2\pi}\left\{A_k \sin^2\left[\frac{\pi}{2} + \frac{1}{2}\arctan\left(\frac{2B_k}{A_k}\right)\right] - B_k \sin\left[\pi + \arctan\left(\frac{2B_k}{A_k}\right)\right]\right\} \\ & + 2\int_{K(\tau)}^{\frac{k_F}{3}} \frac{dk}{2\pi}\left\{A_k \sin^2\left[\frac{1}{2}\arctan\left(\frac{2B_k}{A_k}\right)\right] - B_k \sin\left[\arctan\left(\frac{2B_k}{A_k}\right)\right]\right\}.\end{aligned} \tag{5.23}$$

The second term goes to zero in the large size limit, while the first term gives:

$$\lim_{L\to+\infty} \frac{\langle \hat{H}_{2F}\rangle_{\Psi_3} - E_{FS}}{Lt} = \frac{1}{\pi}\int_0^{K(\tau)} A_k = \frac{2}{\pi}(1-\tau)\sin K(\tau) + \frac{2}{\pi}\sin(\pi n) - \frac{2}{\pi}\sin\left[\pi n - 2K(\tau)\right]. \tag{5.24}$$

The asymptotic behavior of the energy as it approaches the critical points can then be obtained by deriving the one of the zero $K(\tau)$ when τ is close to either of the critical points; the latter is found by expanding the condition $A(k) = 0$ around $k = 0$ and $k = \frac{\pi n}{3}$, obtaining:

$$K(\tau) \sim \frac{\tau - \tau_1}{4\sin(\pi n)} \quad \text{and} \quad K(\tau) \sim \frac{\pi n}{3} - \frac{1}{6}\cot\left(\frac{\pi n}{3}\right)(\tau_2 - \tau) \tag{5.25}$$

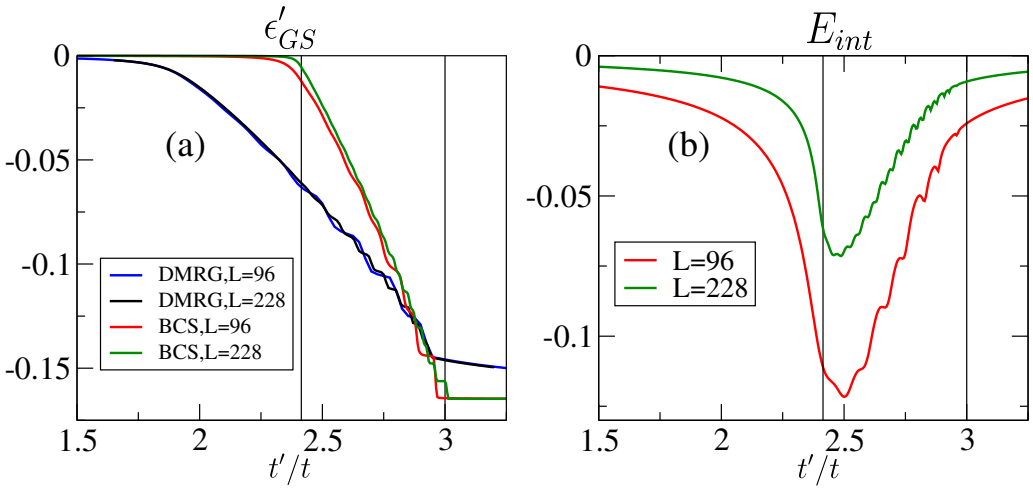

Figure 5.9: (a) First derivative of the ground-state energy density ϵ'_{GS} with respect to $\frac{t'}{t}$ from DMRG and the 3BCS ansatz with $g = 8t$. (b) Interaction energy E_int for the 3BCS ansatz using $g = 8t$. Vertical lines are transition points predicted by the 3BCS model.

As a result, in the limit $\tau \to \tau_1^+$, the energy density behaves as:

$$\frac{\langle \hat{H}_{2F} \rangle_{\Psi_3} - E_{FS}}{Lt} \approx -\frac{(\tau - \tau_1)^2}{4\pi \sin(\pi n)}, \tag{5.26}$$

while in the limit $\tau \to \tau_2^-$, the energy density behaves as:

$$\frac{\langle \hat{H}_{2F} \rangle_{\Psi_3} - E_{FS}}{Lt} \approx \frac{2}{\pi}\sin(\pi n) - \frac{6}{\pi}\sin\left(\frac{\pi n}{3}\right) + \frac{2}{\pi}\sin\left(\frac{\pi n}{3}\right)(\tau_2 - \tau) - \frac{1}{6\pi}\frac{\cos^2\left(\frac{\pi n}{3}\right)}{\sin\left(\frac{\pi n}{3}\right)}(\tau_2 - \tau)^2. \tag{5.27}$$

Hence, we recover the finite jump discontinuities in the second derivative predicted in the framework of the noninteracting 2F model (5.4) to be associated to the appearance/disappearance of a gapless mode when entering/exiting a coexistence phase of fermions and trimers. The recovery of the critical behavior obtained in the case of two noninteracting fluids is not surprising in view of the irrelevance of the interspecies interaction contribution to the variational energy density ϵ_{GS} when $L \to +\infty$. Indeed, as the effect of interactions is incorporated in the second term of Eq. (5.13), which scales as L^{-1} as a function of system size, ϵ_{GS} reduces in the thermodynamic limit to the sole kinetic contribution of the two fluids, which gives rise to the critical properties obtained from model (5.4).

We proceed by comparing the analytical predictions with the numerical DMRG data on the first derivative of the ground-state energy density. By plotting in Fig. 5.9(a) the latter quantity for sizes $L = 96, 228$ as obtained from the numerical results and from the variational approach with $g = 8t$, we are able to reproduce in a qualitative fashion the energetic ground-state properties of model (5.1) within the framework of the 3BCS ansatz. In particular, we underline two distinct features: (i) the step-like behavior of the curve ϵ'_{GS} when approaching the transition to the T_0 phase; (ii) the smooth shoulder of the very same curve close to the transition to the F phase. While the first property is purely a finite-size effect originating even in absence of interspecies interactions from the choice of a small value of L, the second one is instead the effect of a nonnegligible fermion-trimer hybridization, that strongly affects the finite-size data. We support this claim by showing in Fig. 5.9(b) the plot of the value of the variational interaction energy $E_{int} = -\frac{L}{\pi}\int_0^{\frac{k_F}{3}} B_k \sin(2\theta_k) dk$ as a function of $\frac{t'}{t}$, which demonstrates that the smooth shoulder in ϵ'_{GS} appears in the parameter region where interspecies interactions reach their maximal values, whereas the step-like behavior occurs in presence of comparatively smaller values of E_{int}.

As a concluding remark, we speculate on the nature of the critical points from the numerically obtained results displayed in Fig. 5.9(a). The critical point separating the TF-H phase from the T_0 phase agrees qualitatively with the variational prediction of a finite-jump discontinuity in the second derivative of the ground-state energy density. The numerical data do not allow instead for a firm conclusion on the nature of the transition from the F phase to the TF-H phase, as they do not show any clear trend as

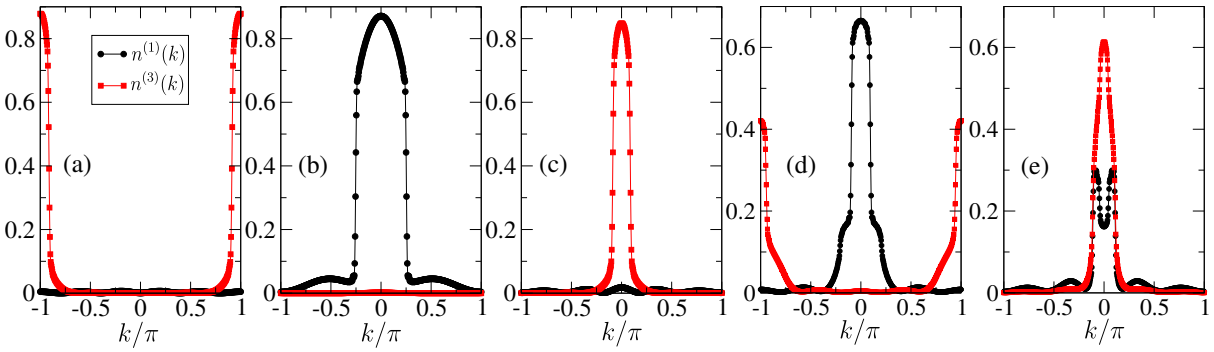

Figure 5.10: Momentum distributions $n^{(1)}(k)$ and $n^{(3)}(k)$ with OBC and $L = 96$ in (a) the T_π phase for $\frac{t'}{t} = -3.5$, in (b) the F phase for $\frac{t'}{t} = 1.0$, in (c) the T_0 phase for $\frac{t'}{t} = 3.5$, in (d) the TF-C phase for $\frac{t'}{t} = -2.7$, and in (e) the TF-H phase for $\frac{t'}{t} = 2.9$.

the size of the system is increased. Despite not being able to identify undisputably the latter criticality, we notice that the variational prediction is hardly affected by the same increase in system size L, despite predicting the recovery of the noninteracting 2F model result. Thus, the scenario in which the 3BCS ansatz describes correctly the thermodynamic limit behavior of the ground-state properties is not to be ruled out and may be hidden by robust finite-size effects.

5.3.4 Occupation factors

We offer a final overview of the phase diagram of model (5.1) by defining the annihilation operators $\hat{F}_j^{(M)}$ for clusters of size M surrounded by two holes via the relation:

$$\hat{F}_j^{(M)} = (1 - \hat{n}_j) \left(\prod_{m=1}^{M} \hat{c}_{j+m} \right) (1 - \hat{n}_{j+M+1}), \tag{5.28}$$

aimed at characterizing the properties of unbound fermions for $M = 1$ and isolated trimers for $M = 3$. Using DMRG, we can access the corresponding momentum distribution, or occupation factor, through:

$$n^{(M)}(k) = \sum_{j,j'} e^{-ik(j-j')} \langle \hat{F}_j^{(M)\dagger} \hat{F}_{j'}^{(M)} \rangle, \tag{5.29}$$

obtained from the corresponding two-point correlators.

Firstly, we provide in Fig. 5.10(a-c) the functions $n^{(1)}(k)$ and $n^{(3)}(k)$ in the T_π, F and T_0 phases. While in the $T_{0,\pi}$ phases $n^{(1)}(k)$ is negligible and $n^{(3)}(k)$ demonstrates the existence of a trimer quasicondensate at $k = 0$ and $k = \pi$, respectively, the F phase displays a standard Fermi sea of unpaired fermions centered at $k = 0$ accompanied by a negligible $n^{(3)}(k)$. These signatures are in striking agreement with the reciprocal space description of the system based on the 2F model (5.4) and its refinement (5.7).

Similar considerations hold for the data presented in Fig. 5.10(d-e) for the TF-C and the TF-H phases. The TF-C phase hosts the simultaneous presence of a quasicondensate of unbound fermions around $k = 0$ and a quasicondensate of unbound trimers centered at $k = \pi$, consistently with the two-band picture suggested by the 2F model. Analogously, in the TF-H phase, the two aforesaid quasicondensated are both located around $k = 0$, as expected. Noticeably, however, in this case the function $n^{(1)}(k)$ develops a hollow around $k = 0$, where $n^{(3)}(k)$ is instead maximal. This behavior is in agreement with the structure of the 3BCS ansatz, where the filling of trimer states around $k = 0$ occurs at the expense of the annihilation of unbound fermions close to $k = 0$ and $k = \pm k_F$. This feature is more visible close to the T_0 phase, where the transition is sharp and the trimer density higher, and less visible close to the F phase.

5.4 Tetramer formation and hybridization

In the present section we extend our investigation to the model Hamiltonian (5.1) with $M = 4$, expected to induce tetramer formation at sufficiently strong coupling. The structure of the phase diagram in its

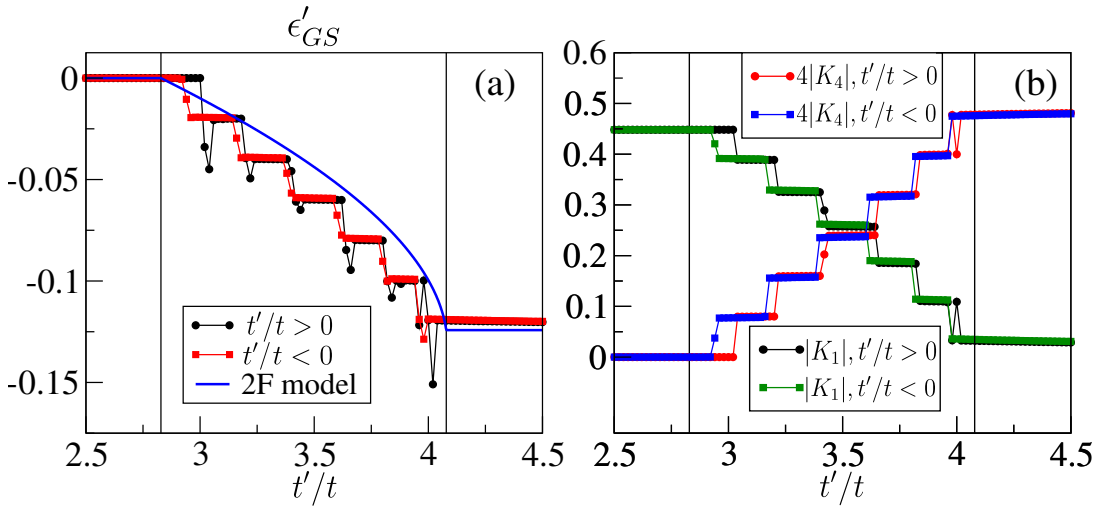

Figure 5.11: Energy observables in the ground-state of (5.1) with $M = 4$ on a lattice with $L = 96$ sites as a function of $\left|\frac{t'}{t}\right|$ for both $t' \leq 0$ and $t' \geq 0$. Vertical lines are transition points predicted by the generalized 2F model (5.4). (a) First derivative of the energy density with respect to $\frac{t'}{t}$ from DMRG and 2F model (5.4). (b) Single-particle and tetramer kinetic energy densities K_1 and $4K_4$.

limiting regimes is analogous to the ones found in the $M = 2$ and $M = 3$ cases, as it features a regular Luttinger liquid phase extending around the noninteracting point $t' = 0$ and two tetramer Luttinger liquid phases for $|t'| \gg t$, where $G(r)$, $P(r)$ and $T(r)$ decay exponentially, while $M(r) = \langle \hat{M}_j^\dagger \hat{M}_{j+r} \rangle$ displays quasi-long-range order.

In order to elucidate the nature of the transitions between the aforementioned limiting phases, we introduce the total single-particle kinetic energy density:

$$K_1 = \frac{1}{L} \sum_j \langle \hat{c}_j^\dagger \hat{c}_{j+1} + H.c. \rangle \tag{5.30}$$

and the total tetramer kinetic energy density:

$$K_4 = \frac{1}{L} \sum_j \langle \hat{M}_j^\dagger \hat{M}_{j+1} + H.c. \rangle. \tag{5.31}$$

Superimposing the numerical data for K_1 and K_4 obtained for $\frac{t'}{t} < 0$ and $\frac{t'}{t} > 0$, we observe in Fig. 5.11(b) a remarkable agreement between the two, contrarily to the case of pairs [26, 110, 111] and trimers [159]. Moreover, such a result strongly suggests the presence of an emergent symmetry between the ground-state properties for $\frac{t'}{t} < 0$ and the ones for $\frac{t'}{t} > 0$. Similar considerations hold in the case of the first derivative of the ground-state energy density, plotted in Fig. 5.11(a), that further displays a remarkable quantitative agreement with its prediction according to model (5.4) with $M = 4$. We conclude therefore that the F phase is separated from both tetramer phases by a coexistence phase delimited by critical points associated to second-order Lifschitz transitions.

The suppression of the effects of interspecies interactions as the molecule size M increases, even when both species quasicondense around momentum $k = 0$, can be explained heuristically in at least two distinct ways. A first qualitative argument that supports this observation relies on realizing that the larger the molecule, the higher is the order in perturbation theory to split it into M unbound fermions. A second, more quantitative observation supports an emergent $t' \to -t'$ symmetry at the level of Hamiltonian (5.1). Indeed, by highlighting the dependence of Hamiltonian (5.1) on the multimer size M, t and t' via the identification $\hat{H} \equiv \hat{H}_M(t, t')$, we see that the unitary transformation $\hat{c}_j \to e^{i\frac{\pi}{M}j}\hat{c}_j$ transforms $\hat{H}_M(t, t')$ into $\hat{H}_M(e^{i\frac{\pi}{M}}t, -t')$. In the limit of large molecules $M \to +\infty$, the phase factor multiplying t tends to 1, connecting $\hat{H}_M(t, t')$ to $\hat{H}_M(t, -t')$. Since the coexistence phase is the generic scenario at low density when molecules quasi-condense at $k = \pi$, the same is expected for quasi-condensation at $k = 0$ on the opposite side.

5.5 Conclusions

In the present chapter, we have generalized the results obtained in Refs. [26, 110, 111] to the case of the class of Hamiltonians consisting of a single-particle hopping term and a correlated multimer-hopping term. The detailed treatment of the case of trimers allowed for the observation of two remarkable coexistence phases between unbound fermions and trimers. While in one of them the interspecies interactions are suppressed, in the other one they noticeably affect the finite-size properties of the system and are interpreted within a BCS-like variational approach to a phenomenological two-fluid model. The investigation ends with the generalization of this scenario to the case of larger molecular bound-states of spinless fermions, where the existence of two coexistence phases of unbound fermions and multimers with increasingly suppressed interspecies interactions shows to be a general feature of this class of Hamiltonians.

The proven success of two-fluid phenomenological approaches in the study of bound-state formation in systems of spinless fermions provides a new set of interpretative ideas and technical tools that are expected to shed further light on the properties of experimentally relevant Hamiltonians for which multimer formation has been predicted [28]. The possibility of having a direct transition between fermionic and trimer phases remains an open question in these models. Moreover, the two-fluid pictures may be instrumental in extending such results to bosonic and/or higher-dimensional systems, so as to probe the robustness of the unveiled paradigm of quantum coexistence to the change in statistics and system's dimensionality.

Chapter 6

Pairing and many-body scars in a chain of spinless fermions

In the present chapter, we present preliminary results on the study of quantum many-body scars of spinless η-pairs in a system of spinless fermions. After a general introduction to the problem of thermalization in isolated quantum many-body systems, we introduce the model Hamiltonian and identify a subset of its eigenstates that can be characterized as condensates of spinless η-pairs and are shown to exhibit the phenomenology of many-body scars. We obtain several exact results concerning the algebraic structure that underlies the fact that these form a tower of energetically equally-spaced energy eigenstates and evaluate the consequence of this spectral property of the Hamiltonian on the dynamics of specific initial states. Moreover, we show that these eigenstates obey a logarithmic entanglement entropy scaling law, contrarily to the expected volume-law scaling of thermal states. We conclude by providing numerical signatures of the atypicality of the spinless η-pairing states via numerical probes such as the level-spacing statistics, the Loschmidt echo dynamics and the half-chain entanglement entropy.

6.1 Introduction

A fundamental question in the study of quantum many-body systems is the emergence of macroscopic thermodynamics from the microscopic unitary evolution of quantum-mechanical systems. In order to better understand this problem, let us consider an initial state $|\psi(0)\rangle$ at a given average energy density with a subextensive energy variance, as it is typically required for thermodynamical statistical ensembles. Then, a quantum system without additional symmetries is said to be *ergodic* or *thermal* if, for any such initial state, the reduced density matrix $\rho_A(t)$ relative to a small subsystem A evolves at late times to a density matrix that is locally indistinguishable from the Gibbs density matrix, i.e.:

$$\lim_{t\to+\infty} \rho_A(t) = \mathrm{Tr}_{\bar{A}}\left(\rho_{eq}\right), \qquad \rho_{eq} = \frac{e^{-\beta \hat{H}}}{Z}, \tag{6.1}$$

where β is an inverse temperature defined by the energy density of the initial state, Z is the corresponding partition function and $\bar{A}$ is the complement of A. We stress here the fact that the notion of thermalization is a local one: globally, it will always be possible to tell apart the state $|\psi(t)\rangle$ from ρ_{eq}.

A sufficient condition to guarantee thermalization in a many-body quantum system is the eigenstate thermalization hypothesis (ETH) [190, 191, 192, 193], which asserts that each eigenstate of a many-body Hamiltonian is thermal, i.e., it satisfies the condition expressed in Eq. (6.1). This implies, among other features, that highly-excited states of ergodic systems exhibit a volume-law scaling of the entanglement entropy of a subsystem, as the effective inverse temperature $\beta \to 0^+$ when eigenstates in the middle of the spectrum are considered. The reduced density matrix of subsystem A approximates as a result the trivial density matrix $\frac{1}{d}\mathbb{I}_d$, where d is the dimension of the Hilbert space $\mathcal{H}_A$ relative to subsystem A and leads to an entanglement entropy scaling as $\log d$. Since $d = d_{loc}^{|A|}$, where $|A|$ is the size of subsystem A and d_{loc} is the dimension of the local Hilbert space at a single lattice site, a volume-law scaling is recovered.

The strategies towards the discovery of systems lacking standard thermalization under unitary time evolution have relied on the presence of an extensive number of integrals of motion, thereby enforcing

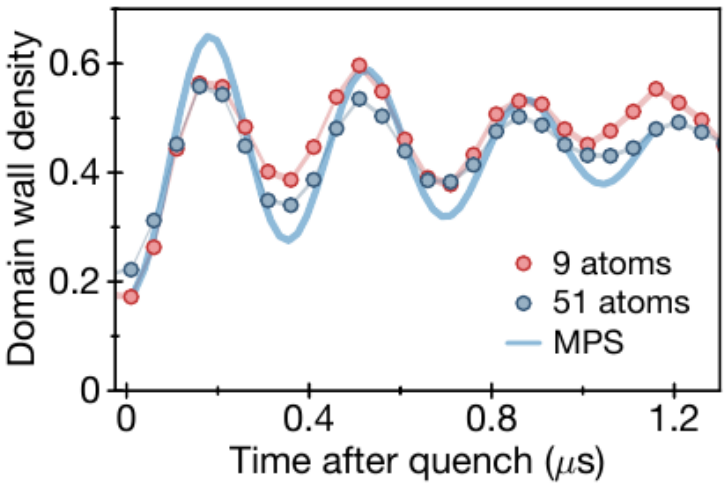

Figure 6.1: After Ref. [14]. Domain-wall density after the quench. The dynamics decay slowly on a timescale of 0.88 μs. Shaded region represents the standard error of the mean. Solid blue line is a fully coherent matrix product state (MPS) simulation with bond dimension D = 256, taking into account measurement fidelity.

the time-evolved state to retain memory of its initial configuration. The two representatives of the aforesaid route towards ETH-breaking are fine-tuned one-dimensional Bethe-ansatz integrable systems, featuring an extensive set of global conserved quantities [194, 195, 196, 197, 198, 199, 200, 201], and strongly disordered systems, where the phenomenon of many-body-localization has been explained by introducing the idea of local integrals of motion [202, 203, 204, 205, 206, 207, 208, 209, 210].

More recently, a novel form of weak ETH-breaking has been introduced. It occurs when the Hamiltonian possesses a measure-zero set of highly-excited eigenstates that display atypical features that are incompatible with the ETH fulfilled by other eigenstates at the same energy density. These states are referred to as *quantum many-body scars* [211, 212, 213, 214]. Despite such eigenstates represent a vanishingly small fraction of the Hilbert space dimension, quantum many-body scars were observed to generate measurable signatures of their existence in the dynamics of certain simple product initial states studied in Rydberg-atom experiments [14] (see Fig. 6.1).

The reason for this phenomenology is rooted in the typical algebraic structure that is generated by these states, which is named restricted spectrum-generating algebra (RSGA) [24]. Let us consider a system described by a Hamiltonian $\hat{H}$. A quasiparticle creation operator $\hat{Q}^\dagger$ provides a RSGA if there exists a linear subspace W that is invariant under the action of $\hat{Q}^\dagger$ such that:

$$\left([\hat{H}, \hat{Q}^\dagger] - \omega \hat{Q}^\dagger\right) W = 0 \tag{6.2}$$

and an eigenstate $|\psi_0\rangle \in W$ of $\hat{H}$ with energy E_0. Then, the states $|\psi_n\rangle = \left(\hat{Q}^\dagger\right)^n |\psi_0\rangle$ are eigenstates of $\hat{H}$ with energy $E_n = E_0 + n\hbar\omega$, as long as they do not vanish. The aforementioned unifying formalism encompasses several instances of quantum many-body scars discussed in the literature [215, 216, 217, 218, 219, 220, 221, 221, 222, 220, 223, 224, 23, 24, 225, 226], where atypical highly-excited eigenstates form towers of equally-spaced energy eigenstates.

As a result, when one considers the time evolution of an initial state with a large overlap with scarred eigenstates, the existence of a tower of states embedded in the spectrum has dramatic consequences on the dynamics. As an example, let us consider an initial state $|\psi(0)\rangle = \sum_n c_n |\psi_n\rangle$ and compute its Loschmidt echo:

$$\mathcal{L}(t) = |\langle\psi(0)|\psi(t)\rangle|^2 = \left|\sum_n |c_n|^2 e^{-i\frac{E_n t}{\hbar}}\right|^2 = \sum_{m,n} |c_n c_m|^2 e^{i\frac{(E_m - E_n)t}{\hbar}}. \tag{6.3}$$

When the system is initialized in the subspace spanned by a tower of equally-spaced eigenstates, the energy differences $E_m - E_n$ are multiples of the energy spacing $\hbar\omega$, thus leading to a periodic Loschmidt

echo $\mathcal{L}(t)$, with period $T = \frac{2\pi}{\hbar\omega}$. Similar considerations can be carried out for the behavior of generic local observables.

Quantum many-body scars display properties that are incompatible with the paradigm of thermalization enforced by the ETH, as we now discuss by making reference to their entanglement and correlation properties. Firstly, scarred eigenstates are entanglement outliers, as they show an anomalously low entanglement content, obeying typically either a logarithmic or an area law, in contrast with the ETH prediction of a volume-law scaling. This property was crucially observed in the theoretical study of a kinetically-constrained model of Rydberg atoms Ref. [227], where it allowed for the identification of the representative properties of atypicality that qualify quantum many-body scars via the states that are responsible for the aforementioned experimental results. Moreover, quasiparticle condensates created on top of a vacuum have been shown to feature off-diagonal long-range order in 1D systems, thus representing a violation of the Mermin-Wagner theorem about thermal states. Such result is not in agreement with the ETH prediction for highly-excited eigenstates, that lie instead nominally at infinite temperature and possess a trivial thermal density matrix.

A crucial step towards the theoretical understanding of quantum many-body scars was played by η-pairing states, firstly discovered by Yang as exact excited eigenstates of the Hubbard model with off-diagonal long-range order [228]. Despite the η-pairing states not representing genuine many-body scars of the Hubbard model due to the presence of a hidden η-pairing $SU(2)$ symmetry, they display the prototypical algebraic properties of towers of scarred eigenstates, as they are generated by the repeated application of a ladder-like operator to a weakly-entangled state, and a subvolume entanglement entropy scaling law [229]. Thus, the η-pairing states have inspired several works aiming at unveiling a universal scarring mechanism allowing for the microscopic emergence of many-body scars, as well as the search for Hubbard-like Hamiltonians with η-pairing-symmetry-breaking terms that preserve analytically tractable towers of η-pairing states as genuine many-body scars [23].

In this work, we unveil the existence of an exact tower of scarred eigenstates of a spinless fermion Hamiltonian by generalizing the mechanism of η-pairing to the case of spinless fermions. Our analysis provides a further illustration of the characteristic properties of towers of scarred eigenstates studied in the literature. The scarred eigenstates are characterized by ETH-violating properties such as the logarithmic scaling of the entanglement entropy in the size of the selected subsystem [227, 230, 219, 231, 222, 23, 229] and the off-diagonal long-range order [231, 222, 232, 233, 234] in the pair correlation function. Moreover, we show how the choice of a superposition of scarred eigenstates as the initial state of the time evolution leads to periodic revivals in the expectation values of local observables [235, 231, 222]. We highlight the peculiar feature of symmetry enhancement in the scarred subspace by drawing connections to the concept of quasi-symmetry [236, 237] and its relation to many-body scar dynamics.

Despite the aforementioned phenomenology being known, we wish to highlight the aspects of our work that have not been significantly underlined in the preceding literature. Firstly, we extend pioneering results on many-body scars in spinful fermionic systems, where η-pairs represent the infinitely long-lived quasiparticles that underlie the corresponding tower of scarred eigenstates [23]. More precisely, we reveal how an analogous structure is realized in a system of spinless fermions. The extended spatial structure of the quasiparticles, namely pairs of spinless fermions, reflects itself into nonlocal expressions for the lowering operator in the scarred subspace (also discussed in Ref. [222]) and for a nontrivial conserved quantity of the many-body scar dynamics.

Moreover, we highlight the fact that our scarred states can be interpreted within the framework of macroscopic quantum coherence in the grand-canonical ensemble by constructing a close analogue of bosonic coherent states [224]. Our result differs from the one expected in the case of a purely bosonic mode as a result of the hard-core nature of the pairs.

The present chapter is organised as follows. In Section 6.2, we introduce the model Hamiltonian and discuss the structure of the interaction term. Section 6.3 is then devoted to the definition of the tower of scarred eigenstates for the Hamiltonian of interest and to the detailed analytical characterization of their spectral and entanglement properties, thereby underlining their consequences on the dynamics. Our analysis ends in Section 6.4 with the presentation of some numerical data. The conclusions are presented in Section 6.5. We mention that, while finalizing this project, another article by K. Tamura and H. Katsura [238] presented results with a significant overlap with our study.

6.2 The model

We consider the model Hamiltonian:

$$\begin{aligned}\hat{H} = &- t\sum_j \left[\hat{c}_j^\dagger \hat{c}_{j+1} + H.c.\right] - J\sum_j \left[\hat{c}_j^\dagger \hat{n}_{j+1}\hat{c}_{j+2} + H.c.\right] + \\ &- \mu\sum_j \hat{n}_j + J\sum_j \left[\hat{n}_{j+1}(\hat{n}_j + \hat{n}_{j+2}) - 2\hat{n}_j\hat{n}_{j+1}\hat{n}_{j+2}\right],\end{aligned} \tag{6.4}$$

where the fermionic creation and annihilation operators satisfy the canonical anticommutation relations $\{c_i, c_j\} = 0$ and $\{\hat{c}_i, \hat{c}_j^\dagger\} = \delta_{i,j}$. The hopping amplitude is t, μ is the chemical potential and J is the pair-hopping amplitude, associated to the motion of two neighboring particles; J is also the parameter of different forms of density-density interactions. We take $J > 0$ and $t > 0$. This kind of correlated pair-hopping has been recently studied in a variety of works and is responsible for several phenomena related to pairing [140, 142, 26, 110, 111, 159]. The Hamiltonian commutes with the total number of particle operator $\hat{N} = \sum_j \hat{n}_j$. Through this article, for simplicity, we always assume L and N to be even and we take open boundary conditions if not explicitly mentioned. To ease readability, we write explicitly the bounds of summation only when they are non-trivial.

6.3 Exact results and towers of states

We now discuss a set of scarred eigenstates for $\hat{H}$. In order to do so, we define the tower of states for $k \in \{0, 1, \dots L/2\}$:

$$|\psi_{k,\pi}\rangle = \frac{1}{\sqrt{\binom{L-k}{k}}}\frac{(\hat{\eta}_\pi^\dagger)^k}{k!}|0\rangle\,, \quad \text{with } \hat{\eta}_\pi^\dagger = \sum_j (-1)^j \hat{c}_j^\dagger \hat{c}_{j+1}^\dagger. \tag{6.5}$$

This set of states is the closest analogue of η-pairing in a spinless fermionic setup as they represent a condensate of pairs at the edge of the first Brillouin zone with fixed number of pairs k (and thus number of fermions $N = 2k$).

The normalization factor follows from combinatorial considerations. Indeed, given N fermions on a lattice of size L, one can map each fermionic configuration where particles form even-sized clusters to a spin configuration with k spin-up states on a spin chain of size $L - k$ via the rules $|\bullet\bullet\rangle \to |\uparrow\rangle\,, |\circ\rangle \to |\downarrow\rangle$. Then, the number of fully-paired fermionic configurations on the original lattice equals the number of ways of distributing k spins-up on a chain of length $L - k$, which is $\binom{L-k}{k}$.

The states introduced in Eq. (6.5) form a tower of energetically equally-spaced eigenstates of $\hat{H}$, satisfying the eigenvalue equation:

$$\hat{H}\,|\psi_{k,\pi}\rangle = -2\mu k\,|\psi_{k,\pi}\rangle\,. \tag{6.6}$$

This result is explicitly derived in Appendix A.1; very briefly, it follows from the destructive interference of the single fermions when single-particle hopping breaks a pair into two fermions (similar mechanisms have been also highlighted in other models, e.g. spin-1 models [239]).

Moreover, the $|\psi_{k,\pi}\rangle$ satisfy the standard restricted spectrum-generating algebra (RSGA) typical of the tower of states:

$$[\hat{H}, \eta_\pi^\dagger]\,|\psi_{k,\pi}\rangle = -2\mu\eta_\pi^\dagger\,|\psi_{k,\pi}\rangle\,, \tag{6.7}$$

and as such they fit exactly in the standard theory of exact many-body scars with linearly-separated energies. Additionally, the states $|\psi_{k,\pi}\rangle$ are the exact frustration-free ground states of the Hamiltonian $\hat{H}_J = +(J/2)\sum_j L_j^\dagger L_j$ for $J > 0$, where

$$\hat{L}_j = \hat{n}_j\hat{n}_{j+1} - \hat{n}_{j+1}\hat{n}_{j+2} + \hat{c}_{j+2}^\dagger \hat{n}_{j+1}\hat{c}_j - \hat{c}_j^\dagger \hat{n}_{j+1}\hat{c}_{j+2}, \tag{6.8}$$

which corresponds to the part proportional to J of the model in Eq. (6.4). Thus, we can interpret them as scars obtained by deforming a frustration-free non-integrable model, the deformation being obtained by adding the single-particle hopping and the chemical potential.

The fact that pairs located at momentum π are eigenstates of the Hamiltonian means that they can be thought of as quasiparticles with infinite lifetime; the equal energy spacing is instead associated to the fact that they are not interacting (see Appendix A.2 for a coordinate Bethe Ansatz argument supporting

the latter observation). It is enough to assume $t \gg |\mu|$ to place them in the middle of the spectrum of $\hat{H}$, of which they become exact eigenstates that lie at an extensive energy above the ground-state one.

It is not difficult to observe that the $|\psi_{k,\pi}\rangle$ feature off-diagonal long-range order; let us introduce:

$$P_k(r) = \langle \psi_{k,\pi} | \hat{c}_j^\dagger \hat{c}_{j+1}^\dagger \hat{c}_{j+r} \hat{c}_{j+r+1} | \psi_{k,\pi} \rangle , \tag{6.9}$$

to denote the pair correlation function evaluated on the state $|\psi_{k,\pi}\rangle$. Then, taking periodic boundary conditions and the thermodynamic limit at fixed density $n = 2k/L$, we obtain

$$\lim_{L\to\infty} P_k(r) = (-1)^{r+1} \frac{n}{2-n} (1-n)^2, \tag{6.10}$$

with $r > 3$. The explicit formula at finite size is given in Appendix A.3. This observation alone is sufficient to motivate the fact that they are exceptional in the spectrum of the Hamiltonian, as they violate the Mermin-Wagner theorem about thermal states in one dimension. As a further proof, we will later also discuss the fact that the entanglement entropy of these states grows logarithmically with the subsystem length, instead of linearly, as it is typically expected for thermal states.

6.3.1 Algebraic properties

As mentioned, the operators $\hat{\eta}_\pi^\dagger$ realise a RSGA in the subspace $\mathcal{S}$ spanned by the $|\psi_{k,\pi}\rangle$. Indeed, the commutator $[\hat{H}, \hat{\eta}_\pi^\dagger]$ reads:

$$[\hat{H}, \hat{\eta}_\pi^\dagger] = -2\mu \hat{\eta}_\pi^\dagger + \hat{O}, \tag{6.11}$$

where the explicit expression for $\hat{O}$ is given in Appendix A.4. There, we also show that the states $|\psi_{k,\pi}\rangle$ belong to the kernel of $\hat{O}$. Therefore, Eq. (6.7) is satisfied and, in turn, the eigenvalue equation (6.6) is proven in a way that is different from that presented in Appendix A.1.

More interestingly, we observe peculiar consequences of the spatial structure of the pairs when considering a lowering operator $\hat{\eta}'_\pi$ satisfying $\hat{\eta}'_\pi |\psi_{k,\pi}\rangle \propto |\psi_{k-1,\pi}\rangle$ for $k \geq 1$ and $\hat{\eta}'_\pi |\psi_{k=0,\pi}\rangle = 0$. The naive guess $\hat{\eta}'_\pi = \hat{\eta}_\pi$ fails, as one can notice by studying the explicit case $k = 2, L = 4$:

$$\hat{\eta}_\pi |\psi_{2,\pi}\rangle = \hat{\eta}_\pi |\bullet\bullet\bullet\bullet\rangle = |\bullet\circ\circ\bullet\rangle - |\circ\circ\bullet\bullet\rangle - |\bullet\bullet\circ\circ\rangle , \tag{6.12}$$

where the filled dots indicate occupied sites, while empty dots denote empty sites. As one can infer from Eq. (6.12), the action of $\hat{\eta}_\pi$ on $|\psi_{k,\pi}\rangle$ generates configurations with unpaired fermions as soon as $k > 1$, thus failing to reproduce the properties of a lowering operator inside the subspace $\mathcal{S}$.

In general, the explicit form of $\hat{\eta}'_\pi$ is rather complicated, we discuss here below for simplicity an expression that works if applied on states $|\psi_{k,\pi}\rangle$ for $k < L/3$, and that is non-local:

$$\hat{\eta}'_\pi = \sum_{\ell=1}^{L-1} \frac{1}{\ell} \sum_{m=0}^{L-1} \frac{e^{2\pi i \frac{m(\ell-\hat{C})}{L}}}{L} \sum_{j=1}^{L-1} e^{-i\pi j} \hat{P}^{(j-1)} \hat{c}_{j+1} \hat{c}_j. \tag{6.13}$$

In Eq. (6.13), the operator $\hat{C} = \sum_{j=1}^{L-1} (1-\hat{n}_j)(1-\hat{n}_{j+1})$ counts the number of consecutive sites that are empty and the sum over m represents a Kronecker delta that selects the value of ℓ that is equal to the eigenvalue of the operator $\hat{C}$. The two operators $\hat{c}_{j+1}\hat{c}_j$ annihilate a pair at sites j and $j+1$ and the projectors $\hat{P}^{(j-1)}$ check that the site j is preceded by an even number of occupied sites and otherwise they annihilate the Fock state. Comparing with the sketch in Eq. (6.12), this term has the goal of avoiding that the unpaired configuration $|\bullet\circ\circ\bullet\rangle$ is generated from the initial state $|\bullet\bullet\bullet\bullet\rangle$. It is possibly interesting to observe that there is a recursion relation obeyed by the projectors:

$$\begin{aligned} \hat{P}^{(0)} &= 1, \\ \hat{P}^{(s)} &= 1 - \hat{n}_s \hat{P}^{(s-1)}, \quad 1 \leq s \leq L. \end{aligned} \tag{6.14}$$

We claim that $\hat{\eta}'_\pi |\psi_k\rangle \propto |\psi_{k-1,\pi}\rangle$. Indeed, if one can show that each of the configurations contributing to the state $|\psi_{k-1,\pi}\rangle$ appears in the expression of the state $\hat{\eta}'_\pi |\psi_k\rangle$ with a unit coefficient (apart from overall normalization factors), then the proof is concluded. Consider any fully-paired Fock state $|c\rangle$ contributing to the state $|\psi_{k-1,\pi}\rangle$. The latter is generated whenever $\hat{\eta}'_\pi$ acts on a configuration contributing to $|\psi_{k,\pi}\rangle$ that can be obtained by adding a pair to the target configuration in $|\psi_{k-1,\pi}\rangle$. The number of such configurations with k pairs equals the expectation value of $\hat{C}$ over the target configuration $|c\rangle$. Therefore, by dividing each contribution that results in $|c\rangle$ by the number of configurations in $|\psi_{k,\pi}\rangle$ that $|c\rangle$ can be reached by, one gets the desired result. This last operation is implemented by the operator expression that precedes the summation over the lattice sites in Eq. (6.13).

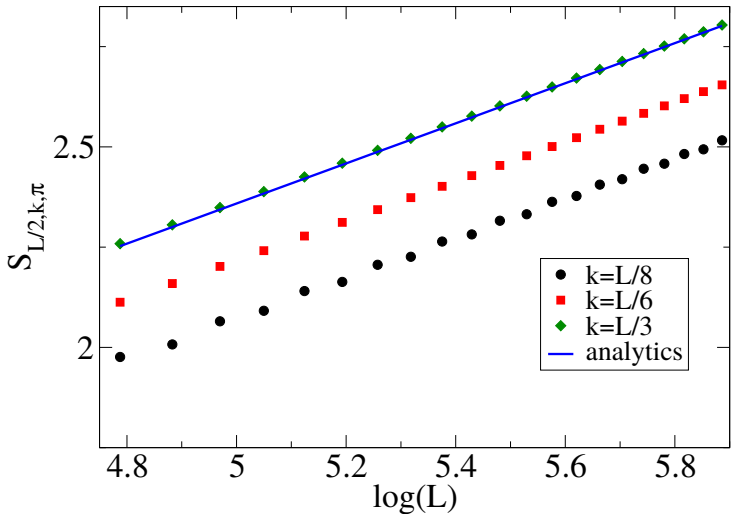

Figure 6.2: Half-chain entanglement entropy of the states $|\psi_{k,\pi}\rangle$ for fillings $n = 2k/L = 1/4,\ 1/3,\ 2/3$ according to Eq. (6.26) as a function of the logarithm of the system size (dots). The blue line is given by the asymptotic expression in Eq. (6.27).

6.3.2 Quasi-symmetries

In this Section we draw connections with the quasi-symmetry picture of many-body scar subspaces [236]. Since the spinless η-pairing states $|\psi_{k,\pi}\rangle$ that generate $\mathcal{S}$ are characterized by infinitely long-lived pair quasiparticles, we infer that the total number of pairs $\hat{N}_p$ is a conserved quantity under time evolution within $\mathcal{S}$. Its explicit form is once more nonlocal, and reads:

$$\hat{N}_p = \sum_{j=1}^{L-1} \hat{P}^{(j-1)} \hat{n}_j \hat{n}_{j+1}. \tag{6.15}$$

The quasi-symmetry property amounts then to the statement that:

$$\hat{U}_\theta \hat{H} \hat{U}_\theta^\dagger |_{\mathcal{S}} = \hat{H}|_{\mathcal{S}}, \tag{6.16}$$

where $\hat{U}_\theta = e^{i\theta \hat{N}_p}$ is a unitary representation of $U(1)$. We conclude that the subspace $\mathcal{S}$ enjoys a nontrivial $U(1)$ quasi-symmetry linked to the infinite lifetime of the η-pairs. Similar considerations can be carried out in the case of the operator $\hat{N}_{stag} = \sum_{j=1}^{L} (-1)^j \hat{n}_j$, which gives rise to an additional $U(1)$ quasisymmetry of the subspace S via the unitary representation $\hat{U}_\varphi = e^{i\varphi \hat{N}_{stag}}$, which enjoys the properties of being a tensor product representation over the Hilbert spaces attached to the lattice sites.

We underline that, according to the definition of quasi-symmetry of a degenerate subspace [236], the unitary representations are required to be tensor product representations over the Hilbert spaces attached to the lattice sites, in order to avoid including complicated transformations without a transparent physical meaning in the definition. While the latter condition is met by the unitary $\hat{U}_\varphi$, it is not satisfied by $\hat{U}_\theta$. However, given the clear physical meaning of the generator $\hat{N}_p$, we choose to include it in the discussion.

6.3.3 Dynamics and quantum coherence

The consequences of Eq. (6.6) on the dynamics of a generic superposition of the states $|\psi_{k,\pi}\rangle$ are easily computed. For an initial state of the form:

$$|\psi(0)\rangle = \sum_{k=0}^{L/2} m_k \, |\psi_{k,\pi}\rangle \, , \quad \sum_k |m_k|^2 = 1, \tag{6.17}$$

the Loschmidt echo takes the form:

$$\mathcal{L}(t) = |\, \langle \psi(0) | \psi(t) \rangle \,|^2 = \left| \sum_k^{L/2} |m_k|^2 e^{i \frac{2\mu k}{\hbar} t} \right|^2 , \tag{6.18}$$

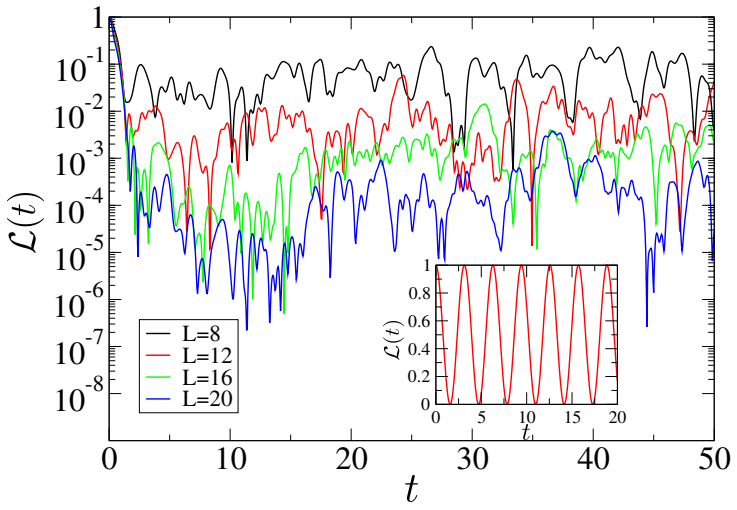

Figure 6.3: Loschmidt echo $\mathcal{L}(t)$ of the time-evolved state $|\psi(t)\rangle$ as a function of the elapsed time t for $t = 1$, $J = 2$, $\mu = -1$, when starting from a product state $|\psi_2\rangle$, see text. Inset: Loschmidt echo $\mathcal{L}(t)$ for a superposition of scarred eigenstates $|\psi_1\rangle$, see text.

and is periodic with period $T = |\pi\hbar/\mu|$. Coherently with the interpretation of the states $|\psi_{k,\pi}\rangle$ as condensates of pairs, we find here that their time evolution is dictated by the chemical potential μ [240].

The time evolution of the expectation value of an operator is also easily computed. We take $\hat{c}_j\hat{c}_{j+1}$ as an example of operator that has matrix elements between states whose number of pairs differs by one; assuming periodic boundary conditions and odd L for simplicity, the dynamics of its expectation value reads:

$$\langle\psi(t)|\hat{c}_j\hat{c}_{j+1}|\psi(t)\rangle = (-1)^{j+1}e^{i\frac{2\mu t}{\hbar}}\sum_{k=0}^{\lfloor L/2\rfloor-1}\frac{m_k^* m_{k+1}\binom{L-2-k}{k}}{\sqrt{\frac{L}{L-k}\binom{L-k}{k}\frac{L}{L-k-1}\binom{L-k-1}{k+1}}}, \tag{6.19}$$

and exhibits a periodic oscillating behaviour. The complicated coefficients in terms of binomial appearing inside the summation take an easier expression when we consider the thermodynamic limit at fixed density $n = 2k/L$. Noticeably, in agreement with Eq. (6.10), it is easy to show that:

$$\lim_{L\to\infty}\langle\psi_{k,\pi}|\,\hat{c}_j\hat{c}_{j+1}\,|\psi_{k+1,\pi}\rangle = (-1)^{j+1}\sqrt{\frac{n}{2-n}}(1-n), \tag{6.20}$$

which allows to conclude that the thermodynamic limit of the pair correlation function, $\lim_{L\to\infty}P_k(r)$, equals

$$\lim_{L\to\infty}\langle\psi_{k+1,\pi}|\,\hat{c}_j^\dagger\hat{c}_{j+1}^\dagger\,|\psi_{k,\pi}\rangle\,\langle\psi_{k,\pi}|\,\hat{c}_{j+r}\hat{c}_{j+r+1}\,|\psi_{k+1,\pi}\rangle \tag{6.21}$$

when $r > 3$. Once more, this expression certifies that the states $|\psi_{k,\pi}\rangle$ feature off-diagonal long-range order.

If the states $|\psi_{k,\pi}\rangle$ can be considered as many-body states with macroscopic coherence and fixed number of particles, states of the form (6.17) can be used to discuss the macroscopic quantum coherence in the more usual grand-canonical ensemble. We can introduce the α states

$$|\alpha\rangle = \mathcal{N}_\alpha\, e^{\alpha\hat{\eta}_\pi^\dagger}\,|0\rangle\,, \qquad \alpha\in\mathbb{C} \tag{6.22}$$

where $\mathcal{N}_\alpha$ is a normalization constant, and by applying the time-evolution operator on $|\alpha\rangle$, one can easily verify that they remain of the same form, and that the parameter α obeys the time-evolution relation:

$$\alpha(t) = e^{i\frac{2\mu}{\hbar}t}\,\alpha(0). \tag{6.23}$$

It is tempting to interpret the α states as the coherent states of a quantum harmonic oscillator, but we stress that even if we assume infinite size, the $\hat{\eta}_\pi$ and $\hat{\eta}_\pi^\dagger$ do not satisfy the canonical commutation relation, and for instance $\hat{\eta}_\pi\,|\alpha\rangle \neq \alpha\,|\alpha\rangle$. This follows from the considerations presented above on the algebraic properties of the $\hat{\eta}_\pi^{(\dagger)}$.

The oscillatory behavior of the coherence parameter α demonstrates transparently that the state $|\alpha\rangle$ returns to itself after a period T and naturally translates into periodic oscillations in the time evolution of suitably chosen local observables, as demonstrated more generally in Eq. (6.19).

We probe the macroscopic coherence of the state $|\alpha\rangle$ by evaluating the expression in Eq. (6.19) for the choice $|\psi(t)\rangle = |\alpha(t)\rangle$. The result takes the following form in the limit $L \to +\infty$ (see Appendix A.5):

$$\langle\alpha(t)|\, e^{i\pi j}\hat{c}_{j+1}\hat{c}_j\, |\alpha(t)\rangle = \frac{2\,\alpha(t)}{\sqrt{1+4|\alpha|^2}\left(1+\sqrt{1+4|\alpha|^2}\right)}. \tag{6.24}$$

While for small values of α the result reproduces the value obtained for the coherent state obtained from a single bosonic mode, the term in the denominator of Eq. (6.24) corrects the result for larger values of α and arises from the hard-core nature of the pairs that populate the system.

6.3.4 Entanglement

In this subsection we compute the scaling of the entanglement entropy of the $|\psi_{k,\pi}\rangle$ for a bipartition of the system into two halves of length $L/2$. We show that they are entanglement outliers, as they display a logarithmic scaling of the half-chain entanglement entropy. To this end, we consider the density matrix $\rho_{k,\pi} = |\psi_{k,\pi}\rangle\langle\psi_{k,\pi}|$ on a system with L sites and we aim to compute the reduced density matrix for the first $\frac{L}{2}$ sites, i.e., $\rho_{k,\pi}^{\left(\frac{L}{2}\right)} = \mathrm{Tr}_{\left[\frac{L}{2}+1,\ldots,L\right]}(\rho_{k,\pi})$. We choose for simplicity the second Renyi entropy, which is defined as follows:

$$S_{\frac{L}{2},k,\pi} = -\log\left\{\mathrm{Tr}\left[\left(\rho_{k,\pi}^{\left(\frac{L}{2}\right)}\right)^2\right]\right\}. \tag{6.25}$$

An analytical generic formula for any k can be obtained in terms of binomial coefficients, and reads:

$$S_{\frac{L}{2},k,\pi} = -\log\left\{\sum_{l=max\{0,\lceil\frac{N-L/2}{2}\rceil\}}^{min\{\frac{N}{2},\lfloor\frac{L/2}{2}\rfloor\}}\left(\frac{\binom{\frac{L}{2}-\frac{N}{2}+l}{\frac{N}{2}-l}\binom{\frac{L}{2}-l}{l}}{\binom{L-\frac{N}{2}}{\frac{N}{2}}}\right)^2 + \sum_{l=max\{0,\lceil\frac{N-L/2-1}{2}\rceil\}}^{min\{\frac{N}{2}-1,\lfloor\frac{L/2-1}{2}\rfloor\}}\left(\frac{\binom{\frac{L}{2}-\frac{N}{2}+l}{\frac{N}{2}-l-1}\binom{\frac{L}{2}-1-l}{l}}{\binom{L-\frac{N}{2}}{\frac{N}{2}}}\right)^2\right\}. \tag{6.26}$$

A more readable analytical expression can be found taking the thermodynamic limit $L \to \infty$ and $k \to \infty$ and fixing the ratio $2k/L = n = 2/3$. In this limit, in Appendix A.6 we show that the formula is well approximated by:

$$S_{\frac{L}{2},k=\frac{L}{3},\pi} \xrightarrow{L\to\infty} \frac{1}{2}\log\left(\frac{6\pi L}{25}\right). \tag{6.27}$$

For more clarity, we have evaluated the resulting entanglement entropy scaling law in Fig. 6.2, where the analytical prediction in Eq. (6.26) is plotted as a function of $\log L$ for several choices of the system filling, i.e., of the number of pairs. The figure confirms the agreement with the scaling for $n = 2/3$ in Eq. (6.27) and demonstrates a scaling as $\log L$ for other filling choices. As already mentioned, a logarithmic scaling of the entanglement entropy signals a non-ETH state, and shows the exceptional character of the $|\psi_{k,\pi}\rangle$.

6.4 Numerical analysis

We proceed by providing numerical benchmarks of the scarred eigenstates discussed in the previous sections by performing exact diagonalization simulations with the QuSpin package [241, 242]. We start by presenting the behaviour of the Loschmidt echo $\mathcal{L}(t)$ when the system is initialized either in the superposition of scarred eigenstates $|\psi_1\rangle = \frac{1}{\sqrt{2}}\left(|\psi_{1,\pi}\rangle + |\psi_{2,\pi}\rangle\right)$ or in the generic product states $|\psi_2\rangle = \prod_{j=1}^{L/4}\hat{c}_{2j}^\dagger\,|0\rangle$. The data presented in Fig. 6.3 show that, while the superposition of scarred eigenstates shows exact revivals, as predicted exactly via Eq. (6.18), the coherent dynamics of a generic product state displays a phenomenology that is consistent with the loss of memory of the initial state, as generically expected for a thermalizing isolated many-body quantum system. The data confirm therefore that the revivals associated to the existence of an exact tower of states embedded in the spectrum is atypical and not observed when the dynamics of a generic intial state is monitored.

A further check is provided by plotting the half-chain entanglement entropy of a system described by Hamiltonian (6.4) on a lattice of size $L = 16$ for $N = 6, 8, 10, 12$. The points highlighted in orange in

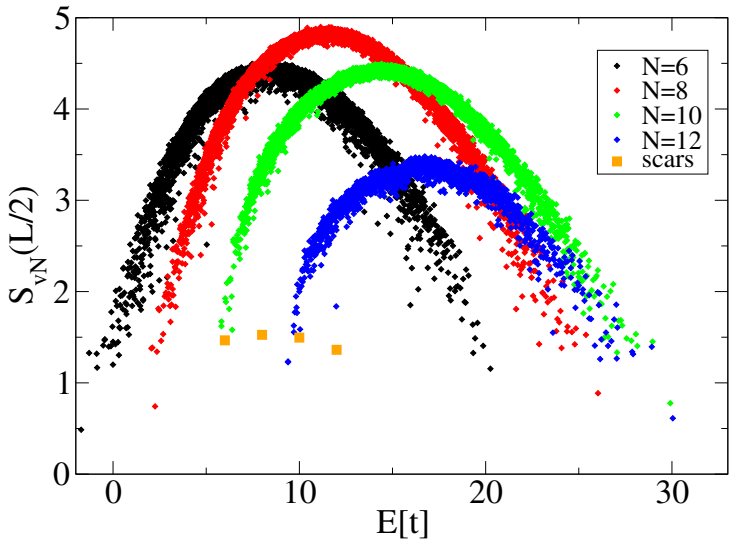

Figure 6.4: Half-chain von Neumann entanglement entropy of the eigenstates of Hamiltonian (6.4) with $t = J = 1$, $\mu = -1$ on a lattice of size $L = 16$ in the sectors with $N = 6, 8, 10, 12$ particles.

Fig. 6.4, which refer to the half-chain entanglement entropy of the scarred eigenstates $\{|\psi_{k,\pi}\rangle\}_{k=3}^{6}$, point towards the anomalously low entanglement content of the scarred eigenstates with respect to generic excited states of the model. This finding is consistent with the non-thermal nature of the unveiled quantum many-body scars and confirms their nature of exceptional states embedded in an otherwise ETH-satisfying spectrum.

We conclude this section by demonstrating the nonintegrability of Hamiltonian (6.4) by means of the study of level-spacing statistics. More specifically, we compute the probability density function of the ratio of consecutive level spacings $r_n = s_n/s_{n-1}$ [243], where $s_n = E_{n+1} - E_n$ is the difference between two consecutive energy levels E_n and E_{n+1} in the spectrum. The comparison between the numerical data and the Wigner-Dyson probability distribution for the GOE ensemble provided in Fig. 6.5 shows a neat quantitative agreement. Moreover, the average of the level-spacing ratio $\tilde{r}_n = min(s_n, s_{n-1})/max(s_n, s_{n-1})$ obtained from the numerical data equals $0.52822\ldots$, compatibly with the theoretical value $\langle\tilde{r}\rangle = 0.53590\ldots$. We are thus able to conclude that the model is not integrable.

6.5 Conclusions

In this work, we have characterized condensates of fermionic pairs as exact quantum many-body scars of a suitably chosen model Hamiltonian of a spinless fermionic chain. We have characterized exactly the spectral and entanglement properties of the tower of eigenstates responsible for their emergence, thereby proving that the latter display subvolume entanglement entropy scaling and that they are energetically equally-spaced. The aforementioned results are corroborated by the numerical analysis of the Loschmidt echo and of the half-chain entanglement entropy, which give clear evidence of the exceptional character of the dynamical properties exhibited by the scarred eigenstates. The latter are indeed atypical, as generic excited eigenstates of the model Hamiltonian are expected to possess standard thermalization properties described within the framework of ETH. Finally, the level-spacing statistics reveals that the system is not integrable and hence that the ETH-breaking involves only a measure-zero set of eigenstates of the Hamiltonian.

The unveiled results open the route towards further investigations. On one side, it will be interesting to investigate whether such a construction is amenable to generalizations to two-dimensional and, more generically, higher-dimensional setups. The spatial structure of the pair complicates the algebraic relations and makes such an extension non-trivial. On the other side, a stimulating challenge for the future would consist in devising quantum-state engineering protocols to prepare the system in the discovered scar states or in a state that is sufficiently close to it to make the revivals visible in an experiment with a quantum simulator.

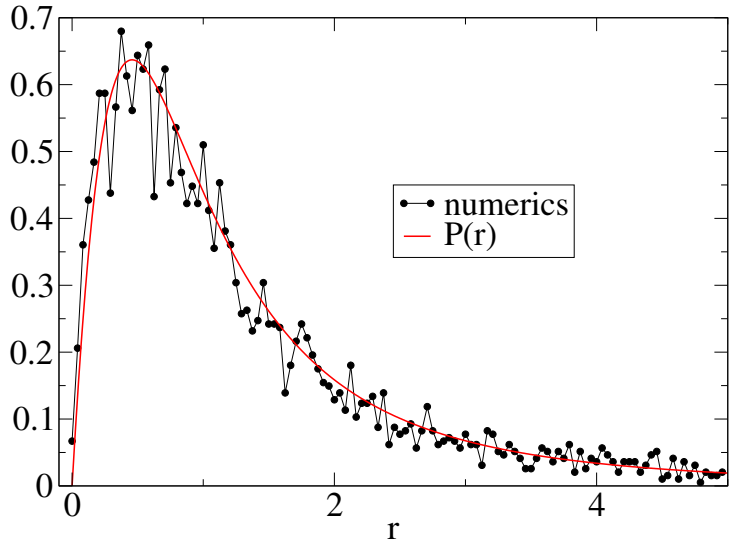

Figure 6.5: The level-spacing statistics of r_n in the middle half of the spectrum of Hamiltonian (6.4) with OBC with $t = J = 1$, $\mu = -1$ on a lattice of size $L = 18$ in the inversion symmetry sector $I = -1$ with $N = 6$ particles (black dots) compared to the Wigner-Dyson probability density function for the same quantity (red line).

Conclusion and perspectives

The focus of this thesis is the fundamental question on how spinless fermions pair in one dimension. The topic of pairing has a long-standing history in the study of the quantum many-body problem, as it lies at the foundation of topical quantum phenomena such as superconductivity and topologically-protected edge modes. Beyond the theoretical interest for their properties, these setups bear the promise of the future realization of outstanding technological achievements such as room-temperature superconductivity and topological quantum computation based on quantum coherence; it is thus natural to address this problem in 1D, where quantum correlations are enhanced.

We addressed the problem of pairing by studying the zero-temperature phase diagram of several lattice models of spinless fermions, where pairing is either induced by density-density interactions or by correlated pair-hopping processes. We captured the properties of the paired phases as well as the features of the phase transitions occurring when entering them by means of a combination of numerical DMRG simulations and analytical treatments. The outcome of our analysis unveils the two main conceptual results of our work.

Firstly, we have discovered that liquids of bound and unbound fermions can coexist in one-dimensional setups of spinless fermions. In particular, we have unveiled that such a phase can be located at the transition between a weak-coupling Luttinger liquid and a Luttinger liquid of pairs, incompatibly with the criticality observed in previous works. More precisely, we have shown in a model with correlated pair hopping that a standard Luttinger-liquid phase around the non-interacting point can be separated from a paired phase by a finite range of parameters where a liquid of unpaired fermions coexists with a liquid of pairs without hybridizing or phase-separating. This unexpected behavior is remarkably unconventional, as it cannot be interpreted straightforwardly as an instability of the single-mode Luttinger liquid describing a system of weakly interacting spinless fermions.

This observation leads directly to the second conceptual key point of our work: the systematic adoption of a two-fluid picture describing the pairing transition in spinless fermionic systems, that is simpler and more intuitive than bosonization-based approaches. In our analysis, we have interpreted this new coexistence phase on a purely phenomenological level, and we have obtained remarkably-accurate results modeling the quantum nature of the setup. In addition to its elegance and intuitive character with respect to nonstandard bosonization approaches, the remarkable microscopic observation of a phenomenology that is interpreted in light of an effective two-fluid model opens the route to the use of a new set of interpretative ideas and technical tools. As an example, we have successfully applied a two-fluid approach to the characterization of a novel phase separation between pairs and unbound fermions in presence of repulsive density-density interactions in the flat-band limit of the investigated model, thereby showing the flexibility of effective two-fluid descriptions.

Coherently with the perspective of generalizing these ideas, we have moved on to tackle models with a generic correlated multimer-hopping interaction in place of the pair-hopping one. We observe that the two-fluid picture is a powerful description of the ground-state properties of a class of Hamiltonians characterized by the kinetic formation of bound states. In particular, it allows to shed light on the mechanism leading to a new paradigm of quantum coexistence between uncoupled fermions and multimers that emerges as an intervening phase separating a weak coupling Luttinger liquid from a Luttinger liquid of molecular bound states in systems of spinless fermions.

Our results raise interesting issues that could be the object of further fruitful research activity. More specifically, a first example of such perspective activity lies in the realm of the violation of the eigenstate-thermalization hypothesis (ETH) in isolated quantum many-body systems. Beyond the standard route of

disorder, intriguing paths towards ETH violation have been the investigation of integrable systems [196, 197, 198, 199, 200, 244, 201, 194, 195], whose dynamics is constrained by the presence of an extensive number of conserved quantities, and disorder-free localization phases [245, 246, 247, 248], where the system displays nonthermal behavior purely as a result of interactions and without the need for the breaking of translational invariance.

The model Hamiltonians that we have studied provide a platform where one can systematically stabilize phases featuring the coexistence of an emergent liquid of unbound fermions with an emergent liquid of composite molecular objects given by n-particle nearest-neighbor clusters. Fascinatingly, the parameters of the system can be tuned in such a way that the liquids hybridize or not, hence allowing to explore alternative scenarios in terms of transport and relaxation properties, ideally ranging from ballistic propagation to interaction-driven slowing down of the dynamics. In the latter case, the observation of ergodicity-breaking quasi-MBL signatures of dynamical origin in the time evolution of imbalanced initial states represents a fascinating long-term goal.

A first route towards the exploration of these properties is an impurity-based quenched protocol where an isolated fermion is added to a liquid of molecules (acting as a bath for the latter) and his ensuing dynamics is monitored and characterized. Depending on the choice of parameters, the unbound fermion dynamics is expected either to show dynamical signatures of the interaction with the liquid of pairs or to provide an unconventional scenario where two emergent species with generically distinct mass do not affect their respective transport properties.

As far as equilibrium properties are concerned, many unanswered questions remain. The existence of analogous coexistence phases in the higher-dimensional counterpart of the models studied in the present thesis is to be determined to probe the robustness of the unveiled quantum coexistence to the increase in the dimensionality of the setup. Similar considerations hold for the generalization of our results to systems of bosons, in order to discuss the role of the statistics, both in one and higher dimension.

Finally, our work gives evidence of the usefulness of a more systematic application of two-fluid models in the study of bound-state formation in low-dimensional systems. For example, the full exploration of an unconventional field-theoretical description of one-dimensional quantum many-body systems based on a two-fluid picture could be a relevant direction of future research efforts. Indeed, the exploitation of the full machinery of renormalization group techniques represents a viable route towards a complete classification of the critical properties that such field theories can display and that could occur in realistic systems featuring multimer formation.

We conclude by mentioning the experimental platforms that are expected to host some of the discovered phases, such as the coexistence phase and the phase separation between pairs and unbound fermions. The most promising setups are flat-band systems, where the suppression of single-particle hopping implies that the resulting physical properties are dominated by the strong correlation effects. Correlated pair-hopping appears naturally in several instances of such systems, which therefore offer a natural route towards the experimental observation of the phenomenology associated to this class of interaction terms. In particular, we expect the emergence of the physical properties resulting from correlated pair-hopping in the Harper model for spinless fermions close to half-filling [249], where we envision such term to appear in the effective low-energy description of the states of a narrow intermediate band.

Appendix A

Appendix

A.1 Proof of Eq. (6.6)

A.1.1 Proof by direct verification

In order to assert the validity of Eq. (6.6), we consider the Hamiltonian $\hat{H}_0 = \hat{U}_0 \hat{H} \hat{U}_0^\dagger$ and prove the analogous relation:

$$\hat{H}_0 \left|\psi_{k,0}\right\rangle = -2\mu k \left|\psi_{k,0}\right\rangle . \tag{A.1}$$

Combining Eq. (A.1) and Eq. (A.59) with the definition of $\hat{H}_0$, we obtain the desired result presented in Eq. (6.6).

To this end, let us consider more explicitly the expression of $\hat{H}_0$:

$$\begin{aligned}\hat{H}_0 =& it \sum_{j=1}^{L-1} \left[\hat{c}_j^\dagger \hat{c}_{j+1} - c_{j+1}^\dagger \hat{c}_j\right] - \mu \sum_{j=1}^{L} \hat{n}_j + \\ &+ 2J \sum_{j=1}^{L-2} [\hat{n}_j \hat{n}_{j+1} + \hat{n}_{j+1}\hat{n}_{j+2} - 2\hat{n}_j \hat{n}_{j+1}\hat{n}_{j+2} + \\ &+ (\hat{c}_j^\dagger \hat{n}_{j+1} \hat{c}_{j+2} + H.c.)].\end{aligned} \tag{A.2}$$

The action of the single-particle hopping term in Eq. (A.2) on the states $\left|\psi_{k,0}\right\rangle$ can be evaluated as follows:

$$\begin{aligned}& it \sum_{j=1}^{L-1} \left[\hat{c}_j^\dagger \hat{c}_{j+1} - c_{j+1}^\dagger \hat{c}_j\right] \left|\psi_{k,0}\right\rangle = \\ &= it \left[\sum_{j=1}^{L-2} \hat{c}_j^\dagger \hat{c}_{j+1} - \sum_{j=2}^{L-1} \hat{c}_{j+1}^\dagger \hat{c}_j\right] \left|\psi_{k,0}\right\rangle = \\ &= it \sum_{j=1}^{L-2} \left[(\hat{c}_j^\dagger - \hat{c}_{j+2}^\dagger)\hat{c}_{j+1}\right] \left|\psi_{k,0}\right\rangle ,\end{aligned} \tag{A.3}$$

where we have discarded the terms $\hat{c}_2^\dagger \hat{c}_1$ and $\hat{c}_{L-1}^\dagger \hat{c}_L$ when going from the first to the second row since their action vanishes on fully paired Fock basis configurations. After the above manipulations, and denoting as $\mathcal{C}$ the set of all pair configurations contributing to the equal-weight superposition defining the state $\left|\psi_{k,0}\right\rangle$, let us evaluate:

$$\begin{aligned}&\left(\hat{c}_j^\dagger - \hat{c}_{j+2}^\dagger\right) \hat{c}_{j+1} \left|\psi_{k,0}\right\rangle = \\ &= \frac{1}{k!\sqrt{\binom{L-k}{k}}} \left[\sum_{\substack{c\in\mathcal{C}: \\ \langle\hat{n}_j\rangle=0, \\ \langle\hat{n}_{j+1}\rangle=1, \\ \langle\hat{n}_{j+2}\rangle=1}} |\cdots \bullet \circ \bullet \ldots\rangle - \sum_{\substack{c\in\mathcal{C}: \\ \langle\hat{n}_j\rangle=1, \\ \langle\hat{n}_{j+1}\rangle=1, \\ \langle\hat{n}_{j+2}\rangle=0}} |\cdots \bullet \circ \bullet \ldots\rangle \right] \\ &= 0.\end{aligned} \tag{A.4}$$

As the above relation holds for $j = 1, \dots, L-2$, one obtains:

$$it \sum_{j=1}^{L-1} \left[\hat{c}_j^\dagger \hat{c}_{j+1} - c_{j+1}^\dagger \hat{c}_j \right] |\psi_{k,0}\rangle = 0. \tag{A.5}$$

The action of the chemical potential on the states $|\psi_{k,\pi}\rangle$ is trivial, as it amounts to counting the number of particles in the given state, and reads:

$$-\mu \sum_{j=1}^{L} \hat{n}_j |\psi_{k,0}\rangle = -2\mu k |\psi_{k,0}\rangle . \tag{A.6}$$

Finally, in order to evaluate the action of the interacting term on $|\psi_{k,0}\rangle$, it is convenient to rewrite it as:

$$2J \sum_{j=1}^{L-2} [\hat{n}_j \hat{n}_{j+1} + \hat{n}_{j+1}\hat{n}_{j+2} - 2\hat{n}_j \hat{n}_{j+1}\hat{n}_{j+2} + \tag{A.7}$$

$$+ (\hat{c}_j^\dagger \hat{n}_{j+1} \hat{c}_{j+2} + H.c.)] = 2J \sum_{j=1}^{L-2} \hat{U}_0 \hat{L}_j^\dagger \hat{U}_0^\dagger \hat{U}_0 \hat{L}_j \hat{U}_0^\dagger, \tag{A.8}$$

where:

$$\hat{U}_0 \hat{L}_j \hat{U}_0^\dagger = \hat{n}_j \hat{n}_{j+1} - \hat{n}_{j+1}\hat{n}_{j+2} - \hat{c}_{j+2}^\dagger \hat{n}_{j+1} \hat{c}_j + \hat{c}_j^\dagger \hat{n}_{j+1} \hat{c}_{j+2}. \tag{A.9}$$

Hence, it suffices to prove that $\hat{U}_0 \hat{L}_j \hat{U}_0^\dagger |\psi_{k,0}\rangle = 0$. By denoting as $\mathcal{C}$ the set of all pair configurations contributing to the equal-weight superposition defining the state $|\psi_{k,0}\rangle$, we obtain:

$$\hat{U}_0 \hat{L}_j \hat{U}_0^\dagger |\psi_{k,0}\rangle = \frac{1}{k! \sqrt{\binom{L-k}{k}}} \Bigg[\sum_{\substack{c\in\mathcal{C}: \\ \langle \hat{n}_j \rangle = 1, \\ \langle \hat{n}_{j+1} \rangle = 1}} |c\rangle - \sum_{\substack{c\in\mathcal{C}: \\ \langle \hat{n}_{j+1} \rangle = 1, \\ \langle \hat{n}_{j+2} \rangle = 1}} |c\rangle + \tag{A.10}$$

$$+ \sum_{\substack{c\in\mathcal{C}: \\ \langle \hat{n}_j \rangle = 0, \\ \langle \hat{n}_{j+1} \rangle = 1, \\ \langle \hat{n}_{j+2} \rangle = 1}} |c\rangle - \sum_{\substack{c\in\mathcal{C}: \\ \langle \hat{n}_j \rangle = 1, \\ \langle \hat{n}_{j+1} \rangle = 1, \\ \langle \hat{n}_{j+2} \rangle = 0}} |c\rangle \Bigg] = 0,$$

where the final result is obtained by combining the first and last summation and the second and third summation, respectively. The result presented in Eq. (6.6) is thus proved.

A.1.2 Algebraic proof

We follow yet another, more rigorous route to prove Eq. (6.6). We aim at showing that, for $k = 0, \dots, \lfloor \frac{L}{2} \rfloor$, the following is true:

$$\left(-t \sum_{j=1}^{L-1} [\hat{c}_j^\dagger \hat{c}_{j+1} + H.c.] + J \sum_{j=1}^{L-2} \hat{L}_j^\dagger \hat{L}_j \right) |\psi_{k,\pi}\rangle = 0. \tag{A.11}$$

We start by considering the single-particle hopping term. In this case, it is straightforward to show that:

$$\left[-t \sum_{j=1}^{L-1} \left(\hat{c}_j^\dagger \hat{c}_{j+1} + H.c. \right), \hat{\eta}_\pi^\dagger \right] = -\hat{c}_1^\dagger \hat{c}_3^\dagger + \tag{A.12}$$

$$+ \sum_{j=2}^{L-2} (-1)^j \left(\hat{c}_{j-1}^\dagger \hat{c}_{j+1}^\dagger + \hat{c}_j^\dagger \hat{c}_{j+2}^\dagger \right) + (-1)^{L-1} \hat{c}_{L-2}^\dagger \hat{c}_L^\dagger = 0, \tag{A.13}$$

which trivially implies:

$$-t \sum_{j=1}^{L-1} \left(\hat{c}_j^\dagger \hat{c}_{j+1} + H.c. \right) |\psi_{k,\pi}\rangle = 0, \quad k = 0, \dots, \lfloor \frac{L}{2} \rfloor \tag{A.14}$$

On the other hand, if we denote $\hat{H}_{int} = J\sum_{j=1}^{L-2} \hat{L}_j^\dagger \hat{L}_j$, in order to prove $\hat{H}_{int}\,|\psi_{k,\pi}\rangle = 0$, we need a preparatory lemma.

Let us consider a Hamiltonian $\hat{H}$ and a set of nonzero states $\{\left(\hat{A}^\dagger\right)^k |0\rangle\}_{k=0}^N$ obtained by repeated application of the operator $\hat{A}^\dagger$ to the vacuum. Let us further define:

$$\hat{H}_0 = \hat{H}, \tag{A.15}$$
$$\hat{H}_1 = [\hat{H}, \hat{A}^\dagger], \tag{A.16}$$
$$\hat{H}_k = [\hat{H}_{k-1}, \hat{A}^\dagger],\ 2 \leq k \leq N. \tag{A.17}$$

Then, if $\hat{H}_k\,|0\rangle = 0$ for $k = 0, \ldots, N$, one has:

$$\hat{H}\left(\hat{A}^\dagger\right)^k |0\rangle = 0,\ \ k = 0, \ldots, N \tag{A.18}$$

Proof. We prove the lemma by showing by induction that:

$$\hat{H}(\hat{A}^\dagger)^n = \sum_{k=0}^{n} \binom{n}{k} (\hat{A}^\dagger)^k \hat{H}_{n-k},\ \ k = 0, \ldots, N. \tag{A.19}$$

The base case $k = 0$ is trivially verified. Thus, let us assume the result is proven for $0 \leq k \leq n$ and show that it holds as a result for $k = n + 1$ as well. We perform the following manipulations:

$$\begin{aligned}\hat{H}(\hat{A}^\dagger)^{n+1} &= \left[\sum_{k=0}^{n} \binom{n}{k} (\hat{A}^\dagger)^k \hat{H}_{n-k}\right] \hat{A}^\dagger = \sum_{k=0}^{n} \binom{n}{k} (\hat{A}^\dagger)^k \left[\hat{H}_{n+1-k} + \hat{A}^\dagger \hat{H}_{n-k}\right] = \\ &= \hat{H}_{n+1} + \sum_{k=1}^{n} \left[\binom{n}{k} + \binom{n}{k-1}\right] (\hat{A}^\dagger)^k \hat{H}_{n+1-k} + (\hat{A}^\dagger)^{n+1} \hat{H}_0 = \sum_{k=0}^{n+1} \binom{n+1}{k} (\hat{A}^\dagger)^k \hat{H}_{n+1-k},\end{aligned} \tag{A.20}$$

thus proving the result. The lemma follows trivially from the assumption that $\hat{H}_k\,|0\rangle = 0$ for $k = 0, \ldots, N$.

We wish to apply the above lemma to the hamiltonian $\hat{H}_{int}$ and the seto of states $\{(\hat{\eta}_\pi^\dagger)^k\,|0\rangle\}_{k=0}^{\lfloor \frac{L}{2} \rfloor}$. To this end, let us consider the parameter-dependent state:

$$|\psi(\alpha)\rangle = e^{\alpha \hat{\eta}_\pi^\dagger} \hat{H}_{int} e^{-\alpha \hat{\eta}_\pi^\dagger} |0\rangle\,. \tag{A.21}$$

On one hand, it can be shown that $|\psi(\alpha)\rangle = 0$ by rewriting $|\psi(\alpha)\rangle$ as:

$$\begin{aligned}|\psi(\alpha)\rangle = e^{\alpha \hat{\eta}_\pi^\dagger} \left(\sum_{j=1}^{L-2} \hat{L}_j^\dagger \hat{L}_j\right) e^{-\alpha \hat{\eta}_\pi^\dagger} |0\rangle &= \prod_{j=1}^{3} e^{\alpha (-1)^j \hat{c}_j^\dagger \hat{c}_{j+1}^\dagger} \hat{L}_1^\dagger \hat{L}_1 \prod_{j=1}^{3} e^{-\alpha (-1)^j \hat{c}_j^\dagger \hat{c}_{j+1}^\dagger} |0\rangle + \\ &+ \sum_{j=2}^{L-3} \prod_{k=j-1}^{j+2} e^{\alpha (-1)^k \hat{c}_k^\dagger \hat{c}_{k+1}^\dagger} \hat{L}_j^\dagger \hat{L}_j \prod_{k=j-1}^{j+2} e^{-\alpha (-1)^k \hat{c}_k^\dagger \hat{c}_{k+1}^\dagger} |0\rangle + \\ &+ \prod_{j=L-3}^{L-1} e^{\alpha (-1)^j \hat{c}_j^\dagger \hat{c}_{j+1}^\dagger} \hat{L}_{L-2}^\dagger \hat{L}_{L-2} \prod_{j=L-3}^{L-1} e^{-\alpha (-1)^j \hat{c}_j^\dagger \hat{c}_{j+1}^\dagger} |0\rangle\end{aligned} \tag{A.22}$$

and showing that each term in the above summation vanishes.

On the other hand, the Baker-Campbell-Hausdorff formula allows to express the latter as:

$$|\psi(\alpha)\rangle = \hat{H}_{int}\,|0\rangle + \alpha[\hat{\eta}_\pi^\dagger, \hat{H}_{int}]\,|0\rangle + \frac{\alpha^2}{2!}[\hat{\eta}_\pi^\dagger, [\hat{\eta}_\pi^\dagger, \hat{H}_{int}]]\,|0\rangle + \ldots, \tag{A.23}$$

up to order $\lfloor \frac{L}{2} \rfloor$. As $|\psi(\alpha)\rangle$ vanishes, each of the states multiplying the corresponding power of α must vanish. Hence, the conditions of the lemma are satisfied and Eq. (A.11) is proved, which in turn implies the validity of Eq. (6.6).

A.2 Coordinate Bethe Ansatz in the fully paired subspace for the interacting term in Hamiltonian (6.4)

We start from the spinless fermion Hamiltonian (6.4) with $t = \mu = 0$ and rewrite it in PBC with a change in the sign of the pair hopping for the terms across the bond among sites L and 1:

$$\hat{H} = J\sum_{j=1}^{L-2}\left[\hat{n}_j\hat{n}_{j+1} + \hat{n}_{j+1}\hat{n}_{j+2} - 2\hat{n}_j\hat{n}_{j+1}\hat{n}_{j+2} - (\hat{c}_j^\dagger\hat{n}_{j+1}\hat{c}_{j+2} + H.c.)\right] + \tag{A.24}$$

$$+ J\left[\hat{n}_{L-1}\hat{n}_L + \hat{n}_L\hat{n}_1 - 2\hat{n}_{L-1}\hat{n}_L\hat{n}_1 + (\hat{c}_{L-1}^\dagger\hat{n}_L\hat{c}_1 + H.c.)\right] + \tag{A.25}$$

$$+ J\left[\hat{n}_L\hat{n}_1 + \hat{n}_1\hat{n}_2 - 2\hat{n}_L\hat{n}_1\hat{n}_2 + (\hat{c}_L^\dagger\hat{n}_1\hat{c}_2 + H.c.)\right]. \tag{A.26}$$

When rewritten in spin-1/2 language and in the sector of even parity (that the fully paired subspace belongs to), it takes the form:

$$\hat{H} = J\sum_{j=1}^{L}\left[\hat{n}_j\hat{n}_{j+1} + \hat{n}_{j+1}\hat{n}_{j+2} - 2\hat{n}_j\hat{n}_{j+1}\hat{n}_{j+2} + (\hat{\sigma}_j^+\hat{n}_{j+1}\hat{\sigma}_{j+2}^- + H.c.)\right], \tag{A.27}$$

where $\hat{n}_j = \frac{1+\hat{\sigma}_j^z}{2}$. In the following, we apply the coordinate Bethe Ansatz technique to the subspace spanned by fully paired configurations and write down Bethe equations for the momenta of the pairs first in the 1-pair problem and then in the 2-pair one, showing the lack of interactions among η-pairs.

A.2.1 1-pair problem

We search for a generic eigenstate in the 1-pair subspace by writing it in the form:

$$|\psi\rangle = \sum_{j=1}^{L} a(j)\hat{\sigma}_j^+\hat{\sigma}_{j+1}^+|\downarrow\rangle, \tag{A.28}$$

where $|\downarrow\rangle$ is the spin down ferromagnetic state. The Schroedinger equation $\hat{H}|\psi\rangle = E|\psi\rangle$ and the periodic boundary conditions read:

$$2Ja(j) + Ja(j-1) + Ja(j+1) = Ea(j), \tag{A.29}$$

$$a(L+j) = a(j). \tag{A.30}$$

Looking for a solution of the form $a(j) = Ae^{ikj}$, one obtains the conditions:

$$E = 2J + 2J\cos(k) \tag{A.31}$$

$$k = \frac{2\pi}{L}n, \;\; n = 0, \ldots, L-1. \tag{A.32}$$

When L is even, the 1-pair eta-pairing state $|\psi\rangle \propto \left(\sum_{j=1}^{L} e^{i\pi j}\hat{\sigma}_j^+\hat{\sigma}_{j+1}^+\right)|\downarrow\rangle$ is recovered.

A.2.2 2-pair problem

We search for a generic eigenstate in the 2-pair subspace by writing it in the form:

$$|\psi\rangle = \sum_{1\le j_1<j_2\le L} a(j_1,j_2)\hat{\sigma}_{j_1}^+\hat{\sigma}_{j_1+1}^+\hat{\sigma}_{j_2}^+\hat{\sigma}_{j_2+1}^+|\downarrow\rangle, \tag{A.33}$$

where one should notice that the term multiplying $a(j_1, j_1+1)$ vanishes. The Schroedinger equation $\hat{H}|\psi\rangle = E|\psi\rangle$ reads now:

$$4Ja(j_1,j_2) + Ja(j_1-1,j_2) + Ja(j_1+1,j_2) + Ja(j_1,j_2-1) + Ja(j_1,j_2+1) = Ea(j_1,j_2), \;\; j_2 > j_1+2 \tag{A.34}$$

$$2Ja(j_1,j_1+2) + Ja(j_1-1,j_2) + Ja(j_1,j_1+3) = Ea(j_1,j_1+2), \;\; j_2 = j_1+2, \tag{A.35}$$

while PBC are enforced through the equation:

$$a(j_1, j_2) = a(j_2, j_1 + L). \tag{A.36}$$

The Ansatz for the coefficients $a(j_1, j_2)$ takes the form:

$$a(j_1, j_2) = A_{12} e^{i(k_1 j_1 + k_2 j_2)} + A_{21} e^{i(k_2 j_1 + k_1 j_2)}. \tag{A.37}$$

The above Ansatz solves Eq. (A.34) with energy $E = 4J + 2J\cos(k_1) + 2J\cos(k_2)$, while Eq. (A.35) is solved by adding to it the terms such that it takes the same form as Eq. (A.34) and setting them to zero. The result of this procedure leads to the condition:

$$2Ja(j_1, j_1 + 2) + Ja(j_1 + 1, j_1 + 2) + Ja(j_1, j_1 + 1) = 0, \tag{A.38}$$

that amounts to requiring that:

$$\frac{A_{21}}{A_{12}} = -\frac{2e^{i2k_2} + e^{i(k_1+2k_2)} + e^{ik_2}}{2e^{i2k_1} + e^{i(k_2+2k_1)} + e^{ik_1}} := S(k_1, k_2), \tag{A.39}$$

where we have defined the scattering matrix $S(k_1, k_2)$ via the expression to its left.

Finally, imposing PBC, one obtains the relations:

$$A_{12} = A_{21} e^{ik_1 L}, \tag{A.40}$$

$$A_{21} = A_{12} e^{ik_2 L}, \tag{A.41}$$

which, owing to the property $S(k, k) = -1$, can be rewritten in the compact form:

$$\prod_{l=1}^{2} S(k_j, k_l) = -e^{-ik_j L}; \;\; j = 1, 2. \tag{A.42}$$

The result can be shown to generalize to the nontrivial three-pair case, thus proving the Bethe-Ansatz solvability of model (A.27) in the subspace spanned by fully-paired configurations.

It should be noticed that the two-pair η-pairing state, obtained for $k_1 = k_2 = \pi$, satisfies Eq. (A.38) for all values of A_{12}, A_{21} and the PBC in Eq. (A.36) for an even value of L, which impose $A_{12} = A_{21}$. The scattering matrix is ill-defined in this case, as the coefficient $a(j_1, j_2)$ reduces to:

$$a(j_1, j_2) \propto e^{i\pi j_1} e^{i\pi j_2}, \tag{A.43}$$

i.e., it factorizes into independent plane waves with quasimomentum π.

A.3 Finite-size formula for $P_k(r)$

We present here an explicit finite-size formula for $P_k(r)$ with $r > 3$. Straightforward combinatorial considerations give the result:

$$P_k(r) = (-1)^{r+1} \frac{\sum_{l=max\left(0, k-1-\lfloor \frac{L-r-2}{2} \rfloor\right)}^{min(k-1, \lfloor \frac{r-2}{2} \rfloor)} \binom{r-2-l}{l} \binom{L-1-r-k+l}{k-l-1}}{\frac{L}{L-k}\binom{L-k}{k}}. \tag{A.44}$$

A.4 The operator $\hat{O}$ annihilates the tower of states

The operator $\hat{O}$ takes the form $\hat{O} = J\sum_{j=2}^{L-2} \hat{O}_j$, where:

$$\begin{aligned} \hat{O}_j =& e^{i\pi(j-1)}(1 - 2\hat{n}_{j-1})\hat{n}_j \hat{c}^\dagger_{j+1} \hat{c}^\dagger_{j+2} + \\ &+ e^{i\pi(j-1)} \hat{c}^\dagger_{j-1} \hat{c}^\dagger_j \hat{n}_{j+1}(1 - 2\hat{n}_{j+2}) + \\ &+ e^{i\pi j} \hat{c}^\dagger_{j-1}(\hat{n}_j + \hat{n}_{j+1}) \hat{c}^\dagger_{j+2}. \end{aligned} \tag{A.45}$$

Hence, it suffices to show that $\hat{O}_j |\psi_{k,\pi}\rangle = 0$ for $2 \leq j \leq L-2$. We adopt the notation $\sum_{c:|x_1,\ldots,x_4\rangle} e^{i\pi \operatorname{sgn}(c)} |y_1,\ldots,y_4\rangle$ to denote the sum over all Fock states $|c\rangle$ contributing to the state $|\psi_{k,\pi}\rangle$ that have the form $|x_1,\ldots,x_4\rangle$ on sites $j-1, j, j+1, j+2$ prior to the application of $\hat{O}_j$ and the form $|y_1,\ldots,y_4\rangle$ after the application of $\hat{O}_j$, and where $\operatorname{sgn}(c) = \sum_{m=1}^{k} j_m$, j_m being the position of the first fermion of the m^{th} pair in the state $|\psi_{k,\pi}\rangle$. Then, it is easy to obtain:

$$\hat{O}_j |\psi_{k,\pi}\rangle = e^{i\pi j} \left(\sum_{c:|\bullet\bullet\circ\circ\rangle} e^{i\pi \operatorname{sgn}(c)} |\bullet\circ\bullet\bullet\rangle + \sum_{c:|\circ\circ\bullet\bullet\rangle} e^{i\pi \operatorname{sgn}(c)} |\bullet\circ\bullet\bullet\rangle + 2 \sum_{c:|\circ\bullet\bullet\circ\rangle} e^{i\pi \operatorname{sgn}(c)} |\bullet\circ\bullet\bullet\rangle \right). \tag{A.46}$$

The number of configurations contributing to the state $|\psi_{k,\pi}\rangle$ that locally, on sites $j-1, j, j+1, j+2$, have the form $|\bullet\bullet\circ\circ\rangle$ is equal to the number of those with the forms $|\circ\circ\bullet\bullet\rangle$ and $|\circ\bullet\bullet\circ\rangle$, and they can be put in a one-to-one correspondence with each other by mapping each configuration in of the aforesaid three collections to the one that is identical to it up to the different occupation of the highlighted sites $j-1, j, j+1, j+2$. Since the local configuration resulting from the application of $\hat{O}_j$ is the same in all three cases, the three summations are carried over the same set of configurations. On the other hand, the sign of each of the configurations in the last summation is the opposite of the sign of the corresponding ones in the first two summations, leading to the desired result $\hat{O}_j |\psi_{k,\pi}\rangle = 0$.

A.5 Macroscopic coherence of the state $|\alpha\rangle$

We derive here explicitly the result shown in Eq. (6.24). The explicit expression for the state $|\alpha\rangle$ reads:

$$|\alpha\rangle = \mathcal{N} \sum_{k=0}^{L/2} \sqrt{\frac{L}{L-k}\binom{L-k}{k}} \alpha^k |\psi_{k,\pi}\rangle, \tag{A.47}$$

where the normalization constant $\mathcal{N}$ satisfies:

$$|\mathcal{N}|^2 = \frac{1}{\sum_{k=0}^{L/2} \frac{L}{L-k}\binom{L-k}{k} |\alpha|^{2k}} \tag{A.48}$$

which results from imposing the normalization condition $\langle\alpha|\alpha\rangle = 1$.

Plugging the expression of the expansion coefficients in Eq. (A.47) into Eq. (6.19), one obtains:

$$\langle\alpha(t)| e^{i\pi j} \hat{c}_{j+1}\hat{c}_j |\alpha(t)\rangle = \alpha e^{i\frac{2\mu t}{\hbar}} \frac{\sum_{k=0}^{L/2-1} \binom{L-k-2}{k} |\alpha|^{2k}}{\sum_{k=0}^{L/2} \frac{L}{L-k}\binom{L-k}{k} |\alpha|^{2k}}. \tag{A.49}$$

If we assume self-consistently that the sums in the numerator and denominator of Eq. (A.49) will be dominated by terms with $k = O(L)$ and apply Stirling's approximation $n! \approx \sqrt{2\pi n} n^n e^{-n}$, one obtains, as a function of the rescaled variable $x = \frac{3k}{L}$:

$$\frac{L}{L-k}\binom{L-k}{k} |\alpha|^{2k} \approx g(x) e^{\frac{L}{3} f(x)}, \tag{A.50}$$

$$\binom{L-k-2}{k} |\alpha|^{2k} \approx h(x) e^{\frac{L}{3} f(x)} \tag{A.51}$$

in the limit of large L, where we have introduced the function:

$$f(x) = (3-x)\log(3-x) - x\log x - (3-2x)\log(3-2x) + (2\log|\alpha|)x, \tag{A.52}$$

$$g(x) = 3\sqrt{\frac{3}{2\pi L}} \sqrt{\frac{1}{x(3-x)(3-2x)}}, \tag{A.53}$$

$$h(x) = \sqrt{\frac{3}{2\pi L}} \sqrt{\frac{(3-2x)^3}{x(3-x)^3}}. \tag{A.54}$$

We proceed by converting the summations over k in Eq. (A.49) into continuous integrals over x and applying the saddle-point integration technique, in order to get to the final result:

$$\langle\alpha(t)|\, e^{i\pi j}\hat{c}_{j+1}\hat{c}_j\,|\alpha(t)\rangle = \alpha e^{i\frac{2\mu t}{\hbar}}\frac{\int_0^{\frac{3}{2}} dx h(x)e^{\frac{L}{3}f(x)}}{\int_0^{\frac{3}{2}} dx g(x)e^{\frac{L}{3}f(x)}} \approx \frac{h(x^*)}{g(x^*)} = \frac{1}{3}\frac{(3-2x^*)^2}{3-x^*}, \tag{A.55}$$

where:

$$x^* = \frac{3}{2}\left(1 - \frac{1}{\sqrt{1+4|\alpha|^2}}\right) \tag{A.56}$$

satisfies $f'(x^*) = 0$. Plugging the expression of x^* into Eq. (A.55), one recovers Eq. (6.24).

A.6 Entanglement entropy of the states $|\psi_{k,\pi}\rangle$

For the sake of convenience, we introduce the states:

$$|\psi_{k,q}\rangle = \frac{1}{\sqrt{\binom{L-k}{k}}}\frac{(\hat{\eta}_q^\dagger)^k}{k!}\,|0\rangle\,, \quad \text{with } \hat{\eta}_q^\dagger = \sum_{j=1}^{L} e^{iqj}\hat{c}_j^\dagger\hat{c}_{j+1}^\dagger. \tag{A.57}$$

Furthermore, we describe a general relation between the states $|\psi_{k,\pi}\rangle$ and the states $|\psi_{k,q}\rangle$. By introducing the unitary operator $\hat{U}_q = \prod_{j=1}^{L} e^{i\frac{\pi+q}{2}j\hat{n}_j}$, one can show that the following relation holds:

$$\hat{U}_q\hat{\eta}_\pi^\dagger\hat{U}_q^\dagger = e^{i\frac{\pi+q}{2}}\hat{\eta}_q^\dagger, \tag{A.58}$$

which in turn implies that:

$$|\psi_{k,q}\rangle = e^{-i\frac{\pi+q}{2}k}\hat{U}_q\,|\psi_{k,\pi}\rangle \tag{A.59}$$

Since the state $|\psi_{k,\pi}\rangle$ is related to the state $|\psi_{k,q}\rangle$ by a unitary transformation, we underline that the states $|\psi_{k,\pi}\rangle$ are eigenstates of $\hat{H}$ if and only if the states $|\psi_{k,q}\rangle$ are eigenstates of $\hat{U}_q\hat{H}\hat{U}_q^\dagger$.

We start by evaluating the half-chain entanglement entropy for the states $|\psi_{k,0}\rangle$. We can distinguish among the configurations in which no pair is placed on the sites $\frac{L}{2}$ and $\frac{L}{2}+1$ and the configurations in which this is instead the case:

$$\begin{aligned}|\psi_{k,0}\rangle =& \frac{1}{\sqrt{\binom{L-k}{k}}}\Bigg[\sum_{n=max\{0,\lceil\frac{N-L/2}{2}\rceil\}}^{min\{\frac{N}{2},\lfloor\frac{L/2}{2}\rfloor\}}\ \sum_{\substack{\{\vec{j}^{(n)}_{P,[1,\dots,\frac{L}{2}]}\}\\ \{\vec{j'}^{\left(\frac{N}{2}-n\right)}_{P,[\frac{L}{2}+1,\dots,L]}\}}} \left|\vec{j}^{(n)}_{P,[1,\dots,\frac{L}{2}]}\right\rangle \left|\vec{j'}^{\left(\frac{N}{2}-n\right)}_{P,[\frac{L}{2}+1,\dots,L]}\right\rangle + \\ &+ \sum_{l=max\{0,\lceil\frac{N-L/2-1}{2}\rceil\}}^{min\{\frac{N}{2}-1,\lfloor\frac{L/2-1}{2}\rfloor\}}\ \sum_{\substack{\{\vec{j}^{(n)}_{P,[1,\dots,\frac{L}{2}-1]}\}\\ \{\vec{j'}^{\left(\frac{N}{2}-1-n\right)}_{P,[\frac{L}{2}+2,\dots,L]}\}}} \left|\vec{j}^{(n)}_{P,[1,\dots,\frac{L}{2}-1]};\bullet\right\rangle \left|\bullet;\vec{j'}^{\left(\frac{N}{2}-1-n\right)}_{P,[\frac{L}{2}+2,\dots,L]}\right\rangle\Bigg],\end{aligned} \tag{A.60}$$

where the symbol $\bullet$ indicates an occupied site and the notation of the form $\left|\vec{j}^{(n)}_{P,[1,\dots,\frac{L}{2}]}\right\rangle$ denote the equal-weight (with unit weight, hence unnormalized) superposition of all possible distributions of n pairs over the sites $i = 1,\dots,\frac{L}{2}$. By denoting as $\mathcal{F}_R$ the set of Fock configurations on the right half of the chain,

the expression of the partial density matrix $\rho_{k,0}^{(\frac{L}{2})} = \mathrm{Tr}_{[\frac{L}{2}+1,\dots,L]}(|\psi_{k,0}\rangle\langle\psi_{k,0}|)$ takes then the form:

$$\begin{aligned}\rho_{k,0}^{(\frac{L}{2})} = \frac{1}{\binom{L-k}{k}} \sum_{k\in\mathcal{F}_R} \Bigg[\sum_{l=max\{0,\lceil\frac{N-L/2}{2}\rceil\}}^{min\{\frac{N}{2},\lfloor\frac{L/2}{2}\rfloor\}} \sum_{\substack{\{\vec{j}^{(n)}_{P,[1,\dots,\frac{L}{2}]}\} \\ \{\vec{l}^{(n)}_{P,[1,\dots,\frac{L}{2}]}\}}} \sum_{\substack{\{\vec{j'}^{(\frac{N}{2}-n)}_{P,[\frac{L}{2}+1,\dots,L]}\} \\ \{\vec{l'}^{(\frac{N}{2}-n)}_{P,[\frac{L}{2}+1,\dots,L]}\}}} \left|\vec{j}^{(n)}_{P,[1,\dots,\frac{L}{2}]}\right\rangle \left\langle\vec{l}^{(n)}_{P,[1,\dots,\frac{L}{2}]}\right| \times \\ \times \left\langle k\middle|\vec{j'}^{(\frac{N}{2}-n)}_{P,[\frac{L}{2}+1,\dots,L]}\right\rangle \left\langle\vec{l'}^{(\frac{N}{2}-n)}_{P,[\frac{L}{2}+1,\dots,L]}\middle|k\right\rangle + \\ + \sum_{l=max\{0,\lceil\frac{N-L/2-1}{2}\rceil\}}^{min\{\frac{N}{2}-1,\lfloor\frac{L/2-1}{2}\rfloor\}} \sum_{\substack{\{\vec{j}^{(n)}_{P,[1,\dots,\frac{L}{2}-1]}\} \\ \{\vec{l}^{(n)}_{P,[1,\dots,\frac{L}{2}-1]}\}}} \sum_{\substack{\{\vec{j'}^{(\frac{N}{2}-n)}_{P,[\frac{L}{2}+2,\dots,L]}\} \\ \{\vec{l'}^{(\frac{N}{2}-n)}_{P,[\frac{L}{2}+2,\dots,L]}\}}} \left|\vec{j}^{(n)}_{P,[1,\dots,\frac{L}{2}-1]};\bullet\right\rangle \left\langle\vec{l}^{(n)}_{P,[1,\dots,\frac{L}{2}-1]};\bullet\right| \times \\ \times \left\langle k\middle|\vec{j'}^{(\frac{N}{2}-1-n)}_{P,[\frac{L}{2}+2,\dots,L]};\bullet\right\rangle \left\langle\bullet;\vec{l'}^{(\frac{N}{2}-1-n)}_{P,[\frac{L}{2}+2,\dots,L]}\middle|k\right\rangle \Bigg].\end{aligned}$$

For every configuration $k \in \mathcal{F}_R$ that results in a nonvanishing scalar product in the above expression, one obtains the unnormalized equal-weight superposition with unit weight of all configurations in the left half of the system that are compatible with it. After normalizing the latter and counting all configurations $k \in \mathcal{F}_R$ that give a nonzero contribution, one obtains:

$$\begin{aligned}\rho_{k,0}^{(\frac{L}{2})} = &\sum_{l=max\{0,\lceil\frac{N-L/2}{2}\rceil\}}^{min\{\frac{N}{2},\lfloor\frac{L/2}{2}\rfloor\}} \left|\varphi_l^{[1,\dots,\frac{L}{2}]}\right\rangle \left\langle\varphi_l^{[1,\dots,\frac{L}{2}]}\right| \frac{\binom{\frac{L}{2}-\frac{N}{2}+l}{\frac{N}{2}-l}\binom{\frac{L}{2}-l}{l}}{\binom{L-\frac{N}{2}}{\frac{N}{2}}} + \\ &+ \sum_{l=max\{0,\lceil\frac{N-L/2-1}{2}\rceil\}}^{min\{\frac{N}{2}-1,\lfloor\frac{L/2-1}{2}\rfloor\}} \left|\varphi_l^{[1,\dots,\frac{L}{2}-1]}\right\rangle |\bullet\rangle \langle\bullet| \left\langle\varphi_l^{[1,\dots,\frac{L}{2}-1]}\right| \frac{\binom{\frac{L}{2}-\frac{N}{2}+l}{\frac{N}{2}-l-1}\binom{\frac{L}{2}-1-l}{l}}{\binom{L-\frac{N}{2}}{\frac{N}{2}}},\end{aligned} \tag{A.61}$$

where $\left|\varphi_l^{[1,\dots,s]}\right\rangle$ denotes the normalized equal-weight superposition of all Fock states with l pairs distributed over s lattice sites and $|\bullet\rangle$ indicates the occupation of site $\frac{L}{2}$. The eigenvalues λ_s of the reduced density matrix $\rho_{k,0}$ can be read off directly Eq. (A.61) as the coefficients of each term of the summations in Eq. (A.61), and the second Renyi entropy can be computed accordingly as $S_{\frac{L}{2},k,0} = -\log\left(\sum_s \lambda_s^2\right)$.

We now proceed to show that the half-chain entanglement entropy of the states $|\psi_{k,\pi}\rangle$ defined in Eq. (6.5) equals the one of the states $|\psi_{k,0}\rangle$ introduced via Eq. (A.59), thus showing that the subvolume entanglement scaling law holds for both towers of states. To this end, we recall the previously defined unitary operator $\hat{U}_0 = \prod_{j=1}^{L} e^{i\frac{\pi}{2}j\hat{n}_j}$. After using Eq. (A.59) and noticing that $\hat{U}_0$ factorizes as $\hat{U}_0 = \hat{U}_{0,[1,\frac{L}{2}]}\hat{U}_{0,[\frac{L}{2}+1,L]}$, where $\hat{U}_{0,[1,\frac{L}{2}]} = \prod_{j=1}^{\frac{L}{2}} e^{i\frac{\pi}{2}j\hat{n}_j}$ and $\hat{U}_{0,[\frac{L}{2}+1,L]} = \prod_{j=\frac{L}{2}+1}^{L} e^{i\frac{\pi}{2}j\hat{n}_j}$, the half-chain reduced density matrix for a generic state $|\psi_{k,\pi}\rangle$ can then be expressed as:

$$\begin{aligned}\rho_{k,\pi}^{(\frac{L}{2})} = &\frac{1}{(k!)^2\binom{L-k}{k}} \hat{U}_{0,[1,\frac{L}{2}]} \cdot \\ &\cdot \mathrm{Tr}_{[\frac{L}{2}+1,\dots,L]}\left[\hat{U}_{0,[\frac{L}{2}+1,L]}(\hat{\eta}_0^\dagger)^k |0\rangle\langle 0| (\hat{\eta}_0)^k \hat{U}^\dagger_{0,[\frac{L}{2}+1,L]}\right] \hat{U}^\dagger_{0,[1,\frac{L}{2}]}.\end{aligned} \tag{A.62}$$

By making use of the cyclic invariance property of the trace, the reduced density matrix for the states $|\psi_{k,\pi}\rangle$ is manifestly shown to be related to the corresponding quantity for the states $|\psi_{k,0}\rangle$ via a similarity transformation implemented by a unitary operator, i.e.:

$$\rho_{k,\pi}^{(\frac{L}{2})} = \hat{U}_{0,[1,\frac{L}{2}]} Tr_{[\frac{L}{2}+1,\dots,L]}\left[|\psi_{k,0}\rangle\langle\psi_{k,0}|\right] \hat{U}^\dagger_{0,[1,\frac{L}{2}]}, \tag{A.63}$$

which leaves the entanglement entropy unaffected.

We are now in a position to estimate the large-L scaling of the second Renyi entropy of the states $|\psi_{k,\pi}\rangle$ analytically in the case $k = L/3$, designed to ensure that the binomial coefficients in the numerator

of the combinatorial coefficient in the first row of Eq. (A.61) are peaked around the same value of $l = L/6 = O(L)$. After introducing the rescaled variable $x = 6l/L$, one obtains by means of the Stirling approximation the asymptotic behaviors:

$$\frac{\binom{\frac{L}{2}-\frac{N}{2}+l}{\frac{N}{2}-l}\binom{\frac{L}{2}-l}{l}}{\binom{L-\frac{N}{2}}{\frac{N}{2}}} \approx g(x)e^{\frac{L}{6}f(x)}, \tag{A.64}$$

$$\frac{\binom{\frac{L}{2}-\frac{N}{2}+l}{\frac{N}{2}-l-1}\binom{\frac{L}{2}-1-l}{l}}{\binom{L-\frac{N}{2}}{\frac{N}{2}}} \approx h(x)e^{\frac{L}{6}f(x)}, \tag{A.65}$$

where the large L limit has been taken and we have introduced the functions:

$$\begin{aligned} f(x) = {} & (1+x)\log(1+x) + (3-x)\log(3-x) - (2-x)\log(2-x) + \\ & - (2x-1)\log(2x-1) - x\log x - (3-2x)\log(3-2x) - 4\log 2, \end{aligned} \tag{A.66}$$

$$g(x) = \sqrt{\frac{3}{\pi L}\frac{(1+x)(3-x)}{x(2-x)(2x-1)(3-2x)}}, \tag{A.67}$$

$$h(x) = \frac{(2-x)(3-2x)}{(3-x)(2x-1)}g(x). \tag{A.68}$$

Armed with these expressions, we proceed to evaluate the argument of Eq. (6.26) by converting the discrete sums over l into continuous integrals over x and applying the saddle-point integration technique:

$$\begin{aligned} & \sum_{l=max\{0,\lceil\frac{N-L/2}{2}\rceil\}}^{min\{\frac{N}{2},\lfloor\frac{L/2}{2}\rfloor\}} \left(\frac{\binom{\frac{L}{2}-\frac{N}{2}+l}{\frac{N}{2}-l}\binom{\frac{L}{2}-l}{l}}{\binom{L-\frac{N}{2}}{\frac{N}{2}}}\right)^2 + \sum_{l=max\{0,\lceil\frac{N-L/2-1}{2}\rceil\}}^{min\{\frac{N}{2}-1,\lfloor\frac{L/2-1}{2}\rfloor\}} \left(\frac{\binom{\frac{L}{2}-\frac{N}{2}+l}{\frac{N}{2}-l-1}\binom{\frac{L}{2}-1-l}{l}}{\binom{L-\frac{N}{2}}{\frac{N}{2}}}\right)^2 \approx \\ & \approx \frac{L}{6}\left(\int_{\frac{1}{2}}^{\frac{3}{2}} dx\, g^2(x)e^{\frac{L}{3}f(x)} + \int_{\frac{1}{2}}^{\frac{3}{2}} dx\, h^2(x)e^{\frac{L}{3}f(x)}\right) \approx \frac{L}{6}e^{\frac{L}{3}f(x^*)}\sqrt{\frac{6\pi}{L|f''(x^*)|}}\left(g^2(x^*)+h^2(x^*)\right), \end{aligned} \tag{A.69}$$

where $x^* = 1$ satisfies $f'(x^*) = 0$ and $f''(x^*) < 0$. After a straightforward substitution of the numerical value of x^* in Eq. (A.69), one gets the result $\frac{5}{\sqrt{6\pi L}}$, which in turns gives the logarithmic scaling in Eq. (6.27) once plugged into Eq. (6.26).

As a final consistency check, we verify that the large L asymptotic behavior of the eigenvalues of the half-chain reduced density matrix $\rho_{k,\pi}^{(\frac{L}{2})}$ preserves the normalization condition that they are subject to. Specifically, we evaluate $\mathrm{Tr}\left[\rho_{k,\pi}^{(\frac{L}{2})}\right]$, namely:

$$\begin{aligned} & \sum_{l=max\{0,\lceil\frac{N-L/2}{2}\rceil\}}^{min\{\frac{N}{2},\lfloor\frac{L/2}{2}\rfloor\}} \frac{\binom{\frac{L}{2}-\frac{N}{2}+l}{\frac{N}{2}-l}\binom{\frac{L}{2}-l}{l}}{\binom{L-\frac{N}{2}}{\frac{N}{2}}} + \sum_{l=max\{0,\lceil\frac{N-L/2-1}{2}\rceil\}}^{min\{\frac{N}{2}-1,\lfloor\frac{L/2-1}{2}\rfloor\}} \frac{\binom{\frac{L}{2}-\frac{N}{2}+l}{\frac{N}{2}-l-1}\binom{\frac{L}{2}-1-l}{l}}{\binom{L-\frac{N}{2}}{\frac{N}{2}}} \approx \\ & \approx \frac{L}{6}\left(\int_{\frac{1}{2}}^{\frac{3}{2}} dx\, g(x)e^{\frac{L}{6}f(x)} + \int_{\frac{1}{2}}^{\frac{3}{2}} dx\, h(x)e^{\frac{L}{6}f(x)}\right) \approx \frac{L}{6}e^{\frac{L}{6}f(x^*)}\sqrt{\frac{12\pi}{L|f''(x^*)|}}\left(g(x^*)+h(x^*)\right) = 1, \end{aligned} \tag{A.70}$$

consistently with the expected result.

Bibliography

[1] J. Bardeen, L. N. Cooper, and J. R. Schrieffer, Phys. Rev. **108**, 1175 (1957), doi.

[2] D. Vollhardt and P. Wolfle, *The superfluid phases of helium 3* (Courier Corporation, 2013).

[3] E. Majorana, Il Nuovo Cimento (1924-1942) **14**, 171 (1937).

[4] A. Y. Kitaev, Physics-Uspekhi **44**, 131 (2001), doi.

[5] N. B. Kopnin and M. M. Salomaa, Phys. Rev. B **44**, 9667 (1991), doi.

[6] J. Alicea, Y. Oreg, G. Refael, F. Von Oppen, and M. Fisher, Nature Physics **7**, 412 (2011).

[7] N. Read and D. Green, Physical Review B **61**, 10267 (2000), doi.

[8] I. Bloch, J. Dalibard, and W. Zwerger, Rev. Mod. Phys. **80**, 885 (2008), doi.

[9] D. Jaksch, C. Bruder, J. I. Cirac, C. W. Gardiner, and P. Zoller, Phys. Rev. Lett. **81**, 3108 (1998), doi.

[10] M. Greiner, O. Mandel, T. Esslinger, T. W. Hänsch, and I. Bloch, Nature **415**, 39 (2002), doi.

[11] L. Jiang *et al.*, Phys. Rev. Lett. **106**, 220402 (2011), doi.

[12] H. M. Price, O. Zilberberg, T. Ozawa, I. Carusotto, and N. Goldman, Phys. Rev. Lett. **115**, 195303 (2015), doi.

[13] N. Barberán *et al.*, New Journal of Physics **17**, 125009 (2015), doi.

[14] H. Bernien *et al.*, Nature **551**, 579 (2017), doi.

[15] L. K. Joshi *et al.*, Phys. Rev. X **12**, 011018 (2022), doi.

[16] T. Giamarchi, *Quantum Physics in One Dimension* (Oxford University Press, 2003).

[17] E. Burovski, G. Orso, and T. Jolicoeur, Phys. Rev. Lett. **103**, 215301 (2009), doi.

[18] G. Orso, E. Burovski, and T. Jolicoeur, Phys. Rev. Lett. **104**, 065301 (2010), doi.

[19] G. Roux, E. Burovski, and T. Jolicoeur, Phys. Rev. A **83**, 053618 (2011), doi.

[20] A. E. Feiguin and F. Heidrich-Meisner, Phys. Rev. B **76**, 220508 (2007), doi.

[21] G. G. Batrouni, M. H. Huntley, V. G. Rousseau, and R. T. Scalettar, Phys. Rev. Lett. **100**, 116405 (2008), doi.

[22] M. Rizzi *et al.*, Phys. Rev. B **77**, 245105 (2008), doi.

[23] S. Moudgalya, N. Regnault, and B. A. Bernevig, Phys. Rev. B **102**, 085140 (2020), doi.

[24] D. K. Mark and O. I. Motrunich, Phys. Rev. B **102**, 075132 (2020), doi.

[25] A. Das *et al.*, Nature Physics **8**, 887 (2012).

[26] J. Ruhman and E. Altman, Phys. Rev. B **96**, 085133 (2017), doi.

[27] C. L. Kane, A. Stern, and B. I. Halperin, Phys. Rev. X **7**, 031009 (2017), doi.

[28] Y. He, B. Tian, D. Pekker, and R. S. K. Mong, Phys. Rev. B **100**, 201101 (2019), doi.

[29] L. P. Gor'kov, Sov. Phys. - JETP (Engl. Transl.); (United States) (1959).

[30] M. Cyrot, Reports on Progress in Physics **36**, 103 (1973), doi.

[31] J. G. Bednorz and K. A. Müller, Zeitschrift für Physik B Condensed Matter **64**, 189 (1986), doi.

[32] B. Keimer, S. A. Kivelson, M. R. Norman, S. Uchida, and J. Zaanen, Nature **518**, 179 (2015), doi.

[33] P. A. Lee, N. Nagaosa, and X.-G. Wen, Rev. Mod. Phys. **78**, 17 (2006), doi.

[34] C. Nayak, S. H. Simon, A. Stern, M. Freedman, and S. Das Sarma, Rev. Mod. Phys. **80**, 1083 (2008), doi.

[35] J. Alicea, Reports on Progress in Physics **75**, 076501 (2012), doi.

[36] L. Fu and C. L. Kane, Phys. Rev. B **79**, 161408 (2009), doi.

[37] M. Z. Hasan and C. L. Kane, Rev. Mod. Phys. **82**, 3045 (2010), doi.

[38] X.-L. Qi and S.-C. Zhang, Rev. Mod. Phys. **83**, 1057 (2011), doi.

[39] R. M. Lutchyn, J. D. Sau, and S. Das Sarma, Phys. Rev. Lett. **105**, 077001 (2010), doi.

[40] Y. Oreg, G. Refael, and F. von Oppen, Phys. Rev. Lett. **105**, 177002 (2010), doi.

[41] G. Moore and N. Read, Nuclear Physics B **360**, 362 (1991), doi.

[42] L. Fu and C. L. Kane, Phys. Rev. Lett. **100**, 096407 (2008), doi.

[43] J. D. Sau, R. M. Lutchyn, S. Tewari, and S. Das Sarma, Phys. Rev. Lett. **104**, 040502 (2010), doi.

[44] I. Bloch, J. Dalibard, and S. Nascimbène, Nature Physics **8**, 267 (2012), doi.

[45] J. F. Sherson *et al.*, Nature **467**, 68 (2010), doi.

[46] W. S. Bakr *et al.*, Science **329**, 547 (2010), eprint, doi.

[47] D. E. Liu, A. Levchenko, and H. U. Baranger, Phys. Rev. Lett. **111**, 047002 (2013), doi.

[48] M. Thakurathi, A. A. Patel, D. Sen, and A. Dutta, Phys. Rev. B **88**, 155133 (2013), doi.

[49] Y.-a. Liao *et al.*, Nature **467**, 567 (2010), doi.

[50] S. Capponi *et al.*, Phys. Rev. A **77**, 013624 (2008), doi.

[51] A. Rapp, G. Zaránd, C. Honerkamp, and W. Hofstetter, Phys. Rev. Lett. **98**, 160405 (2007), doi.

[52] P. Lecheminant *et al.*, International Journal of Modern Physics E **17**, 2110 (2008), eprint, doi.

[53] G. Roux, S. Capponi, P. Lecheminant, and P. Azaria, The European Physical Journal B **68**, 293 (2009), doi.

[54] M. Dalmonte *et al.*, Phys. Rev. B **92**, 045106 (2015), doi.

[55] M. Mattioli, M. Dalmonte, W. Lechner, and G. Pupillo, Phys. Rev. Lett. **111**, 165302 (2013), doi.

[56] P. Calabrese and J. Cardy, Journal of Statistical Mechanics: Theory and Experiment **2004**, P06002 (2004), doi.

[57] T. Mishra, J. Carrasquilla, and M. Rigol, Phys. Rev. B **84**, 115135 (2011), doi.

[58] M. Sitte, A. Rosch, J. S. Meyer, K. A. Matveev, and M. Garst, Phys. Rev. Lett. **102**, 176404 (2009), doi.

[59] P. Lecheminant, A. O. Gogolin, and A. A. Nersesyan, Nuclear Physics B **639**, 502 (2002), doi.

[60] L. Gotta, L. Mazza, P. Simon, and G. Roux, Phys. Rev. Research **3**, 013114 (2021), doi.

[61] G. Ortiz, J. Dukelsky, E. Cobanera, C. Esebbag, and C. Beenakker, Phys. Rev. Lett. **113**, 267002 (2014), doi.

[62] A. Keselman and E. Berg, Phys. Rev. B **91**, 235309 (2015), doi.

[63] N. Lang and H. P. Büchler, Phys. Rev. B **92**, 041118 (2015), doi.

[64] F. Iemini, L. Mazza, D. Rossini, R. Fazio, and S. Diehl, Phys. Rev. Lett. **115**, 156402 (2015), doi.

[65] G. Kells, Phys. Rev. B **92**, 155434 (2015), doi.

[66] F. Iemini *et al.*, Phys. Rev. Lett. **118**, 200404 (2017), doi.

[67] J. Ruhman, E. Berg, and E. Altman, Phys. Rev. Lett. **114**, 100401 (2015), doi.

[68] D. Poilblanc, S. Yunoki, S. Maekawa, and E. Dagotto, Phys. Rev. B **56**, R1645 (1997), doi.

[69] A. K. Zhuravlev, M. I. Katsnelson, and A. V. Trefilov, Phys. Rev. B **56**, 12939 (1997), doi.

[70] A. K. Zhuravlev and M. I. Katsnelson, Phys. Rev. B **61**, 15534 (2000), doi.

[71] A. K. Zhuravlev and M. I. Katsnelson, Phys. Rev. B **64**, 033102 (2001), doi.

[72] S. Ejima, F. Gebhard, S. Nishimoto, and Y. Ohta, Phys. Rev. B **72**, 033101 (2005), doi.

[73] C.-B. Duan and W.-Z. Wang, J. Phys.: Condens. Matter **23**, 365602 (2011), doi.

[74] M. Hohenadler, S. Wessel, M. Daghofer, and F. F. Assaad, Phys. Rev. B **85**, 195115 (2012), doi.

[75] Z.-H. Li, J. Phys.: Condens. Matter **31**, 255601 (2019), doi.

[76] J. Ren, X. Xu, L. Gu, and J. Li, Phys. Rev. A **86**, 064301 (2012), doi.

[77] K. Patrick, V. Caudrelier, Z. Papić, and J. K. Pachos, Phys. Rev. B **100**, 235128 (2019), doi.

[78] M. Szyniszewski and H. Schomerus, Phys. Rev. B **98**, 075139 (2018), doi.

[79] S. Capponi, D. Poilblanc, and T. Giamarchi, Phys. Rev. B **61**, 13410 (2000), doi.

[80] M. A. Cazalilla, J. Phys. B: At. Mol. Opt. Phys. **37**, S1 (2004), doi.

[81] U. Schollwöck, Rev. Mod. Phys. **77**, 259 (2005), doi.

[82] U. Schollwöck, Ann. Phys. **326**, 96 (2011), doi.

[83] F. Nogrette *et al.*, Phys. Rev. X **4**, 021034 (2014), doi.

[84] H. Labuhn *et al.*, Phys. Rev. A **90**, 023415 (2014), doi.

[85] W. Lee, H. Kim, and J. Ahn, Opt. Express **24**, 9816 (2016), doi.

[86] D. Barredo, S. d. Léséleuc, V. Lienhard, T. Lahaye, and A. Browaeys, Science **354**, 1021 (2016), doi.

[87] M. Endres *et al.*, Science **354**, 1024 (2016), doi.

[88] T. L. Nguyen *et al.*, Phys. Rev. X **8**, 011032 (2018), doi.

[89] A. Cooper *et al.*, Phys. Rev. X **8**, 041055 (2018), doi.

[90] I. S. Madjarov *et al.*, Phys. Rev. X **9**, 041052 (2019), doi.

[91] R. G. Cortiñas *et al.*, Phys. Rev. Lett. **124**, 123201 (2020), doi.

[92] T. F. Gallagher, *Rydberg Atoms*Cambridge Monographs on Atomic, Molecular and Chemical Physics (Cambridge University Press, 1994), doi.

[93] N. Sibalić and C. S. Adams, *Rydberg Physics* (IOP, 2018), doi.

[94] H. Weimer, M. Müller, I. Lesanovsky, P. Zoller, and H. P. Büchler, Nat. Phys. **6**, 382 (2010), doi.

[95] H. Labuhn *et al.*, Nature **534**, 667 (2016), doi.

[96] S. de Léséleuc *et al.*, Phys. Rev. Lett. **120**, 113602 (2018), doi.

[97] A. Browaeys and T. Lahaye, Nat. Phys. **16**, 132 (2020), doi.

[98] M. Fishman, S. R. White, and E. M. Stoudenmire, CoRR **abs/2007.14822** (2020), eprint, web.

[99] P. Calabrese and J. Cardy, Journal of Physics A: Mathematical and Theoretical **42**, 504005 (2009), doi.

[100] N. Laflorencie, E. S. Sørensen, M.-S. Chang, and I. Affleck, Phys. Rev. Lett. **96**, 100603 (2006), doi.

[101] I. Affleck, N. Laflorencie, and E. S. Sørensen, J. Phys. A **42**, 504009 (2009), doi.

[102] J. Cardy and C. P., J. Stat. Mech. , P04023 (2010), doi.

[103] M. Szyniszewski and E. Burovski, J. Phys.: Conf. Ser. **592**, 012057 (2015), doi.

[104] S. Rossotti, M. Teruzzi, D. Pini, D. E. Galli, and G. Bertaina, Phys. Rev. Lett. **119**, 215301 (2017), doi.

[105] P. Bak, Rep. Prog. Phys. **45**, 587 (1982), doi.

[106] N. Chepiga and F. Mila, Phys. Rev. Lett. **122**, 017205 (2019), doi.

[107] M. Rader and A. M. Läuchli, Floating Phases in One-Dimensional Rydberg Ising Chains, (2019), eprint.

[108] A. Luther and I. Peschel, Phys. Rev. B **12**, 3908 (1975), doi.

[109] V. Popkov and M. Salerno, Phys. Rev. A **71**, 012301 (2005), doi.

[110] L. Gotta, L. Mazza, P. Simon, and G. Roux, Phys. Rev. Lett. **126**, 206805 (2021), doi.

[111] L. Gotta, L. Mazza, P. Simon, and G. Roux, Phys. Rev. B **104**, 094521 (2021), doi.

[112] L. Fidkowski, R. M. Lutchyn, C. Nayak, and M. P. A. Fisher, Phys. Rev. B **84**, 195436 (2011), doi.

[113] J. D. Sau, B. I. Halperin, K. Flensberg, and S. Das Sarma, Phys. Rev. B **84**, 144509 (2011), doi.

[114] M. Cheng and H.-H. Tu, Phys. Rev. B **84**, 094503 (2011), doi.

[115] C. V. Kraus, M. Dalmonte, M. A. Baranov, A. M. Läuchli, and P. Zoller, Phys. Rev. Lett. **111**, 173004 (2013), doi.

[116] G. Ortiz, J. Dukelsky, E. Cobanera, C. Esebbag, and C. Beenakker, Phys. Rev. Lett. **113**, 267002 (2014), doi.

[117] G. Kells, Phys. Rev. B **92**, 155434 (2015), doi.

[118] N. Lang and H. P. Büchler, Phys. Rev. B **92**, 041118 (2015), doi.

[119] A. Keselman and E. Berg, Phys. Rev. B **91**, 235309 (2015), doi.

[120] F. Iemini, L. Mazza, D. Rossini, R. Fazio, and S. Diehl, Phys. Rev. Lett. **115**, 156402 (2015), doi.

[121] F. Iemini *et al.*, Phys. Rev. Lett. **118**, 200404 (2017), doi.

[122] Z. Wang, Y. Xu, H. Pu, and K. R. A. Hazzard, Phys. Rev. B **96**, 115110 (2017), doi.

[123] Y. Lin and A. J. Leggett, *Effect of Particle Number Conservation on the Berry Phase Resulting from Transport of a Bound Quasiparticle around a Superfluid Vortex*, (2017), unpublished, eprint.

[124] Y. Lin and A. J. Leggett, *Towards a Particle-Number Conserving Theory of Majorana Zero Modes in p+ip Superfluids*, (2018), unpublished, eprint.

[125] X. Y. Yin, T.-L. Ho, and X. Cui, New J. Phys. **21**, 013004 (2019), doi.

[126] M. F. Lapa and M. Levin, Phys. Rev. Lett. **124**, 257002 (2020), doi.

[127] K.-J.-B. Lee and P. Schlottmann, Phys. Rev. B **38**, 11566 (1988), doi.

[128] M. Guerrero, G. Ortiz, and J. E. Gubernatis, Phys. Rev. B **62**, 600 (2000), doi.

[129] P. Azaria, S. Capponi, and P. Lecheminant, Phys. Rev. A **80**, 041604 (2009), doi.

[130] K. A. Penson and M. Kolb, Phys. Rev. B **33**, 1663 (1986), doi.

[131] I. Affleck and J. B. Marston, J. Phys. C: Solid State Phys. **21**, 2511 (1988), doi.

[132] A. Hui and S. Doniach, Phys. Rev. B **48**, 2063 (1993), doi.

[133] A. E. Sikkema and I. Affleck, Phys. Rev. B **52**, 10207 (1995), doi.

[134] G. Bouzerar and G. I. Japaridze, Z. Phys. B **104**, 215 (1997), doi.

[135] G. I. Japaridze, A. P. Kampf, M. Sekania, P. Kakashvili, and P. Brune, Phys. Rev. B **65**, 014518 (2001), doi.

[136] F. Marsiglio and J. E. Hirsch, Phys. Rev. B **41**, 6435 (1990), doi.

[137] L. Arrachea, E. R. Gagliano, and A. A. Aligia, Phys. Rev. B **55**, 1173 (1997), doi.

[138] L. Zadnik and M. Fagotti, SciPost Phys. Core **4**, 10 (2021), doi.

[139] L. Zadnik, K. Bidzhiev, and M. Fagotti, SciPost Phys. **10**, 99 (2021), doi.

[140] R. Z. Bariev, J. Phys. A: Math. Gen. **24**, L549 (1991), doi.

[141] T. Bilitewski and N. R. Cooper, Phys. Rev. A **94**, 023630 (2016), doi.

[142] R. W. Chhajlany, P. R. Grzybowski, J. Stasińska, M. Lewenstein, and O. Dutta, Phys. Rev. Lett. **116**, 225303 (2016), doi.

[143] L. P. Pitaevskii and S. Stringari, *Bose-Einstein Condensation*International Series of Monographs on Physics (Clarendon Press, 2003), web.

[144] S. R. White, Phys. Rev. Lett. **69**, 2863 (1992), doi.

[145] S. R. White, Phys. Rev. B **48**, 10345 (1993), doi.

[146] L. Balents, Phys. Rev. B **61**, 4429 (2000), doi.

[147] M. Tovmasyan, E. P. L. van Nieuwenburg, and S. D. Huber, Phys. Rev. B **88**, 220510(R) (2013), doi.

[148] S. Takayoshi, H. Katsura, N. Watanabe, and H. Aoki, Phys. Rev. A **88**, 063613 (2013), doi.

[149] J. Jünemann *et al.*, Phys. Rev. X **7**, 031057 (2017), doi.

[150] S. D. Huber and E. Altman, Phys. Rev. B **82**, 184502 (2010), doi.

[151] E. Suárez Morell, J. D. Correa, P. Vargas, M. Pacheco, and Z. Barticevic, Phys. Rev. B **82**, 121407 (2010), doi.

[152] M. Xie and A. H. MacDonald, Phys. Rev. Lett. **124**, 097601 (2020), doi.

[153] K. Kobayashi, M. Okumura, S. Yamada, M. Machida, and H. Aoki, Phys. Rev. B **94**, 214501 (2016), doi.

[154] G. Tarnopolsky, A. J. Kruchkov, and A. Vishwanath, Phys. Rev. Lett. **122**, 106405 (2019), doi.

[155] M. Yankowitz *et al.*, Science **363**, 1059 (2019), eprint, doi.

[156] B. Roy and V. Juričić, Phys. Rev. B **99**, 121407 (2019), doi.

[157] R. W. Chhajlany, P. R. Grzybowski, J. Stasińska, M. Lewenstein, and O. Dutta, Phys. Rev. Lett. **116**, 225303 (2016), doi.

[158] L. Zadnik and M. Fagotti, SciPost Phys. Core **4**, 10 (2021), doi.

[159] L. Gotta, L. Mazza, P. Simon, and G. Roux, Phys. Rev. B **105**, 134512 (2022), doi.

[160] H.-W. Hammer and L. Platter, Annual Review of Nuclear and Particle Science **60**, 207 (2010), doi.

[161] E. Braaten and H.-W. Hammer, Annals of Physics **322**, 120 (2007), doi, January Special Issue 2007.

[162] P. Schuck *et al.*, **91**, 123001 (2016), doi.

[163] X.-W. Guan, M. T. Batchelor, and C. Lee, Rev. Mod. Phys. **85**, 1633 (2013), doi.

[164] V. N. Efimov, Yadern. Fiz. **12**, 1080 (1970).

[165] V. Efimov, Nuclear Physics A **210**, 157 (1973), doi.

[166] D. S. Petrov, Phys. Rev. A **67**, 010703 (2003), doi.

[167] S. Piatecki and W. Krauth, Nature Communications **5**, 3503 (2014), doi.

[168] J. Carlson, S. Gandolfi, U. van Kolck, and S. A. Vitiello, Phys. Rev. Lett. **119**, 223002 (2017), doi.

[169] M. Kunitski *et al.*, Science **348**, 551 (2015), doi.

[170] E. Kolganova, A. Motovilov, and W. Sandhas, Few-Body Systems **58**, 35 (2017), doi.

[171] A. Rapp, G. Zaránd, C. Honerkamp, and W. Hofstetter, Phys. Rev. Lett. **98**, 160405 (2007), doi.

[172] X. W. Guan, M. T. Batchelor, C. Lee, and J. Y. Lee, EPL (Europhysics Letters) **86**, 50003 (2009), doi.

[173] S. Backes, I. Titvinidze, A. Privitera, and W. Hofstetter, Phys. Rev. A **86**, 013633 (2012), doi.

[174] P. Niemann and H.-W. Hammer, Phys. Rev. A **86**, 013628 (2012), doi.

[175] J. Pohlmann, A. Privitera, I. Titvinidze, and W. Hofstetter, Phys. Rev. A **87**, 023617 (2013), doi.

[176] P. E. Kornilovitch, EPL (Europhysics Letters) **103**, 27005 (2013), doi.

[177] C. C. N. Kuhn and A. Foerster, New Journal of Physics **14**, 013008 (2012), doi.

[178] P. He, Y. Jiang, X. Guan, and J. He, Journal of Physics A: Mathematical and Theoretical **48**, 015002 (2014), doi.

[179] E. Szirmai, G. Barcza, J. Sólyom, and O. Legeza, Phys. Rev. A **95**, 013610 (2017), doi.

[180] T. Keilmann, I. Cirac, and T. Roscilde, Phys. Rev. Lett. **102**, 255304 (2009), doi.

[181] M. Dalmonte *et al.*, Phys. Rev. A **85**, 063608 (2012), doi.

[182] W. Zhang, R. Li, W. X. Zhang, C. B. Duan, and T. C. Scott, Phys. Rev. A **90**, 033622 (2014), doi.

[183] E.-N. Fan, T. C. Scott, and W.-Z. Zhang, **26**, 043701 (2017), doi.

[184] Y.-Z. You, Z. Chen, X.-Q. Sun, and H. Zhai, Phys. Rev. Lett. **109**, 265302 (2012), doi.

[185] W. Zhang, Y. Yang, L. Guo, C. Ding, and T. C. Scott, Phys. Rev. A **91**, 033613 (2015), doi.

[186] G. Guijarro, G. E. Astrakharchik, J. Boronat, B. Bazak, and D. S. Petrov, Phys. Rev. A **101**, 041602 (2020), doi.

[187] S. Musolino *et al.*, Phys. Rev. Lett. **128**, 020401 (2022), doi.

[188] N. Read and E. Rezayi, Phys. Rev. B **59**, 8084 (1999), doi.

[189] L. Mazza, F. Iemini, M. Dalmonte, and C. Mora, Phys. Rev. B **98**, 201109 (2018), doi.

[190] J. M. Deutsch, Phys. Rev. A **43**, 2046 (1991), doi.

[191] M. Srednicki, Phys. Rev. E **50**, 888 (1994), doi.

[192] M. Rigol, V. Dunjko, and M. Olshanii, Nature **452**, 854 (2008).

[193] J. M. Deutsch, Reports on Progress in Physics **81**, 082001 (2018).

[194] L. Vidmar and M. Rigol, Journal of Statistical Mechanics: Theory and Experiment **2016**, 064007 (2016), doi.

[195] F. H. L. Essler and M. Fagotti, Journal of Statistical Mechanics: Theory and Experiment **2016**, 064002 (2016), doi.

[196] M. Rigol, V. Dunjko, V. Yurovsky, and M. Olshanii, Phys. Rev. Lett. **98**, 050405 (2007), doi.

[197] P. Calabrese, F. H. L. Essler, and M. Fagotti, Phys. Rev. Lett. **106**, 227203 (2011), doi.

[198] B. Pozsgay, Journal of Statistical Mechanics: Theory and Experiment **2013**, P07003 (2013), doi.

[199] M. Fagotti and F. H. L. Essler, Journal of Statistical Mechanics: Theory and Experiment **2013**, P07012 (2013), doi.

[200] T. M. Wright, M. Rigol, M. J. Davis, and K. V. Kheruntsyan, Phys. Rev. Lett. **113**, 050601 (2014), doi.

[201] E. Ilievski *et al.*, Phys. Rev. Lett. **115**, 157201 (2015), doi.

[202] D. Basko, I. Aleiner, and B. Altshuler, Annals of Physics **321**, 1126 (2006), doi.

[203] J. H. Bardarson, F. Pollmann, and J. E. Moore, Phys. Rev. Lett. **109**, 017202 (2012), doi.

[204] M. Serbyn, Z. Papić, and D. A. Abanin, Phys. Rev. Lett. **110**, 260601 (2013), doi.

[205] M. Serbyn, Z. Papić, and D. A. Abanin, Phys. Rev. Lett. **111**, 127201 (2013), doi.

[206] D. A. Huse, R. Nandkishore, and V. Oganesyan, Phys. Rev. B **90**, 174202 (2014), doi.

[207] D. J. Luitz, N. Laflorencie, and F. Alet, Phys. Rev. B **91**, 081103 (2015), doi.

[208] A. Chandran, I. H. Kim, G. Vidal, and D. A. Abanin, Phys. Rev. B **91**, 085425 (2015), doi.

[209] V. Ros, M. Müller, and A. Scardicchio, Nuclear Physics B **891**, 420 (2015), doi.

[210] R. Nandkishore and D. A. Huse, Annual Review of Condensed Matter Physics **6**, 15 (2015), doi.

[211] C. J. Turner, A. A. Michailidis, D. A. Abanin, M. Serbyn, and Z. Papić, Nature Physics **14**, 745 (2018), doi.

[212] S. Moudgalya, B. A. Bernevig, and N. Regnault, Reports on Progress in Physics **85**, 086501 (2022), doi.

[213] Z. Papić, arXiv preprint arXiv:2108.03460 (2021), doi.

[214] A. Chandran, T. Iadecola, V. Khemani, and R. Moessner, Quantum Many-Body Scars: A Quasiparticle Perspective, (2022), doi.

[215] S. Moudgalya, S. Rachel, B. A. Bernevig, and N. Regnault, Phys. Rev. B **98**, 235155 (2018), doi.

[216] S. Moudgalya, N. Regnault, and B. A. Bernevig, Phys. Rev. B **98**, 235156 (2018), doi.

[217] S. Moudgalya, E. OBrien, B. A. Bernevig, P. Fendley, and N. Regnault, Phys. Rev. B **102**, 085120 (2020), doi.

[218] C.-J. Lin and O. I. Motrunich, Phys. Rev. Lett. **122**, 173401 (2019), doi.

[219] S. Chattopadhyay, H. Pichler, M. D. Lukin, and W. W. Ho, Phys. Rev. B **101**, 174308 (2020), doi.

[220] D. K. Mark, C.-J. Lin, and O. I. Motrunich, Phys. Rev. B **101**, 195131 (2020), doi.

[221] N. Shiraishi and T. Mori, Phys. Rev. Lett. **119**, 030601 (2017), doi.

[222] T. Iadecola and M. Schecter, Phys. Rev. B **101**, 024306 (2020), doi.

[223] C. M. Langlett and S. Xu, Phys. Rev. B **103**, L220304 (2021), doi.

[224] N. Shibata, N. Yoshioka, and H. Katsura, Phys. Rev. Lett. **124**, 180604 (2020), doi.

[225] J.-Y. Desaules, A. Hudomal, C. J. Turner, and Z. Papić, Phys. Rev. Lett. **126**, 210601 (2021), doi.

[226] S. Moudgalya, B. A. Bernevig, and N. Regnault, Phys. Rev. B **102**, 195150 (2020), doi.

[227] C. J. Turner, A. A. Michailidis, D. A. Abanin, M. Serbyn, and Z. Papić, Phys. Rev. B **98**, 155134 (2018), doi.

[228] C. N. Yang, Phys. Rev. Lett. **63**, 2144 (1989), doi.

[229] O. Vafek, N. Regnault, and B. A. Bernevig, SciPost Phys. **3**, 043 (2017), doi.

[230] S. Choi *et al.*, Phys. Rev. Lett. **122**, 220603 (2019), doi.

[231] M. Schecter and T. Iadecola, Phys. Rev. Lett. **123**, 147201 (2019), doi.

[232] K. Pakrouski, P. N. Pallegar, F. K. Popov, and I. R. Klebanov, Phys. Rev. Lett. **125**, 230602 (2020), doi.

[233] M. Nakagawa, H. Katsura, and M. Ueda, arXiv (2022), doi.

[234] H. Yoshida and H. Katsura, Phys. Rev. B **105**, 024520 (2022), doi.

[235] A. M. Alhambra, A. Anshu, and H. Wilming, Phys. Rev. B **101**, 205107 (2020), doi.

[236] J. Ren, C. Liang, and C. Fang, Phys. Rev. Lett. **126**, 120604 (2021), doi.

[237] N. O'Dea, F. Burnell, A. Chandran, and V. Khemani, Phys. Rev. Research **2**, 043305 (2020), doi.

[238] K. Tamura and H. Katsura, arXiv (2022), doi.

[239] T. Iadecola, M. Schecter, and S. Xu, Phys. Rev. B **100**, 184312 (2019), doi.

[240] L. P. Pitaevskii and S. Stringari, *Bose-Einstein Condensation* (Oxford University Press, 2003).

[241] P. Weinberg and M. Bukov, SciPost Phys. **2**, 003 (2017), doi.

[242] P. Weinberg and M. Bukov, SciPost Phys. **7**, 20 (2019), doi.

[243] Y. Y. Atas, E. Bogomolny, O. Giraud, and G. Roux, Phys. Rev. Lett. **110**, 084101 (2013), doi.

[244] M. Fagotti, M. Collura, F. H. L. Essler, and P. Calabrese, Phys. Rev. B **89**, 125101 (2014), doi.

[245] M. Schiulaz, A. Silva, and M. Müller, Phys. Rev. B **91**, 184202 (2015), doi.

[246] N. Y. Yao, C. R. Laumann, J. I. Cirac, M. D. Lukin, and J. E. Moore, Phys. Rev. Lett. **117**, 240601 (2016), doi.

[247] A. Smith, J. Knolle, D. L. Kovrizhin, and R. Moessner, Phys. Rev. Lett. **118**, 266601 (2017), doi.

[248] N. D. Oppong *et al.*, Probing transport and slow relaxation in the mass-imbalanced Fermi-Hubbard model, (2020), doi.

[249] Y. E. Kraus, O. Zilberberg, and R. Berkovits, Phys. Rev. B **89**, 161106 (2014), doi.